

**Messung und Simulation des Fragmentationsprozesses  
bei HERMES**

**Measurement and Simulation of the Fragmentation  
Process at HERMES**

Den Naturwissenschaftlichen Fakultäten  
der Friedrich-Alexander-Universität Erlangen-Nürnberg  
zur  
Erlangung des Doktorgrades

vorgelegt von  
**Achim Hillenbrand**  
aus Erlangen

Als Dissertation genehmigt von den  
Naturwissenschaftlichen Fakultäten  
der Universität Erlangen-Nürnberg

Tag der mündlichen Prüfung:	29. September 2005
Vorsitzender der Promotionskommission:	Prof. Dr. D.-P. Häder
Erstberichterstatter:	Prof. Dr. K. Rith
Zweitberichterstatter:	Prof. Dr. U. Katz

# Contents

<b>1</b>	<b>Introduction</b>	<b>1</b>
<b>2</b>	<b>Deep Inelastic Scattering</b>	<b>5</b>
2.1	Kinematics . . . . .	5
2.2	Cross Section . . . . .	8
2.3	The Quark Parton Model . . . . .	10
2.3.1	The Simple Quark Parton Model . . . . .	10
2.3.2	The QCD-improved Quark Parton Model . . . . .	11
2.4	Hadronic Final States & Fragmentation Functions . . . . .	13
2.4.1	Properties of fragmentation functions . . . . .	14
2.4.2	Existing Measurements . . . . .	16
<b>3</b>	<b>The HERMES Experiment</b>	<b>19</b>
3.1	The HERA Accelerator . . . . .	19
3.2	The Internal Gas Target . . . . .	20
3.3	The Spectrometer . . . . .	22
3.3.1	Tracking . . . . .	23
3.3.2	Particle Identification (PID) . . . . .	23
3.4	Data Structure & Data Acquisition System . . . . .	25
3.4.1	Data Structure . . . . .	25
3.4.2	Data Acquisition & Production . . . . .	27
<b>4</b>	<b>Monte Carlo Simulation</b>	<b>31</b>
4.1	The HERMES Monte Carlo Setup . . . . .	32
4.1.1	Event Generators . . . . .	33
4.2	The HERMES Smearing Generator . . . . .	33
4.2.1	Implementation . . . . .	34
4.2.2	Comparison of Tracked and Smeared Data . . . . .	37
4.3	Fragmentation Models . . . . .	38
4.3.1	The Lund Model . . . . .	40
4.3.2	Alternative Models . . . . .	43
4.4	Fragmentation Tuning . . . . .	45
4.4.1	The Fitting Procedure . . . . .	47
4.4.2	Results . . . . .	49

4.4.3	Conclusion . . . . .	55
<b>5</b>	<b>Extraction of Born Multiplicities</b>	<b>57</b>
5.1	Data Selection . . . . .	57
5.1.1	Burst Selection Cuts . . . . .	59
5.1.2	Cuts on Track and Event Level . . . . .	60
5.2	Particle Identification and RICH Unfolding . . . . .	61
5.2.1	Discriminating Leptons and Hadrons . . . . .	62
5.2.2	Identification of Hadrons with the RICH . . . . .	63
5.3	Background Corrections . . . . .	68
5.3.1	Charge Symmetric Background . . . . .	68
5.3.2	Elastic Vector Meson Production . . . . .	70
5.4	Correction for Radiative & Detector Smearing . . . . .	73
5.4.1	Motivation . . . . .	73
5.4.2	The Correction Method . . . . .	75
5.4.3	Practical Implementation . . . . .	78
5.4.4	Error Propagation & Systematic Error . . . . .	82
5.5	$Q^2$ Evolution . . . . .	82
5.6	Summary . . . . .	86
<b>6</b>	<b>Results</b>	<b>91</b>
6.1	Pion Results . . . . .	92
6.2	Kaon Results . . . . .	105
<b>7</b>	<b>Conclusion</b>	<b>111</b>
<b>A</b>	<b>Tables: Multiplicities vs. <math>z</math></b>	<b>113</b>
<b>B</b>	<b>Tables: Multiplicities vs. <math>x_B</math></b>	<b>127</b>
<b>C</b>	<b>Tables: Multiplicities vs. <math>Q^2</math></b>	<b>145</b>
	<b>List of Figures</b>	<b>155</b>
	<b>List of Tables</b>	<b>159</b>
	<b>Bibliography</b>	<b>161</b>
	<b>Acknowledgment</b>	<b>169</b>
	<b>Zusammenfassung</b>	<b>171</b>
	<b>Lebenslauf</b>	<b>173</b>

# Chapter 1

## Introduction

Since the days of Rutherford [Rut11], scattering experiments are the fundamental tool to study the structure and composition of sub-atomic objects as well as the properties of matter under extreme conditions. A vast number of processes have been studied, ranging from the scattering of very simple (fundamental) particles (e.g.  $e^+e^-$  annihilation) to rather complex objects (e.g. scattering of relativistic gold ions at RHIC). Depending on the involved objects and the respective energies, these experiments provide insight in such diverse topics as the nature of the interactions, the spectrum of particles and their internal structure. New experiments, like the heavy ion collider RHIC at BNL, are designed to analyse matter under extreme conditions similar to the beginning of the universe.

The fundamental process studied with the HERMES experiment is deep inelastic scattering (DIS). DIS uses a simple probe — a lepton — to reveal the structure of nucleons. In the most simple form, the interaction is mediated by a virtual photon. Given a high enough energy, the virtual photon can resolve the internal structure of the nucleon by interacting with one of its building blocks, the quarks and antiquarks. Deep inelastic scattering has first been realised at the Stanford Linear Accelerator Center (SLAC) in the 1960s, and it were these results which presented the first experimental evidence for the point-like substructure of the nucleon [Blo69].

In the models interpreting the SLAC results ([Fey69], [Bj69]), these point-like objects were denoted as partons. It was then suggested that these partons in fact are identical to the quarks introduced earlier by Gell-Mann [GM64]. In Gell-Mann's quark model, they served the purpose to explain the spectrum of hadrons observed in the various scattering experiments by postulating that baryons and mesons consist of three quarks or a quark-antiquark pair, respectively. Since the model requires the quarks to have electric charges of fractions of  $1/3$  and  $2/3$  with respect to the electron charge, they were widely considered to be more mathematical objects than real particles. Furthermore, the quarks were supposed to be fermions, and thus subject to the Pauli exclusion principle. But with the  $\Delta^{++}$  there existed a particle which was supposed to consist of three quarks of the lightest kind, with all of their spins aligned to give the  $3/2$  spin of the hadron.

The SLAC results gave new support to the quark theory, and in the early 1970s the studies resulted in the development of Quantum Chromodynamics (QCD). In this model,

quarks carry a new quantum number, the colour charge. This charge gives rise to the strong interaction which is mediated by new exchange bosons, the gluons. The charge comes in three variants, denoted as *red*, *green* and *blue* (and their anti-colours), which explains why three otherwise identical light quarks can share the same state to form the  $\Delta^{++}$  hadron. One speciality of the QCD model is the fact that the exchange bosons themselves also carry colour charge, which leads to the self-coupling of the gluons. Due to this self-coupling, the coupling strength  $\alpha_s$  of the strong interaction depends on the scale on which the interaction is observed. At short distances (which means high energies) the coupling strength approaches zero, which is referred to as the *asymptotic freedom* of quarks. Conversely, with lower energies and larger scales,  $\alpha_s$  increases, so that it would require infinite energy to separate two coloured objects. This gives rise to the *confinement* of quarks and gluons inside colourless particles. This feature is experimentally supported by the fact that to date no free quarks have been observed.

Using the powerful tool of perturbation theory, QCD has been very successful in describing the hard processes between the quasi-free quarks and gluons at short distances and time scales. However, perturbative QCD (pQCD) cannot be applied in the domain of long distances, where  $\alpha_s$  becomes large and the perturbative expansions diverge. This is a major shortcoming; after all, it are the long range effects that lead to the creation of the observable final state hadrons. So effectively, there is a missing link between the part calculable in theory, and the effects observable in the real world. A tool that eventually might overcome this obstacle are lattice QCD calculations, which use a four-dimensional space-time grid to perform numerical calculations not constraint by the size of the coupling constant. But still there are enormous technical difficulties to overcome.

The remedy for the unpleasant situation of not having a clear analytical explanation how hadrons develop out of quarks and gluons is the concept of *factorisation*. Factorisation allows to split a QCD process like DIS into the hard partonic sub-process (the photon-quark scattering), and the long range part related to the initial and final state particles. The former is calculable by pQCD, while the intractable part is transferred into a set of parametrisation functions. In DIS, there are two domains for parametrisation functions: the initial state nucleon is described by parton distribution functions (PDF), while the hadronisation into the final state is parametrised by fragmentation functions.

HERMES was constructed to study the spin dependence of the parton distribution functions. More precisely, it was designed to disentangle the contribution of the individual quark flavours to the total spin of the nucleon. Its development was triggered by the observation of the EMC experiment that only a small part of the nucleon spin can be attributed to its constituent quarks [Ash88]. Recent results represent the most detailed study of the nucleon spin structure to date [Air05].

This work is concerned with the other domain of parametrisations: the fragmentation of quarks into hadrons. The multiplicity of hadrons versus various kinematic observables provide the experimental access to the fragmentation process. Using the great particle identification capabilities of the HERMES spectrometer, charge and hadron type separated hadron yields were extracted. The multiplicities were corrected for various influences, like radiative and detector effects (e.g. acceptance) as well as diffractive contributions to the hadron sample, to obtain universal Born multiplicities.

Another focus of this work is the Monte Carlo simulation of fragmentation. Lacking a strict mathematical description of the process, phenomenological models have to be employed to obtain the final state of a scattering event. Taking the hadron multiplicities as reference, the Lund model used in the HERMES Monte Carlo programs was adjusted to the HERMES kinematics. Also here, the RICH information allowed a more precise tuning than previous efforts.

The outline of this thesis is as follows: In Chapter 2, the framework of deep-inelastic scattering and quark fragmentation is reviewed. The HERMES experiment is described in Chapter 3. Chapter 4 first gives an overview about the Monte Carlo tools used in the collaboration, with an emphasis on the smearing generator which was implemented for the tuning of the Lund model. After a description of the model itself the tuning procedure and its results are presented. Chapter 5 is concerned with the extraction of the hadron multiplicities. The final results are presented in Chapter 6.





# Chapter 2

## Deep Inelastic Scattering

Scattering processes are an essential tool in nuclear and particle physics. Depending on the beam and target objects and their relative energy, scattering processes can provide a wealth of information about the properties of the interactions and insight into the internal structure — if any — of the involved bodies.

In the following, the kinematic quantities used throughout this work are defined. This section is followed by the discussion of the DIS cross section. Its properties are explained by the quark parton model (Sec. 2.3). The last part is concerned with the hadronic final state of a DIS scattering process. The fragmentation functions are introduced, which offer a phenomenological description of the appearance of the final state hadrons. Some examples of the wide range of measurements of the hadronisation process concludes this chapter.

This chapter makes use of Refs. [Hal84], [Bro94], [Ber02] and [Pov04], as well as other sources mentioned throughout the text.

### 2.1 Kinematics

The main process of interest throughout this work is deep-inelastic lepton-nucleon scattering. More precisely, the analysed data was obtained with a positron beam incident on a proton or deuteron target. In deep-inelastic scattering (DIS), the positron interacts with the nucleon in such a way that the target is broken up into several final state hadrons,

$$l + N \rightarrow l' + X. \quad (2.1)$$

In inclusive measurements, only the scattered lepton  $l'$  is detected, while in semi-inclusive measurements one or more of the final state hadrons  $X$  are measured in coincidence.

Figure 2.1 shows a schematic view of this process in the one-photon-exchange approximation. The interaction between the positron and the target can in principle be mediated by a virtual photon,  $\gamma^*$ , or a virtual  $Z$ -boson. However, the beam energy of 27.5 GeV (and thus the maximal transferred energy) is well below the  $Z^0$  mass<sup>1</sup> of 91 GeV, thus the weak interaction can be neglected.

---

<sup>1</sup>Throughout this work, the notation  $\hbar = c = 1$  is used.

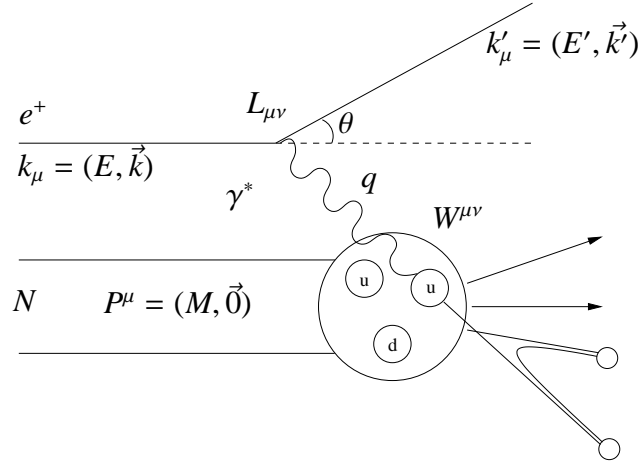


**Figure 2.1**

Schematic view of a deep inelastic scattering event on a proton target.

The kinematics of a scattering event is given by the the four-momenta of the lepton before ( $\mathbf{k} = (E, \vec{k})$ ) and after ( $\mathbf{k}' = (E', \vec{k}')$ ) scattering, as well as the corresponding four-vector of the target nucleon,  $\mathbf{P} = (E_N, \vec{P})$ . With these vectors three Lorentz invariant quantities can be defined which characterise the event:

$$Q^2 = -q^2 = -(\mathbf{k} - \mathbf{k}')^2 \stackrel{lab}{\simeq} 4EE' \sin^2\left(\frac{\theta}{2}\right) \quad (2.2)$$

$$W^2 = (\mathbf{P} + \mathbf{q})^2 \stackrel{lab}{=} M^2 + 2M\nu - Q^2 \quad (2.3)$$

$$s = (\mathbf{P} + \mathbf{k})^2 \stackrel{lab}{\simeq} M^2 + 2ME \quad (2.4)$$

Here,  $M$  denotes the nucleon mass and  $\nu = E - E'$  the energy transfer from the beam particle to the target. The expressions in the laboratory frame hold for fixed targets ( $P = (M, 0)$ ) and energies high enough to neglect the lepton mass.

The spatial resolution of the scattering process is inversely proportional to the negative squared four-momentum  $Q^2$  of the virtual photon.  $W^2$  denotes the squared invariant mass of the hadronic final state. For elastic scattering,  $W^2 = M^2$  so that  $Q^2 - 2M\nu = 0$ . The Björken scaling variable

$$x_B \equiv \frac{Q^2}{2\mathbf{P} \cdot \mathbf{q}} \stackrel{lab}{=} \frac{Q^2}{2M\nu} \quad (2.5)$$

thus yields  $x_B = 1$  for elastic and  $0 < x_B < 1$  for inelastic events and can be understood as a measure for the inelasticity of the event. Finally,  $s$  denotes the squared centre-of-mass energy.

The deep-inelastic scattering reaction can be described as scattering off the individual quarks in the target nucleon, which subsequently breaks apart. The deep-inelastic scattering domain is approximately given by  $Q^2 \gtrsim 1 \text{ GeV}^2$  and  $W^2 \gtrsim 4 \text{ GeV}^2$ . These conditions ensure a high enough resolution to probe the internal structure of the nucleon.

$\mathbf{k} = (E, \vec{k}); \mathbf{k}' = (E', \vec{k}')$	4-momenta of incoming and outgoing $e^+$
$\mathbf{P} \stackrel{lab}{=} (M, \vec{0})$	4-momentum of target nucleon
$\theta, \phi$	polar and azimuthal scattering angle
$\mathbf{q} = (\nu, \vec{q})$	4-momentum of virtual photon
$Q^2 = -q^2 \stackrel{lab}{=} 4EE' \sin^2\left(\frac{\theta}{2}\right)$	Negative squared four-momentum transfer
$\nu = \frac{\mathbf{P} \cdot \mathbf{q}}{M} \stackrel{lab}{=} E - E'$	Energy transfer to the target
$x_B = \frac{Q^2}{2\mathbf{P} \cdot \mathbf{q}} \stackrel{lab}{=} \frac{Q^2}{2M\nu} \quad x_B \in [0;1]$	Björken scaling variable
$y = \frac{\mathbf{P} \cdot \mathbf{q}}{\mathbf{P} \cdot \mathbf{k}} \stackrel{lab}{=} \frac{\nu}{E} \quad y \in [0;1]$	Fractional energy of the virtual photon
$W^2 = (\mathbf{P} + \mathbf{q})^2 \stackrel{lab}{=} M^2 + 2M\nu - Q^2$	Squared mass of the final hadronic state
$\mathbf{p} = (E_h, \vec{p})$	4-momentum of a final state hadron
$z = \frac{\mathbf{P} \cdot \mathbf{p}}{\mathbf{P} \cdot \mathbf{q}} \stackrel{lab}{=} \frac{E_h}{\nu} \quad z \in [0;1]$	Fractional energy of final state hadron $h$
$p_{CM}^{\parallel} = \vec{p} \cdot \frac{\vec{q}}{ \vec{q} } \Big _{\gamma^* \rightarrow N}$	Hadron momentum component parallel to the photon momentum in the centre-of-mass frame
$x_F = \frac{p_{CM}^{\parallel}}{ \vec{q} } \simeq \frac{2p_{CM}^{\parallel}}{W} \quad x_F \in [-1;1]$	Feynman scaling variable
$\eta = \frac{1}{2} \cdot \ln\left(\frac{E_{CM}^h + p_{CM}^{\parallel}}{E_{CM}^h - p_{CM}^{\parallel}}\right)$	Rapidity

**Table 2.1**

Definition of the most important kinematic variables used in deep-inelastic scattering.

Furthermore, the  $W^2$  requirement avoids the elastic scattering region, as well as inelastic scattering in resonance regions with  $W^2 = M_R$  (where  $M_R$  is the mass of the resonance).

All the variables noted so far are inclusive variables; they are well defined by the properties of the scattered positron (and of course the nucleon mass, which is known a priori) and thus can be calculated from an inclusive measurement. Semi-inclusive variables define the characteristics of the individual hadrons. The most important ones are the fraction  $z$  of transferred energy taken by the hadron, the Feynman variable  $x_F$  and the rapidity  $\eta$ :

$$z \equiv \frac{E_h}{\nu}, \quad (2.6)$$

$$x_F \equiv \frac{2p_{\text{CM}}^{\parallel}}{W} \quad \text{and} \quad (2.7)$$

$$\eta \equiv \frac{1}{2} \cdot \ln \left( \frac{E_{\text{CM}}^h + p_{\text{CM}}^{\parallel}}{E_{\text{CM}}^h - p_{\text{CM}}^{\parallel}} \right). \quad (2.8)$$

Here  $p_{\text{CM}}^{\parallel}$  denotes the projection of the hadron momentum in the direction of the virtual photon in the photon-nucleon centre-of-mass system (see Table 2.1). In this reference frame, the Feynman variable  $x_F$  scales the momentum component collinear to the photon momentum to its maximum possible value ( $-1 \leq x_F \leq 1$ ). The rapidity  $\eta$  is a commonly used variable in high-energy hadronic scattering since it conveniently transforms additively under boosts along a special axis (where the natural choice is — as taken here — the collisions axis, given by the virtual photon momentum) [Col97]. In the non-relativistic limit,  $\eta$  becomes the particle velocity along this axis.

## 2.2 Cross Section

The inclusive deep-inelastic scattering cross section can be given as a contraction of the leptonic tensor  $L_{\mu\nu}$  and the hadronic tensor  $W^{\mu\nu}$ ,

$$\frac{d^2\sigma}{dE'd\Omega} = \frac{\alpha^2}{2MQ^4} \cdot \frac{E'}{E} \cdot L_{\mu\nu}W^{\mu\nu}. \quad (2.9)$$

Here,  $\alpha = e^2/(4\pi)$  is the fine structure constant. The tensors describe the emission or absorption of a virtual photon by the respective objects. For the point-like leptons, they can be calculated in Quantum Electrodynamics (QED). For unpolarised scattering it is given in leading order by

$$L_{\mu\nu} = 2 \cdot \left[ k'_\mu k_\nu + k'_\nu k_\mu - g_{\mu\nu} (\mathbf{k}' \cdot \mathbf{k} - m^2) \right], \quad (2.10)$$

with  $m$  denoting the lepton mass and  $g_{\mu\nu}$  the Minkowski metric.

The hadronic tensor has to reflect the hadronic substructure of the target nucleon, and thus cannot be calculated exactly. Fortunately, its structure can be constrained by

symmetry requirements like Lorentz and gauge invariance as well as current and parity conservation, and for the unpolarised (or spin-averaged) case, only two independent structure functions remain:

$$\frac{1}{2M} W_{\mu\nu} = \left( -g_{\mu\nu} - \frac{q_\mu q_\nu}{Q^2} \right) \cdot W_1(\nu, Q^2) + \frac{1}{M^2} \left( p_\mu + \frac{\mathbf{p} \cdot \mathbf{q}}{Q^2} q_\mu \right) \left( p_\nu + \frac{\mathbf{p} \cdot \mathbf{q}}{Q^2} q_\nu \right) \cdot W_2(\nu, Q^2). \quad (2.11)$$

The combination of equations (2.10), (2.11) and (2.9) leads to

$$\frac{d^2\sigma}{dE'd\Omega} = \left( \frac{d\sigma}{d\Omega} \right)_{\text{Mott}} \cdot \left\{ W_2(\nu, Q^2) + 2W_1(\nu, Q^2) \tan^2 \left( \frac{\theta}{2} \right) \right\}. \quad (2.12)$$

where

$$\left( \frac{d\sigma}{d\Omega} \right)_{\text{Mott}} = \frac{4\alpha^2 E'^2}{Q^4} \cos^2 \left( \frac{\theta}{2} \right) \quad (2.13)$$

denotes the Mott cross section which describes the scattering of leptons off a spin-less and point-like particle. The structure functions parametrise the deviation of the nucleon cross section from this point-like particle behaviour, where specifically the additional  $\tan^2$ -dependence is due to the interaction of the positrons with the magnetic moment of the nucleon. In the elastic limit ( $\nu \rightarrow Q^2/(2M)$ ), the structure functions  $W_1$  and  $W_2$  are related to the electric and magnetic nucleon form factors:

$$W_1(\nu, Q^2) = \frac{Q^2}{4M^2} G_M^2(Q^2) \delta \left( \nu - \frac{Q^2}{2M} \right) \quad (2.14)$$

$$W_2(\nu, Q^2) = \frac{G_E^2(Q^2) + \frac{Q^2}{4M^2} G_M^2(Q^2)}{1 + \frac{Q^2}{4M^2}} \delta \left( \nu - \frac{Q^2}{2M} \right) \quad (2.15)$$

Usually, the cross section is expressed in terms of the dimensionless structure functions  $F_1(x_B, Q^2)$  and  $F_2(x_B, Q^2)$ . In the limit of  $Q^2 \rightarrow \infty$  for a fixed ratio of  $Q^2/\mathbf{P} \cdot \mathbf{q}$ , the so called Bjørken limit, they become a function of the Bjørken scaling variable (Eq. (2.5)) alone:

$$MW_1(\nu, Q^2) = F_1(x, Q^2) \rightarrow F_1(x_B), \quad (2.16a)$$

$$\nu W_2(\nu, Q^2) = F_2(x, Q^2) \rightarrow F_2(x_B). \quad (2.16b)$$

This behaviour has been predicted by Bjørken [Bj69] and Feynman [Fey69] and has subsequently been measured at SLAC [Blo70]. It indicates that, at sufficiently high energies, the scattering process occurs on point-like particles that form the constituents of the nucleon. These predictions and measurements form the basis of the quark parton model.

Comparing Eq. (2.12) with the cross section for scattering off point-like spin-1/2 particles

$$\frac{d\sigma}{d\Omega} = \left( \frac{d\sigma}{d\Omega} \right)_{\text{Mott}} \cdot \left\{ 1 + \frac{Q^2}{2M^2} \tan^2 \left( \frac{\theta}{2} \right) \right\} \quad (2.17)$$

yields (taking into account Eq. (2.16))

$$2xF_1(x_B) = F_2(x_B). \quad (2.18)$$

This equation is known as the Callan-Gross relation [Cal69]. Its experimental verification confirmed that the charged partons in the nucleon are indeed spin 1/2 objects.

The cross section is often written as a function of  $Q^2$  and  $x_B$ . In terms of the dimensionless structure functions  $F_1$  and  $F_2$ , it is given by

$$\frac{d\sigma}{dx_B dQ^2} = \frac{4\pi\alpha^2}{x_B Q^4} \left\{ y^2 x_B F_1(x_B, Q^2) + (1-y)F_2(x_B, Q^2) \right\}. \quad (2.19)$$

Here,  $y$  denotes the fraction of the lepton energy transferred to the nucleon (see Table 2.1).

## 2.3 The Quark Parton Model

### 2.3.1 The Simple Quark Parton Model

The quark parton model provides an intuitive explanation for the observed Björken scaling. The nucleon is considered to be composed of point-like constituents, the partons. It is formulated in a reference frame where the nucleon is moving with high momentum, such that transverse momentum components and the rest mass of the constituents and the nucleon itself can be neglected (*infinite momentum frame*). In this model, the deep inelastic scattering occurs as elastic scattering on these constituents. The model implies that the interaction between the individual partons is weak on short distances. If the scattering occurs on sufficiently short time scales, the particles can thus be regarded as quasi-free, and the four-momentum of a parton after scattering is given by

$$(\xi\mathbf{P} + \mathbf{q})^2 = \xi^2 M^2 + 2\xi\mathbf{P} \cdot \mathbf{q} - Q^2 \approx 0, \quad (2.20)$$

where  $\xi$  denotes the fraction of the nucleon momentum carried by the struck quark. Neglecting the nucleon mass yields  $\xi \approx Q^2/(2\mathbf{P} \cdot \mathbf{q})$  and thus allows to relate the momentum fraction with the Björken scaling variable  $x_B$  in the given approximation (see Eq. (2.5)).

The DIS cross section is then given as the incoherent sum of the cross sections for scattering on the individual partons. The structure functions observed are thus composed of the probability distributions to find a certain quark in the nucleon, weighted with their squared charges:

$$F_1(x_B) = \frac{1}{2} \sum_q \int_0^1 d\xi e_q^2 q(\xi) \delta(\xi - x_B) = \frac{1}{2} \sum_q e_q^2 q(x_B) \quad (2.21)$$

$$F_2(x_B) = \sum_q \int_0^1 d\xi e_q^2 \xi q(\xi) \delta(\xi - x_B) = \sum_q x_B e_q^2 q(x_B) \quad (2.22)$$

The sum runs over all quark flavours  $q \in \{u, d, s, c, b, t\}^2$  and the corresponding anti-quarks. The parton distribution functions (PDF)  $q(x_B)$  give the probability to find a quark of the respective flavour with momentum fraction  $x_B$ , while  $e_q$  denotes its fractional charge in terms of the electron charge.

Figure 2.2 shows the  $Q^2$  dependence of the structure function  $F_2(x_B, Q^2)$ . For intermediate  $x_B$  (around 0.25), the function is independent of  $Q^2$ , as expected from the quark parton model (Equation (2.22)). However, for larger and smaller  $x_B$ , this independence is lost. This scale-breaking effect can be explained if interactions between the partons are introduced into the quark parton model, which so far have been neglected.

### 2.3.2 The QCD-improved Quark Parton Model

In the so called QCD-improved quark parton model, quarks interact by the exchange of gluons, which mediate the strong interaction. Figure 2.3 depicts the basic processes possible in strong interaction: quarks can radiate gluons, gluons can split into a  $q\bar{q}$  pair and gluons can couple with other gluons. Similar to QED, the interaction strength arises from a coupling strength,  $\alpha_s = g^2/4\pi$ . It is given in first order QCD as

$$\alpha_s(\mu^2) = \frac{12\pi}{(33 - 2n_f) \cdot \log(\mu^2/\Lambda^2)}. \quad (2.23)$$

$\mu$  is the renormalisation scale, which effectively poses a cut on the time scale in which virtual fluctuations are taken into account. For DIS, it is usually set to  $Q$ . The number of quark flavours is given by  $n_f$ , where usually all flavours with a mass smaller than  $\mu$  are taken into account.  $\Lambda$ , finally, is the QCD scale parameter. For the applicability of perturbation theory,  $\alpha_s$  must be less than 1, so  $\Lambda$  sets the scale for the breakdown of perturbation theory. Depending on the renormalisation scheme and the number of quark flavours,  $\Lambda$  has a value of 200 - 300 MeV.

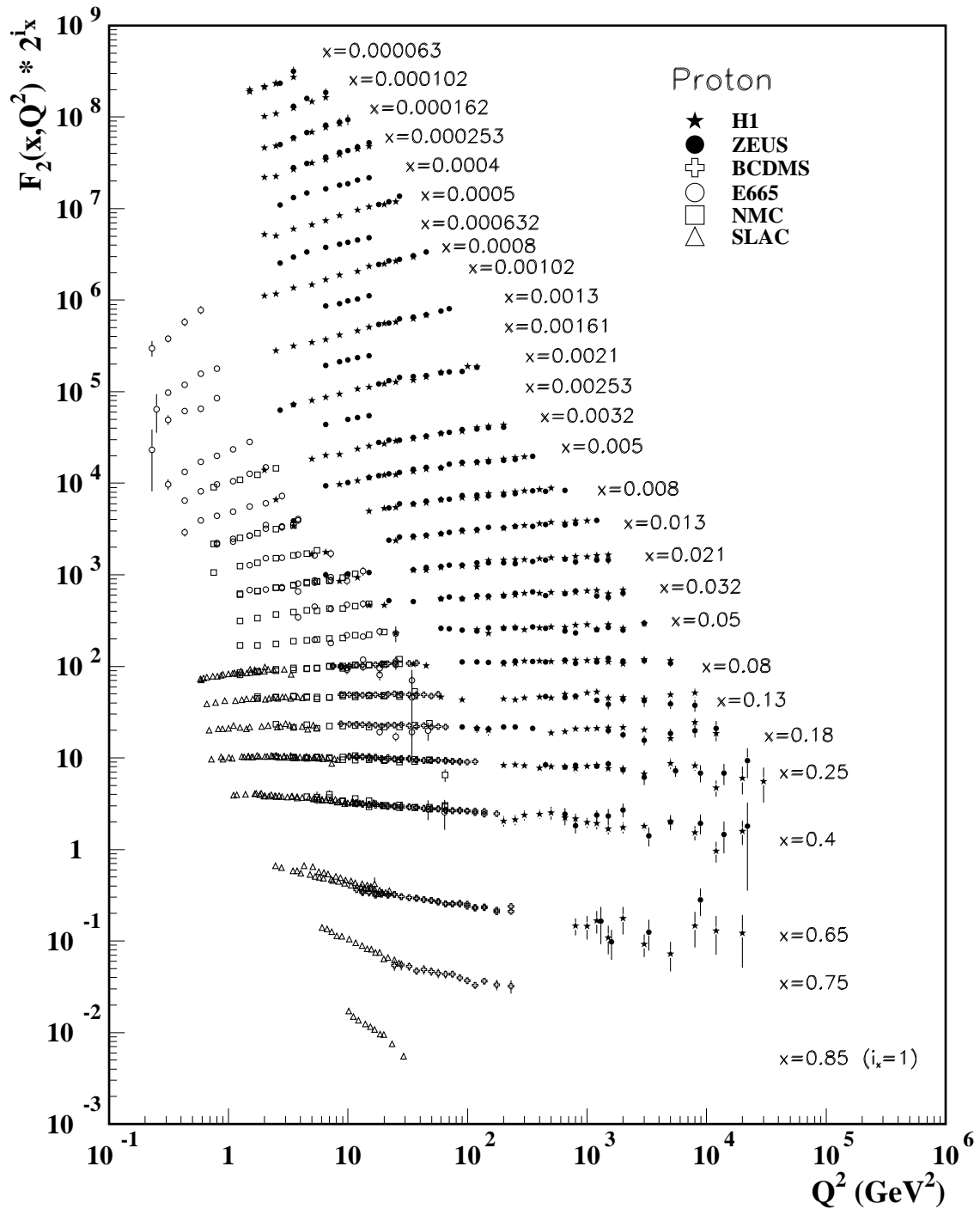
Unlike the electromagnetic coupling constant  $\alpha$ ,  $\alpha_s$  exhibits a strong  $\mu^2$  (or for DIS  $Q^2$ ) dependence. For  $Q^2 \rightarrow \infty$ , the coupling strength  $\alpha_s$  vanishes. By this *asymptotic freedom* the simple quark parton model with non-interacting quarks is recovered. In the other extreme, the coupling strength becomes large as  $Q$  approaches  $\Lambda$ , giving rise to *confinement*, which explains why only colourless objects can be observed in hadronic final states.

The interactions of the partons by the processes shown in Fig. 2.3 together with the  $Q^2$  dependence of the coupling strength explain the scaling violations observed in the structure functions. A photon with a larger four-momentum probes the nucleon with a higher resolution. With increasing resolution the nucleons appear to be composed of a larger number of resolved quarks and gluons, all sharing the total nucleon momentum. The fraction of partons which possess a high share  $x_B$  of the total momentum thus decreases, while the number of partons with low  $x_B$  increases (compare Fig. 2.2).

Quantitatively, this behaviour can be described by the DGLAP<sup>3</sup> evolution equations ([Gri72], [Lip75], [Alt77], [Dok77]). For the quark distributions  $q(x_B, Q^2)$  and the gluon

<sup>2</sup>Practically, of course, the heavy flavour contribution to the quark sea is negligible.

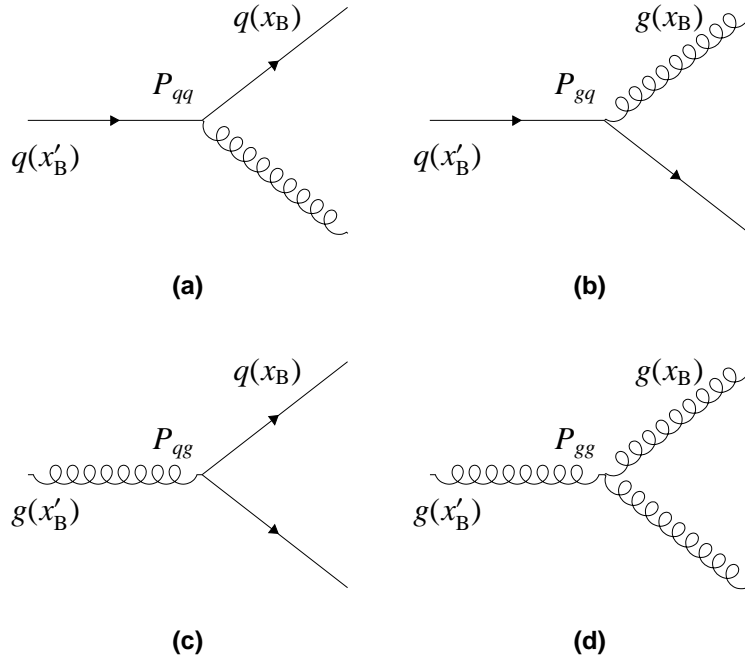
<sup>3</sup>DGLAP=Dokshitzer, Gribov, Lipatov, Altarelli, Parisi



**Figure 2.2**

The proton structure function  $F_2^p$  as a function of  $Q^2$ . Shown are results from  $ep$  collider experiments (ZEUS, H1), as well as fixed target data for  $ep$  (SLAC) and  $\mu p$  (BCDMS, E665, NMC) scattering. For the purpose of plotting,  $F_2^p$  has been multiplied by  $2^{i_x}$ , where  $i_x$  is the  $x$  bin number, ranging from  $i_x = 1$  ( $x = 0.85$ ) to  $i_x = 28$  ( $x = 0.000063$ ). The plot was taken from [Eid04].



**Figure 2.3**

Splitting functions  $P_{ab}(\xi, Q^2)$ .  $b$  denotes the initial parton,  $a$  denotes the final parton with energy fraction  $\xi = x/x'$ .

distributions  $g(x_B, Q^2)$ , they are given as

$$\frac{dq(x, Q^2)}{d \ln Q^2} = \int_x^1 \frac{dx'}{x'} \left[ q(x', Q^2) \cdot P_{qq} \left( \frac{x}{x'} \right) + g(x', Q^2) \cdot P_{qg} \left( \frac{x}{x'} \right) \right] \quad (2.24a)$$

$$\frac{dg(x, Q^2)}{d \ln Q^2} = \int_x^1 \frac{dx'}{x'} \left[ g(x', Q^2) \cdot P_{gg} \left( \frac{x}{x'} \right) + \sum_q q(x', Q^2) \cdot P_{gq} \left( \frac{x}{x'} \right) \right] \quad (2.24b)$$

They mathematically express the fact that, at a given resolution  $Q^2$ , e.g. a quark of flavour  $q$ , carrying the momentum fraction  $x$ , could have been radiated from a parent parton (quark or gluon) which carried a higher fraction  $x'$ . The splitting functions  $P_{ab}(x/x')$  specify the probability that a parton  $b$  with momentum fraction  $x'$  is the origin of parton  $a$  with momentum fraction  $x$ . Or, speaking in terms of resolution, they give the probability to find object  $a$  inside of object  $b$  with a fraction  $x/x'$  of  $b$ 's momentum. Once the parton distributions are known at some scale, the DGLAP equations allow to calculate PDFs at other scales where perturbation theory holds.

## 2.4 Hadronic Final States & Fragmentation Functions

A concept essential to the description of DIS is factorisation. It is assumed that the scattering process of the virtual photon off a nucleon can be divided into two parts:

the hard short distance scattering of the photon off one of the nucleon's constituents (the cross section  $\sigma$  calculable from perturbation theory) and the selection of this constituents according to a soft, long range parton density function.

This notion is extended to the hadronisation of the quark-diquark system into the final state hadrons. Due to confinement, these coloured objects have to settle into colour-singlet states as they separate. The long range nature of the process excludes its description by perturbation theory. Instead, it is parametrised by fragmentation functions  $D_q^h(z, Q^2)$ , which give the average multiplicity of final state hadrons  $h$  produced from an initial quark of flavour  $q$ , depending on the fractional energy  $z$  and the resolution scale  $Q^2$ . The cross section to produce a certain hadron is then given by the convolution of the hard quark-photon scattering part, the parton distribution functions selecting the scattering partner and the fragmentation functions given the probability to produce a certain hadron. A convenient observable to measure this convolution is the differential hadron multiplicity, given in LO QCD by

$$\frac{d\sigma^h(x_B, Q^2, z)}{dx_B dQ^2 dz} = \frac{\sum_q e_q^2 q(x_B, Q^2) D_q^h(Q^2, z)}{\sum_q e_q^2 q(x_B, Q^2)} \cdot \frac{d^2\sigma_{\text{incl}}}{dx_B dQ^2}, \quad (2.25)$$

where  $\sigma_{\text{incl}}$  is the inclusive DIS cross section.

Since fragmentation functions cannot be calculated directly, they have to be derived from fits to experimental data (see Sec. 2.4.2). For the implementation of the hadronisation process in Monte Carlo simulations, phenomenological models are employed, whose parameters then have to be tuned to reproduce experimental data. An overview over the three main schools of fragmentation models is given in Sec. 4.3, where emphasis is given to the Lund string model used in the HERMES Monte Carlo programs. The tuning of the Lund model to HERMES data (more precisely differential hadron multiplicities versus various variables) is described in Sec. 4.4.

### 2.4.1 Properties of fragmentation functions

**Factorisation & Universality.** According to the factorisation theorem, the fragmentation functions should be universal in the sense that they only depend on the initial parton  $a$  and the final state hadron  $h$ , and not on the specific properties of the process from which they were determined. This assumption has been tested by comparing particle spectra (e.g. inclusive charged particle distributions versus  $Q^2$ ) from DIS with corresponding spectra from  $e^+e^-$  annihilation, which were found to be consistent ([Bre99], [Adl97]). Other studies showed that NLO fragmentation functions [Kni00] obtained from fits to  $e^+e^-$  data describe experimental data from  $\gamma\gamma$ ,  $ep$  and  $p\bar{p}$  collisions within the uncertainties [Kni01].

Another experimental signature of factorisation is the independence of the fragmentation functions from  $x_B$ . Evidence for a slight  $x_B$  dependence has been seen at EMC [Ash91] and later also at HERMES [Air01]. However, the new analysis presented in this work shows a much less pronounced  $x_B$  dependence (see Chapter 6), similar to the findings of the E665 collaboration [Ada97].

**Energy and Probability Conservation.** The entire energy of the initial parton is shared by its fragmentation products:

$$\sum_h \int_0^1 z \cdot D_q^h(z) dz = 1 \quad (2.26)$$

Also, the average multiplicity of hadron  $h$  is given by the sum of the contributions of the individual quark flavours:

$$\sum_q \int_0^1 [D_q^h(z) + D_{\bar{q}}^h(z)] dz = n_h \quad (2.27)$$

**Scaling Violation.** In analogy to parton distribution functions, the features of QCD give rise to a  $Q^2$  dependence of the fragmentation functions. This violation of scaling (=  $Q^2$  independence) can be parametrised again by the DGLAP-type equations

$$\frac{dD_j^h(z, Q^2)}{d \ln Q^2} = \sum_i \int_z^1 \frac{d\xi}{\xi} P_{ij} \left( \frac{z}{\xi}, Q^2 \right) D_i^h(\xi, Q^2). \quad (2.28)$$

These equations account for the possibility that the fragmentation of parton  $j$  into hadron  $h$  might occur via the radiation of parton  $i$  which in turn fragments into hadron  $h$ .

**Symmetries.** In principle, fragmentation functions can be defined for any combination of original (struck) quark and final state hadron. However, the framework of the QPM suggests relations between different fragmentation functions based on charge and isospin invariance and valence quark composition of the respective hadron. Charge conjugation invariance implies

$$D_q^{h^+} = D_{\bar{q}}^{h^-} \quad \text{and} \quad D_q^{h^-} = D_{\bar{q}}^{h^+} \quad (2.29)$$

for  $h \in \{\pi, K\}$ . For pions, isospin invariance leads to

$$D_u^{\pi^+} = D_d^{\pi^-}. \quad (2.30)$$

The valence quark composition of the hadrons gives rise to the distinction of the fragmentation functions into *favoured* (valence-type) and *unfavoured* (sea-type) fragmentation functions, the first case meaning that the hadron contains a valence quark of the same flavour as the primary quark. Together with the previous assumptions, this yields for pions

$$\begin{aligned} D_+^{\pi} &= D_u^{\pi^+} = D_{\bar{d}}^{\pi^+} = D_d^{\pi^-} = D_{\bar{u}}^{\pi^-} \\ D_-^{\pi} &= D_u^{\pi^-} = D_{\bar{d}}^{\pi^-} = D_d^{\pi^+} = D_{\bar{u}}^{\pi^+} \\ D_s^{\pi} &= D_s^{\pi^+} = D_{\bar{s}}^{\pi^+} = D_s^{\pi^-} = D_{\bar{s}}^{\pi^-} \end{aligned} \quad (2.31)$$

$D_s^{\pi}$  is the *strange* fragmentation function,  $D_+^{\pi}$  and  $D_-^{\pi}$  denote the favoured and unfavoured fragmentation functions, respectively. Observations show that  $D_+^{\pi} > D_-^{\pi}$ , as name and physical intuition suggest.

These relations have been essential for the extraction of fragmentation functions from experimental data ([Bin95],[Kni00]), since the available information did not allow for e.g. the distinction between the light ( $u, d, s$ ) quark flavours. Only recently ([Alb05]) parametrisations have become available which did not rely on at least part of these assumptions (see Section 2.4.2).

## 2.4.2 Existing Measurements

The fragmentation of quarks and gluons into final state hadrons has been measured in many experiments at different energies using a variety of processes. Most data is available obtained from electron-positron annihilation

$$e^+e^- \rightarrow (\gamma, Z) \rightarrow q\bar{q} \rightarrow h + X.$$

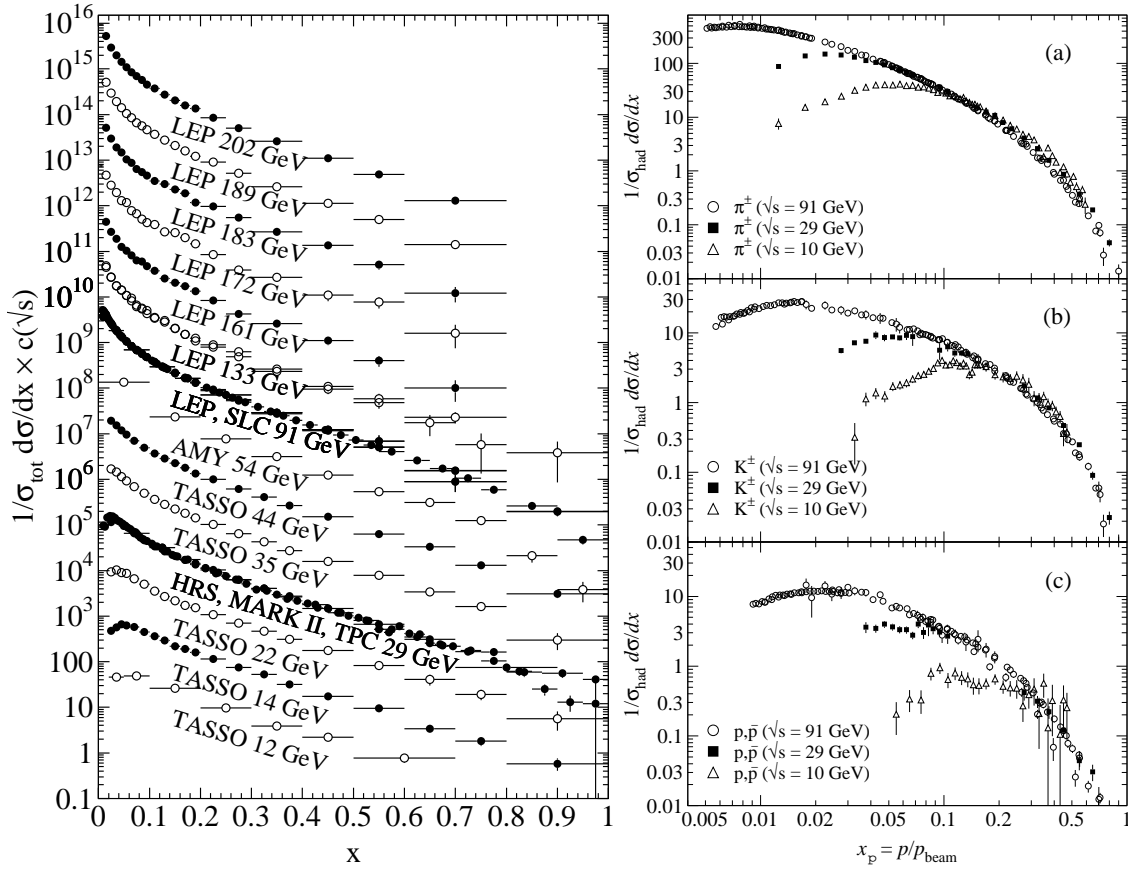
Figure 2.4 shows fragmentation functions obtained by  $e^+e^-$  annihilation by various collaborations over a wide range of c.m. energies. The left hand side shows the production of all charged hadrons as a function of the scaled momentum<sup>4</sup>. By parametrising the fragmentation function at some input scale  $Q_0$  and subsequently evolving the function to different energies using the DGLAP equations (Eq. (2.28)), the strong coupling constant  $\alpha_s$  can be determined by fitting the evolved curves to the measured spectra at the respective energies (see e.g. [Abr97b]). The right hand side shows fragmentation functions separately for charged pions, kaons and (anti-)protons. Both plots were taken from [Eid04] and were compiled from numerous sources, including experiments with lower c.m. energies like TASSO [Bra82] and TPC [Aih88], as well as higher energy data e.g. from the LEP experiments.

The appealing feature of the annihilation process is the relative simplicity compared to e.g. the DIS process studied in this work. The initial scattering takes place between point-like particles whose interaction can be calculated from perturbative QED, while in the case of DIS, the description of the scattering requires the knowledge of the parton distribution functions.

Nevertheless, the flavour of the initial  $q\bar{q}$  is a priori unknown, and until around 1994, data with identified quark flavours was not available [Kni00]. In the last decade, the situation was rectified by  $e^+e^-$  data which used a life time tagging method ([Bus93],[Abr96]) to obtain flavour enriched data samples ([Bus95], [Abe99], [Abr98]), usually distinguishing between samples enriched with light quarks ( $u, d, s$ ) or  $b$  quarks. The method is based mainly on the long life time and large mass of hadrons containing  $b$  and  $c$  quarks, which results in a large number of decay products with a positive impact parameter<sup>5</sup>. Additional information can be obtained by using the correlation between the quantum numbers of high energy particles and those of the primary quarks, a connection which has been studied e.g. in [Abe97]. This effect allows to extract flavour enriched samples distinguishing between the individual light quarks [Abb00].

<sup>4</sup>This denotes the hadron's momentum relative to the beam energy.

<sup>5</sup>The impact parameter is defined as the distance of closest approach of a charged particle track to the reconstructed primary decay vertex. It is positive if the point of closest approach is in the hemisphere of the jet direction.

**Figure 2.4**

Fragmentation functions from  $e^+e^-$  annihilation versus scaled momentum  $x$ . The left side shows the fragmentation function for all charged particles for different c. m. energies  $\sqrt{s}$ . The distributions were scaled by  $c(\sqrt{s} = 10^i)$ , where  $i$  is ranging from  $i = 0$  ( $\sqrt{s} = 12\text{GeV}$ ) to  $i = 13$  ( $\sqrt{s} = 202\text{GeV}$ ). The right side shows the distribution of (a)  $\pi^\pm$ , (b)  $K^\pm$  and (c)  $p, \bar{p}$  versus scaled momentum for three different energies. The plots were taken from [Eid04].

The increasing level of sophistication of the published data is reflected in the fragmentation function parametrisations which became available in the recent years. These parametrisations are obtained by fits to  $e^+e^-$  data, making use of LO or NLO ansätze for the  $e^+e^- \rightarrow q\bar{q}$  cross section and the fragmentation functions  $D_q^h$ . While initial fits to data only distinguished between valence- and sea-type quarks (and gluons) [Bin95], the number of assumptions could subsequently be reduced. Recently, fragmentation functions became available which for the first time featured light quark separation purely derived from data instead of theoretical constraints [Alb05].

In comparison to  $e^+e^-$  annihilation, DIS measurements add the complication of another set of a priori unknown parametrisations, the parton distribution functions. The extraction of fragmentation functions thus usually requires the use of PDF parametrisations. Fragmentation functions have been extracted by EMC ([Aub85],[Arn89]) and HERMES [Gei98]. All analyses assumed isospin symmetry between the target nucleons

(e.g. the  $u$  quark distribution in the proton is identical to the  $d$  quark distribution in the neutron) and charge and isospin symmetry for the fragmentation of  $u$  and  $d$  quarks. The first EMC publication presented favoured and unfavoured fragmentation functions into pions obtained using a deuterium target. By neglecting the sea quark contributions, the isoscalar target allowed the extraction without any assumptions about the parton distributions. However, the significance of the sea quark influence increases with lower  $x_B$ , limiting the validity of the approach. The systematic influence was corrected using a Monte Carlo method. Of course, since the Monte Carlo simulation required a PDF parametrisation as input, some PDF dependence of the final result was introduced.

The later EMC publication relied on PDF parametrisations directly. Sea quarks were taken into account, the strange fragmentation function  $D_s^h$  was taken to be similar to the unfavoured fragmentation function. This less restrictive method allowed to extract  $u$  quark fragmentation functions into charged pions, kaons and (anti-)protons, both for a proton and a deuterium target. The respective fragmentation functions for both target types were found to agree within their statistical errors. The pion results were also compatible with the previous analysis.

The HERMES analysis [Gei98] applied both methods to the HERMES data. Only pion fragmentation functions have been extracted due to the particle identification limitations at the time the data was taken (1996)<sup>6</sup>. The result was found to agree with the EMC data for  $z > 0.4$ .

Another HERMES publication [Air01] presented multiplicities of  $\pi^+$ ,  $\pi^-$  and  $\pi^0$ . While the neutral pion multiplicities were consistent with data from EMC, the charged pion multiplicities showed a poorer agreement with the compared EMC data, a feature that was attributed to the fact that the HERMES multiplicities were compared to fragmentation functions. In [Kre01], the HERMES multiplicities were combined with  $e^+e^-$  results obtained in [Kre00] to directly extract the fragmentation functions  $D_+^\pi$ ,  $D_-^\pi$  and  $D_s^\pi$  (see Eq. (2.31)).

The EMC and earlier HERMES results are compared with the current analysis in Chapter 6.

---

<sup>6</sup>This situation has meanwhile been rectified by the introduction of a dual-radiator RICH detector, see Chapter 3.

# Chapter 3

## The HERMES Experiment

The HERMES experiment is located at the Deutsches Elektronen-Synchrotron (DESY) in Hamburg, Germany. It shares the positron beam of the HERA positron-proton collider<sup>1</sup> with the experiments H1 and ZEUS<sup>2</sup>.

HERMES was designed to study the spin structure of the nucleon. Its conception was triggered by the observation of the EMC experiment, that only a small fraction of the nucleon spin can be contributed to the spins of its valence quarks [Ash88]. To further study the individual quark contributions to the nucleon spin, a facility was needed which features a polarised beam incident on a polarised target. Following feasibility studies, HERMES was commissioned in summer 1995.

Since the start of data taking, the physics scope of HERMES was expanded beyond the original intentions. Today, HERMES data is used to study many aspects of hadron structure, hadron production and hadronic interaction. A fairly recent summary of the HERMES results can be found in [Rit02].

In the following, a short overview of the experimental setup is given, both in terms of hardware (target, detector) and data processing. Detailed reviews can be found in other publications. The target and its components is for example described in [Bau03] and [Nas03]. A long article about the detector is available in [Ack98].

### 3.1 The HERA Accelerator

Figure 3.1 shows an overview of the HERA accelerator. It consists of a positron beam running clock-wise (as seen from above) with an energy of 27.6 GeV and a proton beam running in the opposite direction with an energy of 920 GeV. The rings have a circumference of 6.3 km. While H1 and ZEUS are located at the interaction points of the positron and proton beam lines, HERMES only uses the positrons.

HERA operation can be split into a number of consecutive steps. The beams are filled and ramped to their operational energies. Initial positron currents of up to 50 mA

---

<sup>1</sup>The HERA lepton ring can operate with both electrons and positrons. Since the data used in this work is based on the positron data only, it is here referred to as positron beam.

<sup>2</sup>A fourth HERA experiment — HERA-B — stopped data taking in 2003.

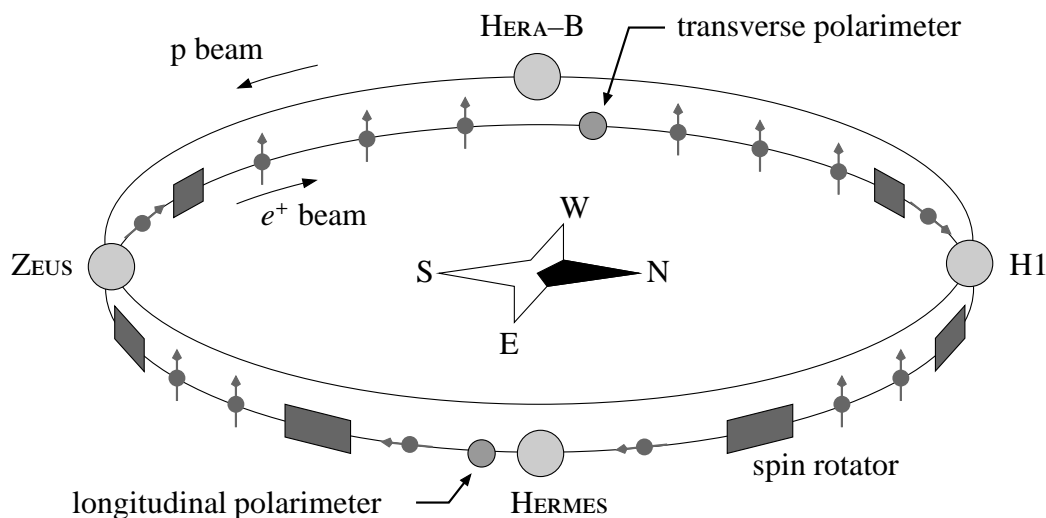


**Figure 3.1**

Schematic view of the HERA accelerator.

have been achieved. Due to interactions with residual gas in the beam line, and also due to the influence of the experiments the positron beam life time is limited to about 12-14 hours. During this time, the current decreases exponentially. To avoid inefficient running with low luminosity, the positron beam is dumped at a current of  $\sim 10$  mA. Since 2000, HERMES makes use of the low currents by injecting at the end of the fills unpolarised gas with high density, allowing for efficient data taking at the expense of the beam life time (see Fig. 3.6).

The polarisation of the beam is achieved by taking advantage of the Sokolov-Ternov effect [Sok64]. Small differences in the spin flip probabilities during the emission of synchrotron radiation cause a transverse (i.e. parallel to the field of the bending magnets) polarisation of the initially unpolarised beam. Longitudinal polarisation is achieved using spin rotators before and after the HERMES experimental area. The polarisation builds up over time and its maximum is strongly sensitive to HERA operation conditions. Beam polarisations of more than 50% have been achieved, routinely.

## 3.2 The Internal Gas Target

The HERMES target is a gas target internal to the positron beam line. In unpolarised mode, it is able to operate using a variety of target gasses, namely  $H_2$ ,  $D_2$ , He,  $N_2$ , Ne Kr and Xe. An important feature for many aspects of HERMES physics is the ability to run with polarised hydrogen and deuterium gas with a polarisation of  $P_z \sim 80\%$ . To achieve polarisation, the gas molecules are dissociated using RF fields. Subsequently, a series of sextupole magnets and RF transmitters is used to select and populate certain hyperfine states. This method is described in detail in [Nas03].

Figure 3.2 shows a schematic view of the target. The target chamber is a cylindrical enclosure which is evacuated using turbo-molecular pumps to a pressure below  $5 \cdot 10^{-7}$



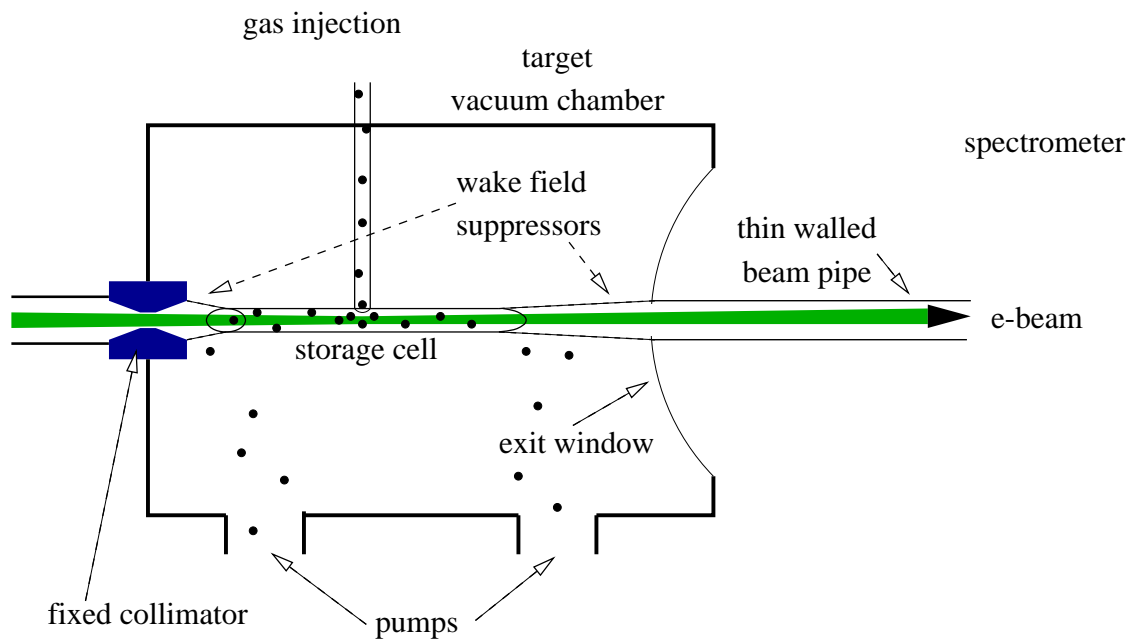


**Figure 3.2**  
Schematic view of the target area.

mbar. The beam enters the target chamber from the left. Collimators at the entrance of the chamber protect the target area from synchrotron radiation produced by the positron beam. The upstream end of the target chamber features an exit foil, which serves the purpose to limit particle interactions with the target material.

As opposed to solid targets, gas targets offer the advantage of low dilution due to undesired material. In case of polarised running, they furthermore allow a higher polarisation, which can be flipped within milliseconds. The main disadvantage lies in the lower target density. While the areal density for solid targets reaches the order of  $10^{25}$  atoms/cm<sup>2</sup>, polarised gas jets typically are below  $2 \cdot 10^{11}$  atoms/cm<sup>2</sup>. This is partly compensated by injecting the gas jet into a storage cell, which is aligned collinear to the positron beam. Thus the gas is constrained to spread along the beam line, yielding an increase of the areal density by two orders of magnitude. For deuterium, target densities of  $2 \cdot 10^{14}$  have been reached. The storage cell is made of thin ( $\sim 75 \mu\text{m}$ ) aluminium foil to minimise particle interactions. Its elliptical shape matches the positron beam profile. In the cell centre, two tubes are attached to the cell. One is used for the injection of the target gas, the other allows for the extraction of a gas sample to analyse the atomic polarisation (using a Breit-Rabi polarimeter) and the fraction of atoms which recombined to gas molecules (using a quadrupole mass spectrometer). Both measurements are necessary to determine the average target polarisation.

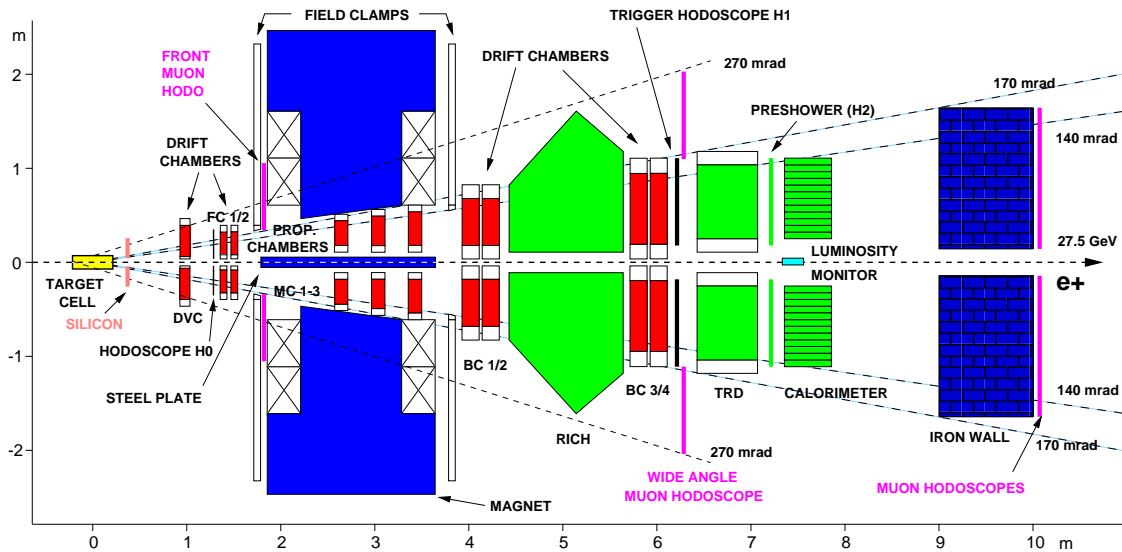


**Figure 3.3**  
Schematic view of the HERMES spectrometer.

### 3.3 The Spectrometer

The HERMES spectrometer is a forward angle instrument designed to detect inclusive and semi-inclusive deep inelastic scattering events. The positron beam pipe traverses the detector at the centre, thus defining the  $z$ -axis of the HERMES coordinate system. The  $y$ -axis is pointing upwards, while the  $x$ -axis is assigned to the horizontal component, pointing outwards (=left) from the ring centre. The proton beam pipe passes through the detector at  $x = 71$  cm, parallel to the positron beam. The detector is thus split into two symmetric halves above and below the HERA plane.

Figure 3.3 shows a profile of the setup. The most prominent component is the spectrometer magnet, which divides the installation in the front and back part of the detector. In the magnet area, steel plates shield the HERA beams from the magnetic field. The magnet defines the upper limits on the geometrical acceptance, which are given by polar angles of  $|\theta_x| < 180$  mrad in horizontal and  $|\theta_y| < 140$  mrad in vertical direction. For the vertical case, the steel plates cause a lower limit of  $|\theta_y| > 40$  mrad.

In conformance with the two basic tasks of the spectrometer, its components can be grouped into two categories: the particle tracking system and the particle identification system. The two groups will be addressed in the following. It should be noted that the HERMES setup incorporates a number of special purpose detectors which are neglected due to their irrelevance for this work. This includes the silicon detector and the muon detectors.

An exhaustive review of the HERMES spectrometer can be found in [Ack98].

### 3.3.1 Tracking

The task of the tracking system is to determine the origin, angles and momentum of the particle tracks. The positions of the particles are mainly registered using drift chambers, which constitute the front and back tracking system, respectively, depending on their position relative to the magnet.

The magnet provides an integrated deflection power of 1.3 Tm, causing a horizontal bending of the particle tracks. The front and back partial tracks are merged by a pattern-matching algorithm, the deflection yields the particles momentum and charge. The procedure is described in detail in [Wan96]. In addition, the back partial tracks are also used to match the signal of the particle identification detectors (see next section) with the corresponding track.

The front tracking system is complemented by an additional drift vertex chamber, which serves to improve the determination of the event vertex and the angular resolution.

### 3.3.2 Particle Identification (PID)

The task to identify the observed particles can be divided into two steps. The first step, the discrimination between electrons and hadrons, is performed using the signals from the lead glass calorimeter, the pre-shower detector and the transition radiation detector (TRD). Hadrons are then subsequently identified using their signal in the RICH detector. The redundancy introduced by using four separate detectors to distinguish between leptons and hadrons not only improves the final result, but is also crucial for the calibration of the individual detectors. The lack of such possibilities for hadron identification with the RICH detector introduces difficulties which will become apparent in section 5.2.2.

**The Calorimeter.** The electromagnetic calorimeter [Ava98] consists of two arrays of 420 radiation hard lead-glass blocks, arranged in 10 rows and 42 columns. Particles incident on the calorimeter wall deposit part of their energy in form of photon showers in the material, which in turn are detected using photomultipliers.

Since leptons deposit almost their entire energy in the calorimeter, the ratio of deposited energy and momentum is peaked around  $E/p \sim 1$ . Hadrons only deposit a fraction of their kinetic energy through ionisation energy loss, resulting in an average  $E/p \sim 0.4 - 0.5$ .

Apart from lepton-hadron discrimination, the calorimeter provides a fast first-level trigger for scattered positrons and allows the determination of the energy of photons coming from radiative effects or  $\pi^0$  and  $\eta$  decays.

**The Pre-shower Detector.** HERMES features three sets of hodoscopes (labelled H0 through H2 in Fig. 3.3), of which H2 (the pre-shower detector) provides particle identification information. For this task, H2 is preceded with a passive radiator (11 mm lead sandwiched between to 1.3 mm stainless steel sheets). While hadrons deposit only a few

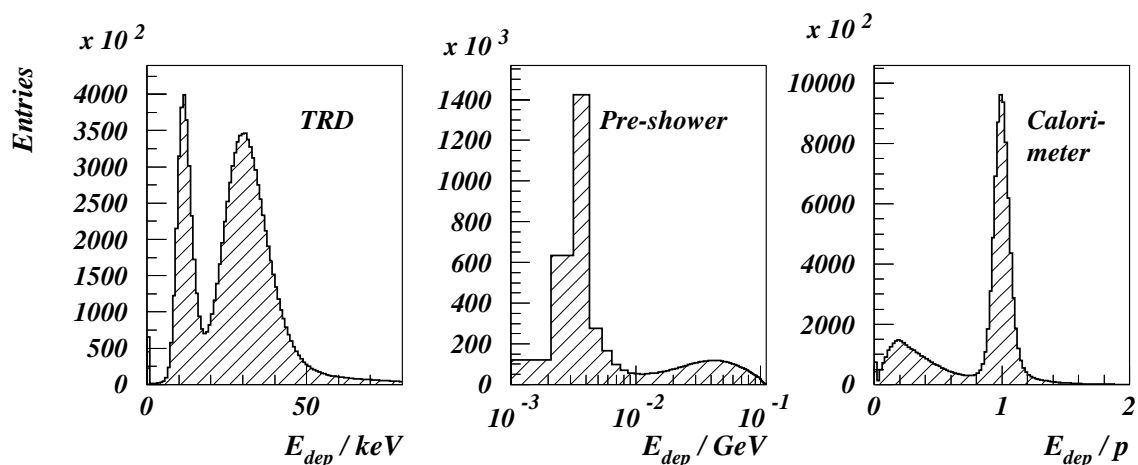


**Figure 3.4**

Momentum integrated response spectra of the PID detectors. Shown is the count rate as a function of deposited energy (normalised to momentum in case of the calorimeter). The distributions reflect the descriptions in the text. The figure was taken from [Wei02] and is extracted from the year 2000 data production.

MeV in the detector, the lepton signal is much broader and at energies between 20 and 40 MeV.

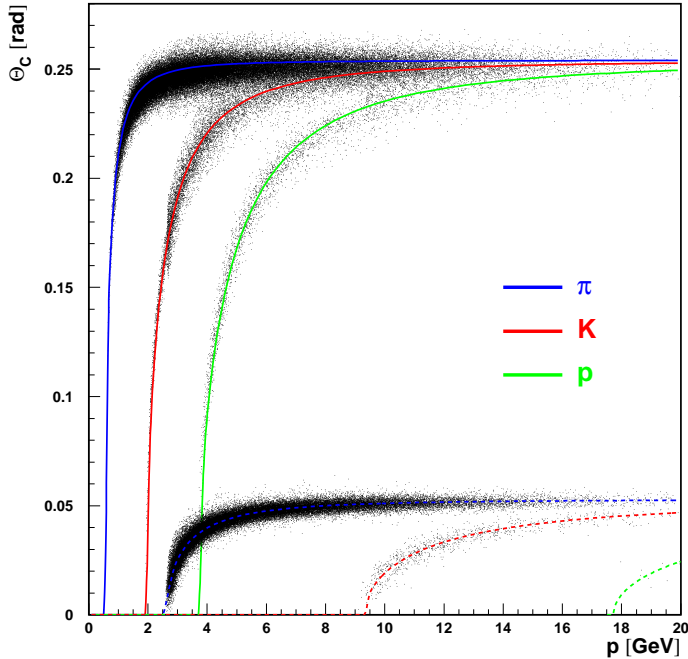
The other two hodoscopes provide trigger information. While H1 provides a fast first-level trigger together with H2 and the calorimeter, H0 was introduced in 1996 to suppress the background generated from the proton beam. Its forward position in the detector allows the separation of particles going 'backwards' in the detector, along with the proton beam line.

**The Transition Radiation Detector (TRD).** Transition radiation is emitted, when charged particles with relativistic energies traverse the boundary between two media with different dielectric constants. The threshold is related to the Lorentz factor and lies at about  $\gamma = E/mc^2 \sim 100$ . For leptons<sup>3</sup> and hadrons with an energy of 5 GeV, the factors are  $\gamma_l \sim 10000$  and  $\gamma_h \sim 35$ , so that only leptons emit transition radiation.

Due to the low emission probability, the TRD is composed of six identical layers, each layer consists of a fibre radiator and an adjacent proportional wire chamber. Both hadrons and leptons produce a signal in the wire chambers due to ionisation of the Xe/CH<sub>4</sub> gas, but in combination with the transition radiation, the energy deposited by the leptons is approximately twice as large.

In summary, the combination of the detector responses enables a lepton-hadron discrimination of better than 98%, using a likelihood method summarised in section 5.2.1. A more thorough review can for example be found in [Wen99].

<sup>3</sup>Here, the term *leptons* denotes electrons and positrons.

**Figure 3.5**

Momentum dependence of the Čerenkov angle for different hadron types and radiators. The upper band corresponds to the aerogel angles, the lower band shows the  $C_4F_{10}$  gas rings.

**The RICH Detector.** Charged particles which traverse a medium with a velocity higher than the speed of light in the medium emit electromagnetic radiation. The angle with which this radiation is emitted specifically depends on the refractive index of the radiators and the velocity of the particle. Thus different particles have a different momentum dependence of their Čerenkov angle due to their different masses.

The task of the RICH detector is to discriminate between pions, kaons and protons in the hadron sample. To do so, the detector utilises a combination of two radiators, a clear silica aerogel (refractive index  $n = 1.03$ ) and a  $C_4F_{10}$  gas radiator ( $n = 1.0014$ ). This relatively new combination allows to span the kinematically difficult region between 2 and 10 GeV, which contains most of the hadrons at HERMES. The resulting distribution of Čerenkov angles is shown in figure 3.5. A more thorough introduction to the RICH detector can be found e.g. in [Ako02].

## 3.4 Data Structure & Data Acquisition System

In the following section a quick overview over the structure of the HERMES data and its data acquisition system is given. The purpose is mainly to introduce some jargon used in this work; and also for completeness. The article [Ack98] contains more information about the particle tracking and the read out electronics. A more thorough review of the HERMES data processing can be found in [Dür95].

### 3.4.1 Data Structure

The largest logical unit to group the HERMES data is given by the *data taking period*, usually labelled by the year of running. It's basically defined by the time between to

major shutdowns, in which HERMES is running with a fixed configuration. During major shutdowns experimental components might change, e.g. by the addition or replacement of detectors. Also HERA might change its operation mode, like for example switching from positron to electron running or vice versa. The data taken during one period is processed several times, taking advantage of increased understanding of the experimental conditions (compare Sec.3.4.2). This *productions* are labelled with the data taking period and a letter denoting the production generation. The data in this thesis, for example, was taken from the 00c1 production, the 3rd reprocessing of the data taken in the year 2000.

The next unit — the *fill* — is defined by the operation of the HERA storage ring, which was already described on page 20. During one fill, the shift crew might switch operating modes, a common example is the switch from normal polarised running to unpolarised running with a high density gas target at the end of a fill.

When HERMES is running, the recorded data is stored in chunks of about 460 MByte size, the *runs*. A new run is also started by the shift crews when the conditions change considerably, e.g. when switching from normal to high density target operation.

Runs are divided into 10 second units called *burst*. In this intervals, slowly varying quantities like beam current and target polarisation are read out and stored in the slowcontrol data tables.

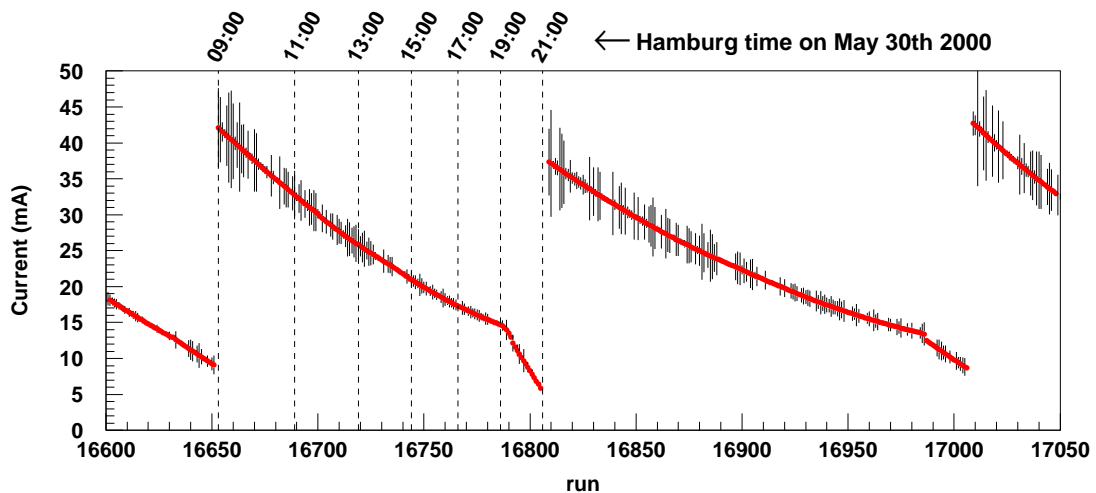


**Figure 3.6**

Two fills from the year 2000 data taking period. The positron beam current drops steadily due to the particle loss caused by interactions in the experimental areas as well as sources like the residual gas in the beam pipe. At the end of the fill, high density gas is injected into the target cell to make better use of the remaining beam, causing a steeper drop of the current. As can be seen by the indicated two hour intervals, a typical positron fill lasts for  $\sim 12$  hours.

Figure 3.6 shows two typical fills of the year 2000 data taking period. To give an idea about the involved time scales, markers have been drawn every two hours for the

first complete fill shown. The fill can be clearly divided into two parts. Between runs 16653 and 16789 data was taken using polarised Deuterium as target gas. Since each run represents about the same amount of data, the number of runs taken per two hour period drops with the beam current<sup>4</sup>. The last part of the fill shows a steeper slope for the beam current, which is caused by the high density target gas. In case of the first fill, the high density gas was Neon, the less steep drop at the end of the second fill is caused by Hydrogen.

### 3.4.2 Data Acquisition & Production

Particles of numerous sources are traversing the spectrometer at any given time, causing signals in the various detectors. A trigger system is used to filter out events whose structures indicate a physical process of interest. If a trigger is generated, a read out of all detector components is initiated. During the read out, no new data can be accepted, so that the number of generated and accepted triggers might differ. The ratio defines the dead time of the experiment

$$\delta_{\text{dead}} = 1 - \frac{T_{\text{acc}}}{T_{\text{gen}}}. \quad (3.1)$$

Several triggers are defined, requiring different sets of signals. *Trigger 21* is the main physics trigger, designed to filter out DIS events from the background noise. It requires:

- Coincident signals in the hodoscopes H0, H1 and H2.
- An energy deposition in the calorimeter above a certain threshold (usually 1.4 GeV for polarised and 3.5 GeV for unpolarised target operation). This signal is usually caused by the scattered beam particle.
- A reasonable timing of the signals. This filters out e.g. particle showers initiated by the proton beam which go backwards in the detector.

The detector read out is performed by the data acquisition system (DAQ). At this stage, the data is still in a raw format, containing channel numbers and digital signal values stored in the EPIO format (Experimental Physics Input Output Package). In a first step, the data is converted by the HERMES decoder (HDC) into the ADAMO format. HDC takes into account further input like calibration data and information about the detector geometry, which are optimised with each generation of data production. External influences like for example the atmospheric pressure can affect the detector responses and are accounted for in the calibration (see Fig. 3.7).

The numerous read out values of the different components have to be converted into information which is usable for the data analysis. This is done by the HERMES reconstruction software (HRC). Using a tree search algorithm, particle tracks are reconstructed from the hit locations in the wire chambers. By combining the front and back partial

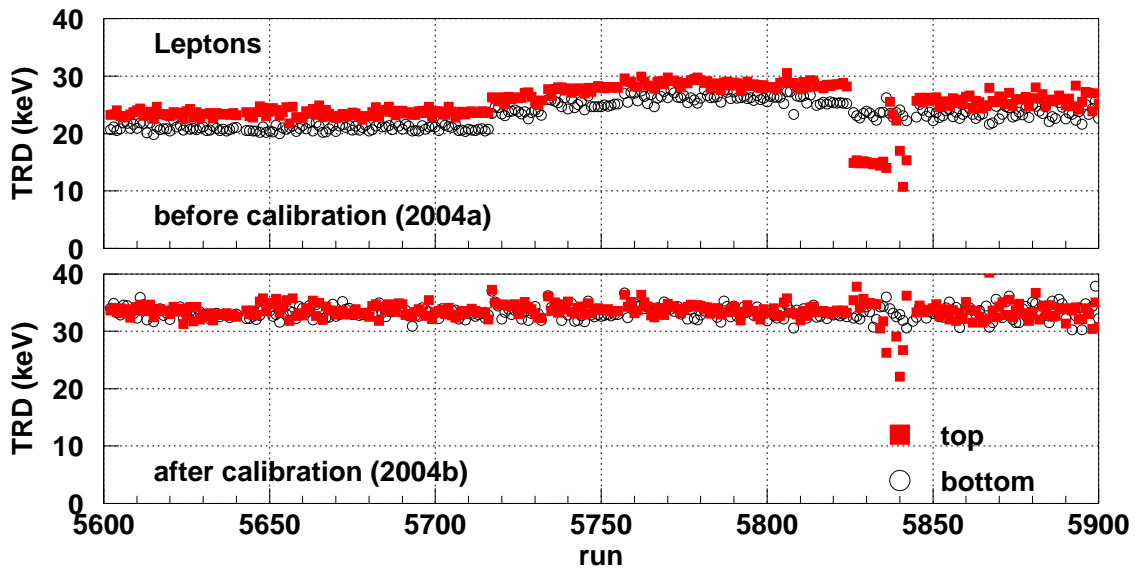


**Figure 3.7**

TRD response to leptons before (upper panel) and after (lower panel) detector calibration. Shown are the values for the top and bottom part of the detector. As can be seen, the uncalibrated response varies over time. After correction, top and bottom part of the detector show an identical, flat leptons signal. For the runs 5825-5835, the high voltage of the top part of the TRD was set to 3000 V instead of the usual 3100 V, resulting in the lower signals in the 'a' and (less so) 'b' production. The other PID detectors were used to select the lepton sample. It should be noted that for the 'a' production, the PID cuts are looser, so that the lepton sample is likely to be less clean.

tracks, the momentum is determined [Wan96]. Based on the reconstructed tracks, the responses of the individual PID detectors are associated with the corresponding particles.

Apart from the time critical detector signals, there are other parameters of interest which are only slowly changing over time. These values are recorded by the slow control system. Examples are information about the state of the HERA beam (current, polarisation, ...) as well as various HERMES operation parameters like voltages, target state and pressure gauges. The parameters are read out in regular intervals in the order of seconds or minutes, and stored chronologically in ADAMO tables. One file per fill is produced. Similar to the physics data, the slow control data is subsequently supplemented with additional expert information (e.g. smoothed polarimeter measurements).

The last step of a data production combines the HRC output and the slow control data to provide a uniform source of information for the analysis programs. During this step, the amount of data is further reduced by leaving out information only relevant for detector studies and not for physics analysis. Also the particle identification is performed at this point, relying on the PID detector responses and calibration information provided

<sup>4</sup>Of course also other factors, like a break in data taking, can influence this value, but according to the logbook this is not the case for this fill.



by the detector experts. Further input is concerned with data quality. The detector experts identify periods with faulty or unreliable detector operation. The corresponding data sets are marked accordingly or even left out of the production. The output is stored run-wise in so called  $\mu$ DST files, which are then used as input for the physics analysis programs.



# Chapter 4

## Monte Carlo Simulation

Monte Carlo simulations are an indispensable tool in particle physics. Many aspects which play a role in the understanding of experimental results — and the influences on them which possibly need to be accounted for — cannot be calculated rigorously in an analytical way. Instead, parametrisations and models are used, that allow to simulate the processes of interest on a statistical basis. For example, the simulation of a DIS event requires information coming from a number of sources: the event kinematics are generated (in terms of  $\nu$  and  $Q^2$ ) according to the differential cross section  $d^2\sigma/d\nu dQ^2$ , the struck quark is chosen using a parton distribution function (PDF) parametrisation (e.g. GRV [Glü98], MRS [Mar00] and — the standard choice at the moment — CTEQ6 [Pum02]). Also the subsequent hadronisation of the *struck quark*  $\Leftrightarrow$  *remnant target* system has to be simulated using phenomenological models. Here, the Lund model [And97] is the tool used in the HERMES Monte Carlo programs. The situation becomes even more complex when further possibilities are taken into account, e.g. radiative effects. The Monte Carlo method allows to extract the distributions resulting from the convolution of all these different probability functions.

Experimental results frequently rely on the ability to quantify influences on the data based on such simulations. The analysis of hadron multiplicities presented in Chapter 5 makes use of Monte Carlo predictions to estimate the dilution of the DIS sample by elastic vector mesons. Also radiative effects and the limited HERMES acceptance are accounted for by comparing Monte Carlo simulations with and without these influences.

In the beginning of this chapter, a short overview is given on the HERMES Monte Carlo program suite (as far as they are relevant for this thesis). A bit more attention is then given to the HERMES smearing generator (HSG), which was implemented as part of this work as a way to circumvent the time consuming detector simulation. HSG can not ultimately replace the full tracking of the particles in the detector, but it proved to be an invaluable tool for Monte Carlo studies. The main application of HSG has been the iterative tuning of the Lund fragmentation model to HERMES energies, and this topic forms the remainder of this chapter. After an introduction to the Lund model, the tuning method is described. In conclusion, the status of the Lund tuning is presented.

## 4.1 The HERMES Monte Carlo Setup

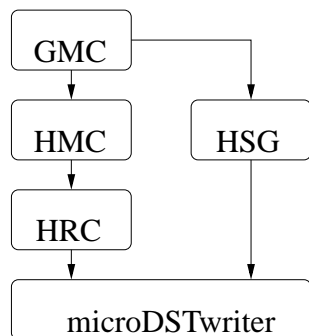


**Figure 4.1**

Overview of the HERMES Monte Carlo chain

The HERMES Monte Carlo consists of a set of programs which act as building blocks for a complete Monte Carlo chain (see Figure 4.1). Each Monte Carlo production starts with a **Generator Monte Carlo (GMC)** program. Several event generators are available which are suitable to simulate different aspects of HERMES physics. Their output can be considered as a simulation of what “really” happens on the physics level. For a reasonable comparison with experimental data, however, further effects have to be taken into account which are inevitably introduced by the measuring process: Depending on the kinematical regime, only a certain part of the particles in fact traverse the detector. There, they might interact with detector (and target) material before their kinematic properties can actually be measured. In the form of (multiple) scattering, these interactions influence the energies and the measured angles of

the tracks. Since the particle momentum is determined by the bending of the tracks induced by the spectrometer magnet, also the momentum determination is affected. Additionally, the radiation of Bremsstrahlung photons biases the detected energy of the particles. Finally, the detector signals have to be interpreted by the reconstruction program. The reconstructed track properties (momentum, angles, particle type, ...) are subject to inefficiencies like the limited detector resolution, misidentifications or even complete particle loss if the signal does not allow to decode the information.

The acceptance and particle interaction effects are calculated by a program called **HERMES Monte Carlo (HMC)**. It contains a model of the HERMES detector and the target based on the GEANT toolkit [Bru78]. For each particle, the transition through the detector is simulated taking into account the interaction cross sections with the material it traverses. The HMC output contains the response of the detector components, such as the signals from the individual wires of the tracking chambers. It is thus similar to the actual detector responses recorded from the experiment, except that it contains in addition the Monte Carlo information such as particle type and the originally generated particle kinematics.

Due to the compatible data format, the HMC output can be fed directly into the **HERMES reconstruction (HRC)** program, which is also used to decode the detector response of the real experiment (see Sec. 3.4.2 on page 27 and [Wan96]). Since the procedure to transfer the detector response into actual track properties is thus identical for experiment and simulation, all possible biases introduced at this stage are automatically accounted for.

As a last step, the data is usually passed through the  $\mu$ DST writer. This step is analogous to the experimental data productions. The result is a data set whose format is compatible to experimental data set, except for the additional Monte Carlo information (true particle type, true track kinematics, ...).

### 4.1.1 Event Generators

The generator Monte Carlo programs usually combine two steps in the event generation: a physics generator simulates the interaction of the initial state particles. The hadronisation of the ensuing system into its final state detectable by the spectrometer is then performed by applying a fragmentation model. The latter task is performed in the HERMES Monte Carlo using the JETSET program, which utilises the Lund string fragmentation model (see Sec. 4.3.1)<sup>1 2</sup>.

For this work, two generator Monte Carlo programs were used. The main work was done using the `gmc_disNG` package. This program uses event generators specialised to simulate deep inelastic scattering: PEPSI [Man92] for polarised scattering, and its predecessor, LEPTO [Ing97a] for the unpolarised case. Apart from the basic DIS process, they can simulate photon-gluon fusion (PGF) and QCD Compton (QCDC) processes. Results from `gmc_disNG` can be compared to experimental data both on cross section level as well as normalised to the number of DIS events. This generator was used for both the tuning of the Lund fragmentation model (see Section 4.4) as well as for the radiative and acceptance correction in the course of the extraction of the Born multiplicities (Sec. 5.4).

While LEPTO and PEPSI are an excellent tool to study the DIS process, the number of considered physics processes is rather limited. In particular, they do not account for the exclusive production of vector mesons, whose influence on the data had to be studied in the course of the multiplicity extraction. For this task, the PYTHIA ([Sjö01],[Sjö03]) event generator has been used<sup>3</sup>. PYTHIA is a general purpose event generator which takes into account a variety of processes. For this work, a special version of PYTHIA 6.2 has been used which was adapted to HERMES energies with special emphasis on the exclusive vector meson production [Lie04].

Apart from these, a number of other generators are available at HERMES, all with a more constrained field of application. Examples are specialised generators for exclusive vector meson production (DIPSI, rhoMC) and heavy flavour events (AROMA [Ing97b]).

## 4.2 The HERMES Smearing Generator

The HERMES smearing generator (HSG) is designed as a replacement for the HMC/HRC part of the Monte Carlo chain. It substitutes the time consuming simulation of the particle interactions with the detector material, which are otherwise calculated using the GEANT detector model. Instead, HSG uses a set of look-up tables which contain information on how the kinematic variables  $\theta_x$ ,  $\theta_y$  and the momentum  $p$  are affected. In some cases, particles can be absorbed completely (or scattered out of acceptance). This is accounted for by applying *loss functions*, which also reflect inefficiencies in the tracking algorithm.

<sup>1</sup>JETSET initially was a stand-alone application (versions 1-7), but it was later included in the PYTHIA 6.1 package, thus the main source of information about the program is the PYTHIA manual [Sjö03].

<sup>2</sup>Also the independent fragmentation model is available as option, but is usually not used in the HERMES Monte Carlo.

<sup>3</sup>PYTHIA is incorporated in the `gmc_pythia6` package.

Naturally, this method constitutes a significant approximation with respect to the original simulation and as such should be used with care. On the other hand, the reduced complexity results in vast time savings. While a full detector simulation of 100000 events takes about 24 hours, HSG reduces the time span to about 15 minutes. This makes the smearing generator a useful tool for initial Monte Carlo studies, once it has been ensured that the approach reproduces the physical features of interest.

The status of HSG is presented here as it was implemented for the tuning of the Lund model. It should be noted that subsequently, additional effort was put into the program to extend its capabilities. A first step was the inclusion of the detection of short tracks in HSG [Die03]. Recently, work has been done to include photons in HSG [Gul04]. This will allow to use HSG for DVCS<sup>4</sup> studies and to reconstruct  $\pi^0$  in HSG generated data.

### 4.2.1 Implementation

HSG was developed for the efforts to tune the Lund model. It was first designed as a set of functions internal to a specific Monte Carlo analysis code [Men01]. In the course of the work presented in this thesis, the algorithm has been reimplemented as a stand-alone application which can be plugged into the chain of HERMES Monte Carlo programs (see Fig. 4.1). HSG was also extended to differentiate between the detector configurations before and after the replacement of the original threshold Čerenkov detector with the RICH in 1998. As can be seen from Fig. 4.3, the introduction of the RICH had a significant impact on the momentum resolution at low particle momentum.

For each of the two configurations, Monte Carlo data was produced which included the full simulation of the detector. For the detector configurations before and after the introduction of the RICH detector (“1997/1999 geometry”), 7.5 and 10 million generated DIS events were used, respectively. Since both the generated and reconstructed track properties are stored in the data structure, the detector effects can be studied. The quantities

$$\Delta p/p = (p^{\text{rec}} - p^{\text{GMC}})/p^{\text{GMC}}, \quad (4.1a)$$

$$\Delta\theta_x = \theta_x^{\text{rec}} - \theta_x^{\text{GMC}}, \quad (4.1b)$$

$$\text{and } \Delta\theta_y = \theta_y^{\text{rec}} - \theta_y^{\text{GMC}} \quad (4.1c)$$

represent the resolution of the detector, where *GMC* denotes the generated values and *rec* the values reconstructed by the tracking algorithm. The variables

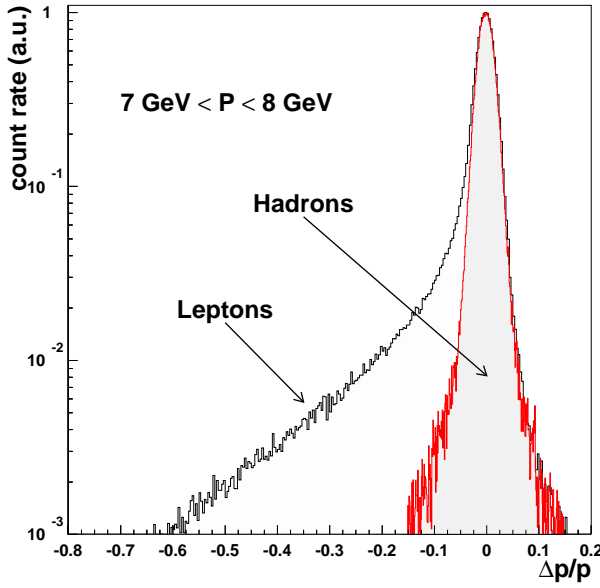
$$\theta_x = \arctan(\cos(\phi) \cdot \tan(\theta)) \quad \text{and} \quad (4.2)$$

$$\theta_y = \arctan(\sin(\phi) \cdot \tan(\theta)) \quad (4.3)$$

are the horizontal and vertical projections of the polar scattering angle  $\theta$ , respectively.

Figure 4.2 shows the quantity  $\Delta p/p$  for hadrons and leptons with a momentum between 7 and 8 GeV. Both leptons and hadrons are subject to a Gaussian smearing

<sup>4</sup>deeply virtual Compton scattering, see e.g. [Ell03], [Kra05a].

**Figure 4.2**

Momentum smearing of electrons/positrons and hadrons. Shown is the difference between the original momentum of the particles as assigned by the Monte Carlo generator and their respective momentum after passing a full GEANT simulation of the HERMES detector. The difference was normalised to the original momentum. The momentum is broadened to a Gaussian distribution by the detector resolution. Additionally, leptons are subject to energy loss by Bremsstrahlung.

around the original momentum value. This symmetric effect is due to the limited resolution of the detector. Additionally,  $e^+$  and  $e^-$  feature tracks with considerably stronger energy loss. This tail is due to radiation of Bremsstrahlung in the detector material.

Similar distributions for all three quantities defined in Eq. 4.1 were obtained in 1 GeV momentum bins for leptons and hadrons separately. This binning reveals the momentum dependence of the detector resolution, which is given by the widths of Gaussian functions fitted to the individual distributions. They are shown in Fig. 4.3 for the two particle groups and the three resolution variables. The empty and full symbols show the result before and after the installation of the RICH detector, respectively. The RICH detector had a negative impact on the resolution due to the additional amount of detector material.

In order to avoid binning effects, the original distributions were scaled with a fit to the momentum dependence of the resolution, yielding histograms with only minor variations in the distribution widths plus the additional radiative tails. They serve as look-up tables for the smearing generator: For a lepton or hadron track with given properties  $p$ ,  $\theta_x$  and  $\theta_y$ , HSG applies modifications to these values selected randomly according to the relevant distributions. Taking into account the scale factor, the new (smeared) track kinematics are obtained by

$$p^{\text{HSG}} = p^{\text{GMC}} \cdot (\Delta p/p \cdot f^{\Delta p/p}(p^{\text{GMC}}) + 1), \quad (4.4)$$

$$\theta_x^{\text{HSG}} = \theta_x^{\text{GMC}} + \Delta\theta'_x \cdot f^{\Delta\theta_x}(p^{\text{GMC}}) \quad (4.5)$$

$$\text{and } \theta_y^{\text{HSG}} = \theta_y^{\text{GMC}} + \Delta\theta'_y \cdot f^{\Delta\theta_y}(p^{\text{GMC}}). \quad (4.6)$$

The fit functions  $f^a(p^{\text{GMC}})$  are also shown in Fig. 4.3.

In addition to particle smearing, there is also the possibility that particles are not registered at all, either due to inefficiencies of the tracking algorithm or due to interactions with the detector material, causing for example the track being bent out of acceptance. By comparing fully tracked and reconstructed data with a sample only including the

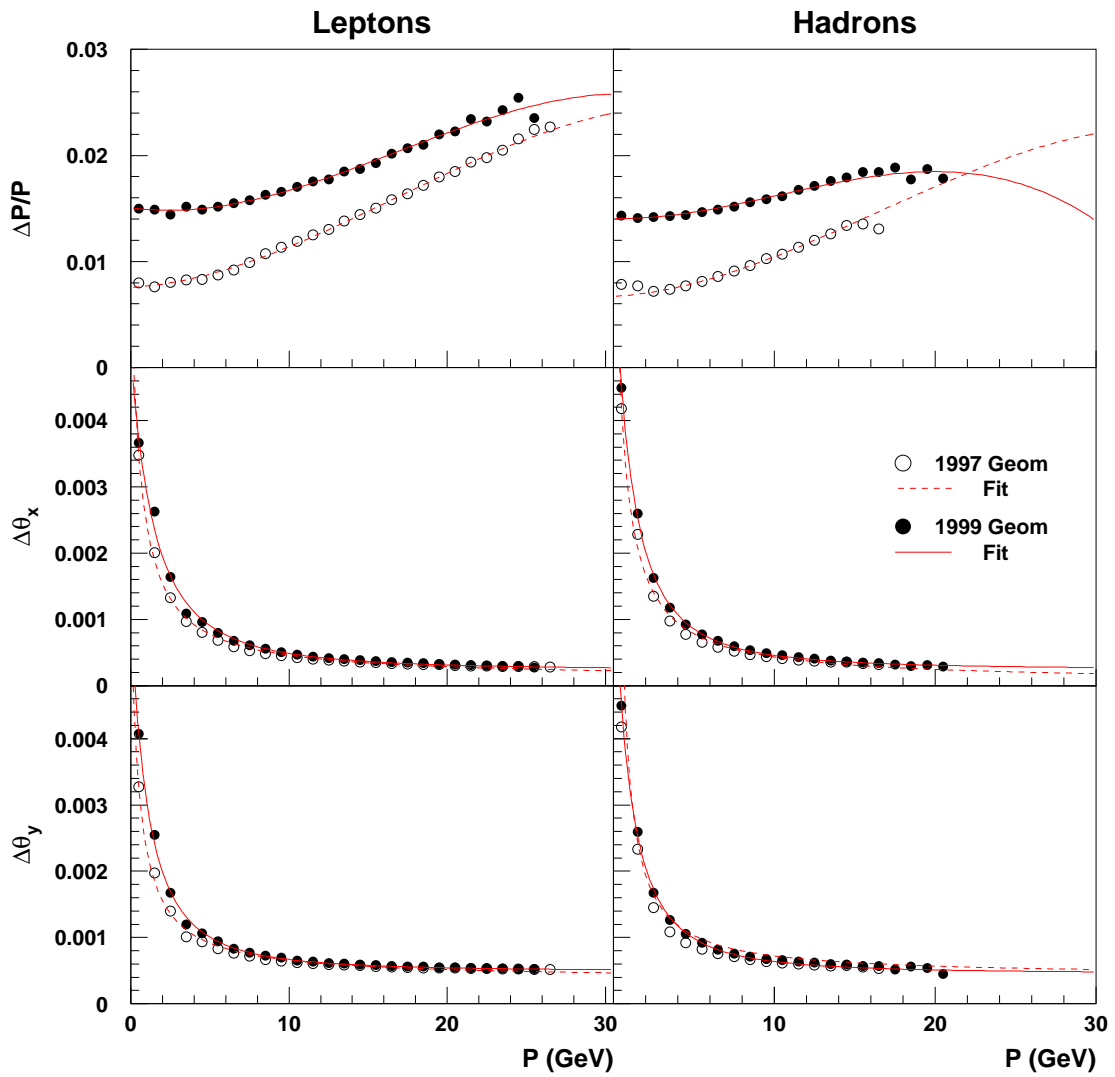


**Figure 4.3**

HERMES detector resolution for the setup before ('1997') and after ('1999') the introduction of the RICH.



smearing, the influence was estimated and fitted (see Fig. 4.4). HSG takes these efficiencies into account by rejecting smeared particles with a probability corresponding to the respective function. Generally, the correction is in the order of a few percent. For kaons, however, the loss is generally larger than 10%, with a strong decline for low momenta. This behaviour can be attributed to the by 50% shorter life time of the kaons with respect to the pions. The life time difference in the laboratory frame is even much larger due to the fact that the Lorentz factor is inversely proportional to the mass and thus  $\gamma_{\text{Pion}} \sim 3 \cdot \gamma_{\text{Kaon}}$  for the same momentum. Thus, a certain fraction of the kaons decays while traversing the detector, which in the standard Monte Carlo is simulated by HMC. HSG has to account for this effect by applying a larger particle loss probability to kaons.

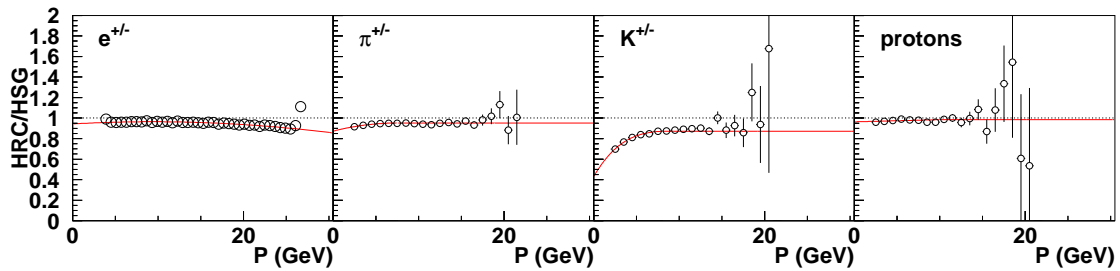


**Figure 4.4**

Loss functions used in HSG for the '1999' setting. The particle loss due to tracking inefficiencies and interactions with the detector material was estimated by comparing the particle yields after full tracking and after applying smearing corrections only, both in HERMES acceptance.

### 4.2.2 Comparison of Tracked and Smeared Data

As stated before, HSG was implemented in this work mainly with the Lund tuning efforts in mind. Thus, the aim was to reproduce the data properties which were used for the tuning, namely the hadron multiplicities versus various variables. In this section, the effect of smearing with HSG is compared to the one of full Monte Carlo tracking using HMC and HRC. For this task, a Monte Carlo production with 20 million generated DIS events was used, which was then fed to HMC/HRC or HSG, respectively. So the input to both alternatives was identical. The cuts correspond to the ones used in the data analysis (Table 5.3 on page 61). In particular, all data sets (including the *GMC* set without detector effects) are subject to a box acceptance cut as specified in the referenced table.

When comparing the results it should be kept in mind that HSG never was designed to be a replacement for tracking with HMC and HRC. The smearing generator is able to reproduce a large part of the detector influence on the data, but the agreement is definitely not perfect. Nevertheless, it has proven to be a very useful tool for Monte Carlo studies and for the tuning of the Lund model.

Figure 4.5 shows the  $Q^2$  and  $W^2$  distributions of semi-inclusive DIS positrons obtained from HSG in comparison to the result without any detector smearing (*generated*

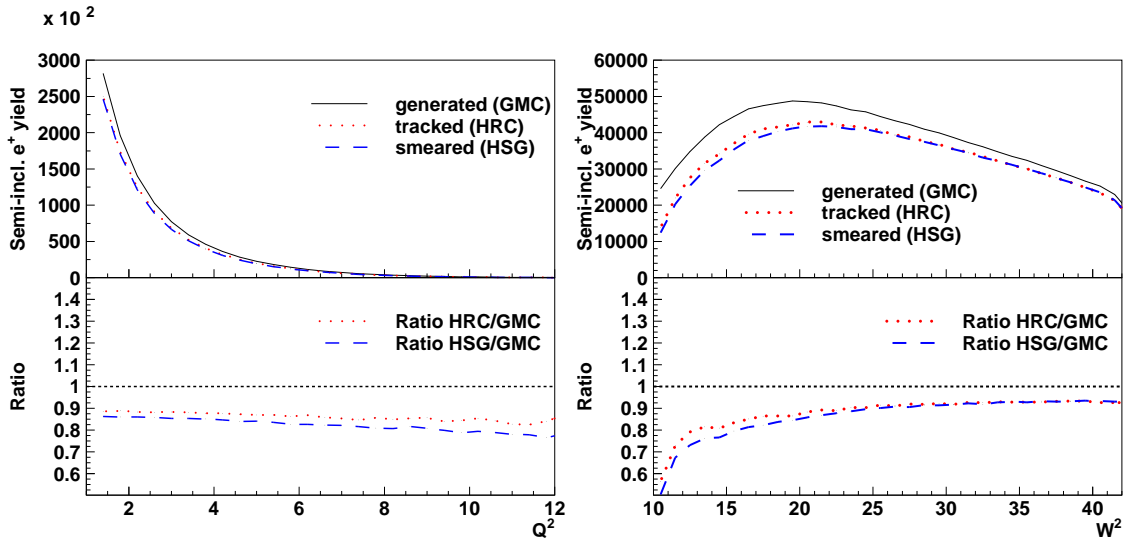


**Figure 4.5**

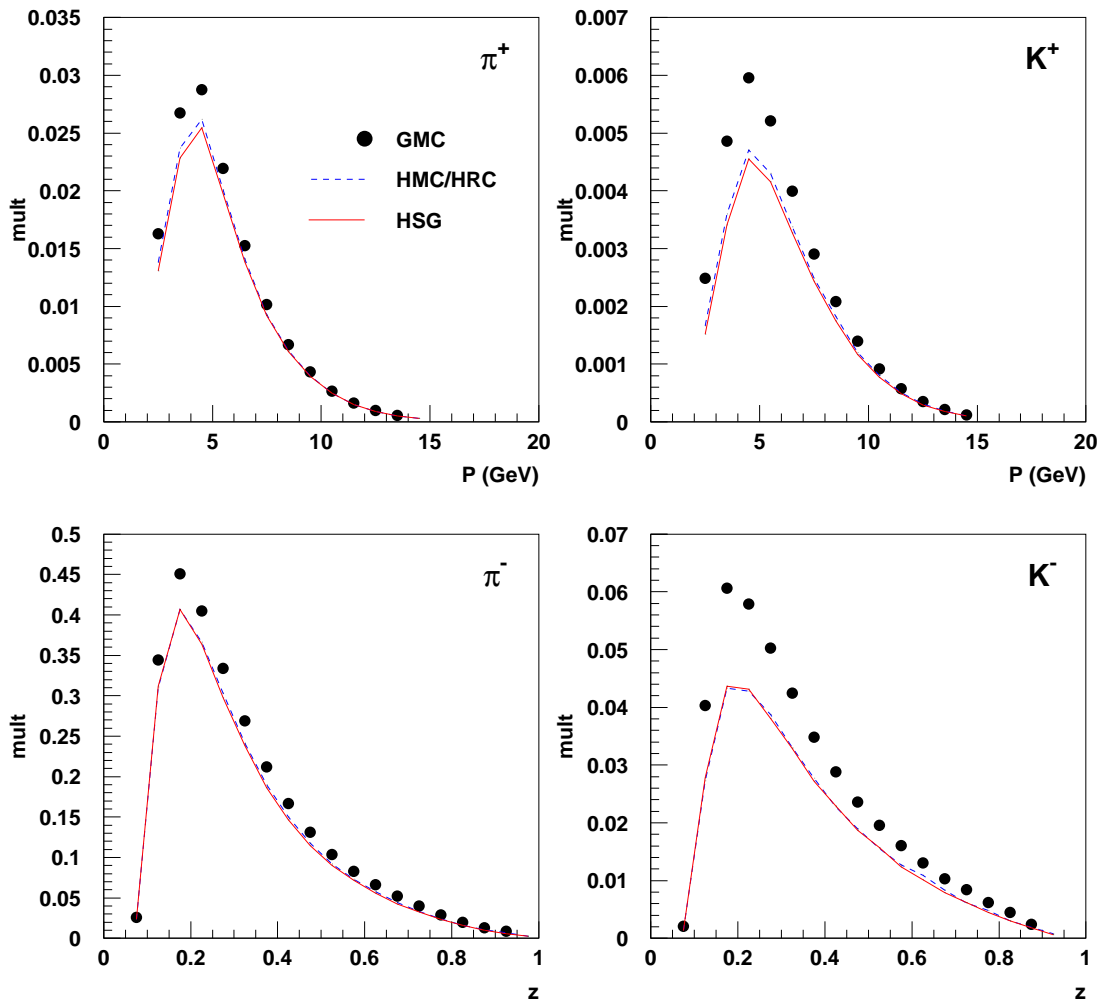
Distribution of semi-inclusive DIS positrons vs.  $Q^2$  and  $W^2$ . Shown are the yields after smearing (HSG) and a full detector simulation (HRC) in comparison with the input data from the Monte Carlo generator (GMC). HSG can largely reproduce the detector and tracking effects on the generated events. The observed discrepancies do not alter the usefulness of HSG for the studies it was designed for.

(GMC)) and with full tracking (*tracked (HRC)*). HSG is able to reproduce a large part of the detector and tracking influence on the  $e^+$  yields. Especially from the ratios in the lower part of the plots, some discrepancies between full tracking and smearing become apparent. For lower  $W^2$ , HSG causes the loss of too many positrons. Versus  $Q^2$ , this effect is distributed almost uniformly over the entire  $Q^2$  range.

A selection of hadron multiplicities is shown in Fig. 4.6. Again, three data sets are shown, corresponding to the multiplicities before detector effects and the multiplicities after full tracking or smearing, respectively. The data was obtained using the same cuts and Monte Carlo productions as the one presented in Fig. 4.5. The multiplicities of  $\pi^-$  and  $K^-$  versus  $z$  on the bottom show a very good agreement between HSG and HMC/HRC. For the multiplicities of positive pions and kaons versus momentum on the top, slight discrepancies in the high statistics region around 5 GeV are visible. Nevertheless, the agreement is good enough to warrant the application of HSG for the tuning of the Lund model.

### 4.3 Fragmentation Models

Fragmentation models bridge the gap between the short time scale, hard scattering process calculable from perturbation theory and the final state particles observed in the detectors. They can be grouped into three main schools of thought: cluster fragmentation, independent fragmentation and string fragmentation. The reason for the fact that differ-

**Figure 4.6**

Hadron multiplicities of  $\pi^+$  and  $K^+$  vs.  $P$  (top) and  $\pi^-$  and  $K^-$  vs.  $z$  (bottom). Given the same input, HSG produces multiplicities in good agreement with the ones obtained by a full detector simulation (HMC/HRC).

ent models with different approaches exist can be seen in the lack of understanding of the hadronisation process from first principles.

In the following, the emphasis is put on the Lund model (Section 4.3.1). It is the most successful and most widely used model to date and furthermore is the model of choice used in the HERMES Monte Carlo programs. Section 4.3.2 summarises the ideas behind the other models. A more profound comparison (and description) of the models can be found in [Sjö88].

### 4.3.1 The Lund Model

The Lund model is based on the *massless relativistic string* as a model for the QCD colour force fields between quarks and gluons. It provides a pictorial approach in modelling the quark (and gluon) dynamics during the fragmentation process. The Lund model is able to reproduce many of the dynamic properties of hadron production. Today it is the most widely used model to simulate the properties of fragmentation processes. In particular, the Lund model is used in conjunction with the HERMES Monte Carlo generators LEPTO, PEPSI and PYTHIA. In the following, a short introduction and overview is given. The basic ideas of the Lund string fragmentation model can be found in [And83a]. Later, the model has been refined and extended. In [And83b], the symmetric fragmentation function (Eq. 4.9) has been introduced. Other additions concern the fragmentation of multiparton jets ([Sjö84b], [Sjö84a]) and an extended baryon production mechanism ( $\rightarrow$  popcorn model, [And85]). A very exhaustive and detailed description can be found in [And97].

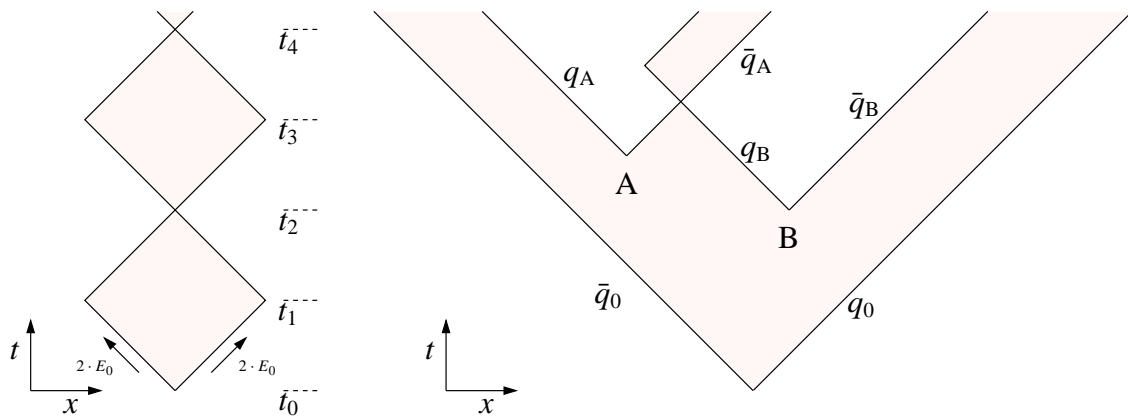


**Figure 4.7**

The massless relativistic string in the Lund model. The left hand side illustrates a bound state of two particles. At the turning points of the particles ( $t_1$ ,  $t_3$ ) the complete energy of the system is contained within the string spanned between the two particles. The process of fragmentation in the Lund model is shown on the right hand side: New  $q\bar{q}$  pairs can be produced along the string, causing a breakup into separate bound states which contain different fractions of the total original energy.

The underlying principle of the Lund model — the massless relativistic string — is illustrated in Fig. 4.7 for the case of  $e^+e^-$ -annihilation. A  $q\bar{q}$ -pair is produced at a

single point in space-time. Owing to the energy obtained in the original process, they start to move apart in opposite directions. The attractive force due to the colour field between the quark and the anti-quark is represented by the massless relativistic string spanned between the two objects. The constant force  $\kappa$  caused by this string gives rise to a linear potential. Thus a stable meson configuration produces a so-called yoyo-mode, in which the system oscillates between states where all energy is contained in the particles' momentum ( $t_0, t_2$ ) and the turning points where the energy is contained in the string of length  $\Delta x$  stretched between the particles ( $E = \kappa \cdot \Delta x$ ). The amount of energy per unit length has been deduced from hadron spectroscopy to be  $\kappa \approx 1$  GeV/fm.

For sufficiently high energies, new  $q\bar{q}$ -pairs can be produced along the force field. This corresponds to creating new end points and thus to the breakup of the string into two parts. As there is no force field between the new particles but an attractive force towards the original ones, the two systems immediately separate from each other and can be treated as isolated.

Several string breaks can occur, until the individual systems reach a cut-off energy threshold. Figure 4.7 shows an example with two string breaks at the vertices  $A = (x_A, t_A)$  and  $B = (x_B, t_B)$ . In this case, the final state would consist of three mesons. For instance,  $\bar{q}_A$  and  $q_B$  from the adjacent vertices A and B form the final state  $S_{AB}$ , whose energy and momentum are given by the vertex positions in space-time:

$$E^2 - p^2 = m^2 = \kappa^2 \left[ (x_A - x_B)^2 - (t_A - t_B)^2 \right]. \quad (4.7)$$

This illustrates the relation of the vertex positions and the mass of the final state containing the string in between and its end point quarks. The interesting consequence of Eq. 4.7 is that, in order for the mass  $m$  to be real, the distance in space-time between the vertices A and B must be space-like. This in turn means that the time-ordering of the string breakups is just a matter of the frame of reference, there is no universal *first* and *last* vertex.

The Lund model uses an iterative approach to simulate the fragmentation process. An iteration essentially consists of three steps:

**Flavour Selection.** In the first step of each iteration, the flavour of the new  $q\bar{q}$  pair is chosen. Massless quarks without transverse momentum could be produced at one point in space-time and then be pulled apart by the force field (as depicted in Fig. 4.7). If the quark masses and transverse momentum are taken into account, however, the quark and anti-quark have to be produced in a certain distance from each other to account for the energy contained in the transverse mass  $m_\perp = \sqrt{m^2 + p_\perp^2}$ . In a quantum mechanical picture, the quarks may be produced at one point to then tunnel out into the classically allowed region. The tunnelling probability is given by

$$P \sim \exp\left(-\frac{\pi m_\perp^2}{\kappa}\right) = \exp\left(-\frac{\pi m^2}{\kappa}\right) \cdot \exp\left(-\frac{\pi p_\perp^2}{\kappa}\right), \quad (4.8)$$

which gives rise to a suppression of heavy quark production ( $u : d : s : c \approx 1 : 1 : 0.3 : 10^{-11}$ ). The  $s\bar{s}$  production probability relative to the lighter quarks is a free parameter of

the model (strangeness suppression factor, PARJ 2), since the quark masses are difficult to assign. Also the Gaussian width of the transverse momentum distribution can be adjusted (see page 49).

**Hadron Selection.** Once the quark flavours which form a new bound state have been selected, the spin and angular momentum state of the compound has to be decided. Concerning the two possible spin couplings, a vector meson to pseudo-scalar meson ratio of 3:1 could be expected due to the relative number of available spin states. However, this effect is countered by the spin-spin interaction of the constituents, which suppresses the vector meson production with respect to pseudo-scalar meson production. The relative probabilities can be set in the parameters PARJ 11 (for mesons containing  $u$  and  $d$  quarks; default: 0.5) and PARJ 12 ( $s$  quarks; 0.6).

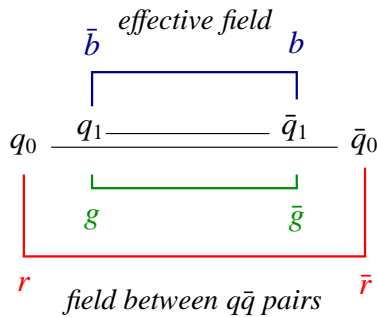


**Figure 4.8**

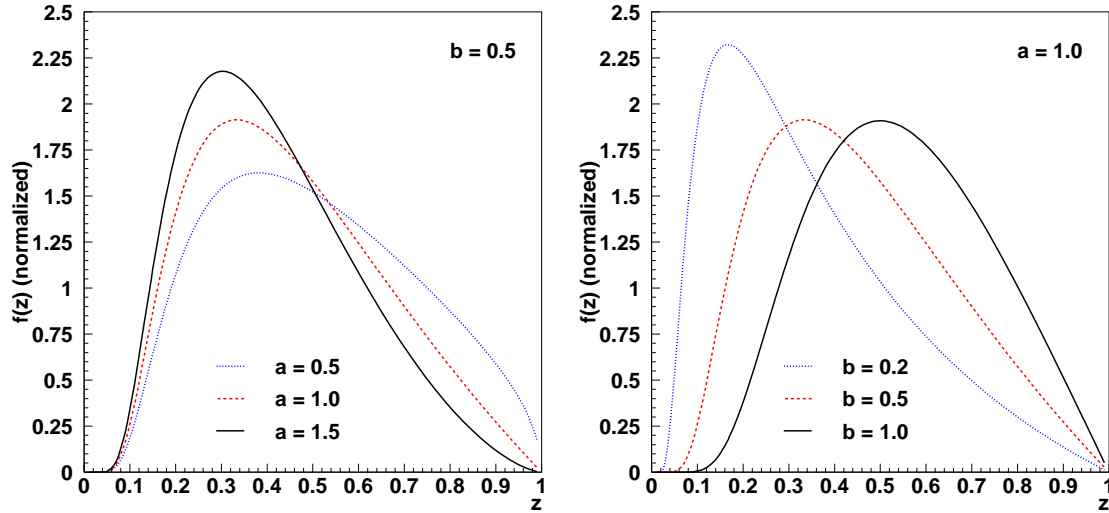
Popcorn baryon production

While mesons emerge rather naturally as bound states consisting of a string with a  $q$  and  $\bar{q}$  as end points, there is no clear and unique way to produce baryons in this model. Three alternatives are implemented in JETSET. In the simplest form, baryons arise by replacing the  $q\text{---}\bar{q}$  pair with a  $\bar{q}\bar{q}\text{---}qq$  configuration (both  $qq$  and  $\bar{q}\bar{q}$  are colour anti-triplet states). Again, the relative probability can be adjusted (PARJ 1). While in this simple model baryon and antibaryon are automatically produced as nearest neighbours, the alternative *popcorn model* allows for one (simple popcorn [And85]) or several (advanced popcorn [Edé97]) mesons to be produced in-between. No diquarks are produced, but baryons arise from the successive production of several  $q_i\bar{q}_i$  pairs with different colours. In Figure 4.8, the initial endpoints  $q_0\bar{q}_0$  are assumed to be of type  $r\bar{r}$  (red and anti-red). Instead of producing another  $\bar{r}r$  pair, e.g. a green  $g\bar{g}$  pair is created. The non-vanishing field in the centre is of type  $\bar{b}b$  ( $b = \text{blue}$ ). A new pair  $q_3\bar{q}_3$  of the right type would now experience an attractive force for the quark and anti-quark towards  $q_0q_1$  and  $\bar{q}_0\bar{q}_1$ , respectively, resulting in a colourless baryon and anti-baryon state. Additional  $b\bar{b}$  pairs can result in meson states between the baryon and anti-baryon.

**String Fragmentation.** At this stage, the hadron (and thus its mass) has already been decided upon, as well as the transverse momentum components. What is left is the choice of the total energy and consequently the particles longitudinal momentum. The fraction  $z$  of the total available energy to be assigned to the new particle is given by the Lund symmetric fragmentation function [And83b]

$$f(z) \sim z^{-1} (1 - z)^a \exp\left(-\frac{bm_{\perp}^2}{z}\right). \quad (4.9)$$

The variables  $a$  (PARJ 41) and  $b$  (PARJ 42) are instrumental to regulate the distribution of energy across the final states. Figure 4.9 shows the characteristics of the function for

**Figure 4.9**

The symmetric Lund fragmentation function (Eq. 4.9) for different values of  $a$  and  $b$ .

varying values of  $a$  (left side) and  $b$  (right side) while keeping the other variable fixed. All functions have been normalised to unity. As can be seen, lower values of  $a$  shift and broaden the distribution towards higher  $z$ , while lower values of  $b$  have the opposite effect.

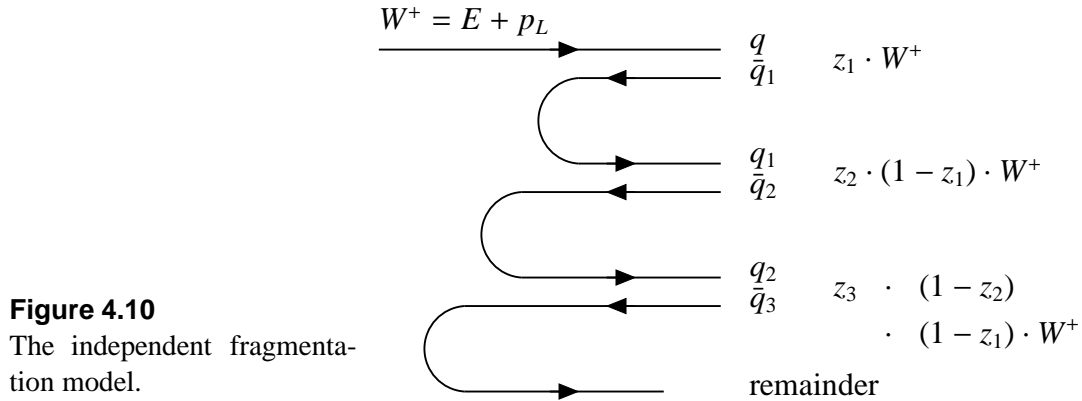
The functional form of Eq. 4.9 is motivated by the requirement that the fragmentation process should be independent of the choice of the direction the fragmentation is performed along the string [And83b]. In fact, at each iteration the Lund algorithm is randomly choosing a string end from which the fragmentation takes place. Once the remaining energy has dropped below a given value (PARJ 33), two hadrons are produced after a final string break. This avoids the problem of putting the last hadron on the mass shell while being at the same time completely constraint by energy and momentum conservation.

## 4.3.2 Alternative Models

### Independent Fragmentation

In many aspects, the independent fragmentation (IF) model is similar to the string fragmentation model. But while in the latter the whole initial parton configuration is taken into account for the fragmentation (e.g.  $q \leftrightarrow qq$  after a DIS process on a baryon valence quark), IF treats the fragmentation of each jet independently.

The fragmentation of the initial quark  $q$  is triggered by the creation of a new  $q_1\bar{q}_1$  pair with opposite and compensating transverse momenta (given by a Gaussian distribution) (Figure 4.10). The energy fraction  $z$  taken by the new meson  $q\bar{q}_1$  is again determined by a distribution function  $f(z)$ . Several functions have been used, a common form is the



Field-Feynman parametrisation

$$f(z) = 1 - a + 3a(1 - z)^2 \quad (4.10)$$

with a default value of  $a = 0.77$  [Fie78].

The concept of independent fragmentation has some shortcomings not found in e.g. the string fragmentation model. One issue are the small violations of conservation of energy, momentum and flavour. These come about, for example, by the fact that the last parton with an energy below a certain threshold (“*remainder*” in Fig. 4.10) is discarded. Furthermore, particles produced with a very small energy fraction  $z$  move backwards in the jet ( $p_L < 0$ ) and are usually also discarded.

Several model extensions exist which fix these issues, the implementations most commonly used are the Hoyer et al. [Hoy79] and Ali et al. [Ali80] programs.

The other problem of the independent fragmentation is that its formulation is not Lorentz-invariant, the outcome depends on the chosen reference frame. As a workaround, the fragmentation is always carried out in the c. m. frame. However, there is neither a physical motivation for this restriction nor does the workaround scale well beyond simple 2-jet events.

### Cluster Fragmentation

The cluster fragmentation model (Fig. 4.11) utilises a QCD parton branching mechanism to obtain the multitude of final state particles. The fragmentation process is basically divided into three steps: First, parton showers evolve the initial partons far off mass-shell into partons nearer to mass-shell. The energy sharing in the branching vertices  $q \rightarrow qg$ ,  $g \rightarrow q\bar{q}$  and  $g \rightarrow gg$  is given by the corresponding Altarelli-Parisi splitting functions  $P_{ab}$  (see Eq. (2.24)). In a second step, partons in the same region of phase space are grouped together into clusters, which in case of high masses fragment into smaller ones. Finally, the clusters decay isotropically into hadrons.

In general, the cluster model contains few adjustable parameters, like the QCD scale parameter  $\Lambda_{\text{QCD}}$  and energy cut-offs. Again various implementations exist, the most prominent ones being the Webber model ([Web84], [Mar84]) implemented in the HERWIG program [Cor01] and the CALTECH-II model [Got87].



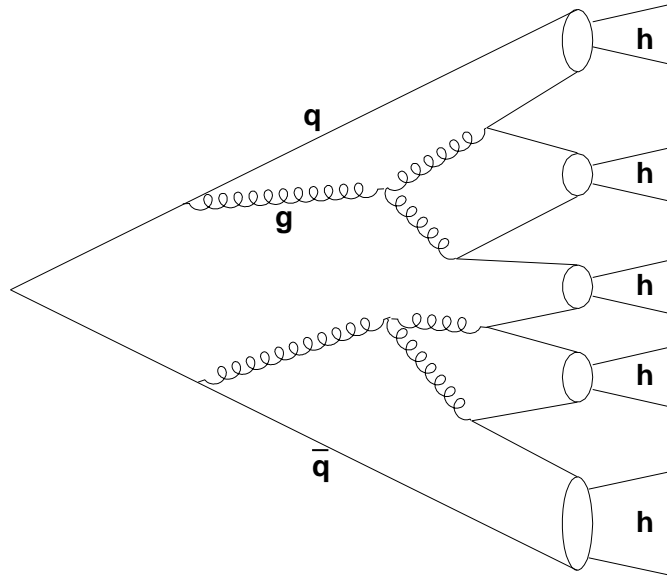


**Figure 4.11**  
Scheme of the cluster fragmentation model

## 4.4 Fragmentation Tuning

The original JETSET parameters that regulate the fragmentation in the Lund model have been tuned for high energy  $e^+e^-$  collisions. At HERMES, two major tuning efforts were undertaken to adjust the model to HERMES energies. At first, the  $a$  and  $b$  parameters of the Lund fragmentation function (Eq. 4.9) and the Gaussian with  $\sigma$  of the the transverse momentum distribution were tuned to yields of positive and negative hadrons versus  $z$  and  $p_t$  in 5  $Q^2$  bins. At this stage detector effects were taken into account applying a detector correction factor to the generated yields. The resulting *Holger tune* is described in [Gei98] and [Tal98].

Afterwards [Men01], further parameters were taken into consideration. The detector correction factors were replaced by the HSG, which at this stage was a function internal to the analysis code. The Monte Carlo data was tuned to  $h^+$  and  $h^-$  yields versus  $z$  and the distribution of all hadrons versus  $p_t$ .

The tuning effort presented here adds additional complexity to previous work by considering the hadron multiplicities for pions, kaons and protons individually, taking into account the information provided by the RICH detector. Also, the later tuning runs took into account the elastic vector meson contribution to pion multiplicities versus  $z$ , which in the high  $z$  region amounts to about 50% of the pions (see Figure 5.7 on page 71). Since LEPTO does not simulate the underlying processes, this contribution has to be subtracted from the experimental data multiplicities in order to compare on the same basis.

Various (and varying) hadron spectra have been included in the tuning process. The latest and best tune presented in Table 4.1 was adjusted to  $\pi^-$ ,  $K^-$  and antiproton dis-

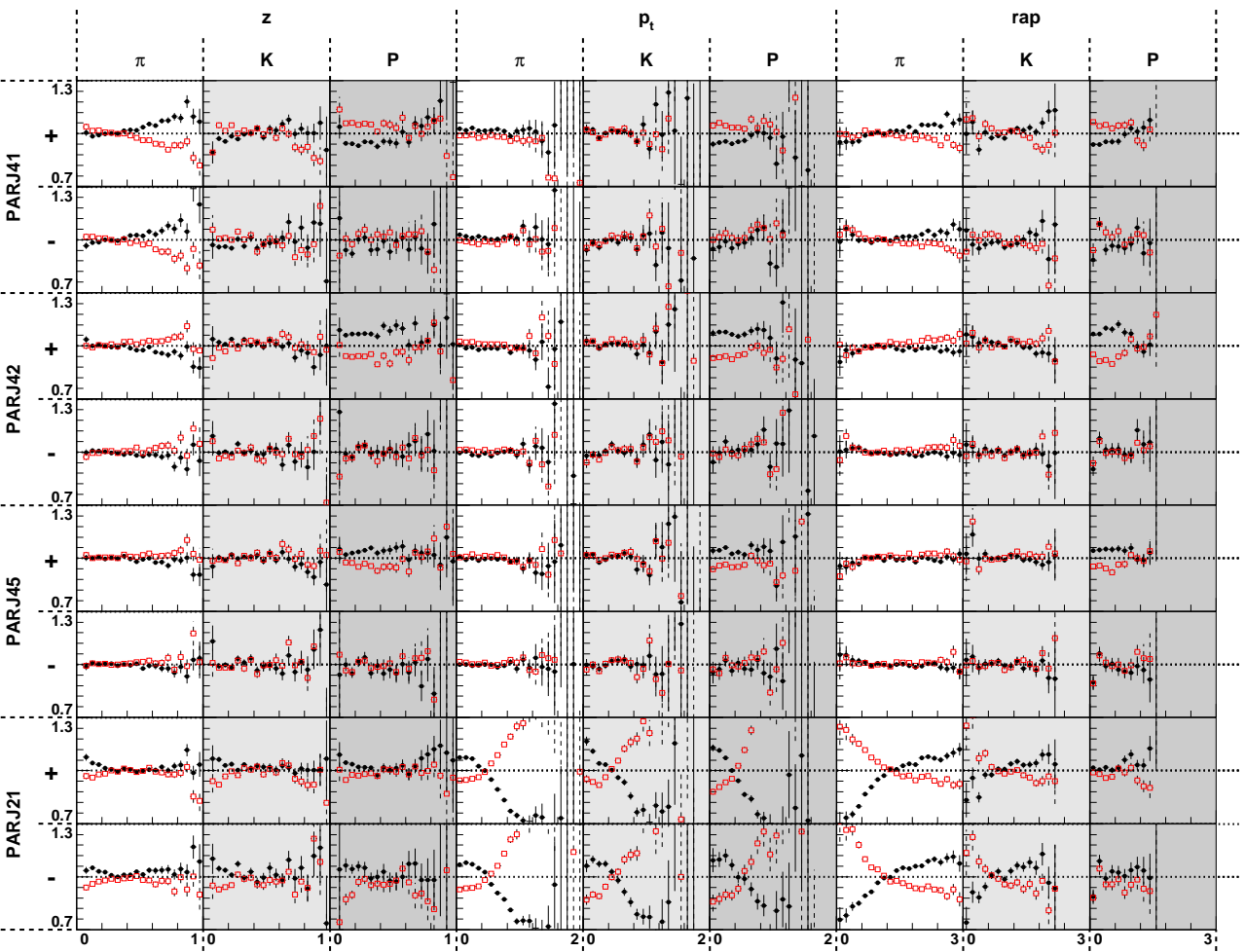


**Figure 4.12**

Influence of the Lund parameters PARJ 41, PARJ 42, PARJ 45 and PARJ 21 on the hadron multiplicities versus  $z$ ,  $p_t$  and rapidity. The parameters were increased (empty symbols) or decreased (solid symbols) by 10% with respect to their 2004c tune values (see Table 4.1). The two rows show the influence on the multiplicities of positive and negative hadrons, respectively.

tributions vs.  $z$ ,  $p_t$  and rapidity. Additionally, the differences between the negative and positive hadron distributions for the three hadron types and variables were taken into account. This choice of tuned properties was motivated by problems to simultaneously adjust the positive and negative kaon multiplicities. A fairly good tune for  $K^-$  would result in a too low  $K^+$  yield, but increasing the  $K^+$  yield automatically lead to an excess of  $K^-$ . As possible cause for this discrepancy an additional (= unsimulated) source for positive kaons was considered (see page 51). The chosen tune properties thus emphasise the negative hadron multiplicities, while still trying to adjust the (for kaons too large) differences between the distributions.

The comparison to the older parameter sets in this table is calculated including the charge separated multiplicities for the three hadrons and the three variables. The  $\chi^2$  was calculated running over all bins of the above-mentioned multiplicities, taking the number of (non-zero) bins as degrees of freedom:

$$\chi_{\text{ndf}}^2 = \frac{1}{n_{\text{bins}}} \sum_{h=\substack{\pi^\pm \\ K^\pm \\ (A^-)P}} \sum_{x=\substack{z \\ p_t \\ \eta}} \sum_i \frac{(m_i^h(x))_{\text{Exp.}}^2 - (m_i^h(x))_{\text{MC}}^2}{(\sigma_i^h(x))_{\text{Exp.}}^2 + (\sigma_i^h(x))_{\text{MC}}^2}. \quad (4.11)$$

Each multiplicity distribution comprised 20 equidistant bins in the range of  $0 \dots 1$  ( $z$ ),  $0 \dots 2$  GeV ( $p_t$ ) and  $0 \dots 3$  (rapidity).

The experimental errors  $(\sigma_i^h(x))_{\text{Exp.}}^2$  included the statistical error as well as the systematic uncertainty introduced by the RICH unfolding. It should be noted, however, that the unfolding errors used for latest tune (and also for the  $\chi^2$  values in Table 4.1) correspond to the now obsolete method used for the June 2004 multiplicity release. More information about the RICH unfolding can be found in Section 5.2.2 on page 63.

In the following, the iterative tuning procedure is described. The parameter space is explained. Finally, the current status of the tuning efforts is presented.

#### 4.4.1 The Fitting Procedure

The goal of the tuning efforts is to improve the consistency of Monte Carlo generated data with experimental results. The main approach is the iterative adjustment of a number of parameters using an algorithm which tries to minimise the  $\chi^2$  between the two data sets. Additionally parameters can be fitted by systematically changing the parameter values. The latter method is reasonable for parameters which are fairly uncorrelated from others.

Even with the HSG, the iterative tuning is very time consuming. Previously ([Men01], [Tal98]), the tuned multiplicities were not distinguished by hadron type. Consequently, it was sufficient to generate in the order of  $10^5$  DIS events per iteration. Since one of the specific aims of the new round of tuning was to make use of the particle information provided by the RICH detector, the multiplicities were broken up into the individual hadron contributions, thus demanding higher statistics. Usually, three million DIS events were generated per iteration.

After each iteration, the multiplicities resulting from the current parameter set were compared to the experimental multiplicities. At this point, a strategy is needed to de-

cide upon the generation of a hopefully better parameter set. Originally, the downhill SIMPLEX method [Nel65] as implemented in the MINUIT package [Jam75] was used. This algorithm has the advantage of being rather robust against fluctuations of the  $\chi^2$  surface. On the other hand, the algorithm is inherently linear, meaning that one parameter set after the other has to be evaluated. Since the HERMES PC Farm essentially provides a multi-processor computing setup, it was desirable to parallelise the evaluation. One way would have been to distribute the generation of events for each step over several computing nodes and combine the statistics once all subprocesses have finished. The disadvantage would have been a higher sensitivity to failures and delays in the Monte Carlo productions. Any problem in any of the  $n$  different nodes involved in the computation would have halted the tuning progress. Additionally, the nodes of the PC Farm are equipped with different processors and might be subject to different work loads. Thus it is not possible to a priori decide which work load distribution would result in a minimal wait time for the last job to finish.

For this reasons, a *genetic algorithm* [Gol89] has been implemented as an alternative method. The principle is illustrated in Figure 4.13. The free parameters of a given set are translated into a string of bits. To do this, for every parameter a minimum and maximum value is defined, as well as the number of bits which will be used to store the parameter value. The first bit then defines whether the parameter value lies in the upper or lower half of the specified interval. Accordingly, the next bit is set by the position within the upper or lower half. Each additional bit thus doubles the precision of the parameter grid.

The algorithm makes use of a number of parameter sets — the so called *population* — which are ordered in terms of their respective  $\chi^2$  (for the initialisation, see below). Two parameter sets are chosen from the list, with a bias towards selecting better sets from the top. These *parents* are then used to generate two new sets by bit by bit crossing of the information using a random mask (see Figure 4.13). For example, the *offspring set 1* consists of the bits of parent 1 when the corresponding mask value is 1, the other bits are taken from parent 2. Offspring 2 is constructed in the opposite fashion.

Evidently, if one or several parameter values are identical for the two parents, both offspring sets will again have the same values. This causes the risk of the population to degenerate, meaning that the limited variety of parameter values prevents the algorithm from testing the full phase space. To compensate that risk, an additional random element is introduced, the *mutation* of individual bits. With a certain probability, any single bit can be flipped. The probability has to be low (in the order of a few percent), otherwise the information gained in the previous iterations (inherited in the form of the parent parameter sets) is obscured too much by the random variations.

The two new parameter sets are then evaluated using a common Monte Carlo setup which consists of the Monte Carlo generator, HSG and the analysis program which extracts the desired multiplicities. For this purpose, the bit strings are converted to their corresponding numerical parameter values. These are written into the card files read in by GMC. Once the Monte Carlo production is finished, the  $\chi^2$  is calculated and the parameter set is sorted into the population.

The advantage of this method lies in the fact that it is easily parallelisable. The supervising program was running on an interactive node on the PC Farm. It produced

as many parameter sets as it had processors at its disposal and for each set submitted a Monte Carlo production job to the batch system. In regular intervals, the supervising program checked for finished jobs, replacing any completed production by a new one with new parameters (after having processed the results from the previous). Increasing the number of parallel productions increases the latency of the information transfer, since for  $i$  parallel jobs the  $n$ th job only draws from the results of  $n-i$  iterations. Nevertheless, the available computing setup at HERMES made this approach very attractive.

For the *initialisation* of the population, two methods have been used. One possibility is to start of with random values within the parameter space. These parameter sets got assigned a high  $\chi^2$  value and subsequently were replaced by tested sets with known (better)  $\chi^2$ . Another possibility was to start a new tuning round based on the knowledge of previous efforts. Upon initialisation, the supervising program could read in tables containing parameter sets and their corresponding  $\chi^2$ , thus having a base to start from.

## 4.4.2 Results

The parameters  $a$  (PARJ 41) and  $b$  (PARJ 42) of the symmetric Lund fragmentation function have the major impact on how the available energy is distributed among the produced hadrons. Larger values of  $a$  shift the hadron production probability towards lower values of  $z$ , while the increase of  $b$  causes the opposite effect (see Figure 4.9). This shift of energy is of course reflected in the multiplicities versus  $p$ ,  $x_F$  and rapidity. Since the default fragmentation settings in LEPTO ( $a = 0.3$ ,  $b = 0.58$ ) show a too broad distribution over  $z$ , all tuning efforts at HERMES resulted in larger values of  $a$  and smaller values of  $b$  (see [Gei98],[Men01] and Table 4.1). This can be explained with the much higher energies to which the default parameters were tuned. In that region, higher order QCD effects cause additional low energy parton emissions. At HERMES energies, these effects can be neglected, which has to be accounted for by the adjustment of the Lund fragmentation function.

Additionally, the Lund fragmentation function can be further modified specifically in the case of diquark fragmentation. The parameter  $a_{qq}$  (PARJ 45) is added to the value of  $a$  if the original or produced object is a diquark. Enlarging this parameter decreased the proton distributions significantly, while at the same time having only a minor influence on the other hadrons. Since tunes before the consideration of this parameter showed an excess of protons, this allowed a better adjustment of the Monte Carlo proton data to the observed yields.

The  $\sigma$  parameter (PARJ 21), which corresponds to the width of the Gaussian  $p_x$  and  $p_y$  transverse momentum distribution, remained very stable during all tuning efforts. Any substantial shift of this parameter dramatically deteriorates the data agreement of the  $p_t$  and rapidity distributions (see Fig. 4.9).

The diquark suppression factor ( $qq_{\text{supp}}$  or PARJ 1) determines the probability ratio of diquark-antidiquark production versus quark-antiquark production:  $\text{PARJ 1} = \mathcal{P}(qq)/\mathcal{P}(q)$ . It has a huge impact on the antiproton yields, since the production of an antiproton requires the creation of a new  $\bar{q}\bar{q}$  pair. Protons are also strongly affected, but since they can also originate from a new antiquark plus the target remnant, the effect is much less pro-

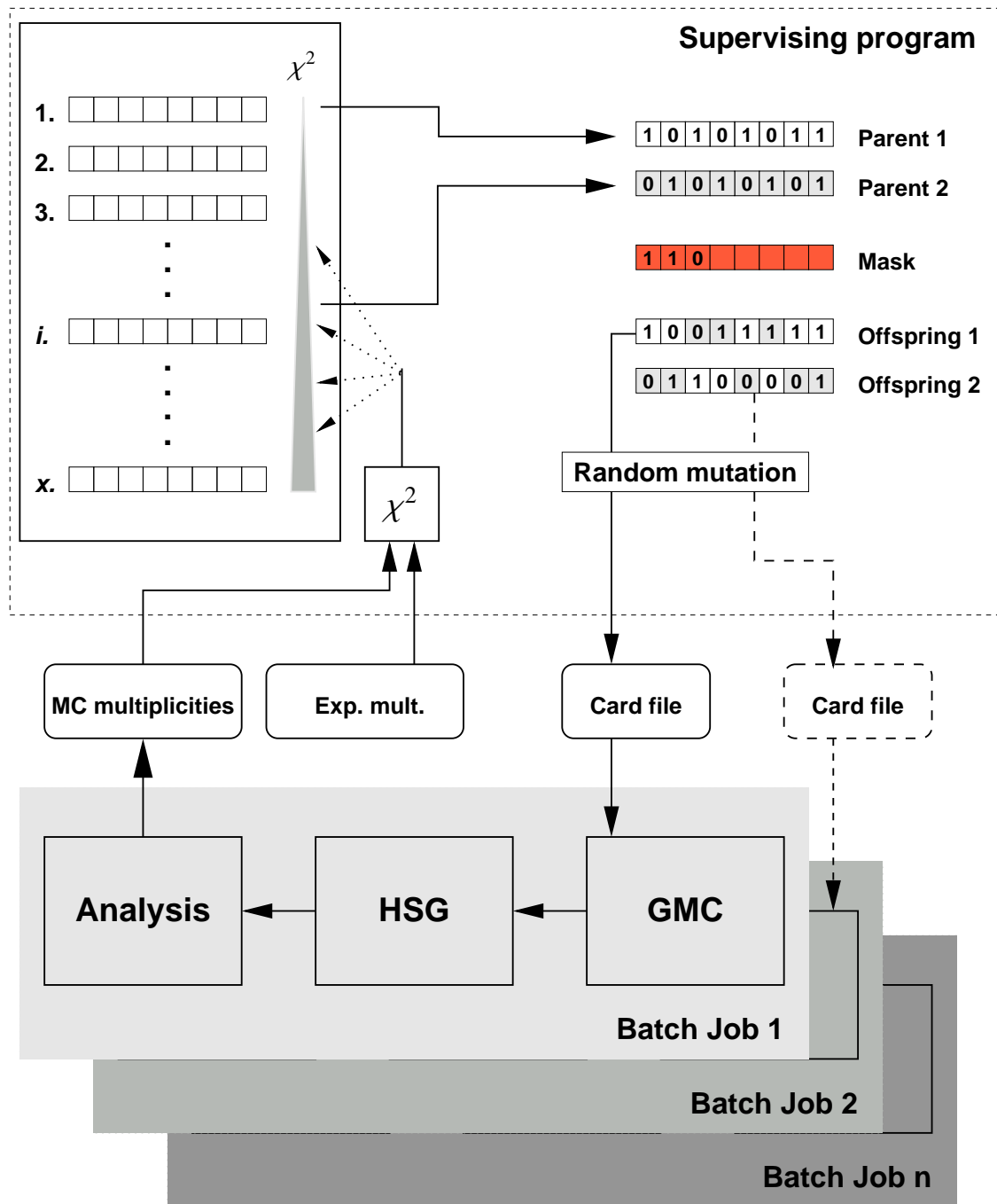


**Figure 4.13**

Schematic overview of the Monte Carlo tuning using a genetic algorithm. The supervising program was running on one of the interactive nodes on the PC Farm. The Monte Carlo productions were submitted to the standard batch system.

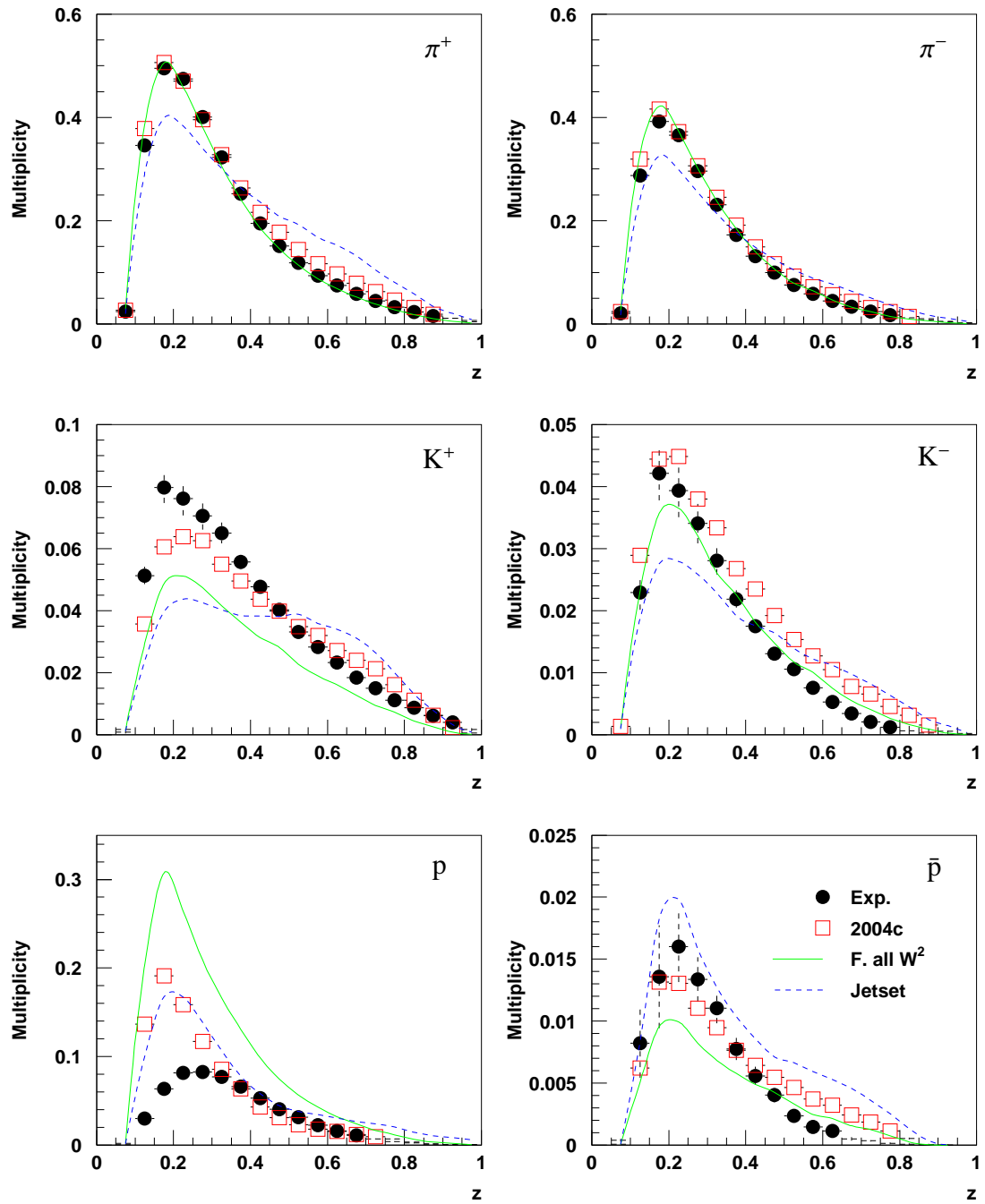
nounced. Of course a higher proton and antiproton yield tends to come on the expense of the other hadrons. However, due to the much larger statistics of kaons and especially pions, the effect is hardly visible.

Table 4.1 shows different parameter sets used at HERMES over time. The  $\chi^2$  values given for each tune are based on the charge separated  $z$ ,  $p_t$  and rapidity distributions of pions, kaons and protons. For every set, 6 million DIS events have been generated. The cuts are equivalent to the ones used in the multiplicity analysis (Table 5.3 on page 61). Additionally,  $z > 0.2$  was required for the  $p_t$  and rapidity multiplicities.

All Monte Carlo productions used for the multiplicity analysis presented in Chapter 5 are based on the 2004c parameter set. This parameter set was tuned using the JETSET default parameters as starting point (first parameter column). Variables for the iterative tuning were PARJ 41, 42, 45, 1, 2 and 21. The set 2004c-high $p_t$  was further optimised by performing a parameter scan on the variables  $f$  (PARJ 23) and  $p_t^f$  (PARJ 24). These two parameters cause a fraction  $f$  of the Gaussian transverse momentum distribution to be a factor  $P_t^f$  larger than the original width  $\sigma$ , thus effectively allowing for non-Gaussian tails. As already stated in [Men01], increasing these two factors considerably improve the agreement with experimental data in the high  $p_t$  area. Since the effect on the other distributions is minimal, these parameters were never included in the iterative fitting.

Figures 4.14, 4.15 and 4.14 compare 2004c with the JETSET default values and the *all*  $W^2$  tune from [Men01]. The cuts used to acquire the multiplicities are the same as for the multiplicity extraction presented in the next chapter (Table 5.3). For the multiplicities versus  $p_t$  and rapidity, only hadrons with  $z > 0.2$  were taken into account. With respect to the *all*  $W^2$  tune, the agreement of many individual hadron distributions could be improved. The pion agreement versus  $z$  in fact is slightly worse. However, the  $p_t$  and rapidity distributions show a considerable improvement. Concerning the protons, the notable excess has been reduced, although — especially versus  $z$  — the yields are still far from perfect. Comparing the antiproton multiplicities versus  $p_t$  and rapidity, it seems that for the latter case the integrated yield from the 2004c parameter set shows a larger excess over the experimental yield than is the case for  $p_t$ . This apparent disagreement is caused by the fact that the antiproton distributions extend to the negative rapidity region, where the excess is partly cancelled. For protons, the situation is similar.

For the kaons, the  $K^+$  multiplicities has been improved at the expense of the negative kaons. This is characteristic for all the tuning efforts: a reasonable match in the  $K^+$  yields results in an excess of  $K^-$ , while improving the  $K^-$  distributions causes too low  $K^+$  yields. The direct handles on the kaon yields — most notably the strange quark and strange vector meson suppression factors (PARJ 2 and 12) — have only a symmetric effect. It was considered that there might be other sources for positive kaons that are not simulated in the Monte Carlo program, thus explaining the shortage of  $K^+$  then the  $K^-$  yields are matched. A possible candidate was the exclusive production of  $K^+$ . However, a recent study [Die05] showed that these channels can only add about 1% to the observed cross section and thus can not be responsible for the  $K^+$  deficiency. This problem has to be studied further.



**Figure 4.14**

Comparison of experimental data with different Lund fragmentation parameter sets as a function of  $z$ .



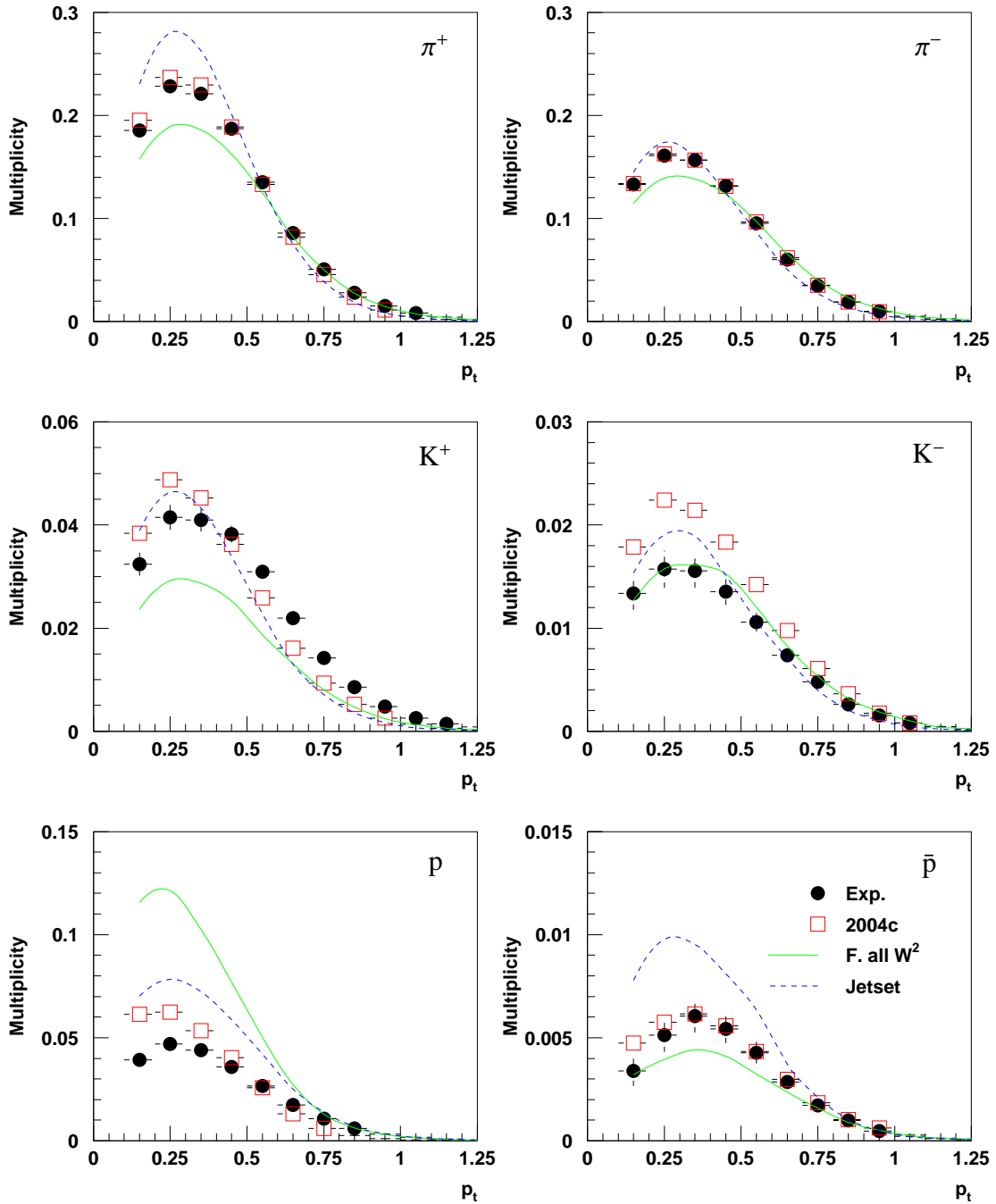
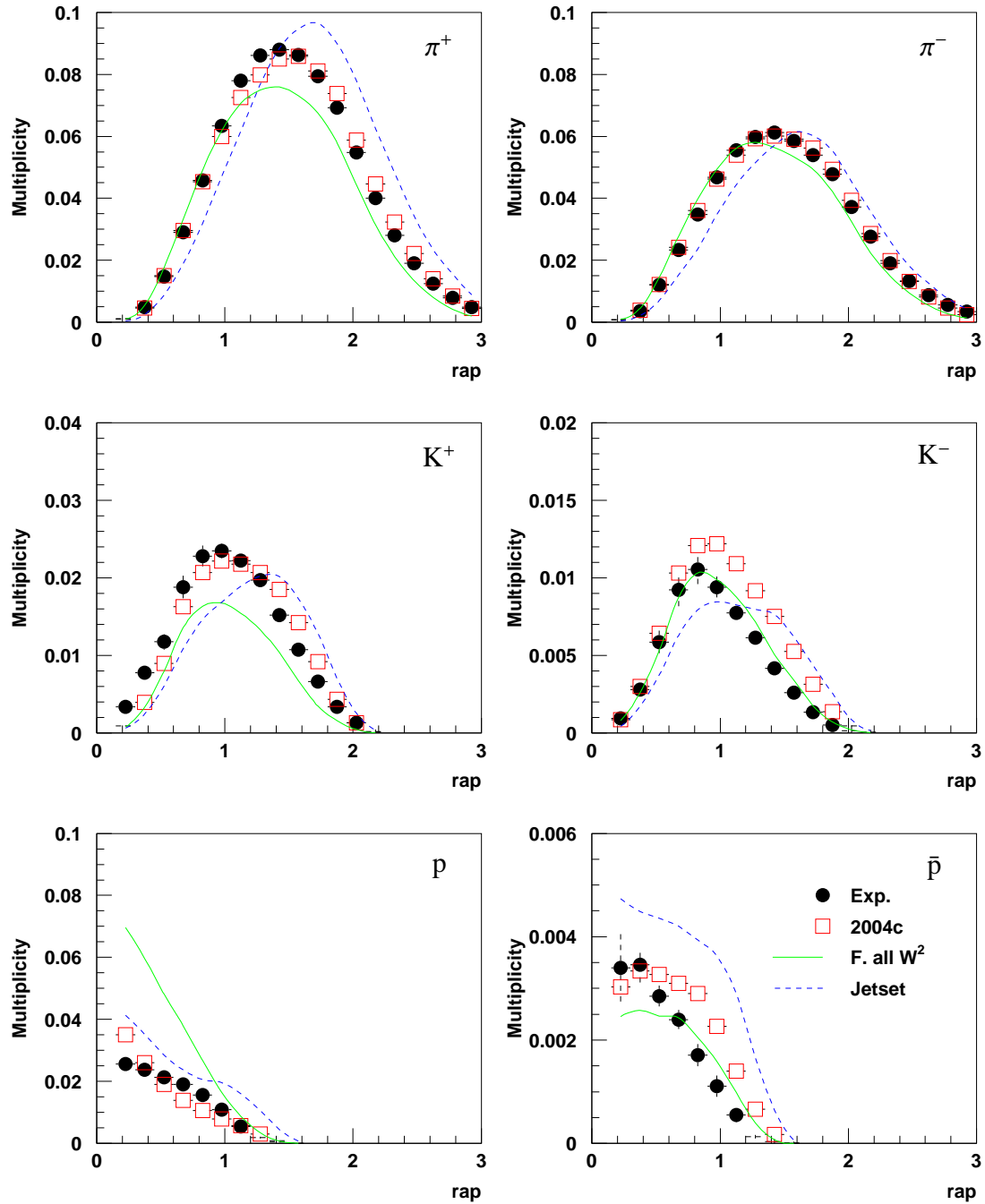


Figure 4.15

Same as Figure 4.14, but versus  $p_t$ .



**Figure 4.16**  
Same as Figure 4.14, but versus rapidity.

Parameter	JETSET	JETSET default	Holger Tune	Felix all $W^2$	Felix high $W^2$	2004c	2004c high $p_t$
$a$	PARJ 41	0.30	0.82	1.74	1.14	1.94	1.94
$b$	PARJ 42	0.58	0.24	0.23	0.35	0.54	0.54
$a_{qq}$	PARJ 45	0.50	0.50	0.50	0.50	1.05	1.05
$qq_{\text{supp}}$	PARJ 1	0.10	0.10	0.02	0.03	0.029	0.029
$q_{\text{supp}}^s$	PARJ 2	0.30	0.16	0.20	0.20	0.28	0.28
$q^s q_{\text{supp}}^s$	PARJ 3	0.40	0.40	0.4	0.4	0.4	0.4
$VM_{\text{supp}}$	PARJ 11	0.50	0.50	0.5	0.5	0.5	0.5
$VM_{\text{supp}}^s$	PARJ 12	0.60	0.60	0.6	0.6	0.6	0.6
$\sigma$	PARJ 21	0.36	0.34	0.37	0.34	0.3812	0.3812
$f$	PARJ 23	0.01	0.01	0.03	0.03	0.01	0.04
$p_T^f$	PARJ 24	2.00	2.00	2.50	2.50	2.00	2.50
$E_0$	PARJ 33	0.80	0.80	0.80	0.80	0.8	0.8
$k_T$	PARL 3	0.44	0.44	0.78	0.85	0.44	0.44
$\chi^2$		226	235	163	129	43	40

**Table 4.1**

Comparison of different Lund parameter sets. The  $\chi^2$  was calculated using the charge separated  $z$ ,  $p_t$  and rapidity distributions of pions, kaons and protons. For all tunes, 6 million DIS events were generated.

### 4.4.3 Conclusion

The current best tune presents an improvement with respect to the previous available parameter sets. Nevertheless, there are areas where additional studies are desirable in order to achieve improvements. Especially, it would be worthwhile to improve both the  $K^+$  and  $K^-$  agreement with the experimental data, without refinement for one charge impairing on the other.

New parameter fits should also take advantage of updated experimental multiplicities. Since the last fits were performed, new RICH unfolding matrices were released, also the method to assign the corresponding systematic errors changed. Both innovations affect the reference data.

While the iterative tuning focused on the reproduction of the multiplicities of pions, kaons and protons, also other properties might be of interest. Studies are underway to improve the hyperon production features of the latest tunes by studying their dependence on the diquark suppression factor (PARJ 1), the strange diquark suppression factor (PARJ 3) and the  $a_{qq}$  parameter (PARJ 45) [Kra05b]. The recent work on the smearing generator with respect to the photon smearing will eventually allow to include  $\pi^0$  multiplicities as tuned properties.

Further tuning efforts will most likely lead to further improvements in the data-Monte Carlo agreement. But, considering the wealth of features and distributions which — depending on the aspects of physics one is interested in — can be required for a *good* tune, it seems highly unlikely to ever achieve a near-perfect agreement. The fragment-

ation parametrisations have already come quite far due to the work done by the various parties.

# Chapter 5

## Extraction of Born Multiplicities

The analysis is based on the unpolarised data set on a proton target and the data set on the deuteron target obtained in the year 2000. It provides high statistics and — due to the RICH detector — the particle identification capabilities necessary to extract the desired charge and hadron type separated multiplicities.

Several steps are required to obtain the final Born multiplicities in  $4\pi$ . Fig. 5.1 provides an overview. The initial experimental multiplicities have to be corrected for inefficiencies in the performance of the RICH detector, the charge symmetric background due to pair production and hadrons from diffractive processes. As a last step, the multiplicities are corrected for the HERMES acceptance and tracking efficiencies, as well as radiative smearing effects.

Table 5.1 summaries the statistics on which this analysis is based on. Note that the given numbers refer to the 'raw' hadron numbers, which do not take into account the misidentifications by the RICH corrected for by the RICH unfolding.

In the following sections, the individual steps are addressed one by one.

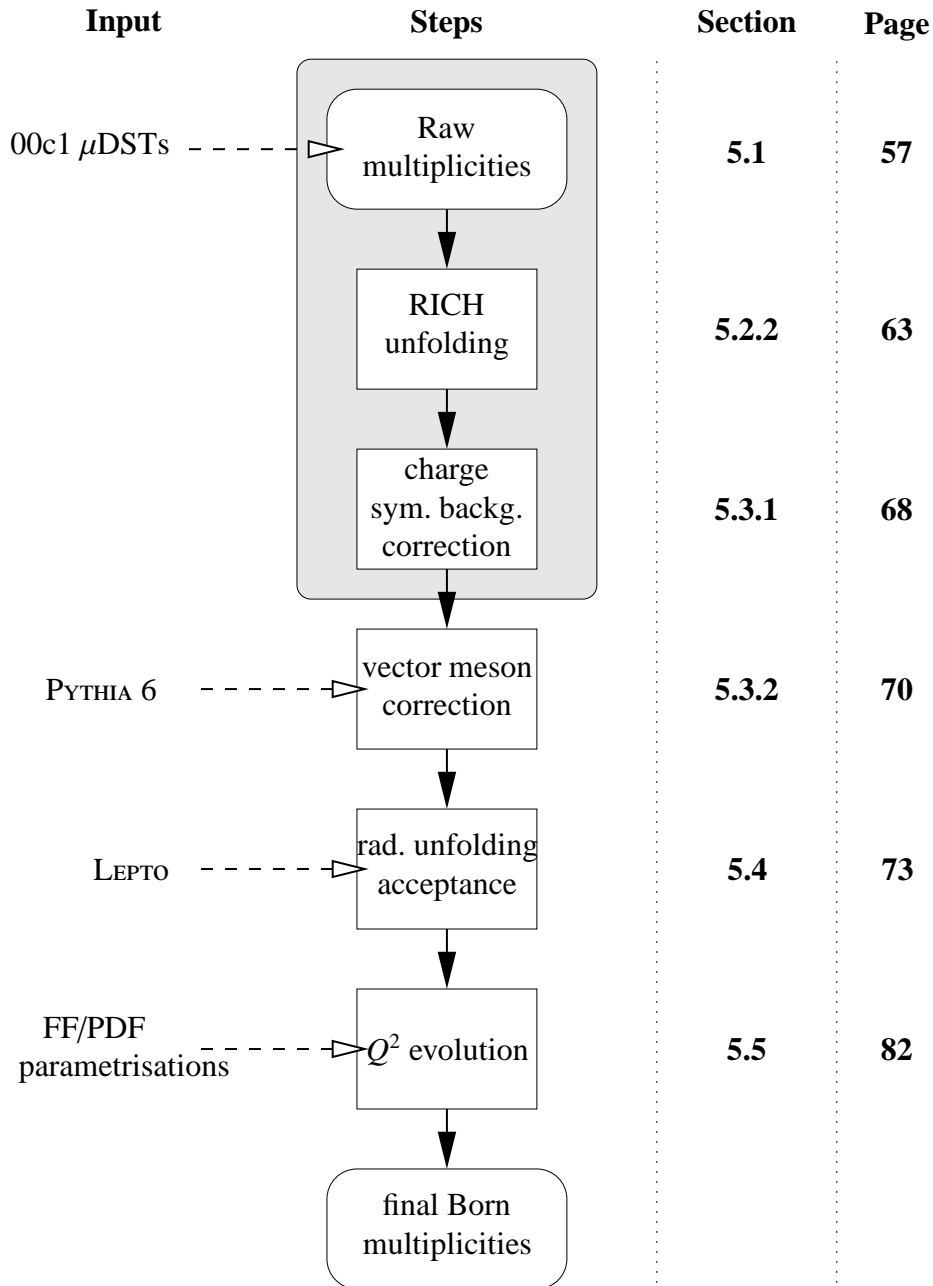
### 5.1 Data Selection

To ensure good quality of the analysed data, numerous cuts and requirements are necessary. As a first step, a run list is compiled which selects the data taking periods with the desired target gas type and operation modes. The available run information also allows a

Target	DIS	Hadrons					
		$\pi^+$	$\pi^-$	$K^+$	$K^-$	p	$\bar{p}$
Proton	5875796	961368	689024	203620	87936	156411	32191
Deuteron	6496826	1078644	875506	227764	110225	175355	40041

**Table 5.1**

Statistics obtained from the deuteron and proton data sets. The hadron numbers refer to the 'raw' data, meaning that they do not account for RICH misidentifications.

**Figure 5.1**

Schematic overview of the analysis steps, starting from the raw multiplicities up to the final Born multiplicities in  $4\pi$ . The grey box indicates the steps which are performed simultaneously when running over the HERMES data. The subsequent corrections are applied successively using correction factors obtained from other sources like Monte Carlo simulations (rad. unfolding, vector meson correction) and parametrisations ( $Q^2$  evolution). For a better orientation, the respective sections and page numbers in this thesis are referenced on the right.

first selection on the data quality, since data runs with unstable or unclear experimental conditions can be excluded. A total of 1549 runs with data on the unpolarised proton target and 25973 runs with data on the deuteron target were selected. From the deuteron data, only a small fraction of 261 runs was taken in the unpolarised target mode. The remaining runs come from the polarised data taking, which represents the by far largest fraction of the year 2000 data. These runs were analysed by an analysis code which applied further cuts to the data. These can be divided into three groups, as to the level in the data structure they are applied to<sup>1</sup>:

- *Burst level cuts* ensure an overall good performance of HERA, the target and the spectrometer
- *Event level cuts* select (as much as possible) DIS events from the data and avoid e.g. resonance regions. The inevitable dilution of the data set with undesired physical processes (like Bhabha scattering or diffractive processes) has to be accounted for in further analysis steps.
- *Track level cuts* require that the individual particle tracks originate in the target chamber and traverse the spectrometer within the geometrical acceptance, avoiding problematic regions at the edge of the detector acceptance. Further kinematic cuts ensure a reliable PID response of the detectors.

### 5.1.1 Burst Selection Cuts

As already mentioned above, these cuts aim to guarantee that all important detector and target components were operational and working. There are different sources of information on which these decisions are based. Many parameters, such as target operation mode, beam conditions, burst length etc. are recorded by the slow control part of the data acquisition. Furthermore, the data quality group and the detector experts gather information from logbook entries, data quality analyses and other sources to identify periods with non-working or unreliable equipment. This knowledge is encoded in status bit patterns which can be checked by the analyser in his/her program.

The following list summarises the checks which were done for this analysis. The cuts are specified quantitatively in Table 5.2.

- ① Dead time correction factors for trigger 21 and all triggers between 0.5 and 1.0
- ② Require a reasonable burst length
- ③ Require a reasonable beam current
- ④ Check `iuDSTbad` bit pattern (this pattern e.g. marks the last burst of a fill, synchronisation problems etc.) and `iuDSTbad2` bit pattern (→ discard bursts with no PID values)

---

<sup>1</sup>For an overview over the HERMES data structure see section 3.4.1.

①	0.5	<	$\frac{g1DAQ.rDeadCorr}{g1DAQ.rDeadCorr21}$	$\leq$	1.
②	0.	<	$g1DAQ.rLength$	$\leq$	1.
③	5.	$\leq$	$g1Beam.rMdmCurr$	$\leq$	50.
④			$!(g1Quality.iuDSTbad)$	$\&$	$0x1e081ff9$
			$!(g1Quality.iuDSTbad2)$	$\&$	$0xc$
⑤			$!(g1Quality.bCaloDead)$	$\&$	$0x81ff01ff$
			$!(g1Quality.bH2LumiDead)$	$\&$	$0xaf2f001f$
⑥			$g1Quality.iTrdDQ$	$=$	3
⑦			$g1Quality.iExpment$	$=$	1

**Table 5.2**

Burst level selection cuts

- ⑤ Check for dead blocks in calorimeter, H2 and the luminosity monitor
- ⑥ Check that the TRD was OK
- ⑦ Check that the run is marked as 'analysable'

### 5.1.2 Cuts on Track and Event Level

The cuts on track and event level are summarised in Table 5.3. The cuts on the lepton vertex ensure that the electrons or positrons originate in the target cell. For hadrons, these cuts are relaxed to allow for the possibility that these hadrons were not produced in the primary interaction in the target cell, but subsequently by decay of one of the primary hadrons. Furthermore, tracks hitting the outer edges of the calorimeter wall are excluded to guarantee that the electromagnetic shower is mostly contained within the calorimeter glass blocks.

The allowed momentum range for hadrons is limited by the particle identification capabilities of the RICH detector. For pions, it would be possible to lower the momentum cut to 1 GeV. Nevertheless, it was chosen to use a uniform lower momentum cut for hadrons in order to avoid potential systematic problems in the unfolding (see section 5.2.2 on page 63). Leptons<sup>2</sup> are required to deposit an energy of at least 3.5 GeV in

<sup>2</sup>Throughout this chapter, *leptons* refers to electrons and positrons.



<b>track level cuts</b>	
Selected trigger	21
Tracking method	NOVC
Vertex $z$ cut for hadrons	$-18.00 < z_v^h < 100.0$ cm
Vertex $d$ cut for hadrons	none
Vertex $z$ cut for leptons	$-18.00 < z_{vx}^l < 18.00$ cm
Vertex $d$ cut for leptons	$0.0 < d_{vx}^l < 0.75$ cm
Calorimeter $x$ position	$-175.0 < x_{\text{Calo}} < 175.0$ cm
Calorimeter $y$ position	$30.0 <  y_{\text{Calo}}  < 108.0$ cm
$E_{\text{Calo}}$ for leptons	$3.50 < E_{\text{Calo}}$
<b>event level cuts</b>	
Total rec. momentum in event	$E_{\text{tot}} < 28.0$ GeV
<b>DIS cuts</b>	
$Q^2$ cut	$Q^2 > 1.0$ GeV <sup>2</sup>
$W^2$ cut	$W^2 > 10.0$ GeV <sup>2</sup>
$y$ cut	$0.1 < y < 0.85$
<b>hadron momentum cuts</b>	
pions, kaons, protons	$2.0 < p < 15.0$ GeV

**Table 5.3**

Kinematic cuts on event kinematics and single track properties

the calorimeter. The total energy of the tracks is restricted to less than 28 GeV. This is a sanity check excluding events with unphysical high (= higher than the beam energy) total energy. Requiring  $Q^2 > 1$  GeV<sup>2</sup> and  $W^2 > 10$  GeV<sup>2</sup> selects the energy scale of deep inelastic scattering and furthermore excludes the resonance region of the photon-nucleon system. The fractional lepton energy transfer is limited to  $0.1 < y < 0.85$  to constrain the influence of radiative effects and the associated uncertainties on the event kinematics.

## 5.2 Particle Identification and RICH Unfolding

Particle identification (PID) is a crucial part of any analysis, especially if — like in this case — a clean separation of different hadron types is required. The HERMES experiment includes four detector components which provide the necessary information for this task: the calorimeter, the pre-shower, the transition radiation detector and the RICH (Ring Imaging Čerenkov detector). The latter replaced the threshold Čerenkov detector in 1998. Based on the fact that different particle types produce different responses in these detectors, the combination of these signals allows for a highly efficient discrimination of leptons and hadrons. In a second step, the tracks identified as hadrons are further

classified as pions, kaons and protons, depending on the measured Čerenkov opening angles in the RICH detector.

### 5.2.1 Discriminating Leptons and Hadrons

In practice, the individual detector responses are converted to conditional probabilities  $P_D(H_{l(h)}|E, p, \theta)$ , yielding the hypothesis that a given particle is a lepton ( $l$ ) or hadron ( $h$ ), based on the track's momentum  $p$ , its polar angle  $\theta$  and the energy deposition  $E$  in the detector  $D$ . These probabilities can be written as a convolution of the probability that a particle with certain momentum and polar angle is a lepton (hadron) — the particle fluxes  $P(H_{l(h)}|p, \theta)$  — and the probability that such a lepton (hadron) with momentum  $p$  deposits the energy  $E$  in the detector — the parent distribution  $P_D(E|H_{l(h)}, p)$ :

$$P_D(H_{l(h)}|E, p, \theta) = \frac{P(H_{l(h)}|p, \theta) \cdot P_D(E|H_{l(h)}, p)}{\sum_{i=l,h} P(H_i|p, \theta) \cdot P_D(E|H_i, p)}. \quad (5.1)$$

The logarithmic ratio of these quantities for leptons and hadrons yields

$$\text{PID} \equiv \log_{10} \frac{P(H_l|E, p, \theta)}{P(H_h|E, p, \theta)} = \text{PID}_D - \log_{10} \Phi, \quad (5.2)$$

where  $\text{PID}_D$  is the (detector dependent) ratio of the parent distributions and  $\Phi$  the (momentum and  $\theta$  depended) flux ratio

$$\Phi \equiv \frac{\phi_h}{\phi_l} = \frac{P(H_h|p, \theta)}{P(H_l|p, \theta)}. \quad (5.3)$$

To combine the information from different detectors, one can add their respective  $\text{PID}_D$  values. For this analysis, the following combinations were used:

$$\text{PID}_2 \equiv \text{PID}_{\text{Cal}} + \text{PID}_{\text{Pre}} \quad (5.4)$$

$$\text{PID}_5 \equiv \text{PID}_{\text{TRD}}. \quad (5.5)$$

Including the flux factor  $\Phi$ , the lepton-hadron separation was based on the following conditions:

$$\text{PID}_2 + \text{PID}_5 - \log_{10} \Phi > 0 \iff \text{lepton}, \quad (5.6)$$

$$\text{PID}_2 + \text{PID}_5 - \log_{10} \Phi < 0 \iff \text{hadron}. \quad (5.7)$$

The parent distributions for the individual detectors were determined directly from the data taken in the respective data taking period. Stringent cuts on the responses of the other PID detectors provide a clean data sample to evaluate these functions. The flux factors are estimated in an iterative approach, since their calculation requires the PID values, which in turn depend on the factors. A more detailed description of the HERMES PID framework and the determination of the necessary functions can be found in [Wen99].

### 5.2.2 Identification of Hadrons with the RICH

Once a track is established to be a hadron, it is further classified using information provided by the RICH detector (see section 3.3.2). Every track has assigned a field specifying the identified hadron type and a quality parameter, defined as

$$\text{smRICH.rQp} = \log_{10} \frac{\mathcal{P}(\text{most likely hadron type})}{\mathcal{P}(\text{2nd most likely hadron type})}. \quad (5.8)$$

To ensure a good performance of the detector and the PID algorithms, this parameter is required to be larger than zero<sup>3</sup>. But even then, there is still a certain level of misidentification due to the limitations in the detector accuracy. These misidentifications have to be corrected using a parametrisation of the detector accuracy.

#### Unfolding the Hadron Multiplicities

The performance of the RICH detector is parametrised in the  $\mathcal{P}$ -matrices. These matrices relate the vector of identified hadrons ( $\vec{I}$ ) with the vector of true hadron types ( $\vec{N}$ )

$$\begin{pmatrix} N_\pi \\ N_K \\ N_P \end{pmatrix} = \begin{pmatrix} \mathcal{P}_\pi^\pi & \mathcal{P}_\pi^K & \mathcal{P}_\pi^P & \mathcal{P}_\pi^X \\ \mathcal{P}_K^\pi & \mathcal{P}_K^K & \mathcal{P}_K^P & \mathcal{P}_K^X \\ \mathcal{P}_P^\pi & \mathcal{P}_P^K & \mathcal{P}_P^P & \mathcal{P}_P^X \end{pmatrix} \cdot \begin{pmatrix} I_\pi \\ I_K \\ I_P \\ I_X \end{pmatrix} \quad (5.9)$$

where  $X$  stands for the unidentified hadrons. The elements  $\mathcal{P}_i^t$  of the matrices thus denote the probability that a hadron of true type  $t$  is identified as a particle of type  $i$ . Elimination of the entries for unidentified hadrons from  $\mathcal{P}$  and  $\vec{I}$  and inversion of the resulting  $3 \times 3$  matrix yields the equation

$$\vec{N} = \mathcal{P}_{\text{trunc}}^{-1} \cdot \vec{I} \quad (5.10)$$

which can be used to obtain the vector of true hadrons from the observed hadron fluxes.

Obviously, this method requires a good knowledge of the detector efficiency. Ideally, this knowledge is gained using an undiluted hadron sample either from a test beam or by using PID information from (an)other detector(s). However, since both approaches were not feasible, alternative methods had to be found.

One option is to tune the RICH Monte Carlo simulation to reproduce the signals produced by *electrons and positrons*, which can be clearly identified using the other detectors. The RICH operation parameters which were considered are for example the  $\gamma$  yields and the distribution of the Čerenkov angles. The most important tune variables were the transparency of the gas and aerogel (influencing the  $\gamma$  yields) and the so called 'mirror roughness', which influences the Čerenkov angle resolution. One result of this effort was the version 2a  $\mathcal{P}$  matrix set, which was the basis of this analysis up to the status presented in the summer 2004 release [Hil04b].

<sup>3</sup>This ensures that there is indeed a most likely particle type. A quality parameter of zero signifies that the two most likely particle types have the same probability to be correct, meaning that no decision is possible.

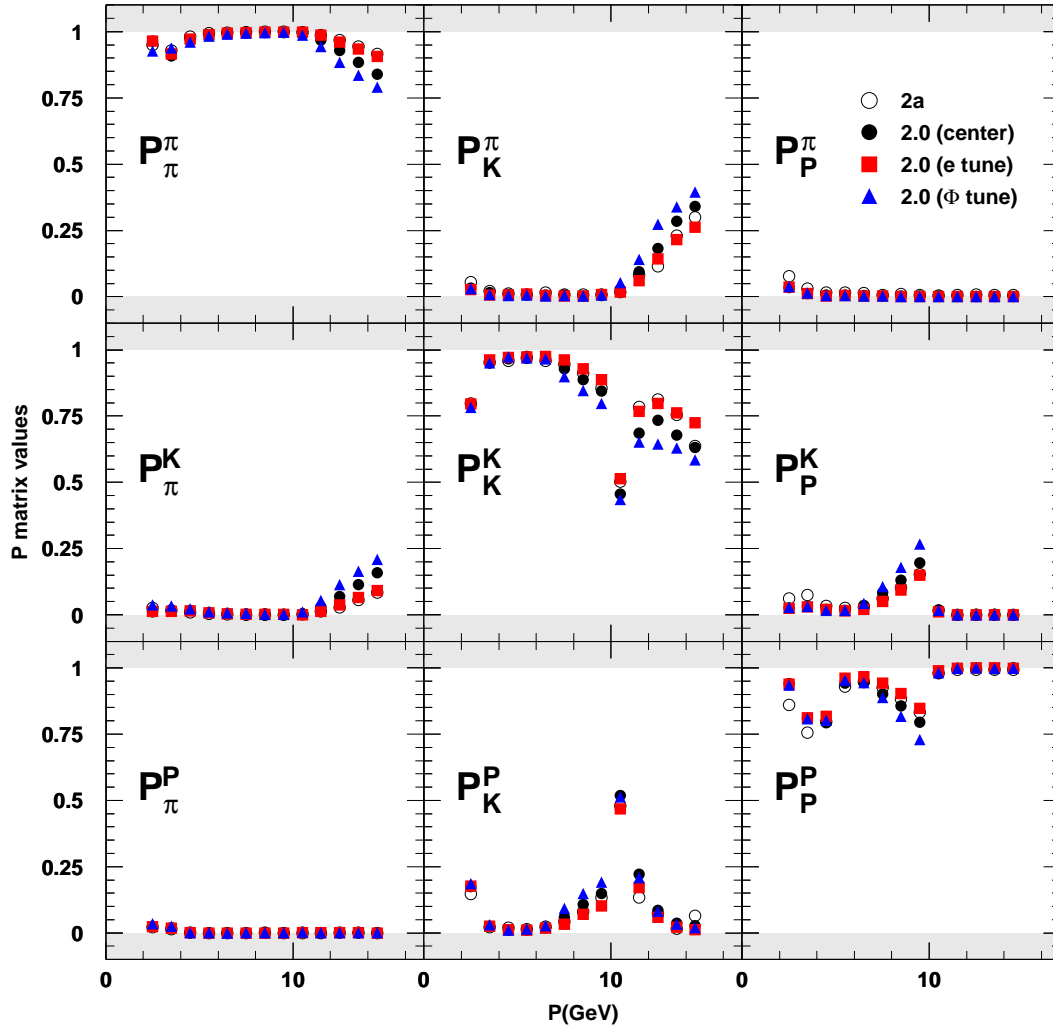


**Figure 5.2**

The  $\mathcal{P}$ -matrices versus momentum for 1 track per detector half. The columns represent the 3 true particle types (left to right: pion, kaon, proton), the rows denote the identified particle types. The off-diagonal fields thus show the probabilities for misidentification. The four data sets represent the version 2a matrix (used for the release in summer 2004 [Hil04b]) and the three new matrix sets [Miy04] used for the results presented in this thesis.

A possible way to obtain clean *hadron samples* from the experiment is the use of decaying particle data. In that case, hadrons can be identified to be decay products of processes such as

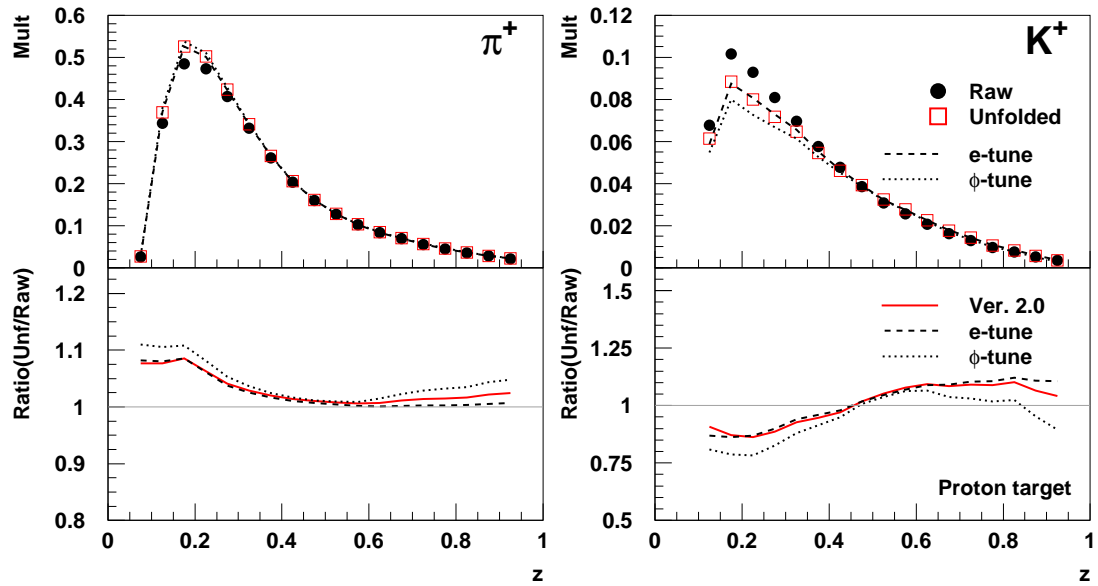
$$\begin{aligned} \phi &\rightarrow 2\text{K}, \\ \text{K}_S &\rightarrow 2\pi, \\ \rho^0 &\rightarrow 2\pi \\ \text{and } \Lambda &\rightarrow p + \pi^-. \end{aligned} \tag{5.11}$$

However, such data samples are limited to certain kinematic regimes and event topologies. For instance, decay particle data usually contains two hadron tracks per detector half, a feature that strongly affects the RICH performance. Even so, the data allowed to test the validity of the tune in the accessible topologies and kinematics. It was discovered that the observed discrepancies between the decay Monte Carlo simulation and the experimental decay data was mostly sensitive to the mirror roughness parameter. Varying this parameter led to another tune of the RICH MC, which allows to estimate the systematic error introduced by the RICH unfolding (see next section).

The RICH performance for a given track depends on several factors. It was chosen to bin the  $\mathcal{P}$ -matrices in terms of the track momentum and the event topology, meaning the number of tracks per detector half. Figure 5.2 shows the  $\mathcal{P}$ -matrices in their momentum binning for the case of 1 track/detector half. The open circles denote the version 2a matrix which was used for the release in June 2004 [Hil04b]. The solid symbols represent the three sets that constitute the version 2.0 matrices used in the current analysis. The *e*-tune matrices correspond to the old version 2a matrices. Since the new matrices were extracted using an independent tune to a different Monte Carlo production, slight deviations from the 2a values can be observed. Tuning the RICH Monte Carlo to agree with clean hadron samples obtained from  $\phi$  decays results in the data set denoted as  $\phi$ -tune. The actual multiplicity values are obtained using the *center* set.

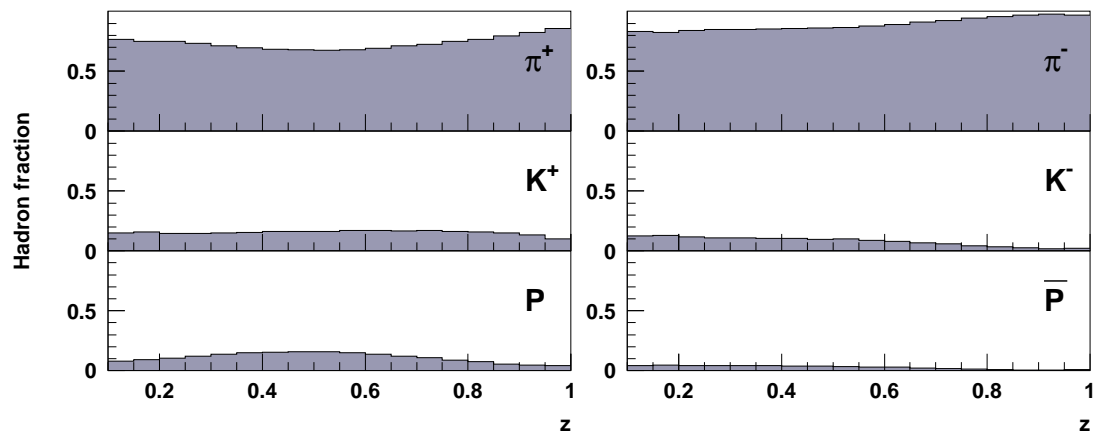
As can clearly be seen, the RICH allows for a very good pion identification across the major part of the design range between 2 and 15 GeV. At very high momenta ( $\geq 12$  GeV), there is a growing likelihood for misidentifications between pions and kaons. In this region the Čerenkov angles of pion and kaon tracks become very similar (see Figure 5.2). Kaons and protons show a strong momentum dependence of the identification efficiencies. In particular the kaon momentum threshold of the gas radiator around 10 GeV has a major influence on kaon and proton related matrix elements.

Figure 5.3 shows the influence of the RICH unfolding on the hadron multiplicities in the cases of  $\pi^+$  and  $\text{K}^+$ . The actual multiplicities are shown in the top part. The solid circles represent the "raw" multiplicities, relying completely on the most likely hadron type as given by the RICH detector. The open squares were obtained by unfolding using the centre values of the version 2.0  $\mathcal{P}$  matrices. The dashed and dotted lines show the result obtained with the *e*-tune and the  $\phi$ -tune, respectively. The relative change is shown as a ratio below. While the pion multiplicity is increased by the correction, the  $\text{K}^+$  multiplicity drops by 20-30% for  $0.1 < z < 0.3$ . The different impact can be understood when considering the sizeable difference in the relative particle fluxes (see Fig. 5.4). Despite the generally better RICH identification capabilities for pions, more pions are



**Figure 5.3**

Comparison of  $\pi^+$  (left) and  $K^+$  (right) multiplicities versus  $z$ , with and without unfolding.



**Figure 5.4**

Relative hadron fluxes vs.  $z$ . Pions are dominating over the entire  $z$  range. For negative hadrons, the pion fractions reach  $\sim 97\%$  at high  $z$ .

misidentified as kaons then vice versa, and this is reflected by the unfolding.

For negative hadrons, the effect is similar. However, the relative changes for the  $K^-$  multiplicities are considerably larger, since the fluxes are much more dominated by the pions (Fig. 5.4).

### Systematic Errors

**A Historical Overview.** Estimating the systematic uncertainties introduced by the RICH unfolding has been a long debated problem. In previous analyses, these uncertainties could be neglected [Wen03]. In this analysis, however, this was not really an option. This is due to the fact that, in contrary to e.g. the analysis mentioned above, the consideration of the RICH inefficiencies introduces a sizeable shift in the resulting distributions. This makes the method of taking the difference between unfolded and raw data as an upper limit of the systematic effects highly undesirable.

In the course of this analysis, several methods have been used to assign a systematic error from RICH unfolding to the multiplicities. These methods were

- an analytic method, as described in [Hom02],
- a matrix error Monte Carlo method, where a large number of random  $\mathcal{P}$  matrix sets was generated, taking the error on the matrix values as widths for the distribution of the individual matrix entries. The unfolding was then done using each of the matrix sets. This method produced a (mostly) Gaussian distribution for each multiplicity bin, whose width represented the uncertainty due to  $\mathcal{P}$  matrix errors.
- an alternative set of  $\mathcal{P}$  matrices. The differences between the multiplicities obtained from this set and the original multiplicities originating from the real set were identified with the systematic error.

The first two methods were presented in the March 2004 release report [Hil04a]. Since it was unclear at that point which method was more reliable, the values obtained from the first method were suggested for release. These values were generally larger and thus provided an upper limit.

The third method was used for the release of the multiplicities in June 2004 [Hil04b]. The new errors  $d\mathcal{P}$  specify the difference between the original  $\mathcal{P}$  matrix set (version 2a) and a new set  $\mathcal{P}_2 = \mathcal{P}_{v2a} + d\mathcal{P}$ , which represents the alternative tune of the RICH Monte Carlo to reproduce the decaying particle data. Both matrix sets were used to obtain unfolded multiplicities. The difference between these two multiplicity sets represented the systematic uncertainty:

$$\delta_{\text{sys}} = \frac{m_{\mathcal{P}_2} - m_{\mathcal{P}_{v2a}}}{\sqrt{3}}, \quad (5.12)$$

where the factor  $\sqrt{3}$  was introduced to obtain the standard deviation on the assumed uniform distribution between the two extremes. This systematic error was to be assigned asymmetrically in the direction of the change when going from  $\mathcal{P}_{v2a}$  to  $\mathcal{P}_2$ . This led to the unpleasant effect that the nominal best values lay strictly on the upper or lower edges

of the error band. Since this seemed to be unphysical, it was decided to release the plots with the errors assigned symmetrically.

**The Present Situation.** It is apparent that neither the asymmetric errors nor the 'artificial' symmetric errors represent a satisfying solution. For that reason it was decided to essentially use 3 sets of  $\mathcal{P}$  matrices [Miy04]:

- The *e-tune matrices* is the matrix obtained from the RICH MC, tuned to simulate a number of RICH operation parameters ( $\gamma$  yields and Čerenkov angles) for electrons
- The  *$\phi$ -matrices* was derived from the *e-tune* matrix by adjusting the mirror roughness parameter to reproduce decay Monte Carlo data.
- The *centre-matrices* results from setting the mirror roughness parameter half way between the values of the *e-tune* (MR = 0.9883333) and the  *$\phi$ -tune* (MR = 0.985)

Using the central matrix set results in the best value for the RICH unfolding, while the two other sets define the boundaries for the systematic uncertainty.

At present, however, this new approach does not generally solve the original problem, namely that the central value of the unfolded multiplicities sits on one end of the systematic error band. This is already apparent from Figure 5.3: looking at the ratios one can see, that for a few bins — notably at low  $z$  for both hadrons and  $z \sim 0.5$  for kaons — the results for the *e-tune* and the  *$\phi$ -tune* are both lower (or higher) than for the version 2.0 central values. The reason can be found in the fact that using the middle value for the mirror roughness does not automatically produce matrix elements in between the ones obtained from using the two extremes. In Figure 5.2 this can be seen in the first bin of  $\mathcal{P}_K^\pi$  and in 10-12 GeV region for  $\mathcal{P}_K^p$ .

As indicated by the name, the  *$\phi$  matrices* only use the information provided by the  $\phi \rightarrow 2K$  decay. It is planned [Miy04] to extend the data sample to also incorporate data from  $K_S$  and  $\Lambda$  decay. First results [Miy05] indicate that the inclusion of more decay channels leads to a lower value for the mirror roughness, reducing the overall systematic error. If the new matrices will allow to extract central multiplicity values in between upper and lower limits remains to be seen.

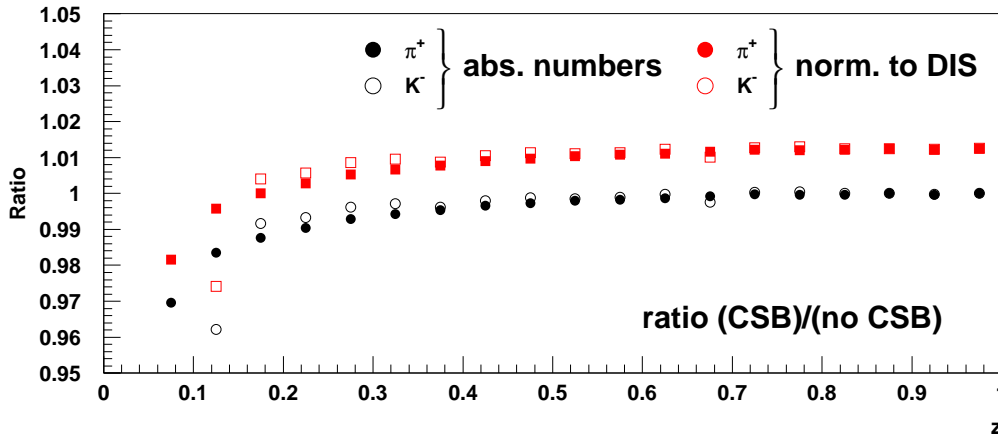
## 5.3 Background Corrections

The process of interest in this analysis is the deep inelastic scattering process. Some of the cuts discussed in section 5.1.2 have been introduced to exclude areas where the physics processes are dominated by resonance reactions. However, some more work is needed to further suppress the influence of undesired processes.

### 5.3.1 Charge Symmetric Background

One possible source of events is the charge symmetric background, e.g. from  $\gamma \rightarrow e^+e^-$  pair production in the detector material or the decay  $\pi^0 \rightarrow e^+e^-\gamma$ . These processes



**Figure 5.5**

Impact of the charge symmetric background correction on the hadron yields. Shown are the ratios between corrected and uncorrected yields for  $\pi^+$  (full symbols) and  $K^-$  (open symbols). The circles depict the ratio between pure hadron yields without normalisation, the squares show the ratio after normalisation to DIS. The total influence of the charge symmetric background correction is below 1% except for very low  $z$ .

lead to the possibility that a positron from the pair production is misidentified as the scattered beam particle<sup>4</sup>. To estimate the influence of these processes, no constraint was imposed on the charge when searching for the leading lepton. This leads to a number of pseudo-DIS events with a 'scattered lepton' charge opposite to the beam charge. Due to the symmetric nature of the original process it can be assumed that the number and kinematic properties of the events from pair production in the DIS sample (= the part of the data with correct charge) is the same. The number of DIS events was consequently reduced by the number of events found to have wrong charge. Also hadron yields were corrected by inverting the respective  $\mathcal{P}$  matrix weights.

The influence on the final hadron multiplicities as a function of  $z$  can be seen in Figure 5.5. As expected, the resulting correction is small. This is even amplified due to the fact that the two effects — reduction of the number of DIS events and reduction of the number of hadrons — partly cancels in the normalisation. The number of DIS events is reduced by  $\approx 1.5\%$ . The correction for the hadron yields is below 1%, except for very low  $z$ . In combination, the hadron yields are increased by 0.5 – 1.5% for  $z > 0.2$ .

Versus  $x_B$ , the influence is shown in Figure 5.6. The charge symmetric background contribution is highest for low  $x_B$ , where the total number of DIS events is reduced by  $\sim 6\%$  by the correction. The same is therefore true for the hadron count rates (full symbols). Due to the stronger decrease of the DIS yield, the normalised multiplicities in fact increase for low  $x_B$ , whereas the net effect is strongest for the highest  $z$  bin (5%).

<sup>4</sup>assuming, of course, an  $e^+$  beam for this argument

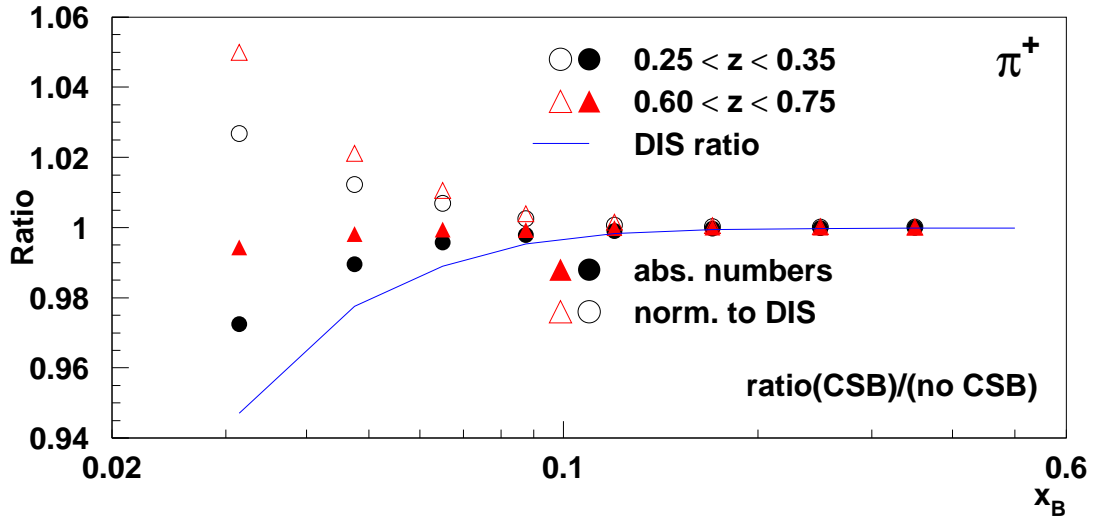


**Figure 5.6**

The influence of the charge symmetric background correction vs.  $x_B$ , shown for the highest (triangles) and lowest (circles)  $z$  bin. While the closed symbols show the ratio of the absolute hadron count rate, the open symbols give the multiplicity ratio. The line shows the ratio of the DIS yields in the respective  $x_B$  bin.

### 5.3.2 Elastic Vector Meson Production

The hadrons extracted from the experimental HERMES data can be produced by a number of processes. A group of processes that can — for certain hadron types and certain kinematic regions — contribute substantially to the observed hadron sample are the elastic diffractive, single and double diffractive processes. There are two vector mesons —  $\rho^0$  and  $\phi$  — whose elastic production is of special interest when looking at pion and kaon multiplicities:

$$ep \rightarrow ep\rho^0 \rightarrow ep2\pi \quad (5.13)$$

$$ep \rightarrow ep\phi \rightarrow ep2K \quad (5.14)$$

The contribution of diffractive events to the semi-inclusive data has been studied extensively using different Monte Carlo models [Lie03].

For this analysis, this contribution has been estimated using the PYTHIA 6 Monte Carlo program, which has been adapted for HERMES kinematics. This specifically includes modifications to the original PYTHIA code to better reproduce the exclusive  $\rho^0$  cross section [Lie04]. The 2004c tune was used to simulate the fragmentation part. Detector effects have been accounted for by using the HERMES Smearing Generator. PYTHIA provides a process ID to specify the type of the event. Events with the IDs 91 (elastic scattering), 92, 93 (single diffractive with one or the other partner breaking up) and 94 (double diffractive) were included in the diffractive sample.

Figure 5.7 shows the fraction of hadrons coming from vector meson decay as a function of  $z$ . The (black) circles give the fractions for a proton target. The triangles show

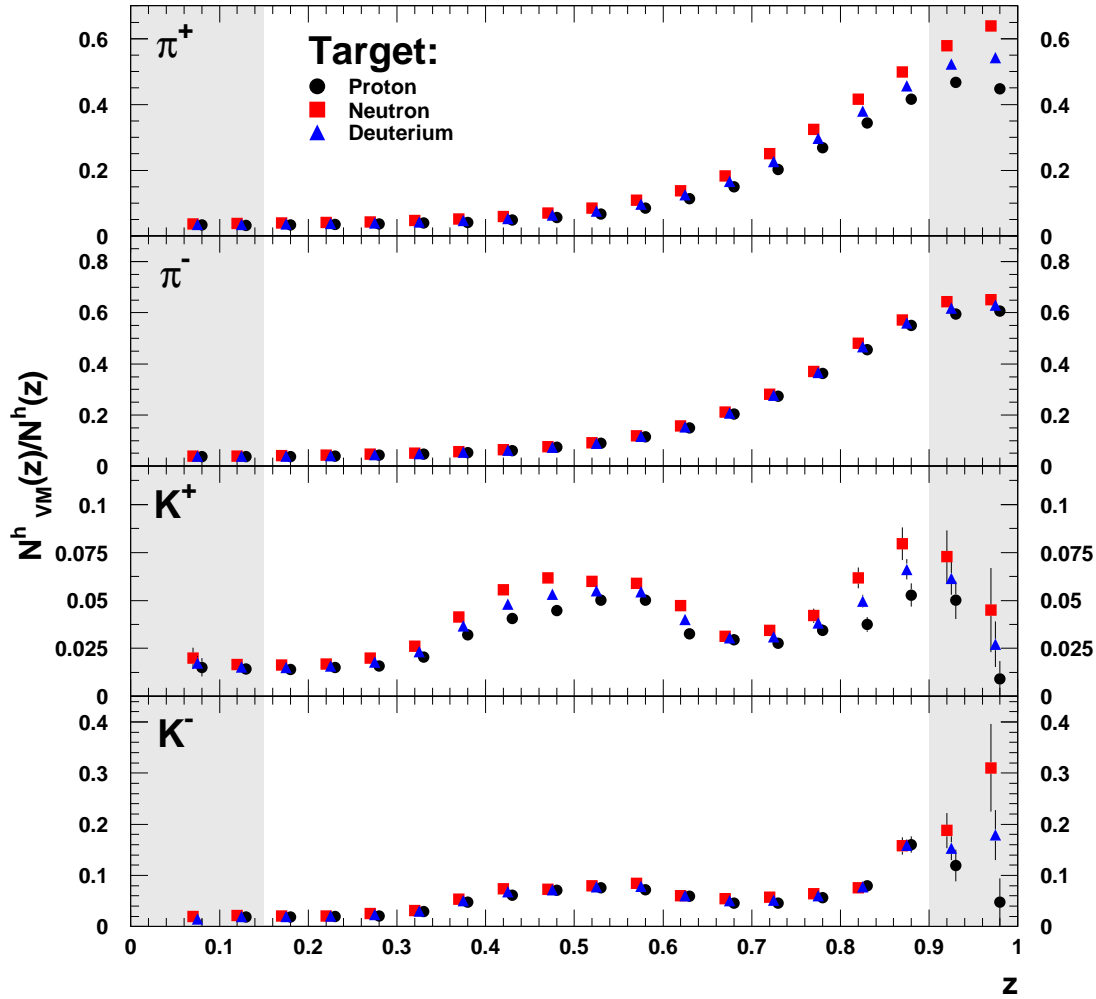


**Figure 5.7**

Exclusive vector meson fractions vs.  $z$  obtained from two PYTHIA Monte Carlo simulations using proton and neutron targets, respectively. The deuteron target fractions were derived by averaging over those two data sets. The white area within the shaded boxes denotes the kinematic domain considered for the final  $4\pi$  result.

the result for the deuterium target. Since PYTHIA does not allow to simulate compound target objects like the deuteron, the deuteron data set had to be deduced from combining the proton fractions with the results for a neutron target, shown as squares.

As can be seen, the correction is largest for pions in the high  $z$  range. This effect can be attributed to the non-flat decay angle distribution of the decay  $\rho \rightarrow \pi^+\pi^-$ . In their rest system, most  $\rho$ s decay with one pion going in the forward direction of the  $\rho$  ( $\cos(\theta) \rightarrow +1$ ), while the other pion then has to go in the backward direction ( $\cos(\theta) \rightarrow -1$ ). This angular distribution is caused by the spin density matrix elements which govern the decay

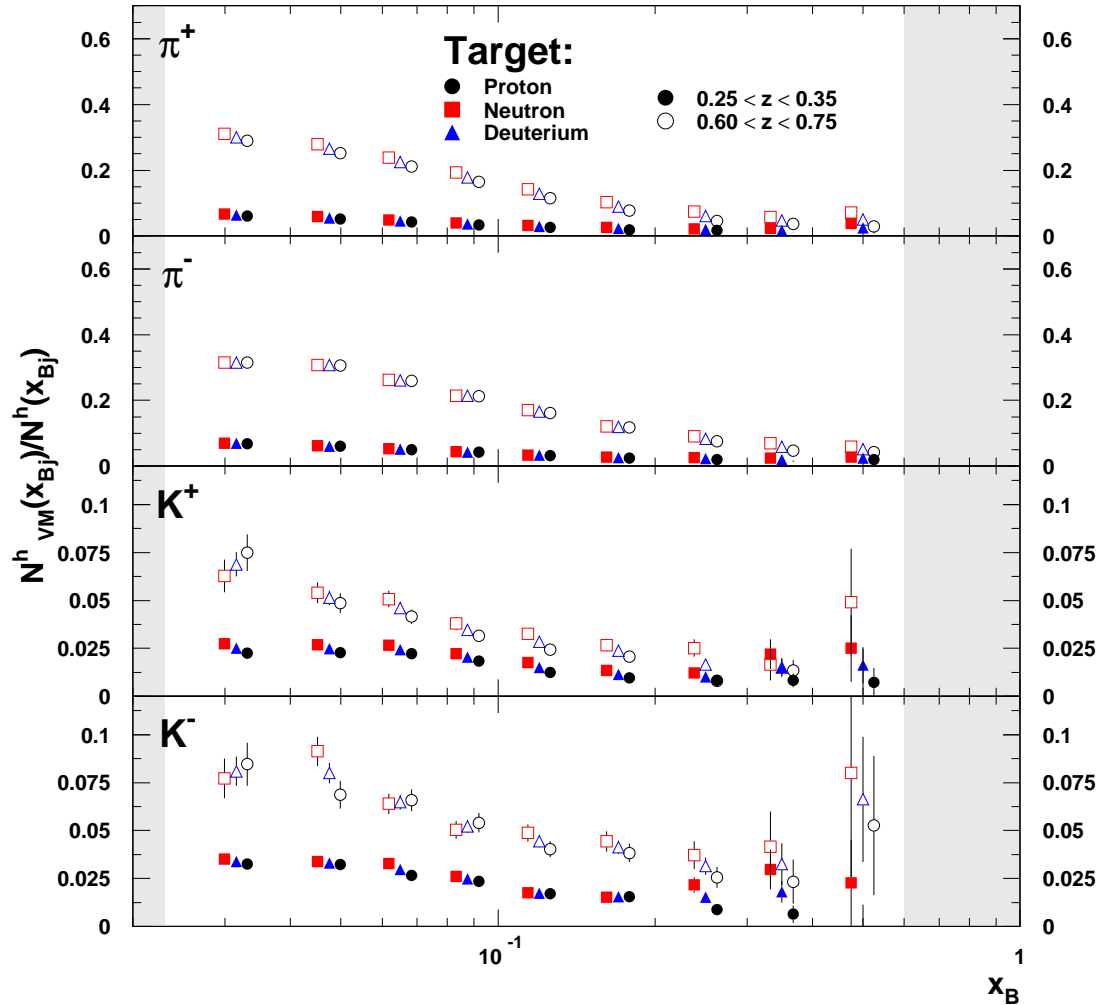


**Figure 5.8**

Similar to figure 5.7 but vs.  $x_B$  in two different  $z$  bins. Shown are the lowest and highest  $z$  region of the 4 bins used in this analysis.

of spin-1 particles [Tyt01].

Boosting into the laboratory frame, this means that the forward pion takes most of the energy of the  $\rho$ . Since  $E_\rho \approx \nu$  in exclusive production,  $z \rightarrow 1$  for the forward pions, while the backward pions have low values of  $z$ . The semi-inclusive pion multiplicity drops almost exponentially with  $z$ , so that the forward pions from exclusive  $\rho$  decay constitute a significant part of the total sample, while the backward pions are only a minor correction.

For a *proton target*, the  $\pi^-$  fractions are consistently higher than the fractions for  $\pi^+$ . This is due to the higher DIS cross section for producing  $\pi^+$ , based on the favoured fragmentation function  $D_u^{\pi^+}$  and the dominance of the  $u$  quarks over the  $d$  quark. The

pion yield from diffractive processes is the same for both charges, resulting in the higher vector meson influence on the negative pions.

The *neutron target* features a higher yield of diffractive hadrons ( $\sim 10\%$ ). At the same time, the  $\pi^+$  yield is lower and the  $\pi^-$  is higher, both with respect to the proton data. While the combined effect leads to higher VM fractions for  $\pi^+$ , the effects almost cancel for negative pions, making the fractions similar for both targets.

Similar effects concerning the charge and target dependence of the fractions can be observed for kaons. However, the decay  $\phi \rightarrow K^+ + K^-$  is much flatter in terms of decay angle distribution. The observed fractions are peaked around  $z \sim 0.5$ . For large  $z$ , there is again a moderate increase due to the strong decline of the DIS statistics.

Figure 5.8 shows the situation versus  $x_B$ . Unsurprisingly, the fractions are largest for the highest  $z$  bin, shown as open symbols. The fractions rise towards lower  $x_B$ , which corresponds to lower  $Q^2$ . This is due to the  $Q^{-6}$  dependence of the diffractive cross section.

**Error Calculation.** Although the diffractive fraction extracted from the PYTHIA simulation results in a correction factor to the experimental data, it is important to be aware that the physical meaning of the correction is the subtraction of a background. This is significant for the way the errors are propagated in this correction step.

Considering the uncorrected multiplicity  $N$  and the correction factor  $C$ , the new multiplicity is given by

$$N' = N(1 - C) = N - B \quad (5.15)$$

where  $B = N \cdot C$  is the background. Treating the background as statistically independent, this yields

$$\sigma_{N'} = \sqrt{\sigma_N^2 + \sigma_B^2} \quad (5.16)$$

$$= \sqrt{N^2\sigma_C^2 + (1 + C^2)\sigma_N^2}. \quad (5.17)$$

So even the smallest correction factor  $C$  results in the inflation of the original error. This is in contrast to the result  $\sigma_{N'} = \sqrt{\sigma_N^2(1 - C)^2 + N^2\sigma_C^2}$ , which is obtained from the middle part of Equation (5.15) when considering the multiplicity  $N$  and an independent correction factor  $C$ . Here the correction could actually decrease the error.

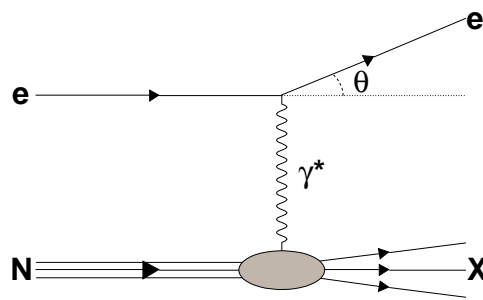
## 5.4 Correction for Radiative & Detector Smearing

### 5.4.1 Motivation

Figure 5.9 depicts the DIS process in first order QCD, which is the process of interest in this analysis. The electron reacts with the nucleon by exchange of a virtual photon. The properties of the scattered electron (namely the energy  $E'$  and the scattering angle  $\theta$ ) are measured in the detector. Taking into account the known initial energy  $E$ , the kinematics of the virtual photon — and thus the kinematics of the entire scattering process

**Figure 5.9**

DIS process in first order QED (Born level). The scattering kinematics are well defined by the properties of the incoming and outgoing electron.



— are well defined by this measurement. In the real world, however, things get more complicated.

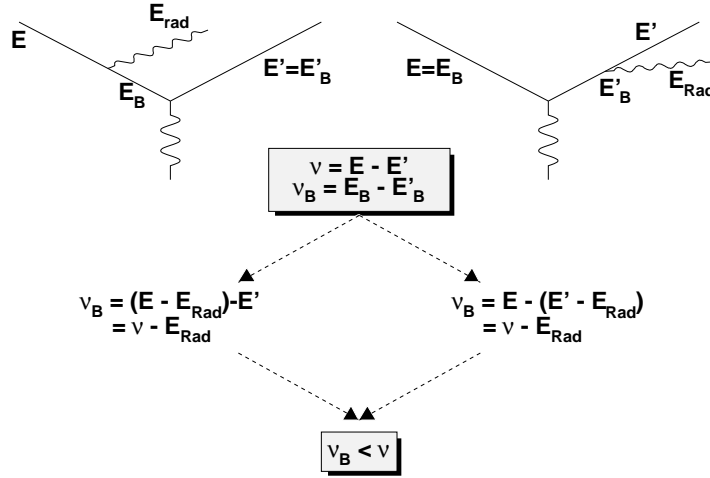
**QED Radiative Effects.** Additionally to the first order — so called Born level — process, there are infinite possibilities for higher order processes, which are suppressed by at least  $O(\alpha)$ . Possible higher order processes are shown in Figure 5.11. While vertex corrections (Fig. 5.11c) and vacuum polarisations (Fig. 5.11d) affect the overall normalisation of the DIS cross section, initial (Fig. 5.11a) and final (Fig. 5.11b) state radiation also hide the true event kinematics from the observer. As can be seen by Figure 5.10, they introduce a systematic bias of the observed kinematics with respect to the true Born level kinematics.

**Detector Effects.** Another layer of uncertainty is introduced by the measuring process itself. While traversing the target and the detector, the final state particles are subject to interactions with material. Scattering processes influence the energy and direction of the tracks. The tracking algorithm assumes the particle tracks to be straight lines in the sections before and after the spectrometer magnet. Their real behaviour causes e.g. deviations between the measured and the true scattering angle. Furthermore, the determination of the particle momenta is affected, since this is done by an algorithm matching the partial tracks in the front and the back half of the detector.

Furthermore, the HERMES spectrometer allows only for the detection of particles leaving the target area in a certain solid angle  $\Delta\Omega$ . To be able to compare the results with other experiments, this spectrometer dependent restrictions have to be accounted for.

All of the effects mentioned above can be simulated using Monte Carlo. In the HERMES Monte Carlo framework, the radiative corrections are usually handled by the RADGEN program [Aku98]. RADGEN was specifically designed to simulate radiative corrections for deep inelastic scattering events with a sufficiently low energy scale, so that electroweak contributions and corrections are negligible.

Interactions of the particles with the detector are accounted for by HMC, the GEANT simulation of the HERMES detector. This program uses a model of the detector to simulate the particle interactions with the different materials they traverse. The calculated detector responses are then passed on to the tracking algorithm.

**Figure 5.10**

Schematic view of the influence of initial and final state radiation on the Born kinematics. The energy transfer  $v$  is always increased by the energy of the Bremsstrahlung-photon. This gives rise to the asymmetric shape of the smearing matrices (Fig. 5.13 and 5.14)

### 5.4.2 The Correction Method

The unfolding formalism used to correct for QED radiative effects, detector smearing and acceptance effects was originally described in [Mil02]. It involves the information from two separate Monte Carlo productions:

- a tracked MC production, including QED effects and a simulation of the detector effects (and thus automatically limited to the HERMES acceptance) and
- a Born Monte Carlo, without the simulation of radiative effects and without any further detector effects.

By design, the tracked Monte Carlo production provides not only the observed kinematics after simulating all effects, but also the true (Born level) kinematics. For the kinematic variable of interest this allows the extraction of the  $N_X \times (N_B + 1)$  matrix  $n(i, j)$ , which specifies the number of events where the *observed* quantity falls in bin  $i$  while the *original* value would have fallen in (Born) bin  $j$ . The indices run from

$$i = 1 \cdots N_X \quad \text{and} \quad (5.18)$$

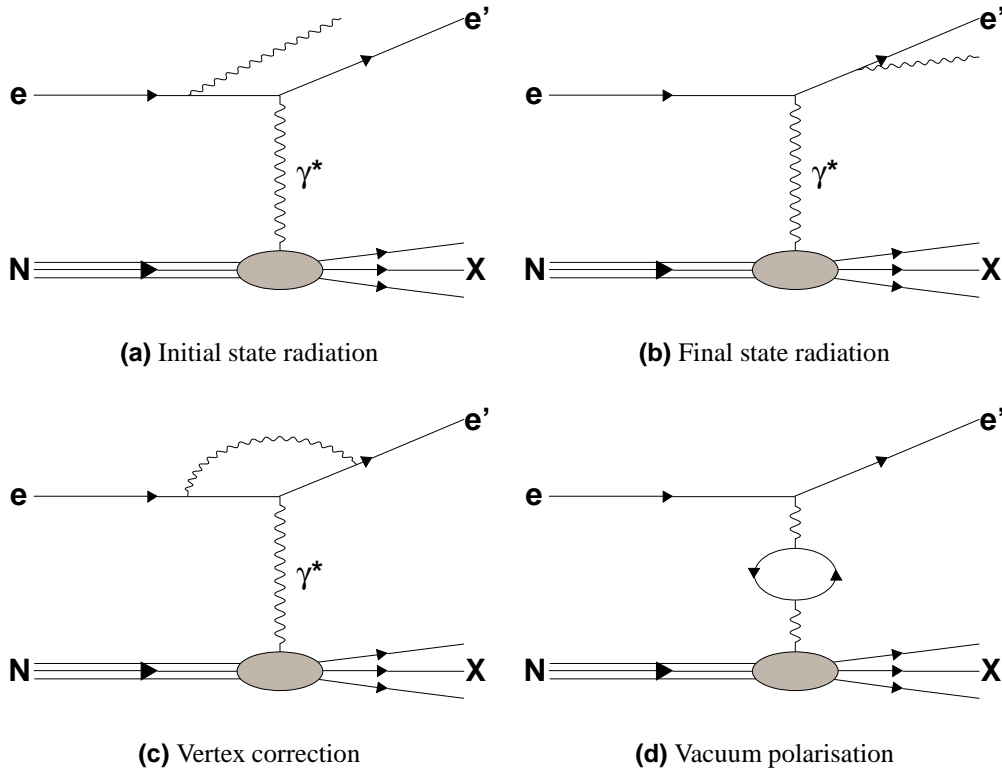
$$j = 0 \cdots N_B. \quad (5.19)$$

$N_X$  and  $N_B$  denote the number of bins for the observed and true values, respectively. As in reference [Mil02], bin  $j = 0$  is used for events which would have been excluded from the sample by the original kinematics but subsequently migrated into the acceptance<sup>5</sup>.

Summing over the Born bins  $j$  yields the experimental distribution

$$n^X(i) = \sum_{j=0}^{N_B} n(i, j), \quad i = 1, \dots, N_X. \quad (5.20)$$

<sup>5</sup>Here, acceptance refers to the geometric acceptance of the detector as well as the phase space selected by further kinematic cuts.

**Figure 5.11**

Higher order QED contributions to the DIS process.

However, the original Born distribution can not be calculated from this data set in a similar way:

$$n^B(j) \neq \sum_{i=1}^{N_X} n(i, j), \quad j = 0, \dots, N_B. \quad (5.21)$$

One reason is the fact that QED radiative processes do not conserve the total DIS cross section. Furthermore, Born events might not end up in the matrix because they migrate out of acceptance or are lost due to (simulated) detector inefficiencies. For these reasons, the Born distributions  $n^B(j)$  have to be obtained from the separate Born data set.

The matrix  $n^X(i, j)$  and the vector  $n^B(j)$  now allow us to calculate the smearing matrix defined as

$$S(i, j) \equiv \frac{\partial \sigma^X(i)}{\partial \sigma^B(j)} = \frac{\partial n^X(i)}{\partial n^B(j)} = \frac{n(i, j)}{n^B(j)}, \quad (5.22)$$

where the last step holds under the assumption that higher order derivatives are negligible. This is the case if only cross sections (and not amplitudes) are involved in the radiative calculation.

The aim of the unfolding procedure is to get the Born multiplicity from the experimental multiplicity, which — for the case of the semi-inclusive variable  $z$  — can be



written as

$$\left( \frac{1}{\sigma^{DIS}} \frac{d\sigma^h}{dz} \right)_{exp} [i] = \frac{X_h(i)}{X_{DIS}} = R_X(i) \quad \text{and} \quad (5.23)$$

$$\left( \frac{1}{\sigma^{DIS}} \frac{d\sigma^h}{dz} \right)_{Born} [i] = \frac{B_h(i)}{B_{DIS}} = R_B(j). \quad (5.24)$$

$X_h(i)$  and  $B_h(i)$  are the observed and Born level yields for hadron  $h$ ,  $X_{DIS}$  and  $B_{DIS}$  are the number of DIS events for the two cases. Corrected and uncorrected values are connected via the smearing matrix ([Mil02])

$$X_h(i) = Lk(i) \sum_{j=0}^{N_B} S_h(i, j) B_h(j) \quad \text{and} \quad (5.25)$$

$$X_{DIS} = Lk \left( S_{DIS} \cdot B_{DIS} + S_{DIS}^0 \cdot B_{DIS}^0 \right). \quad (5.26)$$

In the given example of a multiplicity versus a semi-inclusive variable, the smearing matrix  $S_{DIS}$  is a  $1 \times 2$  matrix, since there is no binning apart from the extra  $j = 0$  bin for events migrating into the cuts by radiative effects. The additional factor  $L$  denotes the experimental luminosity, which (given that one set of data is a subset of the other) is the same for both cases. The unknown vector  $k(i)$  is a normalisation constant which incorporates unsimulated inefficiencies. Assuming that these are uniform over the kinematic range, we can eliminate  $k$  by combining equations 5.25 and 5.26, yielding the experimental multiplicity

$$\frac{X_h(i)}{X_{DIS}} = \frac{\sum_{j=1}^{N_B} S'_h(i, j) B_h(j) + S_h(i, 0) B_h(0)}{S_{DIS} \cdot B_{DIS} + S_{DIS}^0 \cdot B_{DIS}^0}, \quad (5.27)$$

where the nominator on the right-hand side is just the total number of DIS events in the Monte Carlo,  $n_{DIS}^X$ .  $S'_h(i, j)$  is the square matrix which resulted from separating the  $j = 0$  column. If it can be inverted, the Born yield can be written as

$$B_h(j) = \sum_{i=1}^{N_X} [S'_h]^{-1}(j, i) \left[ \frac{X_h(i)}{X_{DIS}} \cdot n_{DIS}^X - S(i, 0) \cdot B_h(0) \right]. \quad (5.28)$$

To obtain the Born multiplicity, the yield has still to be normalised with the DIS cross section

$$R_b(j) = \frac{1}{n_{DIS}^B} \times \sum_{i=1}^{N_X} [S'_h]^{-1}(j, i) \left[ R_X(i) \cdot n_{DIS}^X - n_h(i, 0) \right]. \quad (5.29)$$

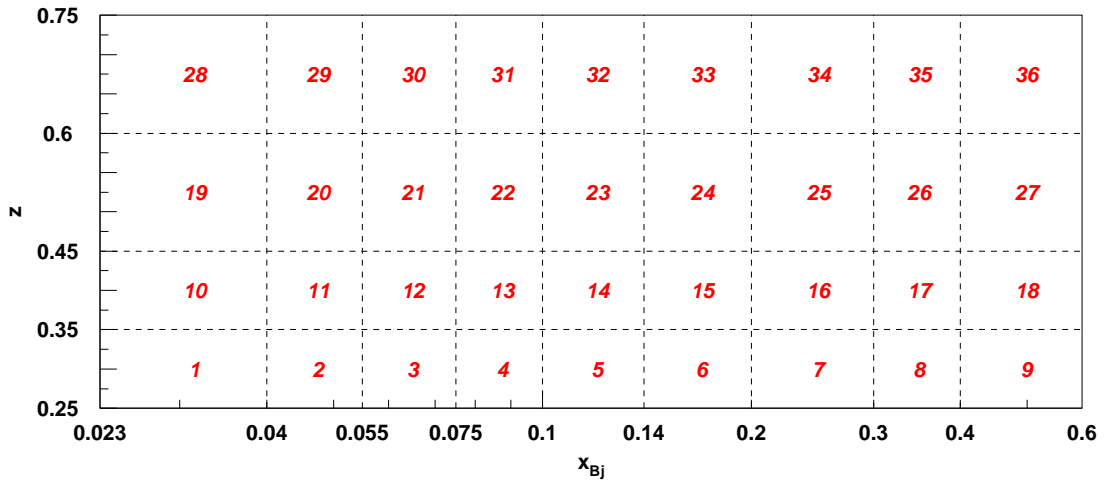
This equation holds assuming that the Monte Carlo simulation correctly reproduces the unpolarised Born cross section

$$n_{DIS}^B = B_{DIS}. \quad (5.30)$$

### 5.4.3 Practical Implementation

**Monte Carlo Productions.** As mentioned before, each target required two separate Monte Carlo productions to gather the information needed to apply the unfolding procedure. In all cases the latest (2004c) Monte Carlo tune was used to simulate the fragmentation process. The CTEQ6L LO parametrisation was chosen for the parton distribution functions. Each data set consisted of  $20 \cdot 10^6$  events. The tracked MC set was generated using the usual cuts, including the requirement that the DIS positron is generated within the HERMES acceptance. Since the Born Monte Carlo sample had to be free of any detector influence, the latter constraint had to be omitted. Instead, only cuts on the event kinematics were imposed. The generated events were required to have kinematics of  $0.1 \text{ GeV}^2 < Q^2 < 30 \text{ GeV}^2$ ,  $4 \text{ GeV}^2 < W^2 < 500 \text{ GeV}^2$ ,  $2 \cdot 10^{-3} < x_B < 0.99$  and  $0.05 < y < 0.95$ ; the constraints thus lie well outside the kinematic cuts of this analysis.

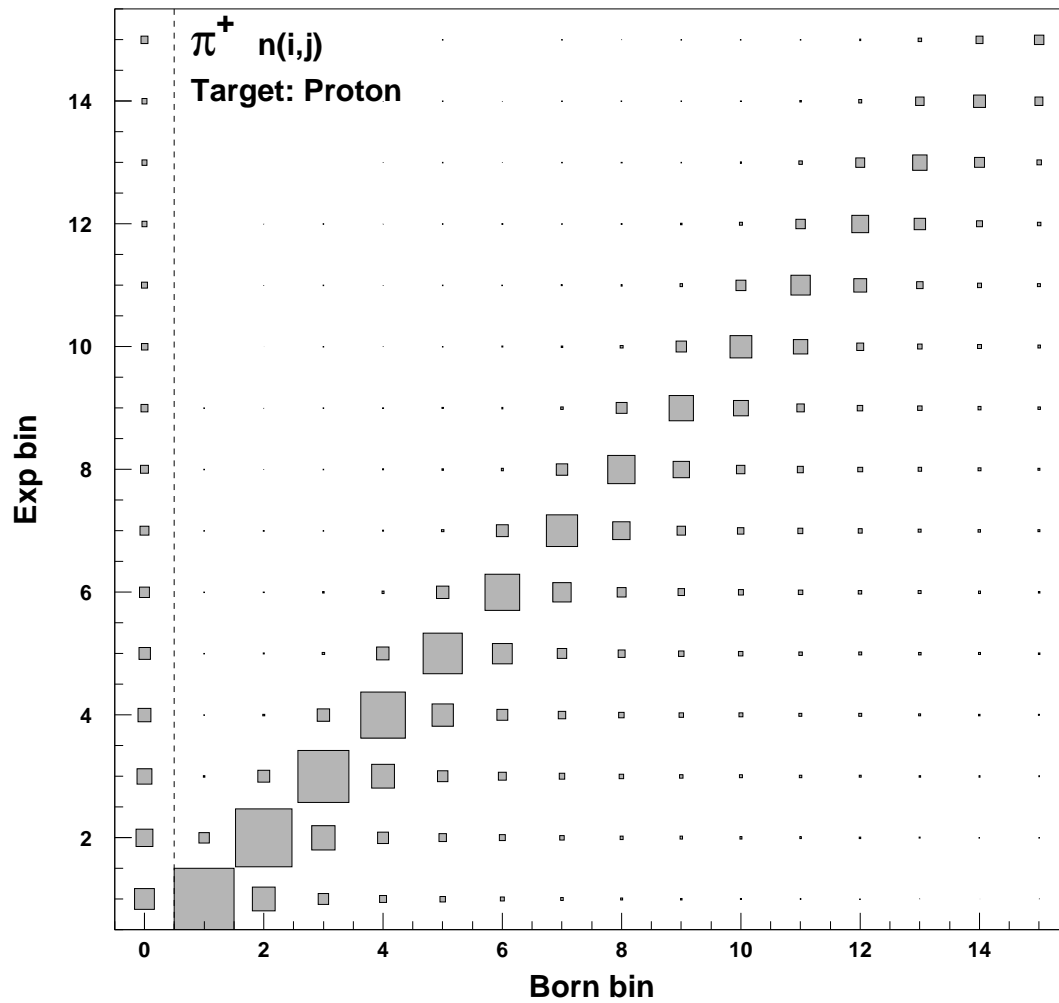
**2-dimensional Unfolding.** Apart from a simple 1-dimensional  $z$  binning, the unfolding procedure also had to be applied to 2-dimensional binnings versus  $z$  and  $x_B$  and  $Q^2$ , respectively. While it might be possible to extend the formalism to using 4-dimensional matrices, a much simpler approach was chosen by 'linearising' and renumbering the bins. The principle is shown in Figure 5.12.



**Figure 5.12**

Bin renumbering scheme for the 2-dimensional binning versus  $z$  and  $x_B$ .

**Resulting Matrices.** Figure 5.13 shows the smearing matrix vs.  $z$  for positive pions. The (symmetric) kinematical smearing by the detector and the track reconstruction only shifts the pions by one or two bins. The clearly asymmetric shape of the matrix is due to the radiative effects, which change the kinematics towards smaller  $z$ . Fig. 5.14 shows the  $n(i, j)$  matrix for  $\pi^+$  in the 'linearised' 2-dimensional binning. The bins are grouped

**Figure 5.13**

The smearing matrix  $n(i, j)$  for  $\pi^+$ . The binning corresponds to the 15 bins vs  $z$  as defined in Tab. A.1.

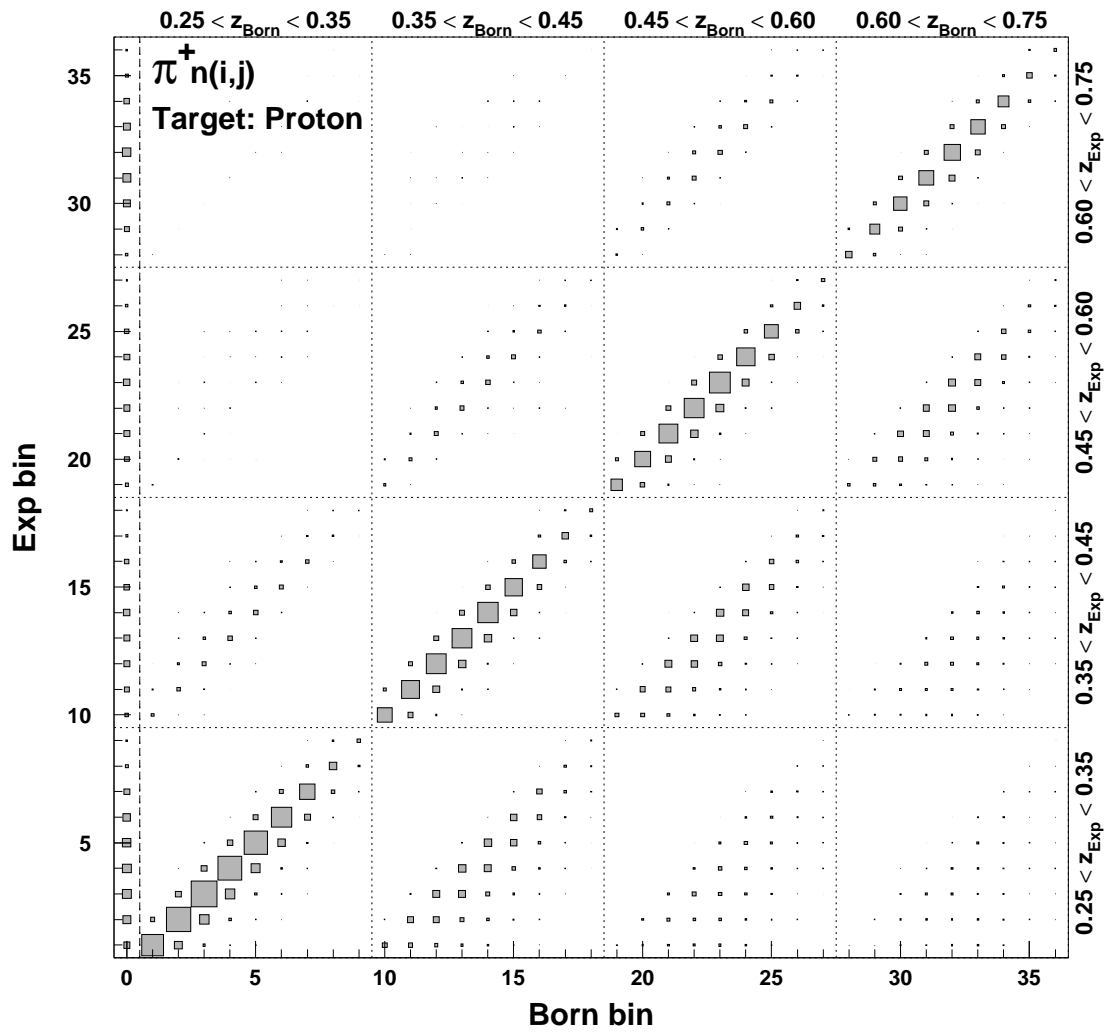


**Figure 5.14**

The smearing matrix  $n(i, j)$  for  $\pi^+$  in the 2-dimensional binning vs.  $x_B$  and  $z$ . The four  $z$  bins are indicated by the dashed line. Each  $z$  bin is divided in 9  $x_B$  bins.

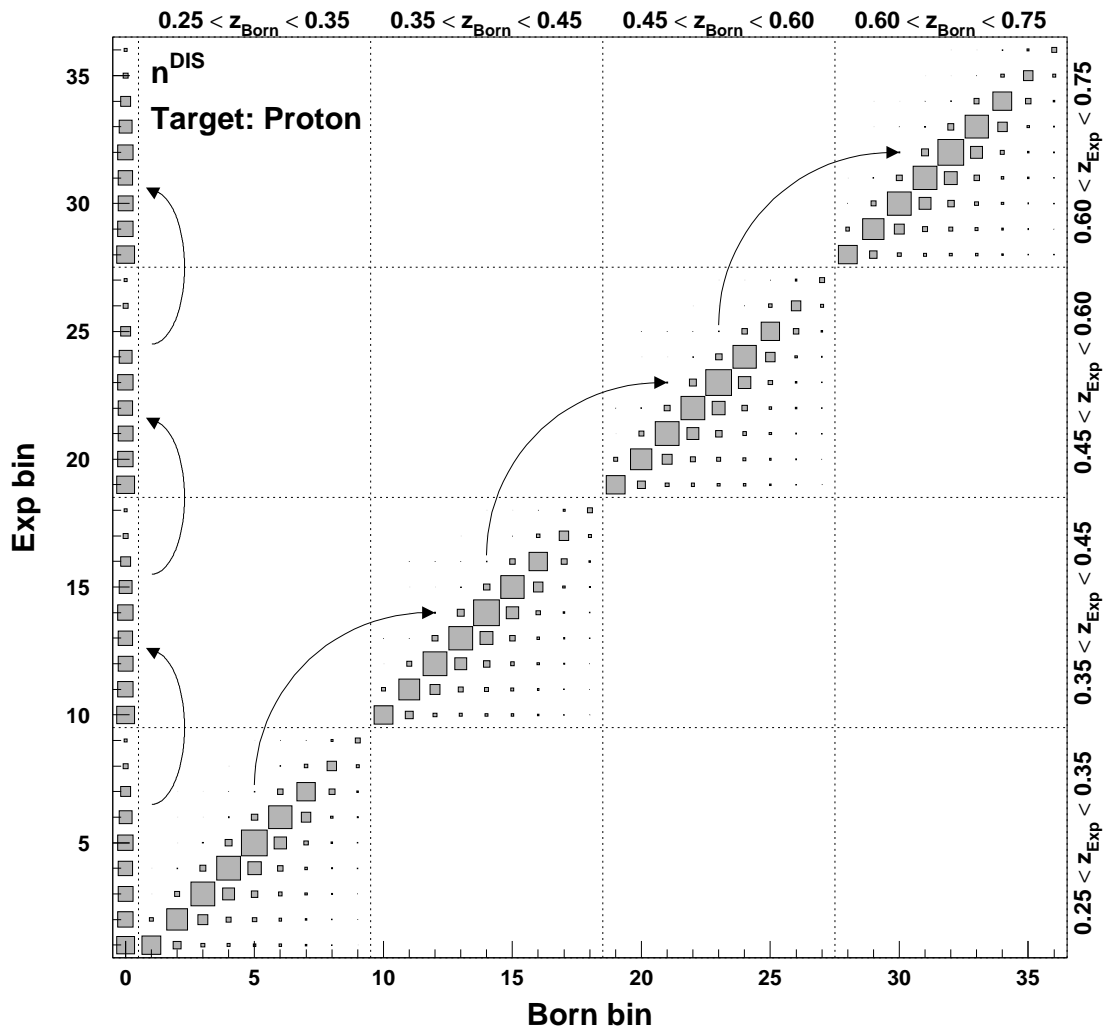


**Figure 5.15**

The matrix  $n_{\text{DIS}}$  in the 2D  $z_x$  binning. The DIS matrix is identical for all  $z$  bins. The DIS matrix is filled by copying the entries in the relevant locations.

in the four  $z$  bins which are indicated by the dashed lines. Each  $z$  bin is separated in 9  $x_B$  bins. Since the radiative smearing causes higher values for the observed  $\nu$ ,  $x_B$  is reduced together with  $z$ .

Figure 5.15 illustrates the DIS smearing matrix in the 2-dimensional binning. Since  $z$  is a semi-inclusive variable, the different  $z$  bins are filled with copies of the event smearing in the  $x_B$  binning.

#### 5.4.4 Error Propagation & Systematic Error

The error propagation is based on the radiative dilution matrix  $D(j, i)$  given as ([Mil02]):

$$D(j, i) = \frac{[S'_h]^{-1}(j, i)n^X(i)}{n^B(j)} \quad (5.31)$$

which propagates the error using the relation

$$\sigma^2(R_{\text{Born}}(j)) = \sum_{i=1}^{n_X} D^2(j, i)\sigma^2(R_x(i)). \quad (5.32)$$

The dilution matrix causes the inflation of the propagated errors [Hil04a].

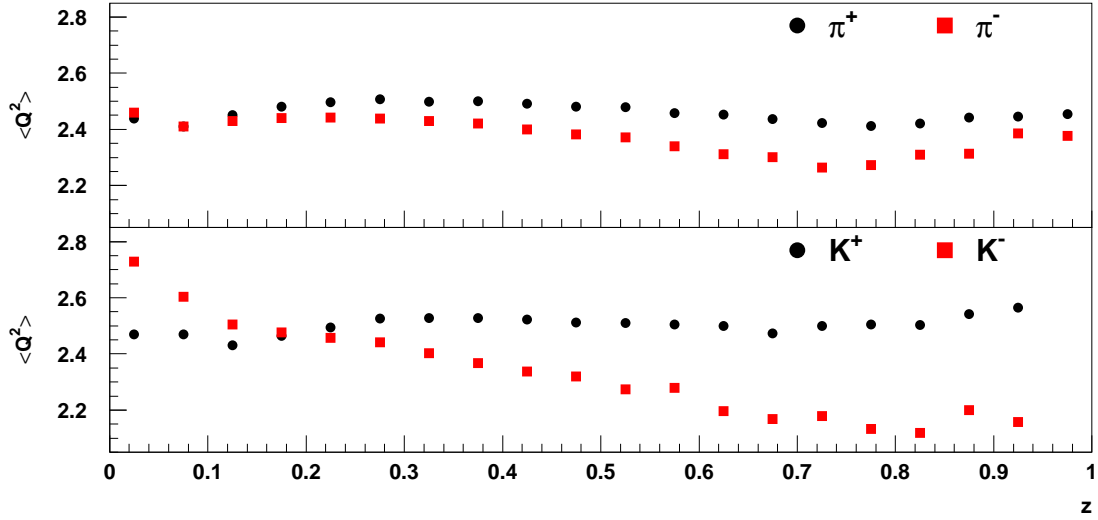
The limited statistics of the Monte Carlo sample used to extract the smearing matrices gives rise to another source for systematic errors. The influence of the statistical uncertainty of the smearing matrix on the unfolded result was determined using a variational technique. A large number of alternative smearing matrices was generated, where each element was varied independently using a Gaussian distribution with the original value as central value. The standard deviation was given by the statistical uncertainty. Each matrix was then used to unfold the hadron multiplicities, resulting in a Gaussian-shaped distribution for each multiplicity value. The systematic uncertainties were then obtained as the standard deviation from these uncertainties.

### 5.5 $Q^2$ Evolution

The property of interest is the dependence of the hadron multiplicities on the variables  $z$  (and  $x_B$ ). In the framework of the quark parton model, the multiplicities can be expressed as a convolution of fragmentation functions  $D_q^h(z, Q^2)$  and parton distribution functions  $q(x_B, Q^2)$ ,

$$\frac{1}{\sigma_{\text{DIS}}} \frac{d\sigma^h(z, Q^2)}{dz} = \frac{\sum_q e_q^2 \int_0^1 dx_B q(x_B, Q^2) D_q^h(z, Q^2)}{\sum_q e_q^2 \int_0^1 dx_B q(x_B, Q^2)}, \quad (5.33)$$

both of which scale logarithmically with  $Q^2$ . However, the extracted hadron multiplicities show varying average  $Q^2$  for different bins, thus the results are a combined effect of changing  $Q^2$  as well as  $z$  (and  $x_B$ ). Figure 5.16 shows the average  $Q^2$  values for the pion and kaon multiplicities versus  $z$ . It is apparent that the average  $Q^2$  varies only slightly with  $z$ . Versus  $x_B$ , however, the  $Q^2$  dependence is much stronger (Fig. 5.17). In order

**Figure 5.16**

Average  $Q^2$  of the multiplicities for several hadron types versus  $z$ . The  $z$  dependence is obviously not very strong. The average  $Q^2$  values have been obtained from the Born Monte Carlo simulation used for radiative and acceptance correction.

to isolate the desired  $z$  and  $x_B$  dependencies, the multiplicities have to be evolved to a common  $Q^2$ . Applying evolution factors is also necessary for a meaningful comparison to other experiments. EMC, for example, has an average  $Q^2$  of 25 GeV<sup>2</sup>.

While the logarithmic scale dependence of the parton distribution functions is described by the DGLAP evolution ([Gri72],[Alt77]), it is not clear how to model the  $Q^2$  dependence of the fragmentation functions, which can not be calculated in perturbative QCD. It was chosen to calculate the evolution factors from Eq. (5.33) using parametrisations for the fragmentation functions as well as the parton distribution functions. For the fragmentation functions, the PKH parametrisation by S. Kretzer [Kre00] was chosen. This model provides charge and flavour separated parametrisations of the form

$$D_q^h = N_0 \cdot z^\alpha (1-z)^\beta. \quad (5.34)$$

The parameters are determined by a fit method applied to flavour separated data near the  $Z^0$  pole for  $\pi^\pm$  and  $K^\pm$  from the SLD [Abe99] collaboration and summed charged hadron data from the ALEPH [Bus95] collaboration. Furthermore, low energy scale data from TPC [Aih88] is included in order for the fragmentation functions to properly reflect QCD scaling violations. The PKH parametrisation is available both in leading and next-to-leading order. For the actual correction factors, the leading order parametrisation was used, the next-to-leading order was used as an input for the systematic error calculation (see below).

For the parton distribution functions the CTEQ6  $\overline{\text{MS}}$  parametrisation was used, which is the current standard distribution of the CTEQ6 'family' [Pum02]. The numerical integration versus  $x_B$  was based on the *extended trapezoidal rule*. The specific algorithm

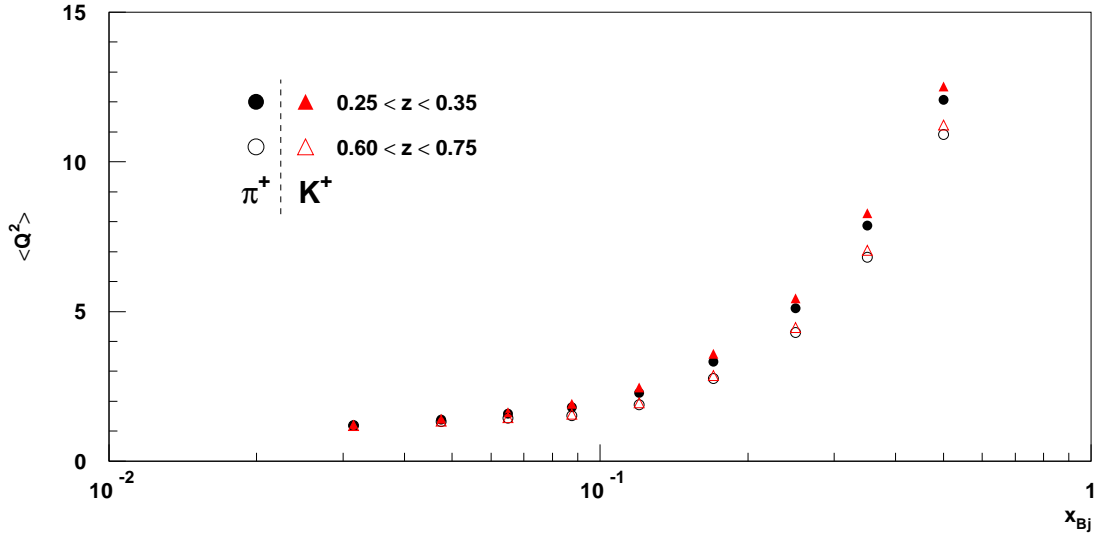


**Figure 5.17**

Average  $Q^2$  for  $\pi^+$  and  $K^+$ . Since  $x_B = Q^2/2mv$ , the average  $Q^2$  rises sharply with  $x_B$ .

allows the subsequent calculation of additional points until the integral converges, meaning that the relative difference between the new and the old result is less than a predefined value. For the integrations in question, a lower limit of  $10^{-5}$  was used. The  $x_B$  integration was done in a range between 0.023 and 0.6. The algorithm is described in detail in Chapters 4.1 and 4.2 in [Pre92].

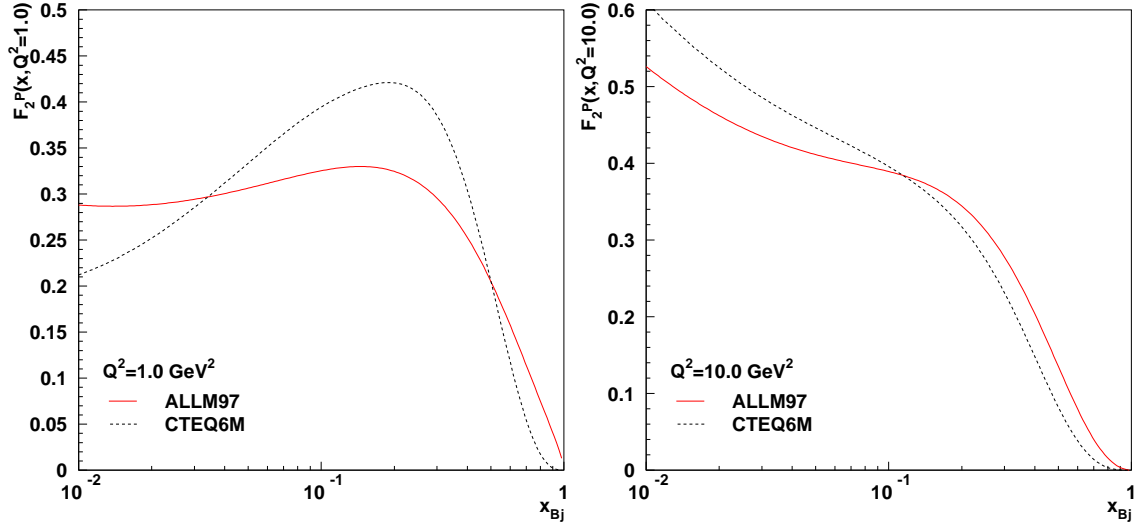
**Systematic Errors.** Clearly, there is some arbitrariness in the choice of parametrisations and parametrisation orders, as well as in the used integration boundaries. To account for that, alternative evolution factors have been calculated using a combination of PDF and FF parametrisations in leading and next-to-leading order, as well as significantly changed integration boundaries (the latter is of course only possible for the evolution factors versus  $z$ , since the factors for the  $x_B$  bins are calculated at their respective values).

A further fact to be considered is the comparatively low  $Q^2$  region of the HERMES experiment. With an average  $Q^2$  of about  $2.5 \text{ GeV}^2$ , it is worthwhile to check whether the CTEQ6 parametrisations of the parton distribution functions really describe the  $F_2(x_B, Q^2)$  nucleon structure function at this  $Q^2$ . Using the relation

$$F_2(x_B, Q^2) = x_B \cdot \sum_q e_q^2 \cdot q(x_B, Q^2) \quad (5.35)$$

the results from the CTEQ6 parametrisations was compared to the values obtained from the ALLM97 parametrisation [Abr97a]. The latter is an update to the ALLM parametrisation, which specifically improves the description of  $\sigma_{\text{tot}}(\gamma^* p)$  in the low  $Q^2$  and low  $x_B$  region.



**Figure 5.18**

The structure function  $F_2^P$ , in one case obtained from the ALLM97 parametrisation, in the other calculated from the CTEQ6M PDFs using Eq. (5.35). The left hand side shows the comparison for a  $Q^2$  of 1  $\text{GeV}^2$ , the right hand side for 10  $\text{GeV}^2$ . It can be seen that the differences increase with lower  $Q^2$ .

Figure 5.18 compares the results for  $Q^2$  values of 1  $\text{GeV}^2$  and 10  $\text{GeV}^2$ . Clearly, there is a growing discrepancy between the  $F_2$  results for decreasing  $Q^2$ . To account for this fact, the parton distribution functions were re-weighted using the factor

$$w_{F_2}(x_B, Q^2) = \frac{F_2^{\text{ALLM97}}(x_B, Q^2)}{x_B \cdot \sum_q e_q^2 q(x_B, Q^2)}, \quad (5.36)$$

so that the re-weighted  $q'(x, Q^2) = w_{F_2}(x, Q^2) \cdot q(x, Q^2)$  reproduce the ALLM97 parametrisation. The PDFs provide the correct normalisation of the inclusive cross section, while at the same time keeping the ratio of the different quark contributions to the nucleon structure.

To summarise, the following alternatives were used to calculate the evolution factors:

- ① CTEQ6  $\overline{\text{MS}}$  or **LO** as PDF
- ② use re-weighted  $q'(x_B, Q^2) = w_q(x_B, Q^2) \cdot q(x_B, Q^2)$  or original  $q(x_B, Q^2)$
- ③ PKH **LO** or **NLO** as FF
- ④  $[x_{\min}; x_{\max}] = [0.023; 0.6]$  or  $[0.01; 0.9]$  as boundaries for the  $x_B$  integration.

The original evolution factors were obtained by always using the first option. Alternatively, 15 (vs  $x_B$ : 7) further sets of evolution factors can be calculated by using all possible combinations. The systematic uncertainty is given by the maximal and minimal values.

In Figure 5.19 the resulting 16 evolution factor sets for the evolution to  $Q^2 = 2.5 \text{ GeV}^2$  are plotted vs.  $z$  for  $\pi^+$  (5.19a) and  $K^+$  (5.19c). Also shown are the relative differences between the set used for the original evolution factors (PDF: re-weighted CTEQ6  $\overline{\text{MS}}$ , FF: PKH in LO; integration between  $0.023 < x_B < 0.6$ ) and the alternatives. The differences are in general less than 0.5 %, the largest difference arises at low  $z$  when using the NLO fragmentation functions. However, these largest uncertainties do not affect the final results, since only the region above  $z = 0.15$  is included.

Due to the larger variation of the average  $Q^2$  versus  $x_B$ , the corresponding evolution factors are naturally higher. For pions, the evolution factors are shown as dashed lines in Fig. 6.11 on page 102 on the right hand plot.

## 5.6 Summary

**The Relative Size of the Different Uncertainties.** The various correction steps introduce new uncertainties which have to be accounted for in the final result. For the multiplicities versus  $z$ , Figure 5.20 shows a compilation of all errors considered for the final results presented in the next chapter. The specific values were taken from the multiplicities including exclusive vector meson correction after evolution to a common  $Q^2$  of  $2.5 \text{ GeV}^2$ . The errors are given in percent of the respective multiplicity value. For the final result, the different error contributions were added quadratically. Since the RICH unfolding and the  $Q^2$  evolution resulted in asymmetric errors, the positive and negative errors are given separately.

It can be seen that the RICH unfolding is dominating the high statistics area at lower  $z$ , especially in the case of kaons. Naturally, the statistical error becomes increasingly important for higher  $z$  and is in almost all cases the largest single contribution in the last bins. The  $Q^2$  evolution error rarely reaches 2% of the respective multiplicity value. For negative kaons the statistics drops dramatically at high  $z$ , leading to very large relative errors.

**Further Studies.** In a recent study [Hil05], the influence of the  $\cos \phi$  dependence of the DIS cross section and the HERMES acceptance on the extracted multiplicities was investigated. The azimuthal angle  $\phi$  of a produced hadron is defined as the angle between the lepton scattering plane and the hadron production plane given by the virtual photon and the produced hadron. The  $\phi$  dependence of the semi-inclusive cross section (Cahn effect) can be parametrised as

$$\frac{d\sigma}{d\phi} = A + B \cos \phi + C \cos 2\phi. \quad (5.37)$$

This behaviour arises from the intrinsic transverse motion of the partons ([Cah78],[Cah89]).

The Monte Carlo productions used for the acceptance correction in Sec. 5.4 did not contain any  $\phi$  dependence. On the other hand, the HERMES acceptance is known to vary with  $\phi$ . Neglecting the  $\phi$  dependence of the DIS cross section thus might lead to under- and overestimations in the acceptance correction.

The study presented in [Hil05] estimated the effects by imposing an artificial  $\phi$  dependence on the Monte Carlo data. The moments were obtained by comparing the experimental  $\phi$  distributions with the ones present in the Monte Carlo sample in the acceptance. The resulting shift of the acceptance correction factor (the ratio of the multiplicity in the acceptance divided by the unconstrained multiplicity in the full solid angle) is an estimate of the error made by using a Monte Carlo production not taking the  $\phi$  dependence into account. For most bins, the variations are rather small. For the multiplicities versus  $z$ , the change is below 5%. Versus  $x_B$ , they can reach 10% for the highest  $x_B$  (and  $z$ ) bins.

The findings of the study can be applied to the multiplicities either as an additional correction to the central values, or as another contribution to the errors. However, at this stage the results are considered rather preliminary. For example, they depend heavily on the treatment of exclusive vector mesons in the extraction. Furthermore, the influence of a possible detector misalignment is not yet fully understood. For this reason, the influence of the azimuthal angle dependence of the DIS cross section has not been considered for the final results presented in the next chapter.

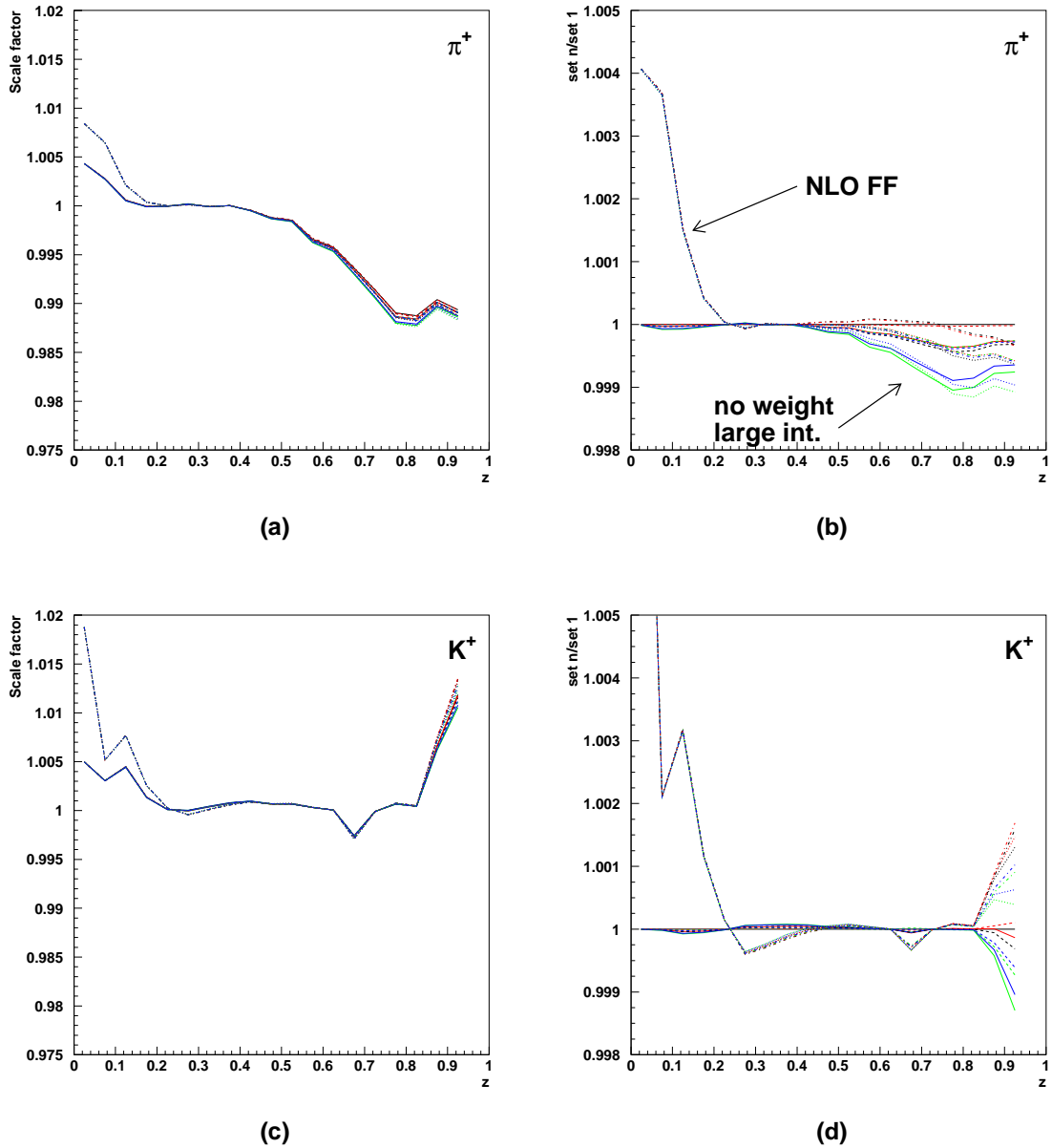


**Figure 5.19**

$Q^2$  evolution factors for  $\pi^+$  (top) and  $K^+$  (bottom) versus  $z$ . The left side shows the factors as obtained from the 16 different setups. The right side shows the ratios between the alternative setups used for the estimation of the systematic error and the original evolution factors. The factors generally differ by less than 0.5%, in the area of largest deviation (at low  $z$ ) the difference is due to the change of the fragmentation functions from LO to NLO.

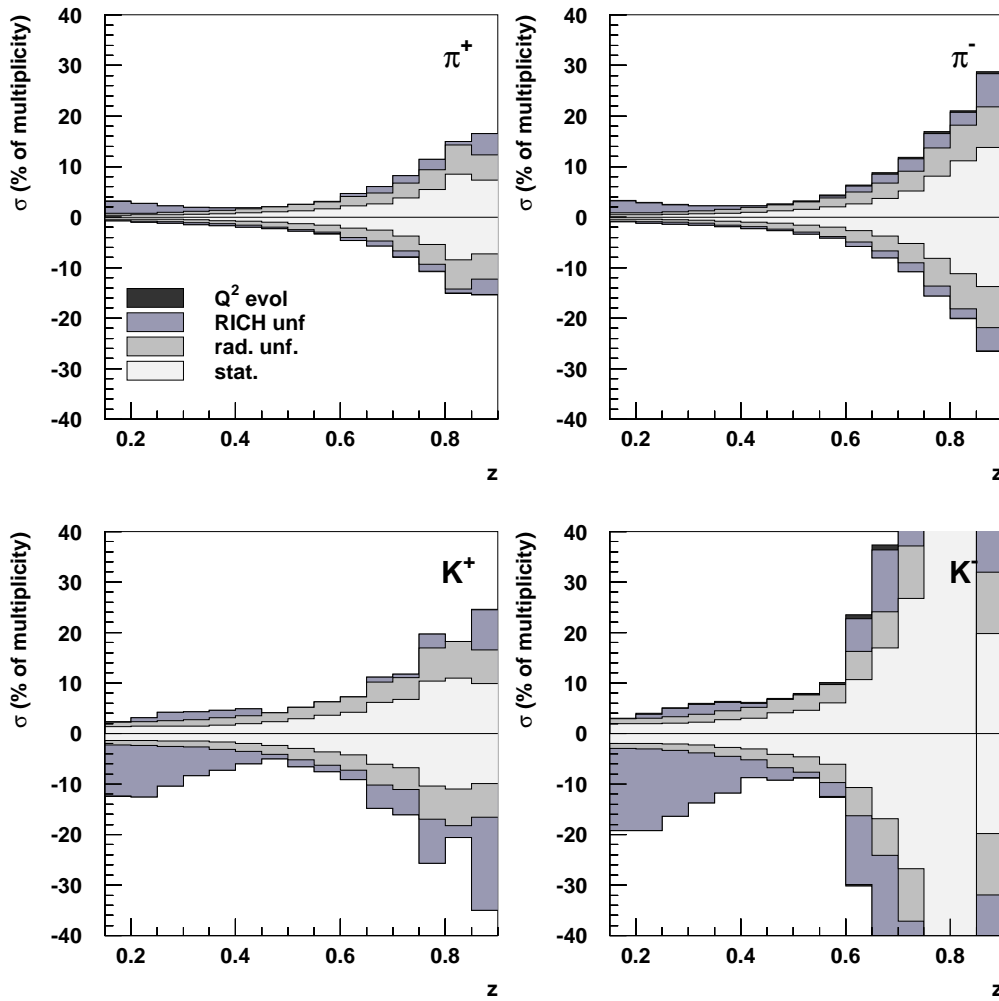


**Figure 5.20**

Overview over the relative size of the uncertainties from different sources. The errors are given in percent of the respective multiplicity value. For the final error shown in the next chapter, the errors have been added quadratically.



# Chapter 6

## Results

In this chapter, the results of the multiplicity extraction described earlier are presented. The set of results comprises charge separated pion (Sec. 6.1) and kaon (Sec. 6.2) multiplicities, in both cases versus  $z$  and — divided into 4  $z$  bins — versus  $x_B$  and  $Q^2$ , respectively. In general, all results of this work presented here include all the corrections described in the previous chapter, they are thus Born multiplicities in the full solid angle ( $4\pi$ ). As an exception, several plots distinguish between the results with and without the correction for diffractive contributions (Sec. 5.3.2). In many plots, the open symbols have been shifted slightly to higher values along the  $x$  axis to allow for a better comparison.

The proton multiplicities have already been released in a similar form in June 2004 [Hil04b]. However, there are several small changes which lead to some differences with respect to the previous results. This changes are

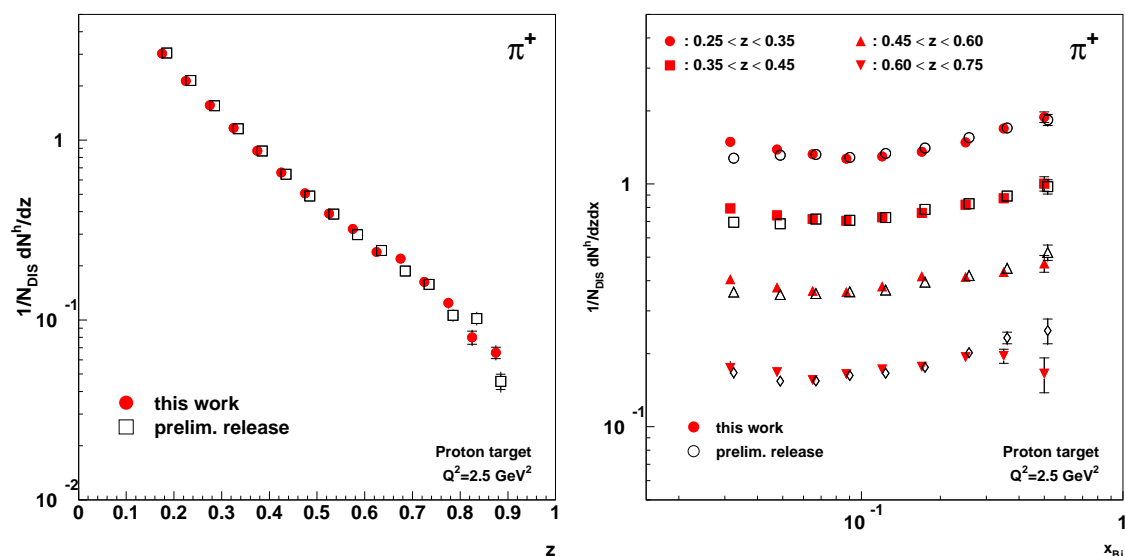


**Figure 6.1**

Comparison of the updated analysis (this work) with the release from June 2004. Shown as an example are the  $\pi^+$  multiplicities versus  $z$  and  $x_B$ .

- new  $\mathcal{P}$  matrices for the RICH unfolding, together with an updated method to estimate the systematic uncertainty,
- a new set of Monte Carlo fragmentation parameters (2004c instead of 2004a), which was consistently used for all steps involving Monte Carlo data (exclusive vector meson correction, radiative and detector effects), and
- the use of a fully tracked Monte Carlo production for the acceptance and radiative correction (the preliminary released data made use of Monte Carlo data produced with HSG).

The preliminary release and the current results are compared in Figure 6.1 for the case of positive pions versus  $z$  and  $x_B$ . The agreement is generally quite good. For kaons, the changes have been a bit larger, since they are more sensitive to changes in the  $\mathcal{P}$  matrices.

## 6.1 Pion Results

Figure 6.2 compares the final multiplicities of positive (top) and negative (bottom) pions vs.  $z$  for the two considered target types. The data sets include the correction for pions from exclusive  $\rho^0$  decays and have been evolved to a common  $Q^2$  of 2.5 GeV<sup>2</sup>. The deuterium data (open squares) has been shifted slightly towards larger values of  $z$ . Figure 6.3 compares the ratios of the pion multiplicities. The upper plots shows the ratio of the two target types for  $\pi^+$  and  $\pi^-$ , the charge ratio is shown in the lower panel, both for the proton and deuterium target. The error bars represent the statistical error only.

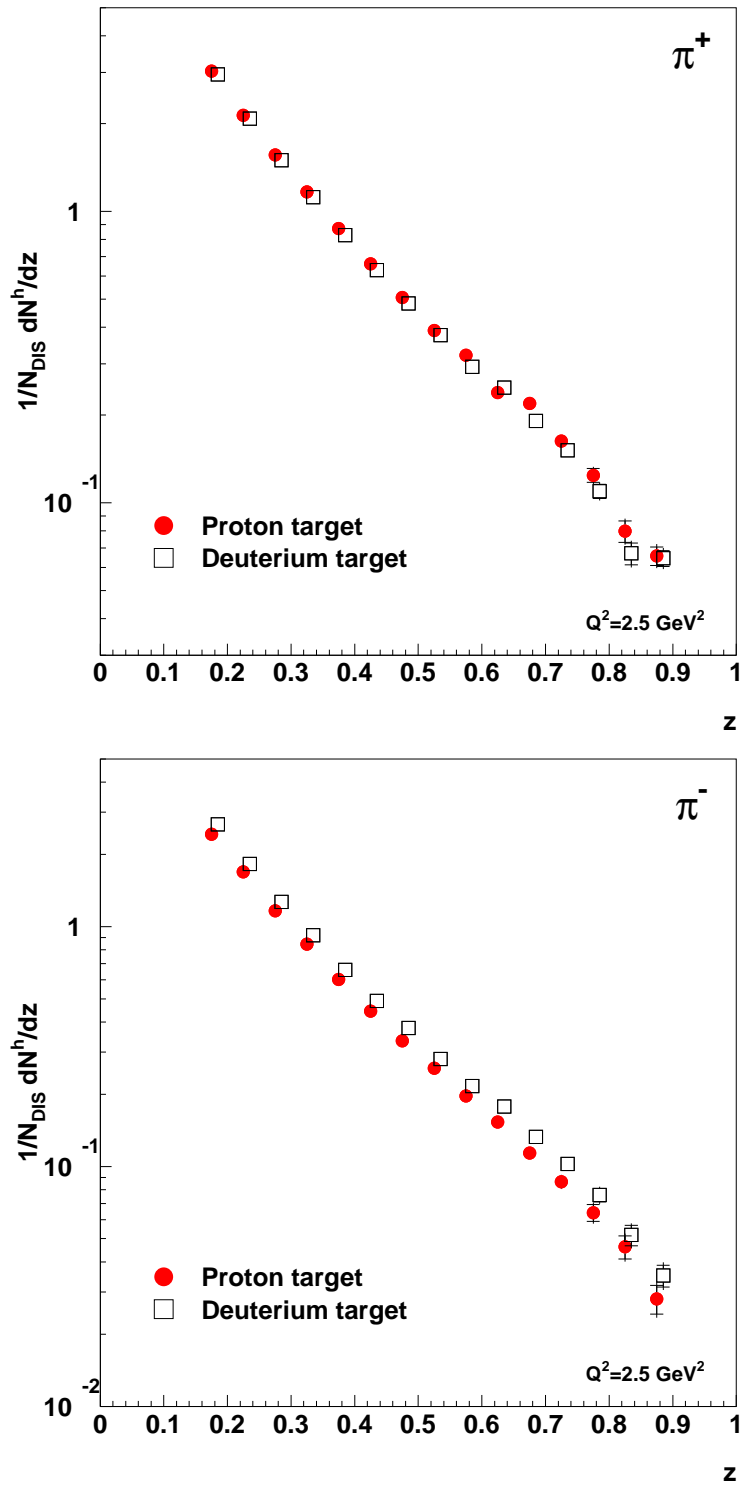
It can be seen that the  $\pi^+$  multiplicities obtained from a proton target are generally larger ( $\sim 5\%$ ). This can be attributed to the different (valence) quark content of the two targets: the  $\pi^+$  multiplicity gives the average number of  $\pi^+$  produced per scattering event involving any quark in the target. For a proton target the likelihood to scatter on a  $u$  quark is larger than for a deuterium target, resulting in a larger fraction of events involving the favoured fragmentation  $D_u^{\pi^+}$ . For  $\pi^-$ , the situation is inverted, leading to an increase of the multiplicity when using deuterium. With  $\sim 10\%$  the effect is about twice as large as for  $\pi^+$ .

The ratio of positive and negative pions in the lower part of Fig. 6.3 shows that for both targets the  $\pi^+$  multiplicity dominates over the  $\pi^-$  multiplicity. This again can be attributed to the  $u$  quark dominance in both targets<sup>1</sup>. The effect is stronger for the proton target, as is to be expected. With increasing  $z$ , favoured fragmentation becomes more dominant. For  $z \rightarrow 1$ , the hadron contains all the energy transferred by the virtual photon and thus essentially must contain the struck quark. Correspondingly, the  $\pi^+/\pi^-$  ratios rise with  $z$ , where the effect is again stronger for the proton.

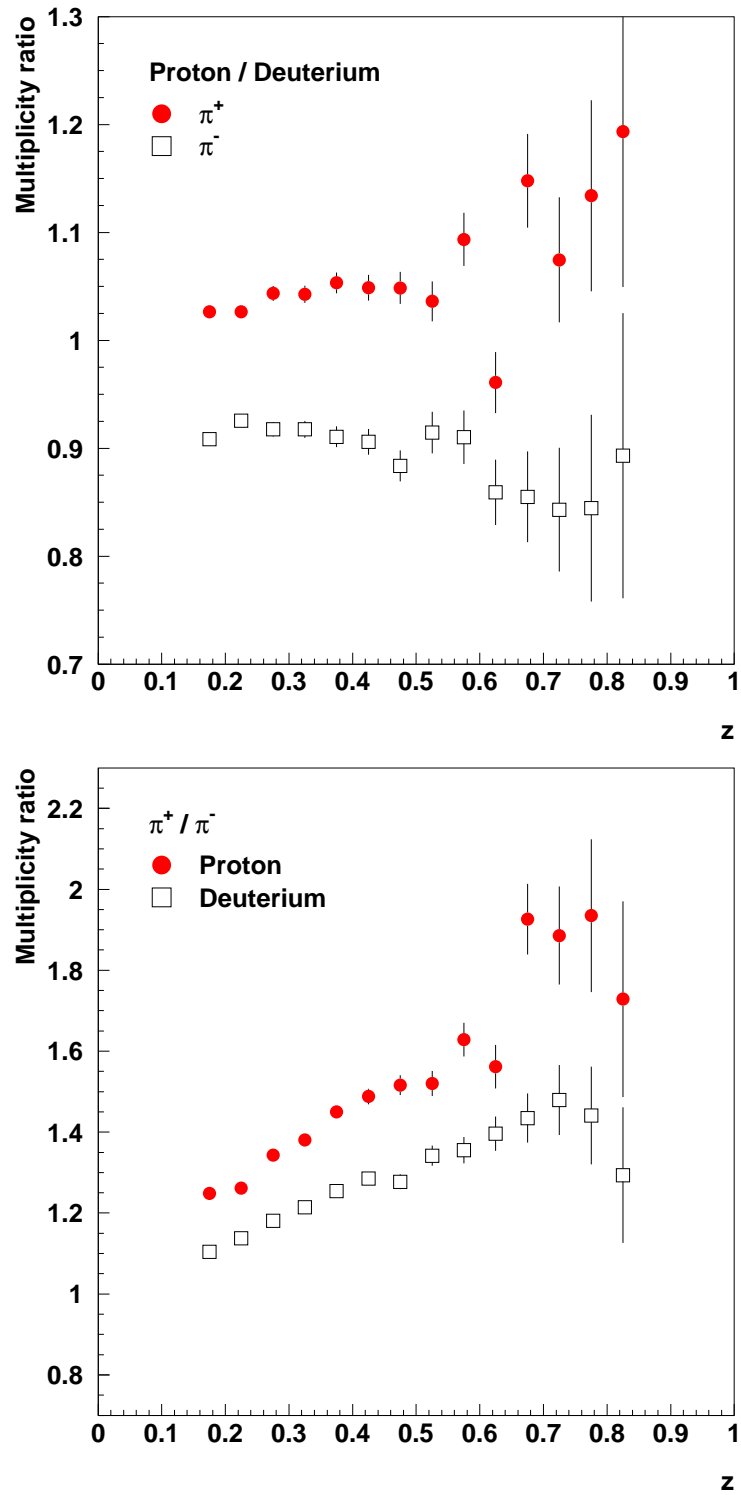
Figure 6.4 shows the charged pion multiplicities versus  $z$  in comparison with the pion multiplicities previously published in [Air01]. The two data sets from the current analysis illustrate the influence of diffractive  $\rho^0$  production on the pion multiplicities.

<sup>1</sup>In case of deuterium this is mainly based on the higher  $u$  quark charge.



**Figure 6.2**

The pion multiplicities vs.  $z$  using a proton (filled symbols) and a deuterium target (open symbols).

**Figure 6.3**

Target (top) and charge (bottom) ratios of pion multiplicities vs.  $z$ . The errors are statistical only.

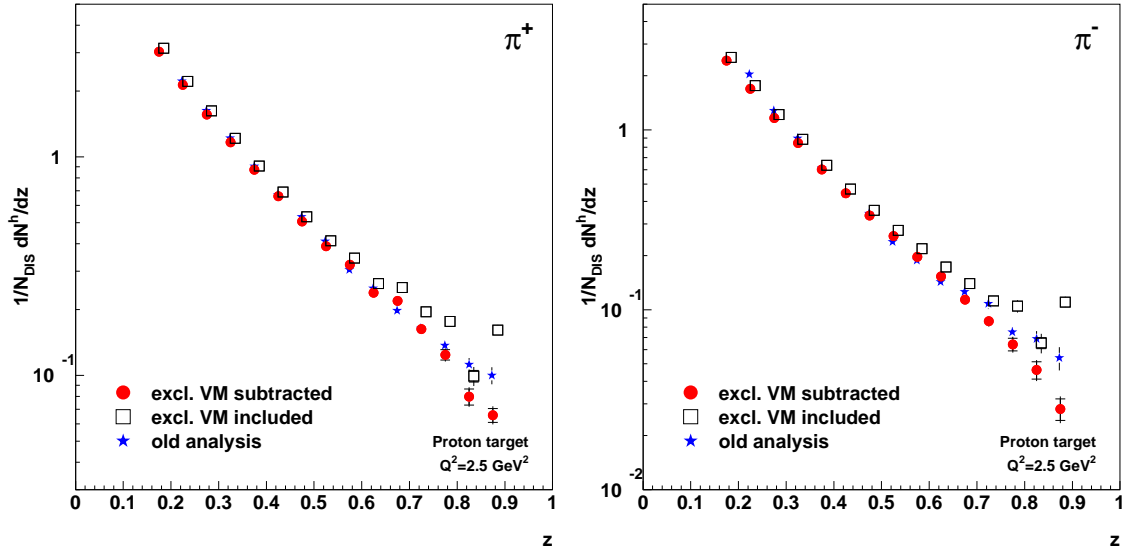


**Figure 6.4**

The pion multiplicities vs.  $z$  using a proton target. The filled symbols have been corrected for contributions from diffractive  $\rho^0$  production, the open symbols show the data without the correction. The data points have been evolved to a common  $Q^2$  of  $2.5 \text{ GeV}^2$ . The new analysis is shown in comparison to the old HERMES analysis published in [Air01].

While an effect of a few percent is visible across the entire  $z$  range, the two data sets start to deviate for  $z > 0.6$  (see also Fig. 5.7 on page 71). The old analysis made use of data collected during the 1996 and 1997 data taking period. For this reason, only pion data is available. The error bars of the old data give the statistical error only. In addition, the systematic uncertainty amounts to 7%. There are some notable differences in the analysis procedure used for the old and new data sets. So did the old analysis not take into account contributions from exclusive vector meson production. Furthermore, a stand alone application was used to simulate radiative effects (POLRAD 2.0, [Aku97]), while the acceptance correction was done separately using ratios of hadron yields in the full solid angle and in the detector acceptance. In this work, both correction steps are performed in one integrated step as described in Sec. 5.4. Nevertheless, the agreement is generally very good. In the high  $z$  region, the old data lies in-between the new values with and without exclusive vector meson correction.

Figure 6.5 compares the HERMES proton results with fragmentation functions published by the EMC collaboration [Arn89], which were obtained from muon-proton scattering at an energy of 280 GeV. For this purpose, the HERMES data has been evolved to EMCs average  $Q^2$  of  $25 \text{ GeV}^2$ . EMC extracted the fragmentation functions using Equation (5.33), taking into account the  $u$ ,  $d$  and  $s$  quark (and corresponding antiquark) distributions as given by a parametrisation by Glück, Hoffmann and Reya [Glü82]. The given errors on the EMC data are due to statistics, the additional systematic error amounts to  $\sim 15\%$  and is mostly due to particle identification uncertainties, but also the fragmentation function extraction method. The two HERMES data sets represent the final multipli-

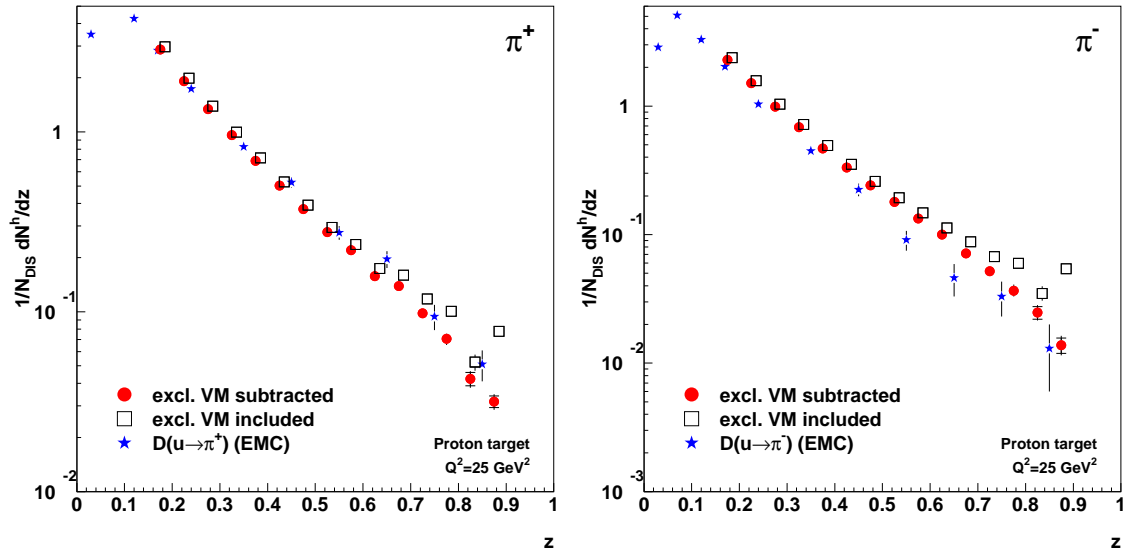


**Figure 6.5**

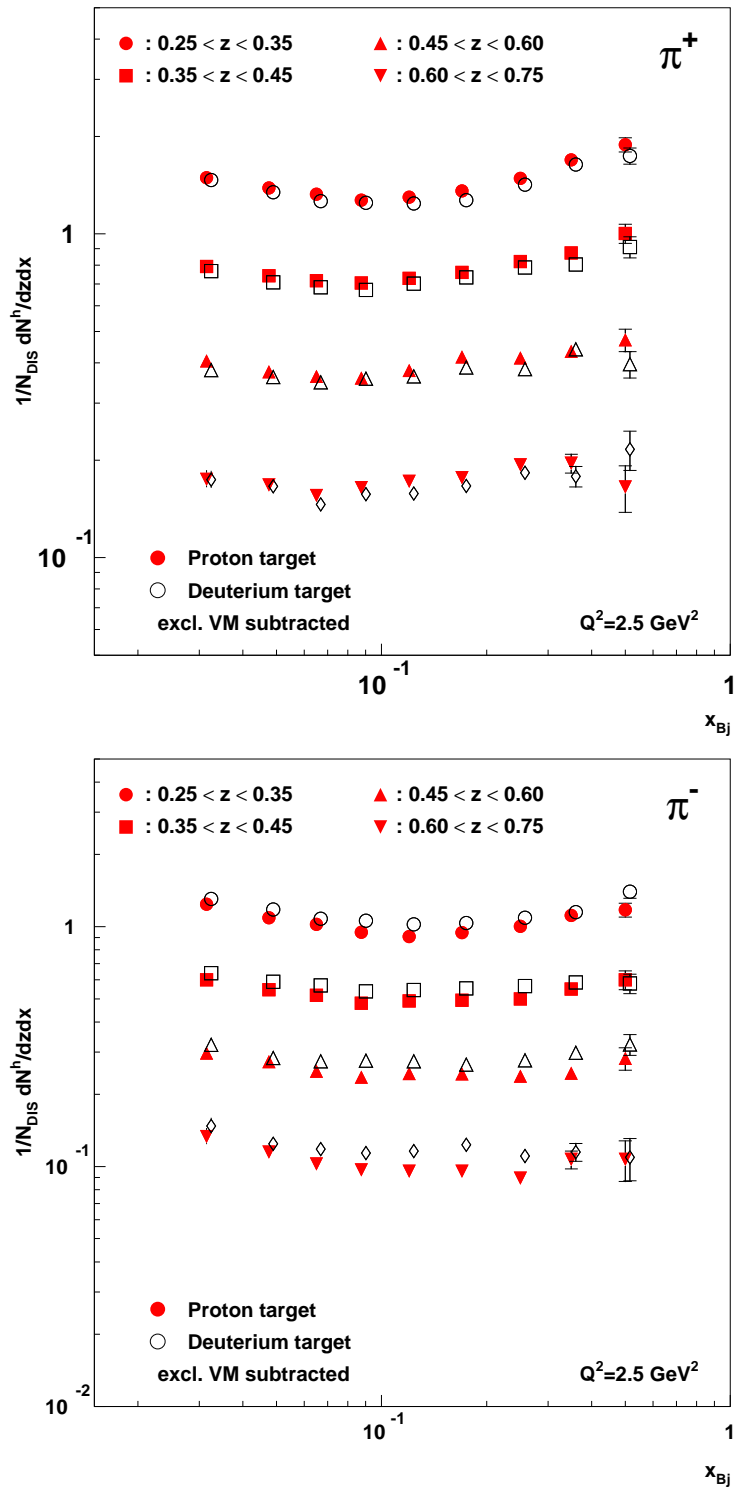
The pion multiplicities vs.  $z$  using a proton target. The filled symbols have been corrected for contributions from diffractive  $\rho^0$  production, the open symbols show the data without the correction. The HERMES data is compared to  $D_u^{\pi^+}$  and  $D_u^{\pi^-}$  fragmentation functions from EMC published in [Arn89] (stars). For this purpose, it has been evolved to a common  $Q^2$  of 25 GeV<sup>2</sup>.

cities with and without correction for the pion contribution from exclusive  $\rho^0$ . As can be seen from the associated statistical errors, they provide substantially improved statistics in comparison to the EMC results.

It should be noted that the compared quantities have a different interpretation. The EMC fragmentation functions  $D_u^h$  give the average number of produced hadrons  $h$  under the condition that a  $u$  quark was struck. The HERMES multiplicities give this number averaged over all DIS events. However, due to the dominance of  $u$  quark scattering (especially in the case of a proton target), the two quantities are expected to be rather similar, which makes a comparison meaningful.

In general, the agreement between HERMES and EMC is quite good, considering that the beam energies at which the measurements were taken differ by a factor of ten. The observed differences can be attributed to the different plotted quantities, namely multiplicities in the case of HERMES and  $u$  quark fragmentation functions in the case of EMC. These findings support the notion that factorisation holds for HERMES energies, or at least in as much as it holds for EMC.

The  $\pi^+$  data agrees rather well within errors with the EMC fragmentation functions, illustrating how strongly the  $\pi^+$  production is dominated by  $u$  quarks scattering. The data set corrected for exclusive vector meson influences shows a better agreement with the EMC data. Diffractive contributions were not accounted for in the EMC analysis, however, at a  $Q^2$  of 25 GeV<sup>2</sup> they are insignificant due to the  $Q^{-6}$  dependence of the cross section.

**Figure 6.6**

The pion multiplicities vs.  $x_B$  in 4  $z$  bins using a proton (filled symbols) and a deuterium target (open symbols).

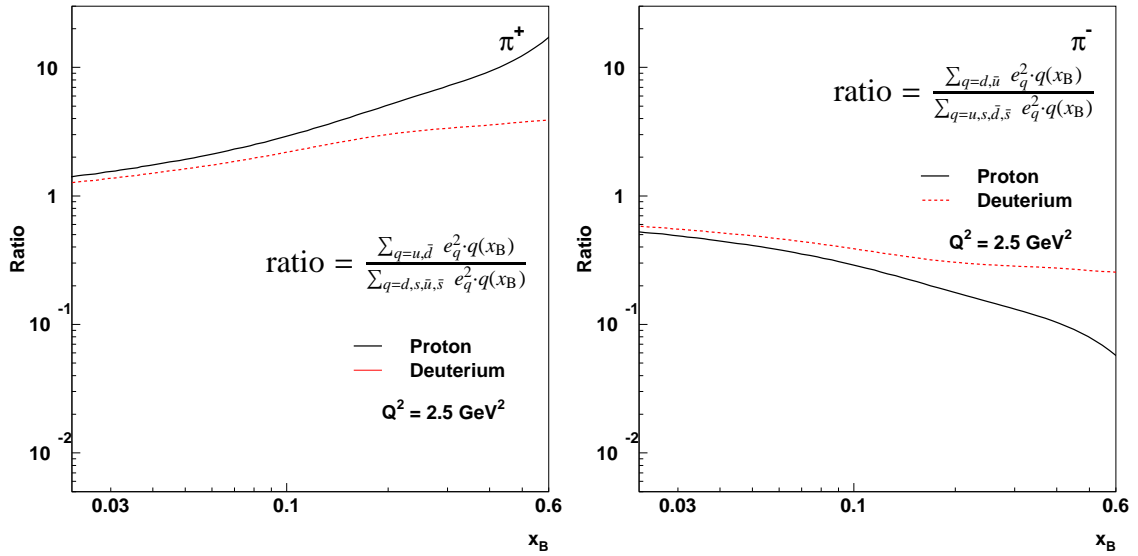


**Figure 6.7**

Enhancement and suppression of favoured fragmentation for  $\pi^+$  and  $\pi^-$  vs.  $x_B$ . The distributions of (anti-)quarks allowing for favoured (unfavoured) fragmentation were added, weighted by the square of their charges. The CTEQ6  $\overline{\text{MS}}$  parametrisation was used.

For negative pions, the EMC data lies systematically below the HERMES results. This is to be expected, since the former represents the unfavoured fragmentation  $u \rightarrow \pi^-$  only, while the multiplicities also include the favoured fragmentation  $d \rightarrow \pi^-$ . Also here, the  $z$  dependence of the corrected multiplicities is in better agreement with EMC than the uncorrected one.

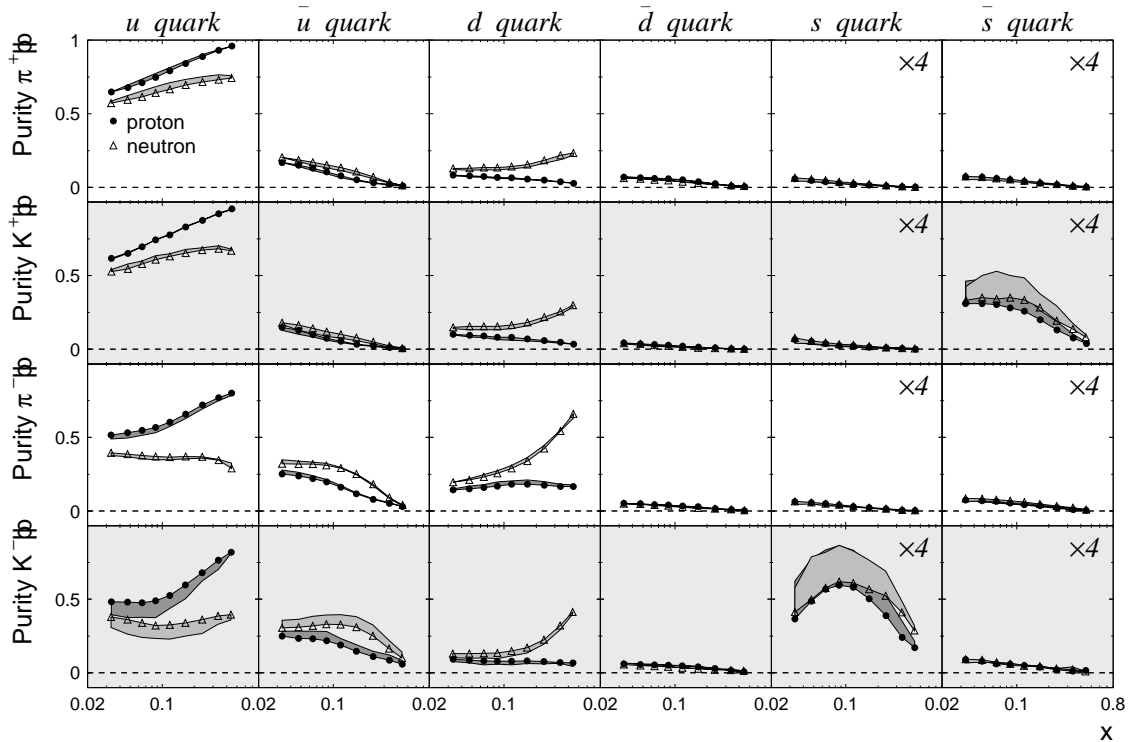
The  $x_B$  dependence of the pion multiplicities is shown in Fig. 6.6. Again the data sets are presented at a common  $Q^2$  of  $2.5 \text{ GeV}^2$  and include the exclusive vector meson correction. The  $\pi^+$  multiplicities (top) exhibit a somewhat stronger  $x_B$  dependence than the  $\pi^-$  (bottom). This behaviour is very similar for the proton and the deuterium data, which differ only in the same fashion as already observed for the  $z$  multiplicities (Fig. 6.2).

The  $x_B$  dependence of the multiplicities is again a test for factorisation, the assumption that the fragmentation of a quark is independent of the initial scattering event it originates from. If factorisation holds, fragmentation functions should not vary with  $x_B$ , since the hadronisation of the struck quark should not be down to the fraction of the nucleon's momentum it initially carried. The multiplicities in Fig. 6.6 show a rather weak  $x_B$  dependence, suggesting that factorisation is a reasonable assumption at HERMES energies. Furthermore,  $x_B$  independence is only expected to hold for quark fragmentation functions. The plotted multiplicities still contain the convolution with the parton distributions inside the nucleon, which of course depend on  $x_B$ . This is illustrated in Figure 6.7 for positive (left) and negative (right) pions: shown is the sum over the quarks allowing for favoured fragmentation divided by the sum over the other quarks which require unfavoured fragmentation to produce the hadron. The ratio was calculated using the CTEQ6

$\overline{\text{MS}}$  parametrisation, weighted with the square of the respective quark charge and taking into account the light quarks ( $u, d, s$ ) and their anti-quarks. For both hadrons, the ratio for a proton and a deutrium target is shown. In the case of  $\pi^+$ , the ratios rise with  $x_B$ , owing to the dominance of the  $u$  quarks. The  $u$  quark dominance also suppresses the ratio for the  $\pi^-$ .

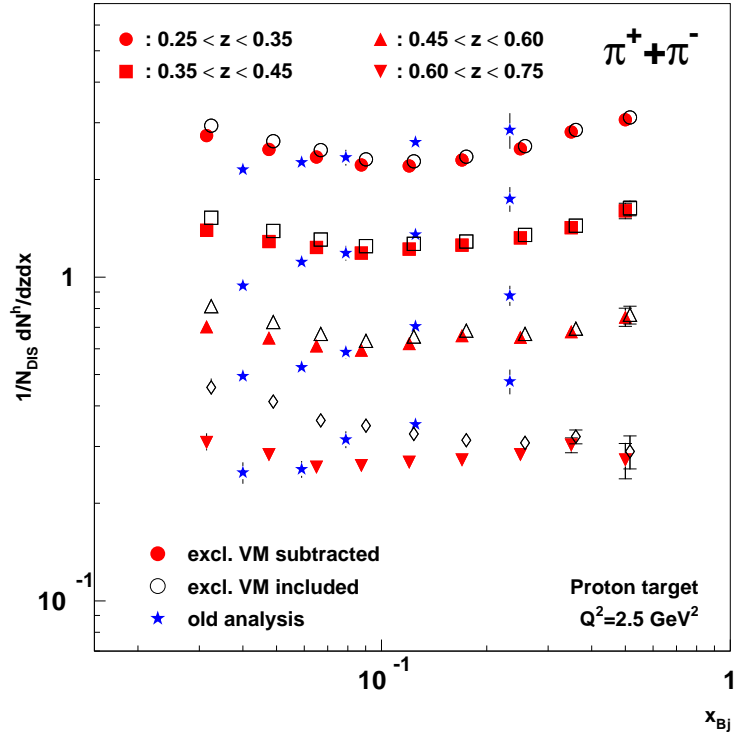
Since the fraction of DIS events allowing for favoured fragmentation is growing with  $x_B$ , it is not surprising that the  $\pi^+$  multiplicities are also increasing. Although the corresponding fraction for negative pions is decreasing with  $x_B$ , the  $\pi^-$  do not decrease at higher  $x_B$ , nevertheless the slope is distinctly smaller compared to  $\pi^+$ . Studies in conjunction with the extraction of the quark helicity distributions [Air05] have shown that  $\pi^-$  production is dominated by the unfavoured  $u$  quark fragmentation: more that 50% of all negative pions originate from scattering events on  $u$  quarks, sharply rising to almost 80% for  $x_B \sim 0.4$  (see Fig. 6.8). This dominance of unfavoured fragmentation seems to cancel the suppression of the scattering on  $d$  and  $\bar{u}$  quarks.

Figure 6.9 compares the new results from the year 2000 data with the previous ana-



**Figure 6.8**

Purities for positive and negative pions as well as positive and negative kaons for scattering on a proton and a free neutron target. The purities give the fraction of scattering events involving a struck quark  $q$  under the condition that a quark  $h$  is produced. The purities were extracted from a Monte Carlo simulation, the shaded bands give the estimated systematic uncertainty based on the use of different fragmentation tunes. This figure was taken from [Air05].



**Figure 6.9**

The sum of the charged pions versus  $x_B$ . The results from the old and new analysis are compared.

lysis of the year 1996/97 data published in [Air01]. The data points represent the sum of charged pions. For the new analysis, the results are given both including exclusive vector mesons and corrected for exclusive vector mesons. Clearly, there is some discrepancy between the two analyses. After first establishing that the multiplicities extracted from the 1996/97 data and the 2000 data agree before applying any corrections<sup>2</sup>, several possible sources for this discrepancy were investigated in [Hil04b]:

- **Different sets of fragmentation parameters were used for the acceptance correction.** While the analysis presented here uses the 2004c set of Lund parameters (see Table 4.1 on page 55), the old analysis relied on an older parameter set (denoted as *Holger tune* in Table 4.1). To investigate the impact of these modifications on the final result, the Monte Carlo tune dependence of the acceptance correction method was studied. The left hand side of Figure 6.10 illustrates the difference between the hadron yields obtained from the parameter sets. The right hand side then shows the corrected *experimental* data, where the correction was performed using the corresponding Monte Carlo production (see Sec. 5.4). Only by using the Jetset default tune (and only for high  $z$ ) a significant deviation can be seen from the result of the other two tunes. But for the two tunes adapted to HERMES ('Holger' and 2004a), the agreement is quite good. In no case does the change of the tune influence the  $x_B$  dependence in a way necessary to explain the differences between

<sup>2</sup>In fact, there are minor momentum-dependent differences related to the different efficiencies of the RICH detector used in 2000 and the threshold Čerenkov detector used in 1996/97. They are, however, insignificant for the problem at hand.



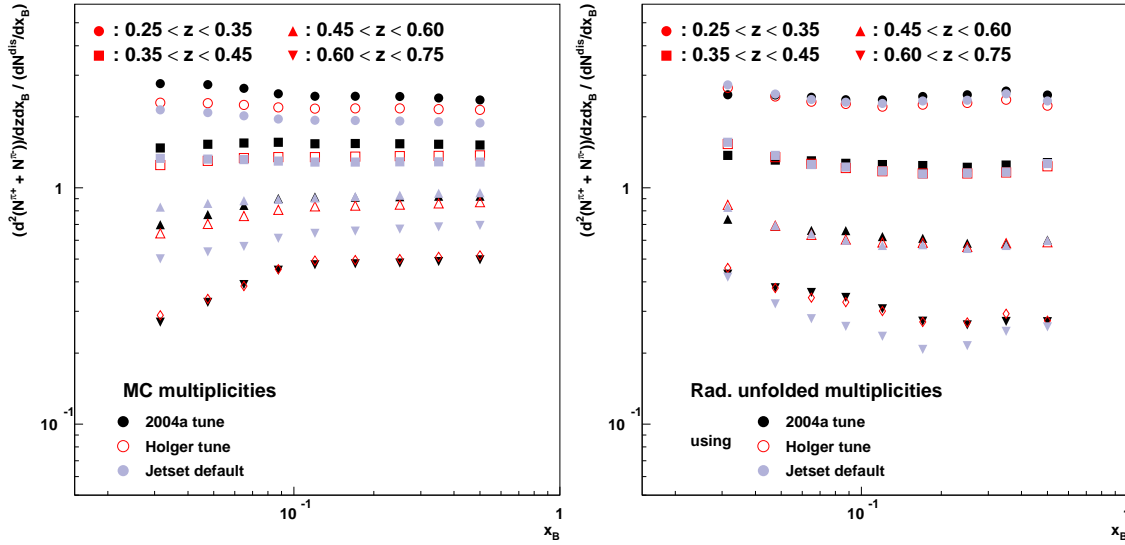


**Figure 6.10**

Independence of the acceptance correction method from the Monte Carlo tune for  $\pi^+ + \pi^-$ . The left plot shows the Monte Carlo multiplicities obtained from three different fragmentation parameter settings. The right hand side shows the acceptance corrected Born multiplicities, as they were obtained by using the corresponding Monte Carlo setting.

the old and the new analysis. It should be noted that the comparison shown here features the 2004a tune used for the multiplicity release in June 2004 instead of 2004c used for the results presented in this work. Nevertheless, the conclusion remains valid, since changing from 2004a to 2004c did not alter the  $x_B$  dependence of the multiplicities (Fig. 6.1).

- **The  $Q^2$  evolution was performed in a different way.** While the correction factors in this analysis were calculated from the full DIS formula (5.33), using parametrisations for the parton distribution functions (CTEQ6 [Pum02]) and fragmentation functions (S. Kretzer [Kre00]), the analysis in [Air01] only used fragmentation function ratios

$$C_{Q^2}(z, Q^2) = \frac{D_u^\pi(z, Q_0^2)}{D_u^\pi(z, Q^2)}, \quad (6.1)$$

with  $Q^2$  being the average value in the respective bin and  $Q_0^2$  ( $=2.5 \text{ GeV}^2$ ) being the target value. For the fragmentation functions, the parametrisation by Kniehl, Kramer and Pötter [Kni00] was used. Figure 6.11a compares the correction factors calculated with Eq. (6.1) using the old (KKP) and new (Kretzer) parametrisations. As can be seen, the new parametrisations should in fact increase the slope with rising  $x_B$ , compared with the old parametrisation. The same observation holds when replacing the old Equation (6.1) with the new Equation (5.33) (Fig. 6.11b).

- **The method for the acceptance correction was changed.** The old analysis used ratios of pion yields within and outside the HERMES acceptance to obtain correction

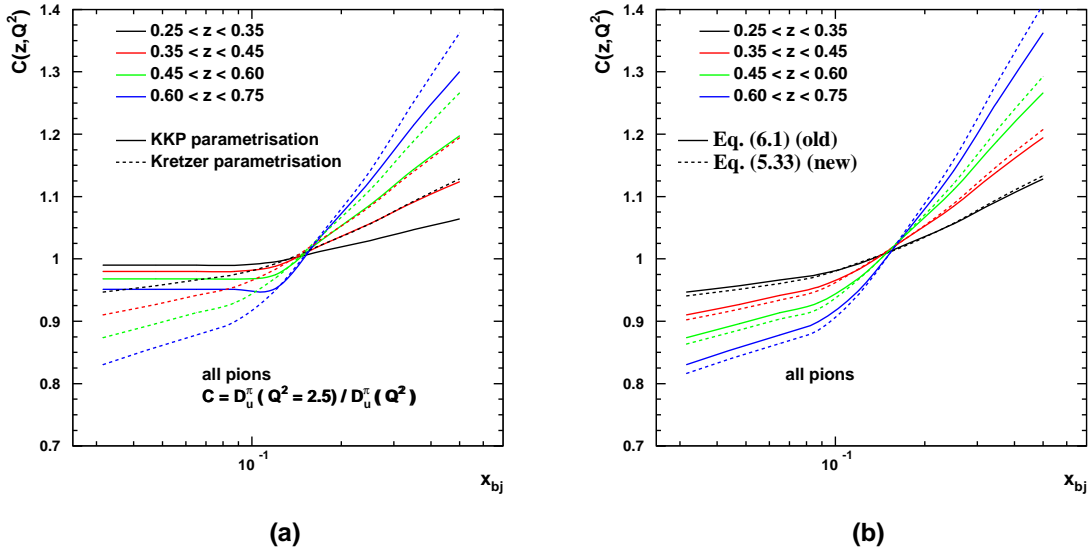


**Figure 6.11**

$Q^2$  evolution factors calculated using different fragmentation function parametrizations (left) and different evolution formula (right). In both cases, the switch from the old analysis method to the new one (FF:KKP  $\rightarrow$  Kretzer; Formula: Eq. (6.1)  $\rightarrow$  Eq. (5.33)) should have rather enhanced the  $x_B$  slope than reduce it.

factors [Bia99]. This method assumes that there is no  $x_B$  dependence of the lepton detection efficiency. However, this is not the case. Figure 6.12 compares acceptance correction factors obtained from ratios of pion yields and ratios of DIS normalised pion multiplicities, respectively<sup>3</sup>. It can be seen that by taking the positron detection efficiency into account, the correction factors are smaller for higher  $x_B$  and larger for low  $x_B$ . The crossing of the two correction factor sets happens in the area of best agreement between old and new results.

In conclusion, the method for acceptance correction is thought to be responsible for a major part of the inconsistencies between the two analyses. In addition, it should be noted that the Monte Carlo programs used for radiative and acceptance correction were heavily modified in the recent years, including numerous bug fixes. This might have had further influences on the result, which can not be specifically accounted for.

The  $Q^2$  dependence of the pion multiplicities is presented in Figure 6.13. The first plot compares the results obtained from the two different targets for  $\pi^+$  and  $\pi^-$  separately. The observed  $Q^2$  dependence is very small as expected from theory. This is demonstrated in Fig. 6.14. Here the multiplicities for the sum of charged pions are compared with the result obtained with the parametrisation by S. Kretzer [Kre05]. While the fragmentation function parametrisation lies generally above the measured multiplicities, the  $Q^2$

<sup>3</sup>In this work, the acceptance correction was performed together with the radiative unfolding by the matrix method described in Sec. 5.4, which takes into account the lepton efficiencies.

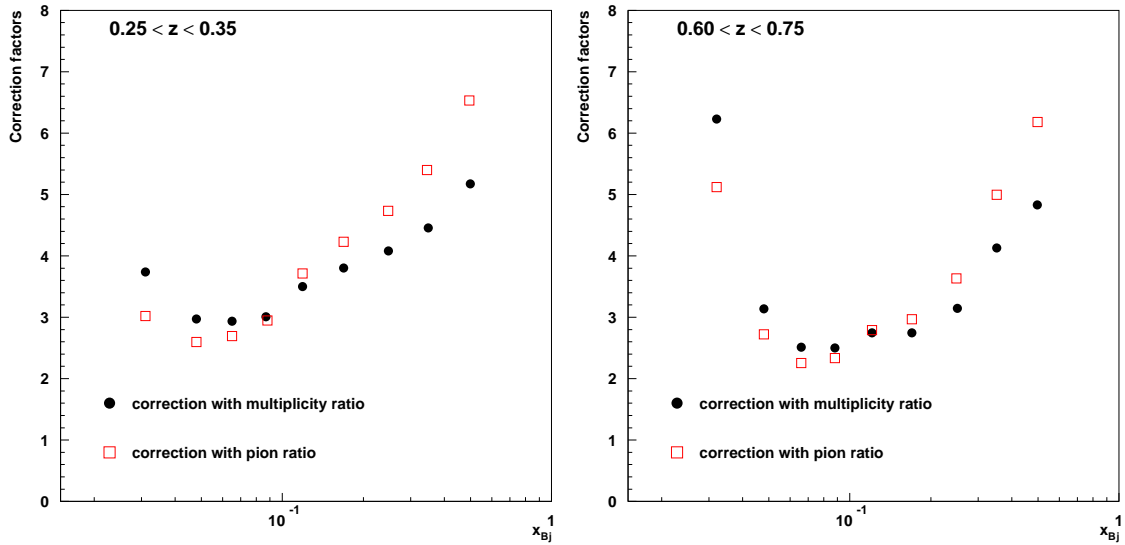


**Figure 6.12**

Acceptance correction factors with (full circles) and without (empty squares) accounting for the scattered lepton detection efficiency. Only taking hadron ratios results in systematically lower (higher) correction factors for small (large)  $x_B$ . Shown are the first and last of the four  $z$  bins.

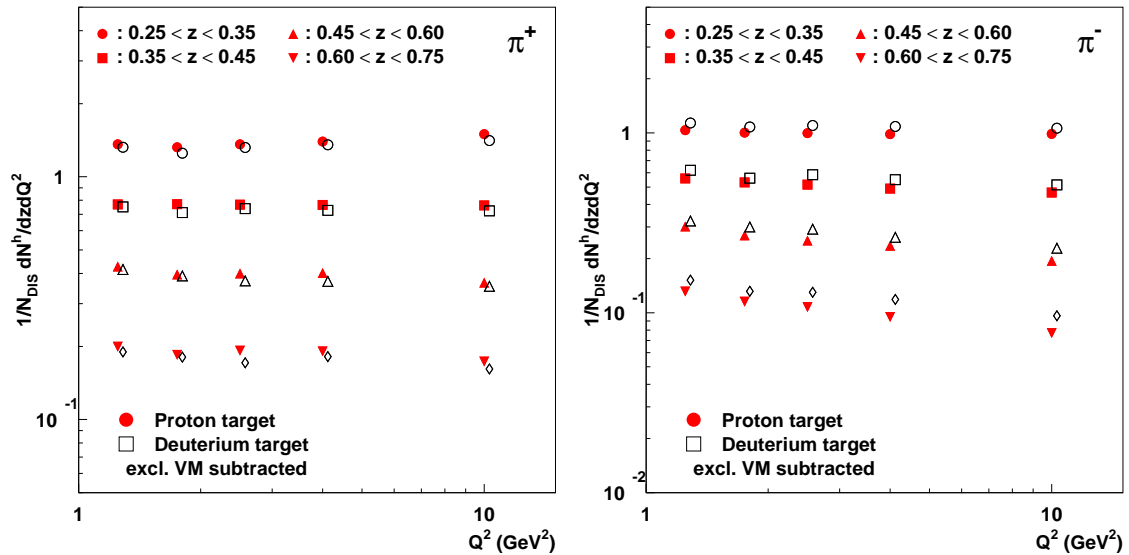


**Figure 6.13**

The pion multiplicities vs.  $Q^2$  in 4  $z$  bins using a proton (filled symbols) and a deuterium target (open symbols).

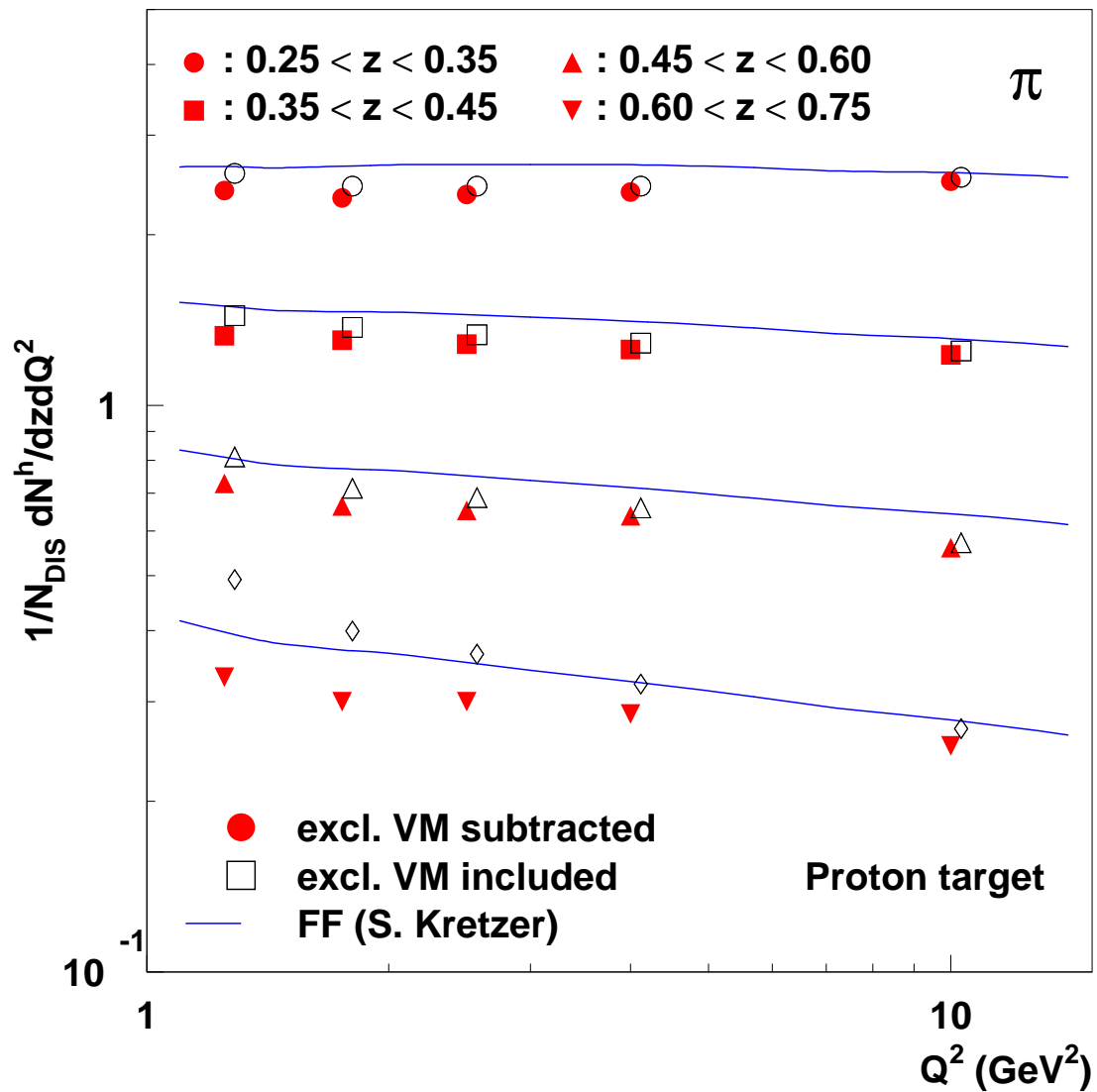


**Figure 6.14**

Comparison of  $(\pi^+ + \pi^-)$  multiplicities vs.  $Q^2$  with a parametrisation by S. Kretzer [Kre05]. The  $Q^2$  dependence is in agreement with the model.

dependence of the experimental data matches the theoretical curves very well. The multiplicities generally show a very weak  $Q^2$  dependence, which is becoming larger with increasing  $z$ . This is consistent with results from E665 [Ada97].

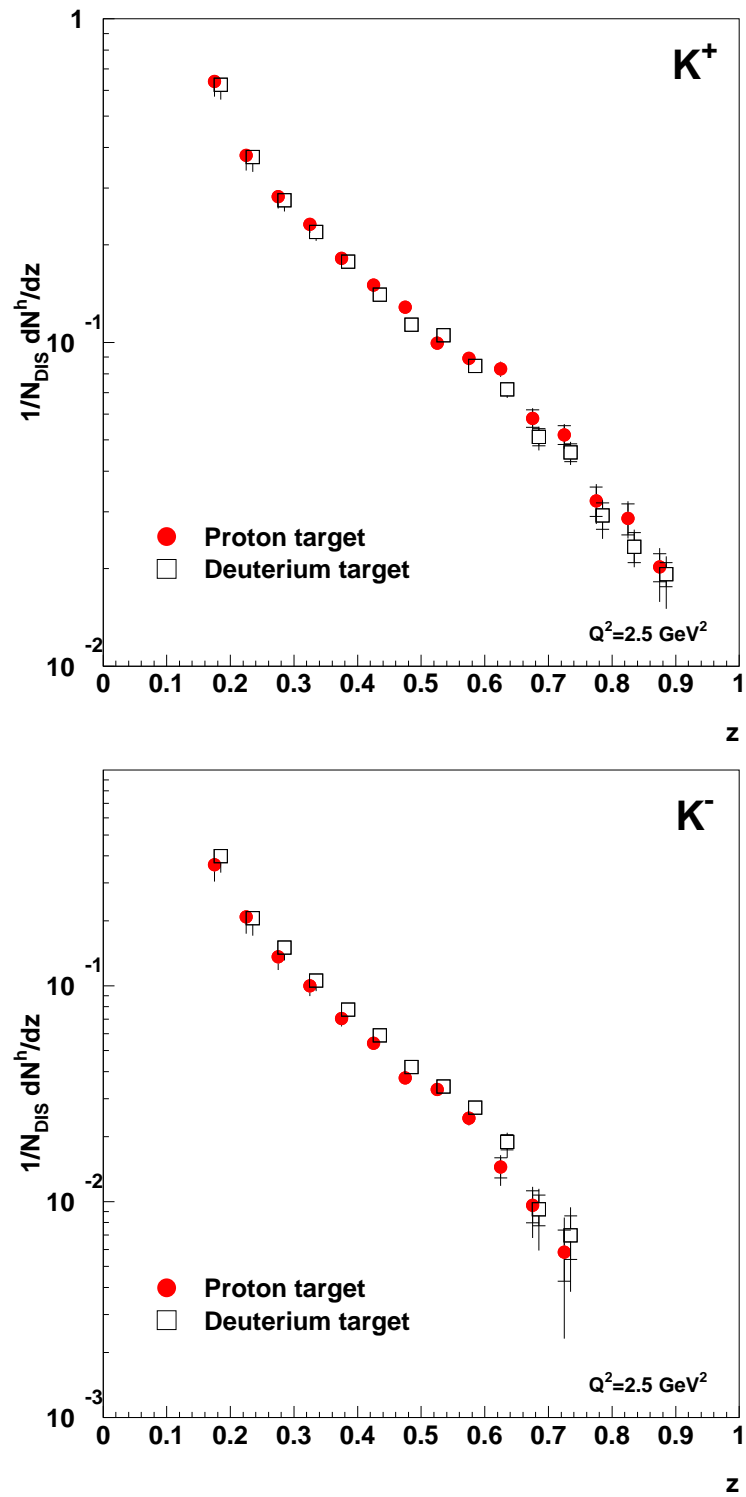
## 6.2 Kaon Results

In addition to the pion multiplicities, also kaon multiplicities have been extracted versus  $z$ ,  $x_B$  and  $Q^2$ . The available statistics for the positive and negative charges differs much more dramatically than it is the case for pions. This is due to the fact that for  $K^-$  (valence quark composition:  $s\bar{u}$ ) favoured fragmentation is only possible for scattering on nucleon sea quarks, while the dominant valence quarks only allow for unfavoured fragmentation. For  $K^+$  ( $u\bar{s}$ ), these restrictions do not apply, causing a  $K^+ : K^-$  ratio of about 72:28 for a proton target (compared to 58:42 for  $\pi^+ : \pi^-$ ).

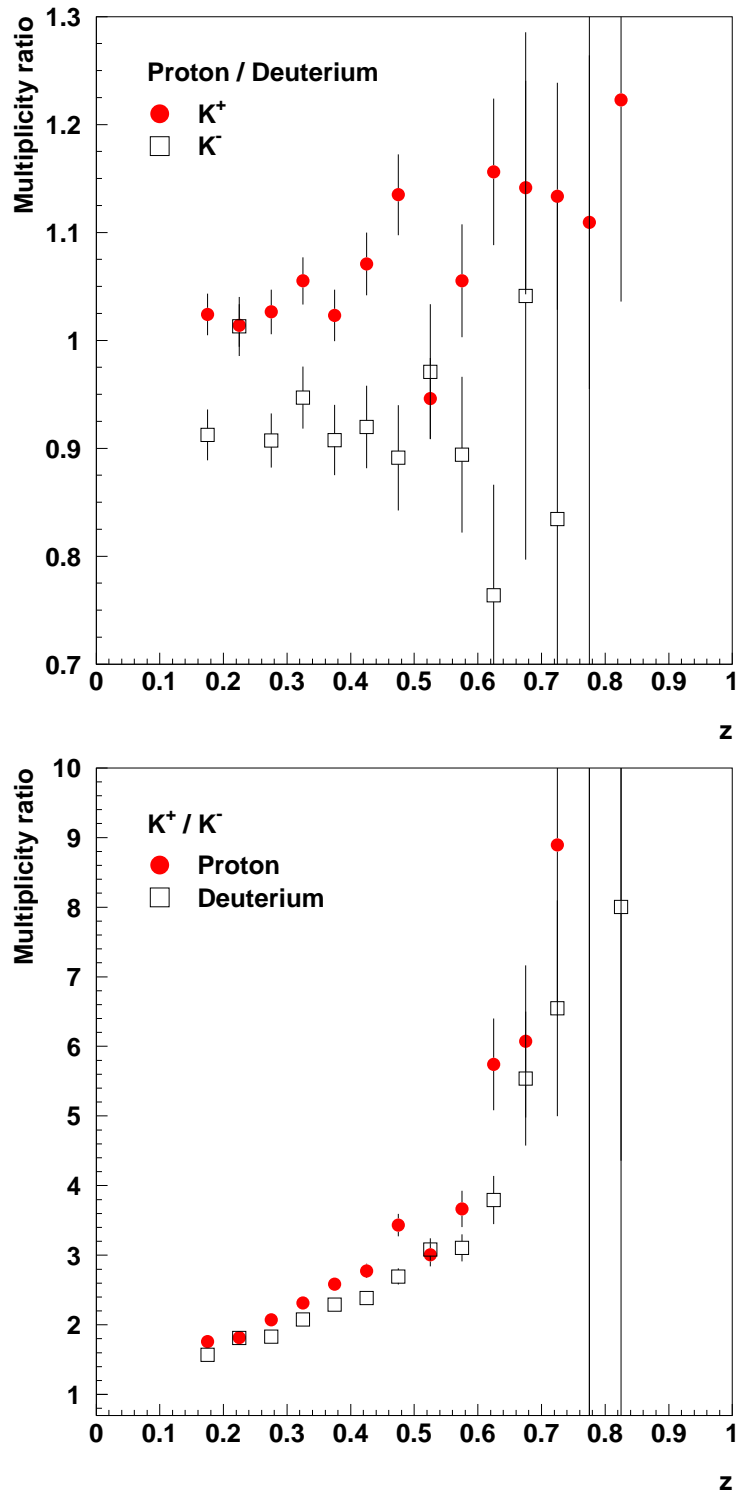
Figure 6.15 shows the kaon multiplicities versus  $z$  for both the proton and deuterium target. At high  $z$  ( $> 0.85$ ), no meaningful  $K^-$  result could be obtained. In this region, the RICH unfolded  $K^-$  multiplicities in fact become negative. This indicates that the current  $\mathcal{P}$  matrices overestimate the misidentifications from pions as kaons. The unfolding of the RICH errors then leads to an increase of the pion yields at the expense of the kaon multiplicities. Since the hadron flux in the high  $z$  domain is so severely dominated by pions ( $\approx 95\%$  of all negative hadrons are  $\pi^-$  for  $z > 0.75$ , Fig. 5.4), even small errors have a dramatic impact on the kaons.

To compare the multiplicities for the two charges and the two targets, the multiplicity ratios of the different targets (top) and the charges (bottom) are plotted in Fig. 6.16. As was the case for the pions, the  $K^+$  multiplicity is larger for the proton target. The ratio of  $K^+$  from proton to  $K^+$  from deuterium seems to rise with larger  $z$ , although a conclusive assessment is difficult due to the large statistical uncertainties. Very striking, on the other hand, is the strong rise of the charge ratio  $K^+/K^-$  with  $z$  for both targets. The slope is substantially larger than in the case of pions (Fig. 6.3). This is in line with the expectation that favoured fragmentation plays a much smaller role for  $K^-$ , since its valence quark content only permits favoured fragmentation from sea quarks.

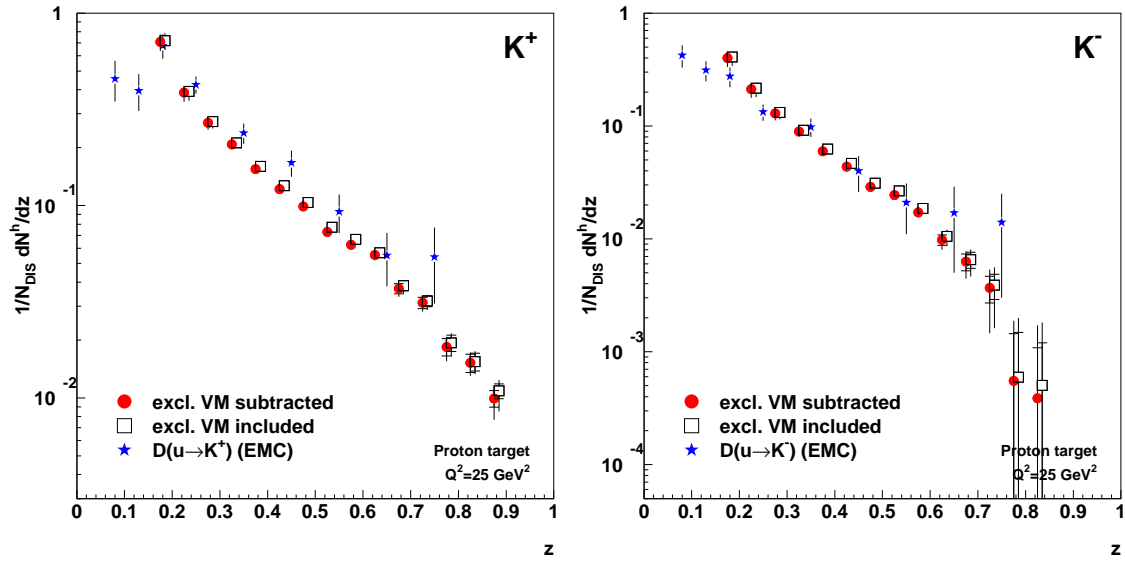
In Fig. 6.17, the kaon multiplicities are compared to fragmentation functions obtained by EMC from muon-proton scattering at a beam energy of 280 GeV [Arn89]. As in Fig. 6.5, the HERMES data was evolved to a common  $Q^2$  of 25 GeV<sup>2</sup> for this purpose. Again, the HERMES results feature a dramatically improved statistical accuracy. For  $K^+$ , the multiplicity lies below the EMC fragmentation function  $D_u^{K^+}$ . This can be attributed again to unfavoured contributions to the kaon production, which reduces the average number of  $K^+$  produced per struck quark compared to the favoured fragmentation  $u \rightarrow K^+$ . On the other hand, the two data sets for negative kaons agree very well within errors. The HERMES multiplicities can be expected to contain very small contributions of favoured  $s$  and  $\bar{u}$  fragmentation — in fact, the purities extracted for the  $\Delta q$  analysis suggest that  $u$  quark fragmentation plays the dominant role in  $K^-$  production [Air05] (Fig. 6.8). This is consistent with the much better agreement with the unfavoured  $D_u^{K^-}$  fragmentation function.

**Figure 6.15**

The kaon multiplicities vs.  $z$  using a proton (filled symbols) and a deuterium target (open symbols).

**Figure 6.16**

Target (top) and charge (bottom) ratios of kaon multiplicities vs.  $z$ . The errors are statistical only.

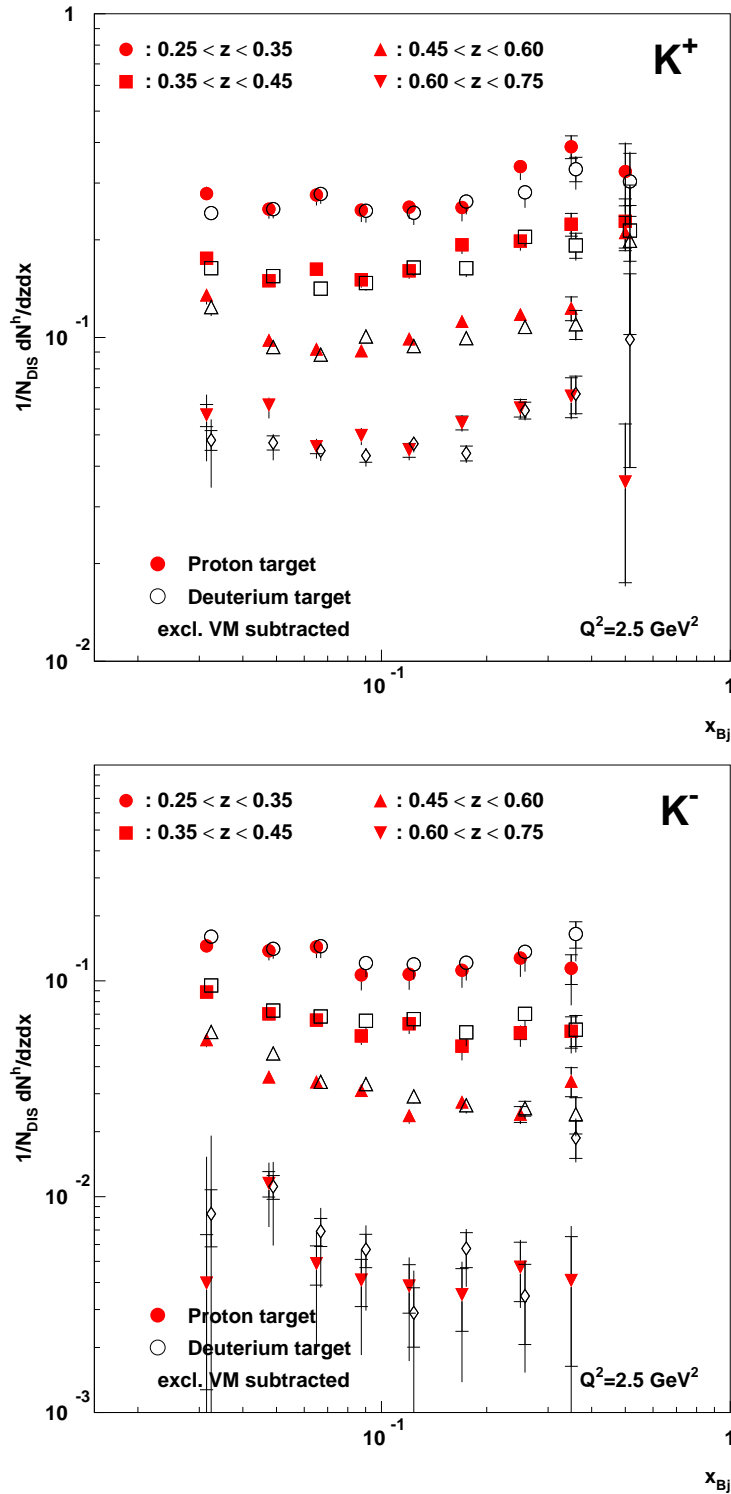


**Figure 6.17**

The kaon multiplicities vs.  $z$  using a proton target. The filled symbols have been corrected for contributions from exclusive  $\phi$  production, the open symbols show the data without the correction. The HERMES data is compared to  $D_u^{K^+}$  and  $D_u^{K^-}$  fragmentation functions from EMC published in [Arn89] (stars). For this purpose, it has been evolved to a common  $Q^2$  of  $25 \text{ GeV}^2$ .

Figures 6.18 and 6.20 show the kaon multiplicities in the usual 4  $z$  bins as a function of  $x_B$  and  $Q^2$ , respectively. The  $Q^2$  dependence seems to be much weaker than it is the case for pions. Versus  $x_B$ , the slope for  $K^+$  is comparable to the positive pions (Fig. 6.6). The  $K^-$  multiplicities, however, decrease with larger  $x_B$ , a tendency which becomes more pronounced in the higher  $z$  bins. A possible explanation for this different behaviour is shown in Fig. 6.19. Similar to the pion case in Fig. 6.7, the sum of the parton distributions of (anti-)quarks allowing for favoured (unfavoured) fragmentation is calculated, taking the quark charges into account. Dividing these quantities then gives a probability ratio signifying how likely a scattering event allows for favoured fragmentation in relation to unfavoured fragmentation. For positive kaons (left), the ratios are very similar to the case of  $\pi^+$ , since both are dominated by the  $u$  quarks. In the case of  $K^-$  (right), however, the suppression of favoured fragmentation at high  $x_B$  becomes quite dramatic. While the ratios vary by about an order of magnitude for  $\pi^\pm$  and  $K^+$ , the  $K^-$  ratio falls by two orders of magnitude. It is thus not surprising that the corresponding multiplicities drop with  $x_B$ , especially in the higher  $z$  region which is more dominated by favoured fragmentation.



**Figure 6.18**

The kaon multiplicities vs.  $x_B$  in 4  $z$  bins using a proton (filled symbols) and a deuterium target (open symbols).

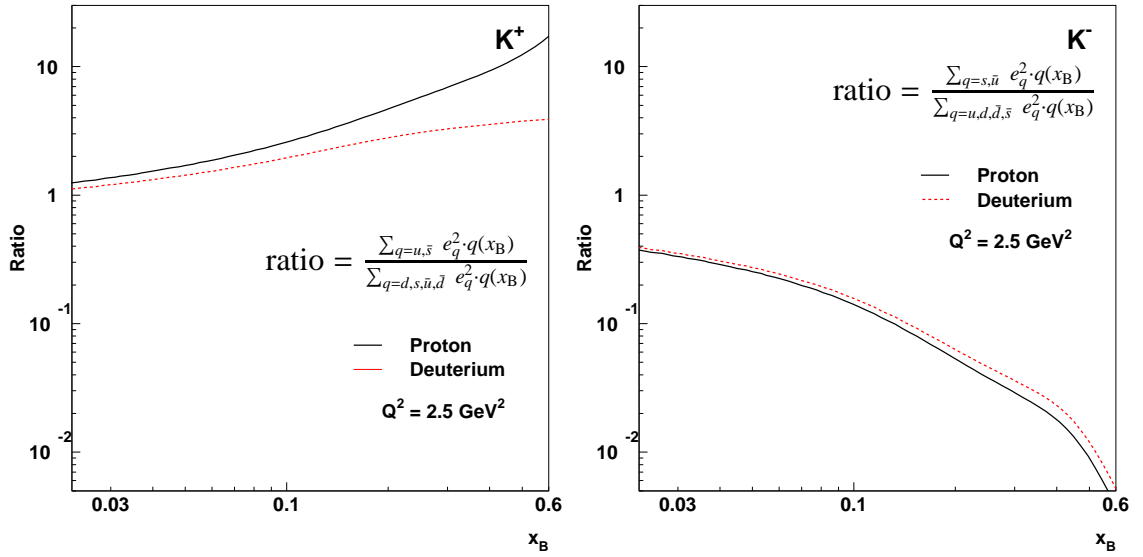


Figure 6.19

Enhancement and suppression of favoured fragmentation for  $K^+$  and  $K^-$  vs.  $x_B$ . The distributions of (anti-)quarks allowing for favoured (unfavoured) fragmentation were added, weighted by the square of their charges. The CTEQ6  $\overline{\text{MS}}$  parametrisation was used.

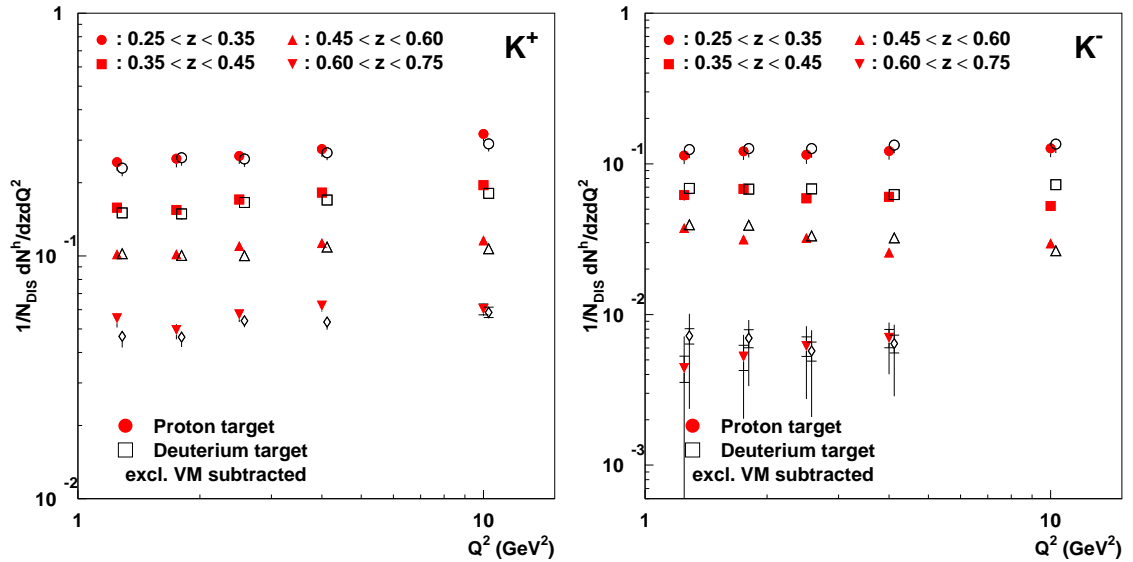


Figure 6.20

The kaon multiplicities vs.  $Q^2$  in 4  $z$  bins using a proton (filled symbols) and a deuterium target (open symbols).

# Chapter 7

## Conclusion

This work has been concerned with the fragmentation process at HERMES. It can be split into two major parts: the Monte Carlo simulation of hadronisation and the extraction of charge and hadron type separated Born multiplicities.

In the Monte Carlo part, the Lund model has been adjusted to reproduce experimental hadron spectra observed with the HERMES experiment. In contrast to earlier tuning efforts, this work for the first time made use of the RICH detector introduced in the year 1998, permitting a clean separation of pions, kaons and protons. This additional information allowed for a more detailed fitting of the model parameters, some of which were not accessible previously. The iterative fitting of the model parameters also took advantage of a new tuning algorithm, which allowed to harness the computing power available with the HERMES PC farm. In the course of the tuning efforts, the HERMES smearing generator (HSG) was implemented, an application which is able to simulate the smearing and loss effects caused by the HERMES detector by applying corrections on a statistical basis. The program allows for Monte Carlo studies to take into account detector effects, while being a factor of  $\sim 100$  faster than a full detector simulation. HSG is indispensable for the tuning of the fragmentation model, but has also been used by various other Monte Carlo projects in the collaboration.

The tuning efforts resulted in a very much advanced parameter set, with drastical improvements especially in the reproduction of the (anti-)proton multiplicities. Open issues remain regarding the simultaneously satisfying description of the  $K^+$  and  $K^-$  multiplicities.

The second part of this work was concerned with the extraction of Born multiplicities for pions and kaons. Pion multiplicities from  $e^+p$  scattering have already been published before [Air01]. In this work the year 2000 data was used, providing higher statistics and improved particle identification due to the RICH detector. In addition, the proton data was complemented by an analysis of data taken with a deuterium target. Furthermore, the analysis was extended in various ways. For example the contribution of exclusive vector mesons to the hadron sample has been accounted for, which dilute the hadrons produced by deep-inelastic scattering. With respect to the old multiplicity analysis, a new method for the correction of radiative and acceptance effects was used.

The extracted multiplicities provide a high statistics data set for  $\pi^+$ ,  $\pi^-$ ,  $K^+$  and  $K^-$ ,

obtained both from a proton and a deuterium target. They will form the basis for the extraction of fragmentation functions and will thus allow to test the universality of the fragmentation process. The multiplicities versus  $z$  show a reasonably good agreement with fragmentation functions by EMC, which were measured at a ten times higher beam energy. The  $Q^2$  dependence of the pion data is in line with QCD expectations. Together with the weak  $x_B$  dependence, the results show that the assumption of factorisation, which is fundamental to the extraction of the quark helicity distributions [Air05], is well justified.

# Appendix A

## Tables: Multiplicities vs. $z$

In this section, the final multiplicities as a function of  $z$  are tabulated. Table A.1 defines the bin numbers used in Tables A.2 to A.13. The results for the proton and the deuterium target are always given on one page. First the results evolved to  $Q^2 = 2.5 \text{ GeV}^2$  are given, where the data corrected for the contribution of exclusive vector mesons precede the uncorrected data. This is followed by the results for  $Q^2 = 25 \text{ GeV}^2$ , in this case only for the proton target (the results with and without vector meson correction are given on one page).

Bin	min	max
1	0.150	0.200
2	0.200	0.250
3	0.250	0.300
4	0.300	0.350
5	0.350	0.400
6	0.400	0.450
7	0.450	0.500
8	0.500	0.550
9	0.550	0.600
10	0.600	0.650
11	0.650	0.700
12	0.700	0.750
13	0.750	0.800
14	0.800	0.850
15	0.850	0.900

The column *mult* gives the multiplicity value,  $\sigma_{\text{stat}}$  the statistical error.  $\sigma_{\text{RICH}}$  represents the syst. error from RICH unfolding,  $\sigma_{\text{MC}}$  the syst. error from the correction for radiative and detector effects.  $\sigma_{\text{evol}}$ , gives the systematic uncertainty from  $Q^2$  evolution.

**Table A.1**  
Binning versus  $z$

$\pi^+$ 

**Target: Proton**  
(*excl. VM subtracted*)

 $Q^2 = 2.5 \text{ GeV}^2$ 

Bin	mult	$\sigma_{\text{stat}}$	$\sigma_{\text{RICH}}$	$\sigma_{\text{MC}}$	$\sigma_{\text{evol}}$
1	3.02701	0.01222	+0.07326 -0.00000	0.00993	+0.00132 -0.00012
2	2.13312	0.00892	+0.04080 -0.00520	0.00807	+0.00009 -0.00002
3	1.56293	0.00736	+0.02097 -0.00494	0.00707	+0.00004 -0.00011
4	1.16725	0.00646	+0.00988 -0.00416	0.00636	+0.00002 -0.00001
5	0.87276	0.00584	+0.00450 -0.00300	0.00576	+0.00000 -0.00000
6	0.65989	0.00541	+0.00146 -0.00240	0.00521	+0.00002 -0.00003
7	0.50582	0.00513	+0.00000 -0.00160	0.00487	+0.00002 -0.00007
8	0.38966	0.00503	+0.00001 -0.00128	0.00461	+0.00002 -0.00006
9	0.32043	0.00508	+0.00023 -0.00091	0.00454	+0.00003 -0.00012
10	0.23887	0.00524	+0.00131 -0.00124	0.00450	+0.00002 -0.00011
11	0.21892	0.00571	+0.00270 -0.00200	0.00471	+0.00001 -0.00014
12	0.16280	0.00619	+0.00241 -0.00188	0.00476	+0.00001 -0.00014
13	0.12421	0.00674	+0.00263 -0.00171	0.00485	+0.00000 -0.00014
14	0.07995	0.00676	+0.00056 -0.00057	0.00465	+0.00000 -0.00009
15	0.06576	0.00480	+0.00282 -0.00203	0.00326	+0.00000 -0.00006

Table A.2

 $\pi^+$ 

**Target: Deuterium**  
(*excl. VM subtracted*)

 $Q^2 = 2.5 \text{ GeV}^2$ 

Bin	mult	$\sigma_{\text{stat}}$	$\sigma_{\text{RICH}}$	$\sigma_{\text{MC}}$	$\sigma_{\text{evol}}$
1	2.94858	0.01113	+0.07228 -0.00000	0.00970	+0.00597 -0.00037
2	2.07807	0.00815	+0.03954 -0.00518	0.00792	+0.00268 -0.00032
3	1.49781	0.00671	+0.01972 -0.00486	0.00685	+0.00127 -0.00029
4	1.11943	0.00587	+0.00956 -0.00408	0.00618	+0.00058 -0.00026
5	0.82861	0.00524	+0.00434 -0.00293	0.00552	+0.00030 -0.00025
6	0.62918	0.00496	+0.00121 -0.00241	0.00508	+0.00017 -0.00027
7	0.48236	0.00471	+0.00004 -0.00149	0.00474	+0.00012 -0.00026
8	0.37607	0.00462	+0.00000 -0.00115	0.00449	+0.00008 -0.00024
9	0.29300	0.00465	+0.00019 -0.00093	0.00436	+0.00008 -0.00024
10	0.24857	0.00487	+0.00171 -0.00143	0.00442	+0.00006 -0.00025
11	0.19071	0.00522	+0.00244 -0.00171	0.00445	+0.00003 -0.00024
12	0.15151	0.00580	+0.00201 -0.00171	0.00460	+0.00001 -0.00022
13	0.10953	0.00615	+0.00224 -0.00157	0.00458	+0.00000 -0.00019
14	0.06699	0.00575	+0.00093 -0.00062	0.00409	+0.00000 -0.00012
15	0.06443	0.00407	+0.00248 -0.00184	0.00286	+0.00000 -0.00013

$\pi^-$  Target: Proton  $Q^2 = 2.5 \text{ GeV}^2$   
(excl. VM subtracted)

Bin	mult	$\sigma_{\text{stat}}$	$\sigma_{\text{RICH}}$	$\sigma_{\text{MC}}$	$\sigma_{\text{evol}}$
1	2.42483	0.01080	+0.05701 -0.00284	0.00869	+0.00371 -0.00000
2	1.69087	0.00785	+0.03191 -0.00572	0.00705	+0.00185 -0.00000
3	1.16385	0.00628	+0.01581 -0.00458	0.00591	+0.00097 -0.00000
4	0.84561	0.00540	+0.00800 -0.00314	0.00518	+0.00059 -0.00000
5	0.60182	0.00481	+0.00377 -0.00206	0.00459	+0.00039 -0.00000
6	0.44347	0.00439	+0.00117 -0.00145	0.00414	+0.00032 -0.00000
7	0.33370	0.00418	+0.00029 -0.00082	0.00388	+0.00033 -0.00000
8	0.25635	0.00405	+0.00018 -0.00080	0.00368	+0.00029 -0.00000
9	0.19677	0.00397	+0.00073 -0.00061	0.00352	+0.00033 -0.00000
10	0.15299	0.00407	+0.00182 -0.00131	0.00348	+0.00033 -0.00000
11	0.11365	0.00422	+0.00204 -0.00151	0.00340	+0.00028 -0.00000
12	0.08634	0.00448	+0.00211 -0.00154	0.00334	+0.00029 -0.00001
13	0.06420	0.00522	+0.00184 -0.00125	0.00355	+0.00024 -0.00002
14	0.04625	0.00516	+0.00117 -0.00086	0.00324	+0.00016 -0.00003
15	0.02808	0.00387	+0.00183 -0.00131	0.00226	+0.00011 -0.00002

$\pi^-$  Target: Deuterium  $Q^2 = 2.5 \text{ GeV}^2$   
(excl. VM subtracted)

Bin	mult	$\sigma_{\text{stat}}$	$\sigma_{\text{RICH}}$	$\sigma_{\text{MC}}$	$\sigma_{\text{evol}}$
1	2.66967	0.01061	+0.06215 -0.00339	0.00936	+0.00926 -0.00000
2	1.82696	0.00756	+0.03441 -0.00644	0.00744	+0.00421 -0.00000
3	1.26842	0.00609	+0.01718 -0.00491	0.00628	+0.00201 -0.00000
4	0.92162	0.00527	+0.00860 -0.00344	0.00554	+0.00099 -0.00000
5	0.66081	0.00469	+0.00391 -0.00223	0.00491	+0.00057 -0.00000
6	0.48943	0.00425	+0.00138 -0.00156	0.00441	+0.00035 -0.00000
7	0.37761	0.00398	+0.00034 -0.00094	0.00408	+0.00032 -0.00000
8	0.28032	0.00387	+0.00011 -0.00072	0.00387	+0.00027 -0.00000
9	0.21618	0.00392	+0.00061 -0.00075	0.00383	+0.00026 -0.00000
10	0.17805	0.00413	+0.00242 -0.00157	0.00392	+0.00024 -0.00000
11	0.13292	0.00430	+0.00246 -0.00179	0.00384	+0.00019 -0.00000
12	0.10240	0.00452	+0.00233 -0.00169	0.00373	+0.00019 -0.00001
13	0.07601	0.00473	+0.00229 -0.00158	0.00356	+0.00016 -0.00003
14	0.05178	0.00503	+0.00121 -0.00083	0.00340	+0.00012 -0.00003
15	0.03510	0.00362	+0.00206 -0.00146	0.00230	+0.00007 -0.00003

Table A.3

$K^+$ 

Target: Proton

 $Q^2 = 2.5 \text{ GeV}^2$ *(excl. VM subtracted)*

Bin	mult	$\sigma_{\text{stat}}$	$\sigma_{\text{RICH}}$	$\sigma_{\text{MC}}$	$\sigma_{\text{evol}}$
1	0.63996	0.00878	+0.00000 -0.06513	0.00542	+0.00077 -0.00004
2	0.37845	0.00539	+0.00287 -0.03856	0.00358	+0.00006 -0.00000
3	0.28213	0.00415	+0.00461 -0.02212	0.00305	+0.00002 -0.00011
4	0.23129	0.00344	+0.00362 -0.01296	0.00279	+0.00002 -0.00007
5	0.18174	0.00309	+0.00273 -0.00754	0.00258	+0.00001 -0.00003
6	0.15028	0.00291	+0.00206 -0.00369	0.00243	+0.00001 -0.00001
7	0.12858	0.00297	+0.00000 -0.00110	0.00236	+0.00001 -0.00000
8	0.09944	0.00294	+0.00000 -0.00136	0.00222	+0.00001 -0.00000
9	0.08919	0.00322	+0.00000 -0.00117	0.00237	+0.00000 -0.00000
10	0.08285	0.00352	+0.00000 -0.00156	0.00249	+0.00000 -0.00000
11	0.05826	0.00357	+0.00058 -0.00269	0.00236	+0.00000 -0.00002
12	0.05183	0.00349	+0.00035 -0.00256	0.00227	+0.00000 -0.00000
13	0.03238	0.00335	+0.00087 -0.00283	0.00214	+0.00000 -0.00000
14	0.02857	0.00313	+0.00000 -0.00069	0.00207	+0.00000 -0.00000
15	0.02023	0.00199	+0.00161 -0.00372	0.00136	+0.00002 -0.00001

Table A.4

 $K^+$ 

Target: Deuterium

 $Q^2 = 2.5 \text{ GeV}^2$ *(excl. VM subtracted)*

Bin	mult	$\sigma_{\text{stat}}$	$\sigma_{\text{RICH}}$	$\sigma_{\text{MC}}$	$\sigma_{\text{evol}}$
1	0.62493	0.00805	+0.00000 -0.06219	0.00529	+0.00209 -0.00005
2	0.37328	0.00495	+0.00267 -0.03691	0.00353	+0.00061 -0.00002
3	0.27489	0.00374	+0.00436 -0.02061	0.00294	+0.00024 -0.00002
4	0.21921	0.00316	+0.00357 -0.01249	0.00270	+0.00012 -0.00001
5	0.17764	0.00284	+0.00292 -0.00715	0.00249	+0.00005 -0.00001
6	0.14032	0.00266	+0.00211 -0.00328	0.00229	+0.00002 -0.00001
7	0.11330	0.00268	+0.00010 -0.00196	0.00221	+0.00000 -0.00002
8	0.10510	0.00277	+0.00000 -0.00129	0.00224	+0.00001 -0.00005
9	0.08453	0.00286	+0.00000 -0.00108	0.00220	+0.00001 -0.00004
10	0.07165	0.00290	+0.00000 -0.00236	0.00213	+0.00001 -0.00006
11	0.05104	0.00313	+0.00026 -0.00263	0.00216	+0.00001 -0.00007
12	0.04572	0.00292	+0.00040 -0.00176	0.00198	+0.00001 -0.00005
13	0.02919	0.00272	+0.00084 -0.00306	0.00181	+0.00001 -0.00004
14	0.02337	0.00248	+0.00000 -0.00090	0.00177	+0.00001 -0.00003
15	0.01924	0.00164	+0.00160 -0.00369	0.00122	+0.00001 -0.00002



$K^-$ **Target: Proton** $Q^2 = 2.5 \text{ GeV}^2$ *(excl. VM subtracted)*

Bin	mult	$\sigma_{\text{stat}}$	$\sigma_{\text{RICH}}$	$\sigma_{\text{MC}}$	$\sigma_{\text{evol}}$
1	0.36328	0.00706	+0.00000 -0.05927	0.00353	+0.00030 -0.00000
2	0.20847	0.00409	+0.00161 -0.03370	0.00232	+0.00026 -0.00000
3	0.13626	0.00281	+0.00217 -0.01765	0.00178	+0.00018 -0.00000
4	0.09992	0.00224	+0.00203 -0.00992	0.00154	+0.00018 -0.00000
5	0.07036	0.00190	+0.00113 -0.00508	0.00130	+0.00014 -0.00000
6	0.05413	0.00166	+0.00043 -0.00192	0.00113	+0.00011 -0.00000
7	0.03746	0.00153	+0.00000 -0.00093	0.00098	+0.00008 -0.00001
8	0.03309	0.00153	+0.00000 -0.00037	0.00099	+0.00011 -0.00003
9	0.02433	0.00148	+0.00000 -0.00068	0.00087	+0.00010 -0.00004
10	0.01443	0.00154	+0.00094 -0.00196	0.00081	+0.00010 -0.00004
11	0.00960	0.00162	+0.00118 -0.00219	0.00069	+0.00009 -0.00004
12	0.00583	0.00156	+0.00198 -0.00309	0.00061	+0.00006 -0.00003
13	0.00090	0.00146	+0.00151 -0.00267	0.00056	+0.00001 -0.00001
14	0.00066	0.00118	+0.00185 -0.00260	0.00055	+0.00001 -0.00001
15	-0.00313	0.00062	+0.00178 -0.00265	0.00038	+0.00005 -0.00002

Table A.5

 $K^-$ **Target: Deuterium** $Q^2 = 2.5 \text{ GeV}^2$ *(excl. VM subtracted)*

Bin	mult	$\sigma_{\text{stat}}$	$\sigma_{\text{RICH}}$	$\sigma_{\text{MC}}$	$\sigma_{\text{evol}}$
1	0.39816	0.00678	+0.00000 -0.06396	0.00380	+0.00128 -0.00000
2	0.20581	0.00385	+0.00132 -0.03504	0.00233	+0.00066 -0.00000
3	0.15020	0.00275	+0.00255 -0.01891	0.00193	+0.00048 -0.00000
4	0.10552	0.00215	+0.00201 -0.01089	0.00160	+0.00029 -0.00000
5	0.07752	0.00184	+0.00127 -0.00556	0.00140	+0.00020 -0.00000
6	0.05885	0.00167	+0.00055 -0.00200	0.00125	+0.00014 -0.00000
7	0.04203	0.00153	+0.00000 -0.00089	0.00107	+0.00012 -0.00001
8	0.03408	0.00153	+0.00000 -0.00060	0.00103	+0.00013 -0.00004
9	0.02722	0.00145	+0.00000 -0.00064	0.00094	+0.00015 -0.00006
10	0.01889	0.00153	+0.00084 -0.00237	0.00084	+0.00015 -0.00007
11	0.00922	0.00150	+0.00151 -0.00284	0.00070	+0.00010 -0.00005
12	0.00698	0.00159	+0.00169 -0.00264	0.00068	+0.00009 -0.00004
13	-0.00014	0.00156	+0.00255 -0.00407	0.00069	+0.00000 -0.00000
14	0.00292	0.00129	+0.00084 -0.00147	0.00072	+0.00005 -0.00002
15	-0.00411	0.00072	+0.00261 -0.00382	0.00049	+0.00008 -0.00004

$\pi^+$ 

**Target: Proton**  
(*excl. VM included*)

 $Q^2 = 2.5 \text{ GeV}^2$ 

Bin	mult	$\sigma_{\text{stat}}$	$\sigma_{\text{RICH}}$	$\sigma_{\text{MC}}$	$\sigma_{\text{evol}}$
1	3.13917	0.01214	+0.07575 -0.00000	0.01028	+0.00137 -0.00013
2	2.21413	0.00885	+0.04227 -0.00539	0.00837	+0.00009 -0.00002
3	1.62343	0.00730	+0.02175 -0.00512	0.00733	+0.00004 -0.00012
4	1.21479	0.00641	+0.01027 -0.00431	0.00662	+0.00002 -0.00001
5	0.90826	0.00579	+0.00466 -0.00310	0.00601	+0.00000 -0.00000
6	0.69062	0.00535	+0.00150 -0.00248	0.00547	+0.00002 -0.00003
7	0.53163	0.00507	+0.00000 -0.00164	0.00517	+0.00002 -0.00007
8	0.41328	0.00495	+0.00000 -0.00132	0.00496	+0.00002 -0.00007
9	0.34388	0.00499	+0.00014 -0.00092	0.00500	+0.00003 -0.00012
10	0.26300	0.00510	+0.00133 -0.00129	0.00514	+0.00002 -0.00012
11	0.25200	0.00550	+0.00304 -0.00225	0.00568	+0.00001 -0.00017
12	0.19556	0.00587	+0.00278 -0.00219	0.00623	+0.00001 -0.00017
13	0.17664	0.00626	+0.00365 -0.00237	0.00716	+0.00000 -0.00020
14	0.09929	0.00615	+0.00049 -0.00059	0.00767	+0.00000 -0.00011
15	0.16128	0.00429	+0.00505 -0.00365	0.00580	+0.00000 -0.00016

Table A.6

 $\pi^+$ 

**Target: Deuterium**  
(*excl. VM included*)

 $Q^2 = 2.5 \text{ GeV}^2$ 

Bin	mult	$\sigma_{\text{stat}}$	$\sigma_{\text{RICH}}$	$\sigma_{\text{MC}}$	$\sigma_{\text{evol}}$
1	3.06922	0.01108	+0.07498 -0.00000	0.01008	+0.00621 -0.00039
2	2.16305	0.00811	+0.04108 -0.00538	0.00822	+0.00279 -0.00033
3	1.56111	0.00667	+0.02052 -0.00505	0.00714	+0.00132 -0.00030
4	1.16967	0.00583	+0.00997 -0.00424	0.00645	+0.00060 -0.00027
5	0.86723	0.00521	+0.00452 -0.00305	0.00579	+0.00032 -0.00027
6	0.66198	0.00493	+0.00125 -0.00252	0.00537	+0.00018 -0.00028
7	0.51100	0.00467	+0.00000 -0.00155	0.00505	+0.00013 -0.00027
8	0.40169	0.00457	+0.00000 -0.00118	0.00488	+0.00009 -0.00025
9	0.31779	0.00458	+0.00008 -0.00094	0.00487	+0.00009 -0.00026
10	0.27826	0.00476	+0.00180 -0.00153	0.00514	+0.00006 -0.00028
11	0.22161	0.00505	+0.00275 -0.00192	0.00551	+0.00003 -0.00027
12	0.18842	0.00552	+0.00239 -0.00205	0.00629	+0.00002 -0.00027
13	0.15833	0.00574	+0.00312 -0.00221	0.00712	+0.00000 -0.00027
14	0.09235	0.00525	+0.00117 -0.00076	0.00721	+0.00000 -0.00016
15	0.16100	0.00364	+0.00483 -0.00357	0.00557	+0.00001 -0.00032

$\pi^-$  Target: Proton  $Q^2 = 2.5 \text{ GeV}^2$   
(excl. VM included)

Bin	mult	$\sigma_{\text{stat}}$	$\sigma_{\text{RICH}}$	$\sigma_{\text{MC}}$	$\sigma_{\text{evol}}$
1	2.52849	0.01071	+0.05925 -0.00295	0.00904	+0.00386 -0.00000
2	1.76419	0.00778	+0.03323 -0.00596	0.00734	+0.00194 -0.00000
3	1.21761	0.00623	+0.01651 -0.00477	0.00618	+0.00102 -0.00000
4	0.88711	0.00535	+0.00837 -0.00327	0.00543	+0.00062 -0.00000
5	0.63460	0.00476	+0.00395 -0.00214	0.00485	+0.00041 -0.00000
6	0.46904	0.00434	+0.00119 -0.00150	0.00442	+0.00034 -0.00000
7	0.35739	0.00412	+0.00025 -0.00083	0.00419	+0.00036 -0.00000
8	0.27591	0.00397	+0.00008 -0.00079	0.00407	+0.00032 -0.00000
9	0.21835	0.00388	+0.00069 -0.00060	0.00402	+0.00037 -0.00000
10	0.17273	0.00394	+0.00194 -0.00140	0.00418	+0.00037 -0.00000
11	0.13978	0.00402	+0.00239 -0.00177	0.00445	+0.00035 -0.00000
12	0.11207	0.00416	+0.00266 -0.00195	0.00495	+0.00038 -0.00002
13	0.10465	0.00471	+0.00283 -0.00192	0.00622	+0.00039 -0.00004
14	0.06524	0.00453	+0.00169 -0.00125	0.00661	+0.00022 -0.00004
15	0.11032	0.00331	+0.00447 -0.00319	0.00528	+0.00042 -0.00009

$\pi^-$  Target: Deuterium  $Q^2 = 2.5 \text{ GeV}^2$   
(excl. VM included)

Bin	mult	$\sigma_{\text{stat}}$	$\sigma_{\text{RICH}}$	$\sigma_{\text{MC}}$	$\sigma_{\text{evol}}$
1	2.78805	0.01056	+0.06470 -0.00352	0.00975	+0.00967 -0.00000
2	1.90829	0.00751	+0.03588 -0.00671	0.00776	+0.00440 -0.00000
3	1.32923	0.00605	+0.01797 -0.00512	0.00657	+0.00210 -0.00000
4	0.96801	0.00523	+0.00900 -0.00359	0.00583	+0.00104 -0.00000
5	0.69773	0.00465	+0.00410 -0.00233	0.00520	+0.00061 -0.00000
6	0.51871	0.00421	+0.00142 -0.00162	0.00470	+0.00037 -0.00000
7	0.40452	0.00394	+0.00028 -0.00094	0.00442	+0.00034 -0.00000
8	0.30230	0.00382	+0.00000 -0.00070	0.00429	+0.00029 -0.00000
9	0.23991	0.00385	+0.00053 -0.00074	0.00441	+0.00028 -0.00000
10	0.20193	0.00401	+0.00260 -0.00168	0.00474	+0.00028 -0.00000
11	0.16445	0.00412	+0.00294 -0.00214	0.00503	+0.00024 -0.00000
12	0.13254	0.00425	+0.00287 -0.00209	0.00556	+0.00025 -0.00001
13	0.12088	0.00432	+0.00350 -0.00241	0.00629	+0.00026 -0.00004
14	0.07814	0.00444	+0.00178 -0.00121	0.00724	+0.00018 -0.00005
15	0.12803	0.00311	+0.00512 -0.00363	0.00560	+0.00027 -0.00010

Table A.7

$K^+$ 

**Target: Proton**  
(*excl. VM included*)

 $Q^2 = 2.5 \text{ GeV}^2$ 

Bin	mult	$\sigma_{\text{stat}}$	$\sigma_{\text{RICH}}$	$\sigma_{\text{MC}}$	$\sigma_{\text{evol}}$
1	0.64924	0.00876	+0.00000 -0.06604	0.00550	+0.00078 -0.00004
2	0.38415	0.00537	+0.00291 -0.03914	0.00363	+0.00006 -0.00000
3	0.28610	0.00413	+0.00467 -0.02245	0.00309	+0.00002 -0.00012
4	0.23526	0.00343	+0.00369 -0.01320	0.00285	+0.00002 -0.00007
5	0.18748	0.00307	+0.00282 -0.00779	0.00266	+0.00001 -0.00003
6	0.15678	0.00288	+0.00215 -0.00385	0.00253	+0.00001 -0.00001
7	0.13469	0.00293	+0.00000 -0.00115	0.00247	+0.00001 -0.00000
8	0.10503	0.00290	+0.00000 -0.00143	0.00233	+0.00001 -0.00000
9	0.09540	0.00318	+0.00000 -0.00124	0.00249	+0.00000 -0.00000
10	0.08522	0.00349	+0.00000 -0.00161	0.00257	+0.00000 -0.00000
11	0.06033	0.00354	+0.00059 -0.00278	0.00243	+0.00000 -0.00002
12	0.05286	0.00347	+0.00035 -0.00260	0.00233	+0.00000 -0.00000
13	0.03398	0.00332	+0.00091 -0.00295	0.00222	+0.00000 -0.00000
14	0.02900	0.00310	+0.00000 -0.00066	0.00216	+0.00000 -0.00000
15	0.02216	0.00196	+0.00170 -0.00395	0.00144	+0.00002 -0.00001

Table A.8

 $K^+$ 

**Target: Deuterium**  
(*excl. VM included*)

 $Q^2 = 2.5 \text{ GeV}^2$ 

Bin	mult	$\sigma_{\text{stat}}$	$\sigma_{\text{RICH}}$	$\sigma_{\text{MC}}$	$\sigma_{\text{evol}}$
1	0.63475	0.00803	+0.00000 -0.06313	0.00536	+0.00212 -0.00005
2	0.37907	0.00494	+0.00271 -0.03749	0.00359	+0.00062 -0.00003
3	0.27936	0.00374	+0.00443 -0.02096	0.00299	+0.00025 -0.00002
4	0.22349	0.00315	+0.00364 -0.01276	0.00276	+0.00012 -0.00001
5	0.18400	0.00282	+0.00302 -0.00741	0.00258	+0.00005 -0.00001
6	0.14760	0.00264	+0.00223 -0.00345	0.00241	+0.00002 -0.00001
7	0.12006	0.00266	+0.00011 -0.00208	0.00234	+0.00000 -0.00002
8	0.11147	0.00274	+0.00000 -0.00136	0.00237	+0.00001 -0.00005
9	0.09055	0.00283	+0.00000 -0.00114	0.00233	+0.00001 -0.00004
10	0.07474	0.00289	+0.00000 -0.00247	0.00221	+0.00001 -0.00006
11	0.05243	0.00312	+0.00027 -0.00270	0.00224	+0.00001 -0.00007
12	0.04702	0.00290	+0.00040 -0.00178	0.00204	+0.00001 -0.00005
13	0.03039	0.00271	+0.00088 -0.00318	0.00189	+0.00001 -0.00004
14	0.02428	0.00246	+0.00000 -0.00090	0.00188	+0.00001 -0.00003
15	0.02123	0.00162	+0.00173 -0.00397	0.00132	+0.00001 -0.00002

Table A.9

 $K^-$ Target: Proton  
(excl. VM included) $Q^2 = 2.5 \text{ GeV}^2$ 

Bin	mult	$\sigma_{\text{stat}}$	$\sigma_{\text{RICH}}$	$\sigma_{\text{MC}}$	$\sigma_{\text{evol}}$
1	0.37057	0.00705	+0.00000 -0.06041	0.00360	+0.00031 -0.00000
2	0.21266	0.00408	+0.00165 -0.03437	0.00236	+0.00026 -0.00000
3	0.13884	0.00280	+0.00221 -0.01800	0.00182	+0.00018 -0.00000
4	0.10238	0.00223	+0.00208 -0.01018	0.00158	+0.00018 -0.00000
5	0.07379	0.00188	+0.00118 -0.00533	0.00136	+0.00014 -0.00000
6	0.05770	0.00164	+0.00045 -0.00205	0.00121	+0.00011 -0.00000
7	0.04043	0.00152	+0.00000 -0.00101	0.00106	+0.00009 -0.00001
8	0.03606	0.00151	+0.00000 -0.00042	0.00107	+0.00013 -0.00004
9	0.02638	0.00147	+0.00000 -0.00072	0.00094	+0.00011 -0.00004
10	0.01549	0.00153	+0.00102 -0.00212	0.00085	+0.00011 -0.00005
11	0.01001	0.00162	+0.00122 -0.00228	0.00072	+0.00009 -0.00004
12	0.00614	0.00155	+0.00203 -0.00317	0.00063	+0.00006 -0.00003
13	0.00097	0.00145	+0.00165 -0.00290	0.00058	+0.00001 -0.00001
14	0.00085	0.00118	+0.00180 -0.00252	0.00058	+0.00002 -0.00001
15	-0.00344	0.00061	+0.00223 -0.00333	0.00040	+0.00005 -0.00003

 $K^-$ Target: Deuterium  
(excl. VM included) $Q^2 = 2.5 \text{ GeV}^2$ 

Bin	mult	$\sigma_{\text{stat}}$	$\sigma_{\text{RICH}}$	$\sigma_{\text{MC}}$	$\sigma_{\text{evol}}$
1	0.40647	0.00677	+0.00000 -0.06524	0.00387	+0.00131 -0.00000
2	0.20992	0.00385	+0.00134 -0.03574	0.00238	+0.00068 -0.00000
3	0.15345	0.00274	+0.00259 -0.01932	0.00197	+0.00049 -0.00000
4	0.10819	0.00215	+0.00207 -0.01119	0.00165	+0.00030 -0.00000
5	0.08149	0.00183	+0.00134 -0.00585	0.00148	+0.00021 -0.00000
6	0.06339	0.00165	+0.00059 -0.00214	0.00134	+0.00015 -0.00000
7	0.04534	0.00151	+0.00000 -0.00096	0.00116	+0.00013 -0.00001
8	0.03711	0.00152	+0.00000 -0.00065	0.00112	+0.00014 -0.00004
9	0.02988	0.00144	+0.00000 -0.00073	0.00102	+0.00016 -0.00007
10	0.02010	0.00153	+0.00089 -0.00252	0.00089	+0.00016 -0.00007
11	0.00967	0.00150	+0.00159 -0.00299	0.00073	+0.00010 -0.00005
12	0.00744	0.00159	+0.00168 -0.00263	0.00072	+0.00010 -0.00005
13	-0.00020	0.00156	+0.00288 -0.00457	0.00073	+0.00000 -0.00000
14	0.00335	0.00129	+0.00058 -0.00109	0.00076	+0.00006 -0.00003
15	-0.00451	0.00071	+0.00323 -0.00476	0.00052	+0.00009 -0.00005

$\pi^+$ 

**Target: Proton**  
(*excl. VM subtracted*)

 $Q^2 = 25 \text{ GeV}^2$ 

Bin	mult	$\sigma_{\text{stat}}$	$\sigma_{\text{RICH}}$	$\sigma_{\text{MC}}$	$\sigma_{\text{evol}}$
1	2.86522	0.01157	+0.06935 -0.00000	0.00940	+0.17907 -0.01728
2	1.91509	0.00800	+0.03663 -0.00467	0.00724	+0.07701 -0.01532
3	1.33868	0.00630	+0.01796 -0.00423	0.00605	+0.03424 -0.01353
4	0.95803	0.00530	+0.00811 -0.00341	0.00522	+0.01751 -0.01191
5	0.68907	0.00461	+0.00356 -0.00237	0.00455	+0.01111 -0.01017
6	0.50275	0.00412	+0.00111 -0.00183	0.00397	+0.00832 -0.00864
7	0.37235	0.00378	+0.00000 -0.00117	0.00359	+0.00687 -0.00729
8	0.27730	0.00358	+0.00001 -0.00091	0.00328	+0.00533 -0.00604
9	0.22012	0.00349	+0.00016 -0.00063	0.00312	+0.00418 -0.00528
10	0.15786	0.00346	+0.00087 -0.00082	0.00297	+0.00282 -0.00410
11	0.13868	0.00362	+0.00171 -0.00127	0.00299	+0.00221 -0.00389
12	0.09812	0.00373	+0.00145 -0.00113	0.00287	+0.00148 -0.00294
13	0.07065	0.00383	+0.00149 -0.00097	0.00276	+0.00091 -0.00225
14	0.04232	0.00358	+0.00030 -0.00030	0.00246	+0.00046 -0.00142
15	0.03167	0.00231	+0.00136 -0.00098	0.00157	+0.00026 -0.00111

Table A.10

 $\pi^+$ 

**Target: Proton**  
(*excl. VM included*)

 $Q^2 = 25 \text{ GeV}^2$ 

Bin	mult	$\sigma_{\text{stat}}$	$\sigma_{\text{RICH}}$	$\sigma_{\text{MC}}$	$\sigma_{\text{evol}}$
1	2.97139	0.01149	+0.07170 -0.00000	0.00973	+0.18570 -0.01792
2	1.98783	0.00794	+0.03795 -0.00484	0.00751	+0.07994 -0.01590
3	1.39050	0.00625	+0.01863 -0.00438	0.00628	+0.03557 -0.01405
4	0.99704	0.00526	+0.00843 -0.00354	0.00543	+0.01822 -0.01239
5	0.71710	0.00457	+0.00368 -0.00245	0.00474	+0.01156 -0.01059
6	0.52617	0.00408	+0.00114 -0.00189	0.00417	+0.00871 -0.00905
7	0.39135	0.00373	+0.00000 -0.00121	0.00380	+0.00722 -0.00766
8	0.29412	0.00352	+0.00000 -0.00094	0.00353	+0.00565 -0.00641
9	0.23623	0.00343	+0.00010 -0.00063	0.00343	+0.00449 -0.00567
10	0.17381	0.00337	+0.00088 -0.00085	0.00340	+0.00310 -0.00452
11	0.15964	0.00349	+0.00193 -0.00143	0.00360	+0.00255 -0.00447
12	0.11786	0.00354	+0.00167 -0.00132	0.00376	+0.00178 -0.00353
13	0.10047	0.00356	+0.00208 -0.00135	0.00407	+0.00130 -0.00320
14	0.05256	0.00325	+0.00026 -0.00031	0.00406	+0.00057 -0.00176
15	0.07768	0.00207	+0.00243 -0.00176	0.00280	+0.00064 -0.00273

Table A.11

$\pi^-$  Target: Proton  $Q^2 = 25 \text{ GeV}^2$   
(*excl. VM subtracted*)

Bin	mult	$\sigma_{\text{stat}}$	$\sigma_{\text{RICH}}$	$\sigma_{\text{MC}}$	$\sigma_{\text{evol}}$
1	2.28835	0.01019	+0.05380 -0.00268	0.00820	+0.16004 -0.00000
2	1.51019	0.00701	+0.02850 -0.00511	0.00630	+0.07227 -0.00000
3	0.98916	0.00534	+0.01344 -0.00389	0.00502	+0.03307 -0.00000
4	0.68667	0.00438	+0.00649 -0.00255	0.00420	+0.01818 -0.00000
5	0.46894	0.00375	+0.00294 -0.00160	0.00358	+0.01194 -0.00000
6	0.33276	0.00330	+0.00088 -0.00109	0.00311	+0.00948 -0.00000
7	0.24173	0.00303	+0.00021 -0.00059	0.00281	+0.00813 -0.00000
8	0.17956	0.00284	+0.00012 -0.00056	0.00258	+0.00691 -0.00000
9	0.13327	0.00269	+0.00049 -0.00042	0.00238	+0.00560 -0.00000
10	0.09998	0.00266	+0.00119 -0.00086	0.00227	+0.00444 -0.00000
11	0.07143	0.00265	+0.00128 -0.00095	0.00214	+0.00330 -0.00000
12	0.05189	0.00269	+0.00127 -0.00093	0.00201	+0.00254 -0.00000
13	0.03661	0.00298	+0.00105 -0.00071	0.00203	+0.00184 -0.00000
14	0.02473	0.00276	+0.00063 -0.00046	0.00173	+0.00128 -0.00000
15	0.01378	0.00190	+0.00090 -0.00064	0.00111	+0.00073 -0.00000

$\pi^-$  Target: Proton  $Q^2 = 25 \text{ GeV}^2$   
(*excl. VM included*)

Bin	mult	$\sigma_{\text{stat}}$	$\sigma_{\text{RICH}}$	$\sigma_{\text{MC}}$	$\sigma_{\text{evol}}$
1	2.38617	0.01011	+0.05592 -0.00278	0.00853	+0.16688 -0.00000
2	1.57567	0.00695	+0.02968 -0.00532	0.00656	+0.07540 -0.00000
3	1.03485	0.00529	+0.01403 -0.00405	0.00525	+0.03459 -0.00000
4	0.72036	0.00434	+0.00680 -0.00266	0.00441	+0.01908 -0.00000
5	0.49448	0.00371	+0.00307 -0.00167	0.00378	+0.01259 -0.00000
6	0.35195	0.00326	+0.00089 -0.00112	0.00332	+0.01003 -0.00000
7	0.25889	0.00299	+0.00018 -0.00060	0.00304	+0.00871 -0.00000
8	0.19326	0.00278	+0.00005 -0.00055	0.00285	+0.00743 -0.00000
9	0.14789	0.00263	+0.00047 -0.00041	0.00273	+0.00621 -0.00000
10	0.11288	0.00257	+0.00127 -0.00091	0.00273	+0.00501 -0.00000
11	0.08784	0.00252	+0.00150 -0.00111	0.00280	+0.00405 -0.00000
12	0.06735	0.00250	+0.00160 -0.00117	0.00297	+0.00329 -0.00000
13	0.05969	0.00269	+0.00162 -0.00109	0.00355	+0.00300 -0.00000
14	0.03488	0.00242	+0.00090 -0.00067	0.00354	+0.00180 -0.00000
15	0.05415	0.00163	+0.00219 -0.00157	0.00259	+0.00287 -0.00000

$K^+$ 

Target: Proton

 $Q^2 = 25 \text{ GeV}^2$ *(excl. VM subtracted)*

Bin	mult	$\sigma_{\text{stat}}$	$\sigma_{\text{RICH}}$	$\sigma_{\text{MC}}$	$\sigma_{\text{evol}}$
1	0.70809	0.00971	+0.00000 -0.07207	0.00599	+0.06498 -0.00268
2	0.38648	0.00550	+0.00293 -0.03938	0.00366	+0.02399 -0.00179
3	0.26933	0.00396	+0.00440 -0.02112	0.00291	+0.01078 -0.00141
4	0.20810	0.00310	+0.00326 -0.01166	0.00251	+0.00483 -0.00120
5	0.15477	0.00264	+0.00232 -0.00642	0.00220	+0.00160 -0.00093
6	0.12159	0.00236	+0.00167 -0.00298	0.00196	+0.00002 -0.00075
7	0.09904	0.00228	+0.00000 -0.00084	0.00182	+0.00000 -0.00137
8	0.07301	0.00216	+0.00000 -0.00100	0.00163	+0.00000 -0.00144
9	0.06246	0.00226	+0.00000 -0.00082	0.00166	+0.00000 -0.00151
10	0.05531	0.00235	+0.00000 -0.00104	0.00166	+0.00000 -0.00152
11	0.03702	0.00227	+0.00037 -0.00171	0.00150	+0.00004 -0.00115
12	0.03124	0.00211	+0.00021 -0.00154	0.00137	+0.00018 -0.00111
13	0.01843	0.00191	+0.00050 -0.00161	0.00122	+0.00023 -0.00075
14	0.01521	0.00167	+0.00000 -0.00037	0.00110	+0.00035 -0.00071
15	0.00994	0.00098	+0.00079 -0.00183	0.00067	+0.00038 -0.00053

Table A.12

 $K^+$ 

Target: Proton

 $Q^2 = 25 \text{ GeV}^2$ *(excl. VM included)*

Bin	mult	$\sigma_{\text{stat}}$	$\sigma_{\text{RICH}}$	$\sigma_{\text{MC}}$	$\sigma_{\text{evol}}$
1	0.71836	0.00969	+0.00000 -0.07307	0.00608	+0.06592 -0.00272
2	0.39229	0.00548	+0.00297 -0.03997	0.00371	+0.02435 -0.00181
3	0.27312	0.00394	+0.00446 -0.02143	0.00295	+0.01093 -0.00143
4	0.21167	0.00308	+0.00332 -0.01188	0.00256	+0.00492 -0.00122
5	0.15965	0.00261	+0.00240 -0.00664	0.00227	+0.00165 -0.00096
6	0.12685	0.00233	+0.00174 -0.00311	0.00205	+0.00002 -0.00079
7	0.10374	0.00225	+0.00000 -0.00089	0.00190	+0.00000 -0.00143
8	0.07712	0.00213	+0.00000 -0.00105	0.00171	+0.00000 -0.00152
9	0.06680	0.00223	+0.00000 -0.00087	0.00174	+0.00000 -0.00161
10	0.05690	0.00233	+0.00000 -0.00108	0.00171	+0.00000 -0.00156
11	0.03833	0.00225	+0.00038 -0.00177	0.00154	+0.00004 -0.00119
12	0.03187	0.00209	+0.00021 -0.00157	0.00141	+0.00019 -0.00113
13	0.01934	0.00189	+0.00052 -0.00168	0.00127	+0.00025 -0.00079
14	0.01544	0.00165	+0.00000 -0.00035	0.00115	+0.00035 -0.00072
15	0.01088	0.00096	+0.00084 -0.00194	0.00071	+0.00042 -0.00058



$K^-$ 

**Target: Proton**  
(*excl. VM subtracted*)

 $Q^2 = 25 \text{ GeV}^2$ 

Bin	mult	$\sigma_{\text{stat}}$	$\sigma_{\text{RICH}}$	$\sigma_{\text{MC}}$	$\sigma_{\text{evol}}$
1	0.40025	0.00778	+0.00000 -0.06530	0.00389	+0.04160 -0.00010
2	0.21179	0.00416	+0.00164 -0.03424	0.00235	+0.01656 -0.00007
3	0.12937	0.00267	+0.00206 -0.01676	0.00169	+0.00765 -0.00006
4	0.08939	0.00201	+0.00181 -0.00888	0.00137	+0.00407 -0.00005
5	0.05964	0.00161	+0.00095 -0.00430	0.00110	+0.00212 -0.00004
6	0.04365	0.00134	+0.00035 -0.00155	0.00091	+0.00136 -0.00004
7	0.02883	0.00118	+0.00000 -0.00072	0.00076	+0.00108 -0.00025
8	0.02437	0.00113	+0.00000 -0.00027	0.00073	+0.00110 -0.00041
9	0.01719	0.00105	+0.00000 -0.00048	0.00062	+0.00092 -0.00040
10	0.00981	0.00105	+0.00064 -0.00134	0.00055	+0.00064 -0.00029
11	0.00629	0.00106	+0.00077 -0.00144	0.00045	+0.00048 -0.00023
12	0.00369	0.00098	+0.00125 -0.00195	0.00038	+0.00032 -0.00016
13	0.00055	0.00089	+0.00092 -0.00163	0.00034	+0.00006 -0.00003
14	0.00039	0.00070	+0.00109 -0.00153	0.00033	+0.00004 -0.00002
15	-0.00177	0.00035	+0.00100 -0.00150	0.00022	+0.00021 -0.00013

Table A.13

 $K^-$ 

**Target: Proton**  
(*excl. VM included*)

 $Q^2 = 25 \text{ GeV}^2$ 

Bin	mult	$\sigma_{\text{stat}}$	$\sigma_{\text{RICH}}$	$\sigma_{\text{MC}}$	$\sigma_{\text{evol}}$
1	0.40828	0.00776	+0.00000 -0.06655	0.00397	+0.04244 -0.00010
2	0.21605	0.00415	+0.00167 -0.03492	0.00240	+0.01690 -0.00007
3	0.13182	0.00266	+0.00210 -0.01709	0.00173	+0.00779 -0.00006
4	0.09160	0.00200	+0.00186 -0.00911	0.00142	+0.00417 -0.00005
5	0.06255	0.00160	+0.00100 -0.00452	0.00116	+0.00223 -0.00005
6	0.04653	0.00132	+0.00037 -0.00165	0.00097	+0.00145 -0.00004
7	0.03111	0.00117	+0.00000 -0.00078	0.00082	+0.00116 -0.00027
8	0.02656	0.00111	+0.00000 -0.00031	0.00079	+0.00120 -0.00044
9	0.01864	0.00104	+0.00000 -0.00051	0.00066	+0.00099 -0.00043
10	0.01053	0.00104	+0.00069 -0.00144	0.00058	+0.00068 -0.00032
11	0.00656	0.00106	+0.00080 -0.00149	0.00047	+0.00050 -0.00024
12	0.00388	0.00098	+0.00129 -0.00200	0.00040	+0.00034 -0.00017
13	0.00059	0.00089	+0.00101 -0.00177	0.00036	+0.00006 -0.00003
14	0.00050	0.00069	+0.00106 -0.00148	0.00034	+0.00006 -0.00003
15	-0.00194	0.00035	+0.00126 -0.00187	0.00023	+0.00023 -0.00014



# Appendix B

## Tables: Multiplicities vs. $x_B$

In this section, the final multiplicities as a function of  $x_B$  in four  $z$  bins are tabulated. Table B.1 defines the bin numbers used in Tables B.2 to B.17. The results for the proton and the deuterium target are shown alternating. The results corrected for the contribution of exclusive vector mesons are shown first, followed by the results including this contribution.

Bin	$z$		$x_B$		Bin	$z$		$x_B$	
	min	max	min	max		min	max	min	max
1	0.250	0.350	0.0230	0.0400	19	0.450	0.600	0.0230	0.0400
2	0.250	0.350	0.0400	0.0550	20	0.450	0.600	0.0400	0.0550
3	0.250	0.350	0.0550	0.0750	21	0.450	0.600	0.0550	0.0750
4	0.250	0.350	0.0750	0.1000	22	0.450	0.600	0.0750	0.1000
5	0.250	0.350	0.1000	0.1400	23	0.450	0.600	0.1000	0.1400
6	0.250	0.350	0.1400	0.2000	24	0.450	0.600	0.1400	0.2000
7	0.250	0.350	0.2000	0.3000	25	0.450	0.600	0.2000	0.3000
8	0.250	0.350	0.3000	0.4000	26	0.450	0.600	0.3000	0.4000
9	0.250	0.350	0.4000	0.6000	27	0.450	0.600	0.4000	0.6000
10	0.350	0.450	0.0230	0.0400	28	0.600	0.750	0.0230	0.0400
11	0.350	0.450	0.0400	0.0550	29	0.600	0.750	0.0400	0.0550
12	0.350	0.450	0.0550	0.0750	30	0.600	0.750	0.0550	0.0750
13	0.350	0.450	0.0750	0.1000	31	0.600	0.750	0.0750	0.1000
14	0.350	0.450	0.1000	0.1400	32	0.600	0.750	0.1000	0.1400
15	0.350	0.450	0.1400	0.2000	33	0.600	0.750	0.1400	0.2000
16	0.350	0.450	0.2000	0.3000	34	0.600	0.750	0.2000	0.3000
17	0.350	0.450	0.3000	0.4000	35	0.600	0.750	0.3000	0.4000
18	0.350	0.450	0.4000	0.6000	36	0.600	0.750	0.4000	0.6000

**Table B.1**  
Binning versus  $x_B$  in 4  $z$  bins

$\pi^+$ Target: Proton  
(excl. VM subtracted) $Q^2 = 2.5 \text{ GeV}^2$ 

Table B.2

Bin	mult	$\sigma_{\text{stat}}$	$\sigma_{\text{RICH}}$	$\sigma_{\text{MC}}$	$\sigma_{\text{evol}}$
1	1.49200	0.01348	+0.00915 -0.00707	0.01201	+0.02892 -0.00011
2	1.38732	0.01202	+0.01001 -0.00756	0.01018	+0.01904 -0.00110
3	1.32628	0.01110	+0.01283 -0.00582	0.00931	+0.01344 -0.00094
4	1.27172	0.01156	+0.01712 -0.00355	0.00940	+0.00868 -0.00056
5	1.29881	0.01162	+0.01939 -0.00305	0.00921	+0.00241 -0.00007
6	1.35854	0.01408	+0.02152 -0.00286	0.00978	+0.00000 -0.00637
7	1.48381	0.01925	+0.02486 -0.00160	0.01114	+0.00000 -0.01529
8	1.69224	0.04386	+0.02639 -0.00017	0.01804	+0.00000 -0.02434
9	1.88727	0.09581	+0.01311 -0.00000	0.02813	+0.00000 -0.03248
10	0.79400	0.01071	+0.00000 -0.00292	0.00951	+0.00500 -0.00005
11	0.74235	0.00877	+0.00264 -0.00278	0.00753	+0.00356 -0.00084
12	0.71769	0.00803	+0.00167 -0.00315	0.00685	+0.00282 -0.00077
13	0.70611	0.00827	+0.00243 -0.00286	0.00695	+0.00217 -0.00049
14	0.72941	0.00816	+0.00477 -0.00231	0.00687	+0.00082 -0.00008
15	0.75977	0.00977	+0.00515 -0.00234	0.00711	+0.00000 -0.00162
16	0.82188	0.01338	+0.00317 -0.00258	0.00776	+0.00000 -0.00488
17	0.87387	0.03037	+0.00000 -0.00341	0.01172	+0.00000 -0.00818
18	1.00231	0.06820	+0.00000 -0.00413	0.01852	+0.00000 -0.01241

Bin	mult	$\sigma_{\text{stat}}$	$\sigma_{\text{RICH}}$	$\sigma_{\text{MC}}$	$\sigma_{\text{evol}}$
19	0.40504	0.00651	+0.00043 -0.00191	0.00583	+0.00050 -0.00002
20	0.37472	0.00518	+0.00000 -0.00125	0.00442	+0.00069 -0.00062
21	0.36294	0.00452	+0.00078 -0.00110	0.00386	+0.00065 -0.00060
22	0.35889	0.00465	+0.00001 -0.00111	0.00393	+0.00062 -0.00041
23	0.37852	0.00458	+0.00000 -0.00120	0.00382	+0.00037 -0.00010
24	0.41650	0.00555	+0.00000 -0.00126	0.00397	+0.00000 -0.00057
25	0.41428	0.00735	+0.00000 -0.00126	0.00404	+0.00000 -0.00238
26	0.43401	0.01692	+0.00212 -0.00084	0.00603	+0.00000 -0.00435
27	0.47061	0.03771	+0.00193 -0.00132	0.00912	+0.00000 -0.00634
28	0.17469	0.00562	+0.00923 -0.00664	0.00435	+0.00000 -0.00042
29	0.16779	0.00395	+0.00310 -0.00246	0.00304	+0.00000 -0.00058
30	0.15574	0.00328	+0.00202 -0.00178	0.00255	+0.00000 -0.00048
31	0.16439	0.00364	+0.00204 -0.00145	0.00296	+0.00000 -0.00037
32	0.17195	0.00350	+0.00137 -0.00112	0.00279	+0.00010 -0.00009
33	0.17661	0.00421	+0.00149 -0.00101	0.00284	+0.00000 -0.00006
34	0.19337	0.00596	+0.00121 -0.00066	0.00310	+0.00000 -0.00069
35	0.19563	0.01315	+0.00009 -0.00018	0.00436	+0.00000 -0.00141
36	0.16519	0.02711	+0.00126 -0.00067	0.00603	+0.00000 -0.00168

$\pi^+$ Target: Deuterium  
(excl. VM subtracted) $Q^2 = 2.5 \text{ GeV}^2$ 

Table B.3

Bin	mult	$\sigma_{\text{stat}}$	$\sigma_{\text{RICH}}$	$\sigma_{\text{MC}}$	$\sigma_{\text{evol}}$	Bin	mult	$\sigma_{\text{stat}}$	$\sigma_{\text{RICH}}$	$\sigma_{\text{MC}}$	$\sigma_{\text{evol}}$
1	1.46639	0.01211	+0.00875 -0.00706	0.01149	+0.02901 -0.00000	19	0.37931	0.00588	+0.00008 -0.00193	0.00548	+0.00067 -0.00000
2	1.34613	0.01082	+0.00948 -0.00749	0.00977	+0.01862 -0.00044	20	0.36108	0.00460	+0.00000 -0.00123	0.00418	+0.00060 -0.00024
3	1.26116	0.01002	+0.01255 -0.00528	0.00886	+0.01290 -0.00040	21	0.34793	0.00410	+0.00058 -0.00100	0.00370	+0.00057 -0.00026
4	1.24828	0.01062	+0.01673 -0.00372	0.00922	+0.00861 -0.00021	22	0.35717	0.00431	+0.00002 -0.00113	0.00385	+0.00056 -0.00016
5	1.24172	0.01066	+0.01841 -0.00311	0.00887	+0.00231 -0.00000	23	0.36312	0.00428	+0.00000 -0.00113	0.00371	+0.00033 -0.00000
6	1.27296	0.01307	+0.02046 -0.00246	0.00934	+0.00000 -0.00619	24	0.38719	0.00516	+0.00000 -0.00116	0.00380	+0.00000 -0.00053
7	1.41834	0.01825	+0.02417 -0.00143	0.01081	+0.00000 -0.01502	25	0.38193	0.00697	+0.00000 -0.00112	0.00388	+0.00000 -0.00220
8	1.63812	0.04395	+0.02631 -0.00096	0.01785	+0.00000 -0.02422	26	0.43965	0.01736	+0.00167 -0.00079	0.00618	+0.00000 -0.00440
9	1.74244	0.10094	+0.02007 -0.00000	0.02773	+0.00000 -0.03060	27	0.39588	0.03743	+0.00262 -0.00028	0.00856	+0.00000 -0.00519
10	0.76792	0.00929	+0.00000 -0.00292	0.00881	+0.00512 -0.00000	28	0.17396	0.00526	+0.00920 -0.00701	0.00426	+0.00018 -0.00044
11	0.70789	0.00782	+0.00276 -0.00279	0.00713	+0.00333 -0.00033	29	0.16629	0.00352	+0.00327 -0.00249	0.00290	+0.00000 -0.00036
12	0.68443	0.00716	+0.00158 -0.00314	0.00649	+0.00263 -0.00033	30	0.14592	0.00295	+0.00164 -0.00141	0.00243	+0.00000 -0.00027
13	0.67076	0.00749	+0.00243 -0.00280	0.00664	+0.00202 -0.00018	31	0.15693	0.00332	+0.00218 -0.00132	0.00276	+0.00000 -0.00019
14	0.70165	0.00756	+0.00495 -0.00209	0.00669	+0.00081 -0.00000	32	0.15793	0.00324	+0.00122 -0.00102	0.00266	+0.00008 -0.00000
15	0.73460	0.00918	+0.00443 -0.00240	0.00692	+0.00000 -0.00157	33	0.16665	0.00392	+0.00119 -0.00103	0.00270	+0.00000 -0.00007
16	0.78706	0.01271	+0.00263 -0.00277	0.00756	+0.00000 -0.00464	34	0.18309	0.00545	+0.00084 -0.00064	0.00287	+0.00000 -0.00071
17	0.80499	0.02993	+0.00000 -0.00355	0.01140	+0.00000 -0.00743	35	0.17843	0.01296	+0.00090 -0.00067	0.00424	+0.00000 -0.00137
18	0.91165	0.06768	+0.00000 -0.00390	0.01756	+0.00000 -0.01081	36	0.21586	0.02986	+0.00027 -0.00050	0.00636	+0.00000 -0.00224

$\pi^-$ Target: Proton  
(excl. VM subtracted) $Q^2 = 2.5 \text{ GeV}^2$ 

Table B.4

Bin	mult	$\sigma_{\text{stat}}$	$\sigma_{\text{RICH}}$	$\sigma_{\text{MC}}$	$\sigma_{\text{evol}}$
1	1.24092	0.01243	+0.00855 -0.00480	0.01095	+0.02522 -0.00000
2	1.08861	0.01052	+0.00946 -0.00550	0.00869	+0.01636 -0.00000
3	1.02109	0.00975	+0.01096 -0.00453	0.00789	+0.01160 -0.00000
4	0.94685	0.00988	+0.01370 -0.00337	0.00780	+0.00722 -0.00000
5	0.90742	0.00974	+0.01407 -0.00299	0.00737	+0.00187 -0.00000
6	0.94299	0.01163	+0.01594 -0.00304	0.00777	+0.00000 -0.00480
7	1.00350	0.01592	+0.01632 -0.00336	0.00886	+0.00030 -0.01054
8	1.11384	0.03595	+0.01652 -0.00337	0.01422	+0.00056 -0.01599
9	1.17399	0.07765	+0.00710 -0.00518	0.02219	+0.00067 -0.01996
10	0.59964	0.00905	+0.00000 -0.00157	0.00783	+0.00402 -0.00000
11	0.54546	0.00762	+0.00240 -0.00153	0.00629	+0.00301 -0.00000
12	0.51639	0.00692	+0.00183 -0.00199	0.00566	+0.00232 -0.00000
13	0.47920	0.00693	+0.00234 -0.00189	0.00561	+0.00158 -0.00000
14	0.48959	0.00669	+0.00374 -0.00175	0.00544	+0.00052 -0.00000
15	0.49382	0.00789	+0.00326 -0.00168	0.00546	+0.00000 -0.00075
16	0.49865	0.01057	+0.00272 -0.00182	0.00584	+0.00022 -0.00184
17	0.54825	0.02442	+0.00000 -0.00236	0.00916	+0.00042 -0.00307
18	0.60024	0.05398	+0.00034 -0.00280	0.01420	+0.00053 -0.00428

Bin	mult	$\sigma_{\text{stat}}$	$\sigma_{\text{RICH}}$	$\sigma_{\text{MC}}$	$\sigma_{\text{evol}}$
19	0.29726	0.00569	+0.00178 -0.00173	0.00497	+0.00073 -0.00012
20	0.27374	0.00445	+0.00052 -0.00071	0.00372	+0.00081 -0.00000
21	0.24982	0.00381	+0.00098 -0.00060	0.00312	+0.00067 -0.00000
22	0.23580	0.00381	+0.00037 -0.00064	0.00309	+0.00051 -0.00000
23	0.24432	0.00374	+0.00000 -0.00075	0.00300	+0.00020 -0.00000
24	0.24334	0.00429	+0.00000 -0.00071	0.00294	+0.00000 -0.00020
25	0.23758	0.00571	+0.00000 -0.00074	0.00300	+0.00016 -0.00071
26	0.24444	0.01289	+0.00065 -0.00053	0.00443	+0.00030 -0.00135
27	0.28221	0.03061	+0.00161 -0.00065	0.00729	+0.00042 -0.00228
28	0.13328	0.00499	+0.00960 -0.00706	0.00393	+0.00051 -0.00053
29	0.11470	0.00347	+0.00295 -0.00222	0.00257	+0.00049 -0.00029
30	0.10249	0.00267	+0.00208 -0.00152	0.00201	+0.00041 -0.00020
31	0.09689	0.00280	+0.00151 -0.00105	0.00214	+0.00033 -0.00015
32	0.09570	0.00257	+0.00139 -0.00097	0.00195	+0.00010 -0.00001
33	0.09562	0.00299	+0.00129 -0.00082	0.00193	+0.00000 -0.00002
34	0.08950	0.00394	+0.00097 -0.00055	0.00196	+0.00009 -0.00014
35	0.10694	0.00911	+0.00057 -0.00033	0.00300	+0.00022 -0.00040
36	0.10718	0.02063	+0.00023 -0.00027	0.00460	+0.00028 -0.00068

$\pi^-$ Target: Deuterium  
(excl. VM subtracted) $Q^2 = 2.5 \text{ GeV}^2$ 

Table B.5

Bin	mult	$\sigma_{\text{stat}}$	$\sigma_{\text{RICH}}$	$\sigma_{\text{MC}}$	$\sigma_{\text{evol}}$
1	1.30204	0.01142	+0.00879 -0.00513	0.01092	+0.02593 -0.00000
2	1.17789	0.00996	+0.01050 -0.00567	0.00903	+0.01704 -0.00000
3	1.07807	0.00915	+0.01147 -0.00475	0.00807	+0.01168 -0.00000
4	1.05730	0.00981	+0.01509 -0.00366	0.00845	+0.00774 -0.00000
5	1.02306	0.00964	+0.01598 -0.00342	0.00806	+0.00203 -0.00000
6	1.03397	0.01157	+0.01707 -0.00358	0.00826	+0.00007 -0.00505
7	1.08715	0.01586	+0.01748 -0.00354	0.00929	+0.00042 -0.01118
8	1.14986	0.03643	+0.01850 -0.00283	0.01440	+0.00067 -0.01609
9	1.39831	0.08690	+0.00737 -0.00606	0.02524	+0.00066 -0.02312
10	0.63943	0.00854	+0.00000 -0.00157	0.00798	+0.00402 -0.00000
11	0.58964	0.00719	+0.00264 -0.00162	0.00650	+0.00288 -0.00000
12	0.56894	0.00658	+0.00205 -0.00217	0.00595	+0.00225 -0.00000
13	0.53764	0.00685	+0.00240 -0.00213	0.00603	+0.00157 -0.00000
14	0.54435	0.00657	+0.00412 -0.00181	0.00582	+0.00051 -0.00000
15	0.55180	0.00778	+0.00374 -0.00195	0.00585	+0.00005 -0.00090
16	0.56427	0.01079	+0.00239 -0.00203	0.00631	+0.00031 -0.00228
17	0.58565	0.02491	+0.00000 -0.00273	0.00951	+0.00050 -0.00366
18	0.57908	0.05400	+0.00000 -0.00283	0.01367	+0.00042 -0.00483

Bin	mult	$\sigma_{\text{stat}}$	$\sigma_{\text{RICH}}$	$\sigma_{\text{MC}}$	$\sigma_{\text{evol}}$
19	0.32114	0.00534	+0.00177 -0.00156	0.00506	+0.00048 -0.00003
20	0.28357	0.00411	+0.00038 -0.00082	0.00374	+0.00057 -0.00000
21	0.27418	0.00362	+0.00097 -0.00069	0.00326	+0.00049 -0.00000
22	0.27636	0.00378	+0.00023 -0.00076	0.00338	+0.00041 -0.00000
23	0.27417	0.00365	+0.00000 -0.00071	0.00321	+0.00017 -0.00000
24	0.26583	0.00426	+0.00000 -0.00078	0.00312	+0.00003 -0.00024
25	0.27735	0.00589	+0.00000 -0.00081	0.00332	+0.00023 -0.00098
26	0.29796	0.01406	+0.00103 -0.00064	0.00510	+0.00039 -0.00193
27	0.32233	0.03206	+0.00176 -0.00053	0.00756	+0.00035 -0.00306
28	0.14746	0.00474	+0.01039 -0.00734	0.00412	+0.00034 -0.00055
29	0.12434	0.00316	+0.00329 -0.00245	0.00259	+0.00028 -0.00028
30	0.11832	0.00259	+0.00222 -0.00161	0.00217	+0.00022 -0.00020
31	0.11382	0.00282	+0.00197 -0.00128	0.00238	+0.00016 -0.00014
32	0.11611	0.00277	+0.00198 -0.00136	0.00227	+0.00005 -0.00000
33	0.12315	0.00323	+0.00147 -0.00094	0.00225	+0.00001 -0.00002
34	0.11058	0.00420	+0.00138 -0.00076	0.00218	+0.00013 -0.00021
35	0.11491	0.00995	+0.00046 -0.00038	0.00328	+0.00023 -0.00050
36	0.10905	0.02185	+0.00055 -0.00035	0.00472	+0.00019 -0.00078

$K^+$ Target: Proton  
(excl. VM subtracted) $Q^2 = 2.5 \text{ GeV}^2$ 

Table B.6

Bin	mult	$\sigma_{\text{stat}}$	$\sigma_{\text{RICH}}$	$\sigma_{\text{MC}}$	$\sigma_{\text{evol}}$
1	0.27799	0.00748	+0.00695 -0.00763	0.00517	+0.00862 -0.00051
2	0.24917	0.00680	+0.00561 -0.01462	0.00440	+0.00546 -0.00033
3	0.27559	0.00657	+0.00395 -0.01871	0.00424	+0.00424 -0.00023
4	0.24714	0.00657	+0.00278 -0.01853	0.00406	+0.00227 -0.00010
5	0.25279	0.00656	+0.00339 -0.01940	0.00404	+0.00012 -0.00000
6	0.25218	0.00793	+0.00312 -0.02179	0.00419	+0.00001 -0.00224
7	0.33684	0.01226	+0.00570 -0.02730	0.00584	+0.00000 -0.00562
8	0.38768	0.03123	+0.00771 -0.03675	0.01035	+0.00000 -0.00847
9	0.32556	0.07058	+0.01910 -0.03833	0.01467	+0.00000 -0.00819
10	0.17552	0.00631	+0.00233 -0.00000	0.00443	+0.00146 -0.00047
11	0.14977	0.00493	+0.00309 -0.00183	0.00331	+0.00090 -0.00028
12	0.16242	0.00445	+0.00291 -0.00406	0.00317	+0.00074 -0.00020
13	0.15062	0.00457	+0.00213 -0.00612	0.00317	+0.00046 -0.00010
14	0.16051	0.00431	+0.00187 -0.00702	0.00308	+0.00008 -0.00001
15	0.19344	0.00587	+0.00179 -0.01037	0.00376	+0.00001 -0.00037
16	0.19822	0.00775	+0.00303 -0.00941	0.00402	+0.00000 -0.00076
17	0.22332	0.01796	+0.00238 -0.01068	0.00670	+0.00000 -0.00113
18	0.22830	0.03951	+0.00508 -0.00711	0.01035	+0.00000 -0.00120

Bin	mult	$\sigma_{\text{stat}}$	$\sigma_{\text{RICH}}$	$\sigma_{\text{MC}}$	$\sigma_{\text{evol}}$
19	0.13515	0.00513	+0.00000 -0.00605	0.00359	+0.00000 -0.00198
20	0.09809	0.00335	+0.00029 -0.00162	0.00221	+0.00000 -0.00105
21	0.09204	0.00273	+0.00005 -0.00044	0.00187	+0.00000 -0.00071
22	0.09098	0.00279	+0.00000 -0.00124	0.00189	+0.00000 -0.00049
23	0.09908	0.00269	+0.00020 -0.00167	0.00186	+0.00000 -0.00019
24	0.11215	0.00330	+0.00005 -0.00177	0.00206	+0.00023 -0.00000
25	0.11762	0.00454	+0.00114 -0.00171	0.00226	+0.00059 -0.00004
26	0.12301	0.01048	+0.00159 -0.00255	0.00354	+0.00095 -0.00008
27	0.21076	0.02556	+0.00233 -0.00000	0.00683	+0.00211 -0.00014
28	0.05754	0.00449	+0.00746 -0.01513	0.00262	+0.00000 -0.00190
29	0.06181	0.00281	+0.00048 -0.00430	0.00187	+0.00000 -0.00148
30	0.04591	0.00218	+0.00051 -0.00238	0.00145	+0.00000 -0.00088
31	0.04979	0.00223	+0.00000 -0.00183	0.00154	+0.00000 -0.00076
32	0.04483	0.00219	+0.00000 -0.00162	0.00143	+0.00000 -0.00029
33	0.05444	0.00270	+0.00000 -0.00103	0.00149	+0.00017 -0.00000
34	0.06051	0.00380	+0.00000 -0.00150	0.00161	+0.00063 -0.00002
35	0.06578	0.00932	+0.00074 -0.00244	0.00255	+0.00108 -0.00004
36	0.03577	0.01829	+0.00022 -0.00099	0.00392	+0.00075 -0.00002



$K^+$ Target: Deuterium  
(excl. VM subtracted) $Q^2 = 2.5 \text{ GeV}^2$ 

Table B.7

Bin	mult	$\sigma_{\text{stat}}$	$\sigma_{\text{RICH}}$	$\sigma_{\text{MC}}$	$\sigma_{\text{evol}}$	Bin	mult	$\sigma_{\text{stat}}$	$\sigma_{\text{RICH}}$	$\sigma_{\text{MC}}$	$\sigma_{\text{evol}}$
1	0.24181	0.00629	+0.00584 -0.00773	0.00439	+0.00753 -0.00029	19	0.12413	0.00441	+0.00000 -0.00529	0.00318	+0.00000 -0.00169
2	0.24875	0.00600	+0.00556 -0.01387	0.00417	+0.00550 -0.00019	20	0.09340	0.00287	+0.00071 -0.00117	0.00203	+0.00000 -0.00089
3	0.27712	0.00613	+0.00420 -0.01714	0.00427	+0.00431 -0.00013	21	0.08849	0.00247	+0.00000 -0.00061	0.00177	+0.00000 -0.00062
4	0.24618	0.00619	+0.00252 -0.01884	0.00409	+0.00232 -0.00005	22	0.10058	0.00267	+0.00000 -0.00094	0.00198	+0.00000 -0.00048
5	0.24245	0.00627	+0.00339 -0.01866	0.00398	+0.00018 -0.00000	23	0.09395	0.00248	+0.00006 -0.00175	0.00179	+0.00000 -0.00016
6	0.26289	0.00769	+0.00329 -0.02114	0.00431	+0.00000 -0.00238	24	0.09948	0.00298	+0.00029 -0.00185	0.00186	+0.00019 -0.00001
7	0.28076	0.01138	+0.00450 -0.02626	0.00513	+0.00000 -0.00486	25	0.10763	0.00424	+0.00084 -0.00127	0.00214	+0.00053 -0.00005
8	0.33103	0.02881	+0.00747 -0.03263	0.00895	+0.00000 -0.00760	26	0.10975	0.01133	+0.00180 -0.00147	0.00328	+0.00082 -0.00008
9	0.30335	0.06695	+0.02195 -0.02917	0.01290	+0.00000 -0.00809	27	0.19871	0.09664	+0.00297 -0.00369	0.00658	+0.00190 -0.00008
10	0.16340	0.00542	+0.00258 -0.00000	0.00394	+0.00137 -0.00030	28	0.04812	0.00337	+0.00669 -0.01313	0.00200	+0.00000 -0.00153
11	0.15454	0.00444	+0.00325 -0.00200	0.00324	+0.00094 -0.00017	29	0.04725	0.00234	+0.00095 -0.00465	0.00151	+0.00000 -0.00107
12	0.14135	0.00397	+0.00287 -0.00414	0.00286	+0.00066 -0.00009	30	0.04465	0.00188	+0.00000 -0.00197	0.00129	+0.00000 -0.00081
13	0.14733	0.00417	+0.00237 -0.00575	0.00307	+0.00045 -0.00005	31	0.04307	0.00196	+0.00000 -0.00199	0.00141	+0.00000 -0.00061
14	0.16424	0.00428	+0.00228 -0.00757	0.00316	+0.00010 -0.00000	32	0.04689	0.00199	+0.00000 -0.00138	0.00134	+0.00000 -0.00028
15	0.16352	0.00506	+0.00233 -0.00784	0.00323	+0.00000 -0.00035	33	0.04384	0.00233	+0.00000 -0.00119	0.00126	+0.00014 -0.00000
16	0.20421	0.00764	+0.00212 -0.00998	0.00415	+0.00000 -0.00088	34	0.05947	0.00356	+0.00000 -0.00105	0.00152	+0.00063 -0.00002
17	0.19252	0.01714	+0.00270 -0.00843	0.00610	+0.00000 -0.00111	35	0.06695	0.00891	+0.00050 -0.00154	0.00241	+0.00110 -0.00002
18	0.21353	0.04171	+0.00368 -0.00852	0.00953	+0.00000 -0.00133	36	0.09850	0.05884	+0.00161 -0.00310	0.00396	+0.00207 -0.00000

$K^-$ Target: Proton  
(*excl. VM subtracted*) $Q^2 = 2.5 \text{ GeV}^2$ 

Table B.8

Bin	mult	$\sigma_{\text{stat}}$	$\sigma_{\text{RICH}}$	$\sigma_{\text{MC}}$	$\sigma_{\text{evol}}$
1	0.14489	0.00514	+0.00474 -0.00526	0.00309	+0.00456 -0.00016
2	0.13741	0.00491	+0.00461 -0.01184	0.00277	+0.00327 -0.00000
3	0.14356	0.00476	+0.00196 -0.01547	0.00268	+0.00250 -0.00000
4	0.10633	0.00437	+0.00158 -0.01532	0.00218	+0.00108 -0.00000
5	0.10722	0.00445	+0.00128 -0.01567	0.00221	+0.00005 -0.00000
6	0.11198	0.00542	+0.00103 -0.01822	0.00237	+0.00004 -0.00123
7	0.12736	0.00750	+0.00122 -0.02169	0.00299	+0.00013 -0.00259
8	0.11399	0.01797	+0.00084 -0.03173	0.00483	+0.00015 -0.00311
9	0.20243	0.04408	+0.00007 -0.03430	0.01127	+0.00026 -0.00654
10	0.08866	0.00417	+0.00216 -0.00000	0.00258	+0.00071 -0.00015
11	0.07020	0.00335	+0.00115 -0.00012	0.00190	+0.00051 -0.00000
12	0.06560	0.00293	+0.00127 -0.00255	0.00170	+0.00041 -0.00000
13	0.05553	0.00272	+0.00079 -0.00396	0.00150	+0.00023 -0.00000
14	0.06322	0.00275	+0.00083 -0.00571	0.00160	+0.00003 -0.00000
15	0.04977	0.00303	+0.00078 -0.00618	0.00142	+0.00002 -0.00017
16	0.05752	0.00413	+0.00064 -0.00676	0.00172	+0.00009 -0.00038
17	0.05834	0.00967	+0.00096 -0.00692	0.00296	+0.00012 -0.00050
18	0.10052	0.02621	+0.00231 -0.00806	0.00706	+0.00020 -0.00100

Bin	mult	$\sigma_{\text{stat}}$	$\sigma_{\text{RICH}}$	$\sigma_{\text{MC}}$	$\sigma_{\text{evol}}$
19	0.05338	0.00318	+0.00000 -0.00173	0.00180	+0.00000 -0.00077
20	0.03584	0.00203	+0.00037 -0.00062	0.00110	+0.00004 -0.00030
21	0.03397	0.00160	+0.00000 -0.00033	0.00093	+0.00006 -0.00020
22	0.03100	0.00154	+0.00000 -0.00077	0.00088	+0.00003 -0.00011
23	0.02370	0.00130	+0.00000 -0.00126	0.00072	+0.00000 -0.00003
24	0.02744	0.00160	+0.00007 -0.00141	0.00080	+0.00007 -0.00000
25	0.02409	0.00207	+0.00016 -0.00089	0.00082	+0.00016 -0.00000
26	0.03427	0.00526	+0.00000 -0.00089	0.00217	+0.00032 -0.00000
27	0.06373	0.01214	+0.00113 -0.00079	0.00587	+0.00069 -0.00000
28	0.00397	0.00269	+0.01099 -0.01647	0.00068	+0.00000 -0.00014
29	0.01149	0.00154	+0.00228 -0.00391	0.00069	+0.00002 -0.00024
30	0.00489	0.00101	+0.00165 -0.00280	0.00060	+0.00001 -0.00008
31	0.00410	0.00101	+0.00099 -0.00190	0.00069	+0.00001 -0.00006
32	0.00385	0.00098	+0.00075 -0.00179	0.00060	+0.00000 -0.00002
33	0.00350	0.00113	+0.00073 -0.00169	0.00061	+0.00001 -0.00000
34	0.00470	0.00144	+0.00034 -0.00058	0.00058	+0.00007 -0.00000
35	0.00408	0.00244	+0.00039 -0.00105	0.00208	+0.00009 -0.00000
36	-0.14079	0.00656	+0.00038 -0.00007	0.02043	+0.00366 -0.00000

$K^-$ Target: Deuterium  
(excl. VM subtracted) $Q^2 = 2.5 \text{ GeV}^2$ 

Table B.9

Bin	mult	$\sigma_{\text{stat}}$	$\sigma_{\text{RICH}}$	$\sigma_{\text{MC}}$	$\sigma_{\text{evol}}$
1	0.16002	0.00487	+0.00522 -0.00554	0.00324	+0.00502 -0.00013
2	0.14064	0.00462	+0.00465 -0.01330	0.00276	+0.00332 -0.00000
3	0.14477	0.00448	+0.00238 -0.01659	0.00264	+0.00247 -0.00000
4	0.12084	0.00445	+0.00172 -0.01638	0.00249	+0.00123 -0.00000
5	0.11926	0.00428	+0.00115 -0.01732	0.00235	+0.00000 -0.00002
6	0.12138	0.00538	+0.00127 -0.02012	0.00256	+0.00003 -0.00129
7	0.13604	0.00775	+0.00093 -0.02409	0.00320	+0.00015 -0.00273
8	0.16441	0.02301	+0.00098 -0.03349	0.00669	+0.00032 -0.00449
9	0.38486	0.15921	+0.00000 -0.07031	0.02119	+0.00078 -0.01236
10	0.09506	0.00401	+0.00270 -0.00008	0.00269	+0.00075 -0.00012
11	0.07285	0.00317	+0.00142 -0.00044	0.00199	+0.00052 -0.00000
12	0.06818	0.00275	+0.00144 -0.00251	0.00174	+0.00040 -0.00000
13	0.06524	0.00283	+0.00101 -0.00471	0.00175	+0.00025 -0.00000
14	0.06645	0.00274	+0.00097 -0.00660	0.00168	+0.00003 -0.00000
15	0.05759	0.00303	+0.00076 -0.00698	0.00160	+0.00002 -0.00020
16	0.07022	0.00433	+0.00081 -0.00755	0.00203	+0.00012 -0.00045
17	0.05929	0.00974	+0.00129 -0.00771	0.00307	+0.00018 -0.00050
18	0.08390	0.02845	+0.00318 -0.00498	0.00696	+0.00027 -0.00081

Bin	mult	$\sigma_{\text{stat}}$	$\sigma_{\text{RICH}}$	$\sigma_{\text{MC}}$	$\sigma_{\text{evol}}$
19	0.05782	0.00300	+0.00000 -0.00228	0.00185	+0.00000 -0.00081
20	0.04600	0.00205	+0.00067 -0.00103	0.00127	+0.00005 -0.00038
21	0.03394	0.00147	+0.00000 -0.00011	0.00090	+0.00005 -0.00020
22	0.03313	0.00149	+0.00000 -0.00080	0.00094	+0.00003 -0.00012
23	0.02912	0.00135	+0.00000 -0.00143	0.00080	+0.00000 -0.00003
24	0.02650	0.00159	+0.00011 -0.00137	0.00081	+0.00006 -0.00000
25	0.02563	0.00205	+0.00018 -0.00149	0.00084	+0.00017 -0.00000
26	0.02411	0.00464	+0.00015 -0.00099	0.00177	+0.00027 -0.00000
27	0.06668	0.01340	+0.00046 -0.00056	0.00616	+0.00086 -0.00000
28	0.00830	0.00245	+0.01056 -0.01680	0.00068	+0.00000 -0.00027
29	0.01113	0.00141	+0.00293 -0.00496	0.00066	+0.00001 -0.00023
30	0.00689	0.00103	+0.00155 -0.00286	0.00062	+0.00002 -0.00012
31	0.00569	0.00100	+0.00115 -0.00243	0.00069	+0.00001 -0.00008
32	0.00290	0.00089	+0.00125 -0.00245	0.00059	+0.00000 -0.00002
33	0.00574	0.00106	+0.00056 -0.00151	0.00055	+0.00002 -0.00000
34	0.00346	0.00140	+0.00049 -0.00120	0.00059	+0.00005 -0.00000
35	0.01871	0.00369	+0.00003 -0.00005	0.00220	+0.00047 -0.00000
36	-0.14329	0.00804	+0.00002 -0.00033	0.02278	+0.00438 -0.00000

$\pi^+$ Target: Proton  
(*excl. VM included*) $Q^2 = 2.5 \text{ GeV}^2$ 

Table B.10

Bin	mult	$\sigma_{\text{stat}}$	$\sigma_{\text{RICH}}$	$\sigma_{\text{MC}}$	$\sigma_{\text{evol}}$
1	1.59420	0.01328	+0.00975 -0.00752	0.01280	+0.03090 -0.00011
2	1.46787	0.01187	+0.01056 -0.00796	0.01073	+0.02014 -0.00116
3	1.38931	0.01099	+0.01341 -0.00607	0.00971	+0.01407 -0.00099
4	1.32064	0.01147	+0.01774 -0.00367	0.00971	+0.00901 -0.00058
5	1.33752	0.01155	+0.01993 -0.00313	0.00946	+0.00248 -0.00007
6	1.38763	0.01402	+0.02194 -0.00292	0.00997	+0.00000 -0.00650
7	1.51314	0.01918	+0.02530 -0.00163	0.01134	+0.00000 -0.01559
8	1.71431	0.04375	+0.02670 -0.00017	0.01825	+0.00000 -0.02466
9	1.91047	0.09555	+0.01325 -0.00000	0.02844	+0.00000 -0.03288
10	0.86408	0.01049	+0.00000 -0.00318	0.01036	+0.00544 -0.00006
11	0.79573	0.00862	+0.00283 -0.00297	0.00808	+0.00381 -0.00090
12	0.75732	0.00793	+0.00176 -0.00332	0.00723	+0.00298 -0.00081
13	0.73858	0.00819	+0.00255 -0.00298	0.00725	+0.00227 -0.00051
14	0.75537	0.00810	+0.00494 -0.00238	0.00709	+0.00085 -0.00009
15	0.77605	0.00973	+0.00526 -0.00238	0.00726	+0.00000 -0.00165
16	0.83658	0.01334	+0.00321 -0.00262	0.00789	+0.00000 -0.00497
17	0.88510	0.03030	+0.00000 -0.00345	0.01187	+0.00000 -0.00828
18	1.02078	0.06801	+0.00000 -0.00419	0.01882	+0.00000 -0.01264

Bin	mult	$\sigma_{\text{stat}}$	$\sigma_{\text{RICH}}$	$\sigma_{\text{MC}}$	$\sigma_{\text{evol}}$
19	0.46377	0.00627	+0.00020 -0.00199	0.00677	+0.00057 -0.00003
20	0.41648	0.00503	+0.00000 -0.00130	0.00499	+0.00077 -0.00069
21	0.39231	0.00443	+0.00078 -0.00114	0.00421	+0.00071 -0.00064
22	0.38027	0.00458	+0.00000 -0.00116	0.00419	+0.00065 -0.00044
23	0.39538	0.00453	+0.00000 -0.00124	0.00400	+0.00038 -0.00010
24	0.42931	0.00552	+0.00000 -0.00130	0.00410	+0.00000 -0.00059
25	0.42209	0.00733	+0.00000 -0.00128	0.00412	+0.00000 -0.00242
26	0.44095	0.01687	+0.00215 -0.00085	0.00612	+0.00000 -0.00442
27	0.47891	0.03762	+0.00196 -0.00134	0.00924	+0.00000 -0.00645
28	0.25570	0.00517	+0.01302 -0.00937	0.00624	+0.00000 -0.00062
29	0.23627	0.00367	+0.00415 -0.00329	0.00410	+0.00000 -0.00081
30	0.21184	0.00310	+0.00257 -0.00226	0.00319	+0.00000 -0.00065
31	0.21300	0.00351	+0.00244 -0.00174	0.00341	+0.00000 -0.00048
32	0.20518	0.00341	+0.00155 -0.00126	0.00308	+0.00011 -0.00011
33	0.19917	0.00415	+0.00161 -0.00110	0.00302	+0.00000 -0.00007
34	0.20735	0.00592	+0.00126 -0.00069	0.00322	+0.00000 -0.00074
35	0.20751	0.01307	+0.00009 -0.00019	0.00447	+0.00000 -0.00150
36	0.17453	0.02699	+0.00130 -0.00069	0.00613	+0.00000 -0.00177

$\pi^+$ Target: Deuterium  
(*excl. VM included*) $Q^2 = 2.5 \text{ GeV}^2$ 

Table B.11

Bin	mult	$\sigma_{\text{stat}}$	$\sigma_{\text{RICH}}$	$\sigma_{\text{MC}}$	$\sigma_{\text{evol}}$
1	1.57280	0.01199	+0.00936 -0.00755	0.01229	+0.03111 -0.00000
2	1.42917	0.01073	+0.01004 -0.00792	0.01034	+0.01977 -0.00046
3	1.32602	0.00995	+0.01317 -0.00553	0.00927	+0.01356 -0.00042
4	1.29985	0.01057	+0.01738 -0.00386	0.00957	+0.00896 -0.00022
5	1.28248	0.01062	+0.01897 -0.00320	0.00914	+0.00238 -0.00000
6	1.30461	0.01303	+0.02092 -0.00251	0.00955	+0.00000 -0.00635
7	1.44945	0.01820	+0.02465 -0.00146	0.01103	+0.00000 -0.01535
8	1.66991	0.04383	+0.02677 -0.00098	0.01816	+0.00000 -0.02469
9	1.79703	0.10054	+0.02062 -0.00000	0.02844	+0.00000 -0.03156
10	0.84080	0.00916	+0.00000 -0.00321	0.00966	+0.00561 -0.00000
11	0.76192	0.00773	+0.00298 -0.00300	0.00769	+0.00358 -0.00035
12	0.72604	0.00709	+0.00168 -0.00333	0.00688	+0.00279 -0.00035
13	0.70414	0.00744	+0.00257 -0.00293	0.00696	+0.00213 -0.00019
14	0.72867	0.00753	+0.00515 -0.00216	0.00694	+0.00084 -0.00000
15	0.75484	0.00915	+0.00455 -0.00246	0.00711	+0.00000 -0.00161
16	0.80494	0.01267	+0.00269 -0.00283	0.00772	+0.00000 -0.00474
17	0.81834	0.02987	+0.00000 -0.00360	0.01158	+0.00000 -0.00756
18	0.93201	0.06750	+0.00000 -0.00398	0.01792	+0.00000 -0.01105

Bin	mult	$\sigma_{\text{stat}}$	$\sigma_{\text{RICH}}$	$\sigma_{\text{MC}}$	$\sigma_{\text{evol}}$
19	0.43626	0.00572	+0.00000 -0.00197	0.00643	+0.00077 -0.00000
20	0.40557	0.00449	+0.00000 -0.00130	0.00477	+0.00067 -0.00027
21	0.37826	0.00404	+0.00056 -0.00104	0.00407	+0.00062 -0.00028
22	0.38184	0.00426	+0.00000 -0.00119	0.00413	+0.00060 -0.00017
23	0.38126	0.00425	+0.00000 -0.00118	0.00390	+0.00035 -0.00000
24	0.40087	0.00514	+0.00000 -0.00120	0.00394	+0.00000 -0.00055
25	0.39182	0.00695	+0.00000 -0.00114	0.00397	+0.00000 -0.00226
26	0.45100	0.01731	+0.00171 -0.00080	0.00631	+0.00000 -0.00451
27	0.40918	0.03731	+0.00269 -0.00028	0.00874	+0.00000 -0.00537
28	0.25882	0.00490	+0.01319 -0.01006	0.00619	+0.00027 -0.00065
29	0.23920	0.00332	+0.00446 -0.00339	0.00398	+0.00000 -0.00052
30	0.20393	0.00282	+0.00213 -0.00183	0.00307	+0.00000 -0.00038
31	0.20772	0.00321	+0.00265 -0.00162	0.00324	+0.00000 -0.00025
32	0.19298	0.00318	+0.00140 -0.00117	0.00297	+0.00009 -0.00000
33	0.19187	0.00388	+0.00131 -0.00113	0.00290	+0.00000 -0.00008
34	0.20026	0.00541	+0.00089 -0.00068	0.00302	+0.00000 -0.00077
35	0.19240	0.01289	+0.00095 -0.00071	0.00438	+0.00000 -0.00147
36	0.23475	0.02967	+0.00029 -0.00053	0.00658	+0.00000 -0.00243

$\pi^-$ Target: Proton  
(*excl. VM included*) $Q^2 = 2.5 \text{ GeV}^2$ 

Table B.12

Bin	mult	$\sigma_{\text{stat}}$	$\sigma_{\text{RICH}}$	$\sigma_{\text{MC}}$	$\sigma_{\text{evol}}$
1	1.33745	0.01225	+0.00919 -0.00515	0.01178	+0.02718 -0.00000
2	1.16202	0.01038	+0.01007 -0.00585	0.00925	+0.01746 -0.00000
3	1.07752	0.00965	+0.01153 -0.00475	0.00829	+0.01225 -0.00000
4	0.99190	0.00979	+0.01430 -0.00351	0.00814	+0.00756 -0.00000
5	0.93920	0.00968	+0.01453 -0.00308	0.00762	+0.00193 -0.00000
6	0.96866	0.01158	+0.01634 -0.00312	0.00797	+0.00000 -0.00493
7	1.02627	0.01586	+0.01666 -0.00342	0.00906	+0.00031 -0.01078
8	1.13133	0.03584	+0.01675 -0.00341	0.01443	+0.00057 -0.01624
9	1.20298	0.07734	+0.00727 -0.00529	0.02266	+0.00069 -0.02046
10	0.66227	0.00886	+0.00000 -0.00175	0.00865	+0.00443 -0.00000
11	0.59254	0.00748	+0.00261 -0.00166	0.00684	+0.00327 -0.00000
12	0.54925	0.00683	+0.00194 -0.00212	0.00604	+0.00247 -0.00000
13	0.50764	0.00685	+0.00248 -0.00200	0.00592	+0.00168 -0.00000
14	0.51146	0.00664	+0.00392 -0.00182	0.00567	+0.00054 -0.00000
15	0.51034	0.00785	+0.00337 -0.00174	0.00563	+0.00000 -0.00078
16	0.51132	0.01053	+0.00279 -0.00186	0.00598	+0.00022 -0.00189
17	0.55733	0.02435	+0.00000 -0.00240	0.00931	+0.00042 -0.00313
18	0.61278	0.05381	+0.00034 -0.00285	0.01447	+0.00054 -0.00437

Bin	mult	$\sigma_{\text{stat}}$	$\sigma_{\text{RICH}}$	$\sigma_{\text{MC}}$	$\sigma_{\text{evol}}$
19	0.34979	0.00546	+0.00175 -0.00180	0.00595	+0.00086 -0.00014
20	0.30981	0.00431	+0.00041 -0.00068	0.00432	+0.00092 -0.00000
21	0.27523	0.00372	+0.00098 -0.00060	0.00350	+0.00074 -0.00000
22	0.25511	0.00375	+0.00035 -0.00067	0.00336	+0.00056 -0.00000
23	0.25941	0.00370	+0.00000 -0.00078	0.00320	+0.00021 -0.00000
24	0.25421	0.00425	+0.00000 -0.00073	0.00308	+0.00000 -0.00020
25	0.24469	0.00569	+0.00000 -0.00076	0.00309	+0.00016 -0.00073
26	0.25160	0.01284	+0.00067 -0.00055	0.00454	+0.00031 -0.00139
27	0.28620	0.03054	+0.00164 -0.00066	0.00740	+0.00042 -0.00231
28	0.20078	0.00456	+0.01404 -0.01032	0.00582	+0.00077 -0.00080
29	0.17638	0.00319	+0.00428 -0.00322	0.00376	+0.00076 -0.00044
30	0.14879	0.00251	+0.00282 -0.00206	0.00270	+0.00060 -0.00029
31	0.13445	0.00267	+0.00192 -0.00134	0.00262	+0.00045 -0.00021
32	0.12220	0.00249	+0.00166 -0.00116	0.00227	+0.00013 -0.00001
33	0.11404	0.00293	+0.00146 -0.00093	0.00215	+0.00000 -0.00002
34	0.10015	0.00389	+0.00104 -0.00060	0.00209	+0.00010 -0.00016
35	0.11386	0.00905	+0.00060 -0.00034	0.00312	+0.00024 -0.00043
36	0.11470	0.02051	+0.00024 -0.00028	0.00476	+0.00030 -0.00073

$\pi^-$ Target: Deuterium  
(*excl. VM included*) $Q^2 = 2.5 \text{ GeV}^2$ 

Table B.13

Bin	mult	$\sigma_{\text{stat}}$	$\sigma_{\text{RICH}}$	$\sigma_{\text{MC}}$	$\sigma_{\text{evol}}$
1	1.40378	0.01131	+0.00946 -0.00551	0.01174	+0.02795 -0.00000
2	1.25857	0.00988	+0.01118 -0.00603	0.00962	+0.01820 -0.00000
3	1.13908	0.00908	+0.01209 -0.00499	0.00849	+0.01234 -0.00000
4	1.10817	0.00975	+0.01578 -0.00382	0.00882	+0.00812 -0.00000
5	1.06015	0.00960	+0.01652 -0.00354	0.00834	+0.00210 -0.00000
6	1.06367	0.01153	+0.01752 -0.00367	0.00849	+0.00007 -0.00519
7	1.11559	0.01582	+0.01790 -0.00363	0.00950	+0.00043 -0.01147
8	1.17455	0.03634	+0.01886 -0.00288	0.01468	+0.00068 -0.01644
9	1.43838	0.08662	+0.00757 -0.00622	0.02588	+0.00068 -0.02378
10	0.70677	0.00842	+0.00000 -0.00174	0.00883	+0.00444 -0.00000
11	0.64028	0.00710	+0.00287 -0.00175	0.00708	+0.00313 -0.00000
12	0.60725	0.00652	+0.00219 -0.00231	0.00636	+0.00241 -0.00000
13	0.56976	0.00680	+0.00255 -0.00226	0.00637	+0.00166 -0.00000
14	0.56895	0.00654	+0.00431 -0.00189	0.00607	+0.00053 -0.00000
15	0.57032	0.00775	+0.00386 -0.00201	0.00604	+0.00005 -0.00093
16	0.57896	0.01076	+0.00245 -0.00208	0.00648	+0.00032 -0.00234
17	0.59850	0.02485	+0.00000 -0.00279	0.00971	+0.00052 -0.00374
18	0.58793	0.05391	+0.00000 -0.00287	0.01389	+0.00042 -0.00491

Bin	mult	$\sigma_{\text{stat}}$	$\sigma_{\text{RICH}}$	$\sigma_{\text{MC}}$	$\sigma_{\text{evol}}$
19	0.37655	0.00518	+0.00168 -0.00155	0.00606	+0.00056 -0.00004
20	0.32068	0.00401	+0.00024 -0.00079	0.00434	+0.00064 -0.00000
21	0.30238	0.00355	+0.00097 -0.00069	0.00367	+0.00054 -0.00000
22	0.29821	0.00373	+0.00017 -0.00078	0.00369	+0.00044 -0.00000
23	0.29127	0.00362	+0.00000 -0.00073	0.00344	+0.00018 -0.00000
24	0.27792	0.00424	+0.00000 -0.00080	0.00326	+0.00003 -0.00025
25	0.28663	0.00587	+0.00000 -0.00083	0.00343	+0.00023 -0.00101
26	0.30669	0.01403	+0.00106 -0.00066	0.00523	+0.00040 -0.00198
27	0.33199	0.03197	+0.00180 -0.00055	0.00774	+0.00036 -0.00315
28	0.22159	0.00441	+0.01517 -0.01073	0.00610	+0.00051 -0.00082
29	0.19067	0.00295	+0.00477 -0.00357	0.00379	+0.00043 -0.00043
30	0.17207	0.00246	+0.00302 -0.00219	0.00293	+0.00032 -0.00029
31	0.15782	0.00271	+0.00251 -0.00163	0.00294	+0.00022 -0.00020
32	0.14898	0.00270	+0.00238 -0.00163	0.00267	+0.00006 -0.00000
33	0.14642	0.00318	+0.00166 -0.00107	0.00253	+0.00001 -0.00002
34	0.12462	0.00416	+0.00150 -0.00083	0.00236	+0.00015 -0.00024
35	0.12485	0.00989	+0.00049 -0.00040	0.00344	+0.00025 -0.00055
36	0.11844	0.02174	+0.00058 -0.00037	0.00490	+0.00020 -0.00084

$K^+$ Target: Proton  
(*excl. VM included*) $Q^2 = 2.5 \text{ GeV}^2$ 

Table B.14

Bin	mult	$\sigma_{\text{stat}}$	$\sigma_{\text{RICH}}$	$\sigma_{\text{MC}}$	$\sigma_{\text{evol}}$
1	0.28358	0.00744	+0.00710 -0.00779	0.00529	+0.00880 -0.00052
2	0.25385	0.00676	+0.00573 -0.01493	0.00449	+0.00556 -0.00033
3	0.28123	0.00653	+0.00403 -0.01912	0.00434	+0.00432 -0.00024
4	0.25164	0.00654	+0.00283 -0.01886	0.00413	+0.00231 -0.00010
5	0.25555	0.00654	+0.00343 -0.01962	0.00408	+0.00012 -0.00000
6	0.25427	0.00791	+0.00315 -0.02198	0.00423	+0.00001 -0.00226
7	0.33934	0.01224	+0.00574 -0.02750	0.00589	+0.00000 -0.00566
8	0.39093	0.03117	+0.00777 -0.03705	0.01043	+0.00000 -0.00854
9	0.32774	0.07050	+0.01923 -0.03860	0.01478	+0.00000 -0.00824
10	0.18379	0.00623	+0.00244 -0.00000	0.00465	+0.00153 -0.00049
11	0.15713	0.00486	+0.00326 -0.00193	0.00348	+0.00095 -0.00029
12	0.17068	0.00439	+0.00306 -0.00427	0.00332	+0.00077 -0.00021
13	0.15630	0.00452	+0.00221 -0.00635	0.00329	+0.00047 -0.00010
14	0.16504	0.00427	+0.00192 -0.00722	0.00316	+0.00008 -0.00001
15	0.19806	0.00583	+0.00184 -0.01061	0.00384	+0.00001 -0.00038
16	0.20244	0.00771	+0.00309 -0.00961	0.00410	+0.00000 -0.00078
17	0.22768	0.01787	+0.00242 -0.01088	0.00681	+0.00000 -0.00115
18	0.23449	0.03918	+0.00520 -0.00729	0.01056	+0.00000 -0.00124

Bin	mult	$\sigma_{\text{stat}}$	$\sigma_{\text{RICH}}$	$\sigma_{\text{MC}}$	$\sigma_{\text{evol}}$
19	0.14564	0.00503	+0.00000 -0.00650	0.00386	+0.00000 -0.00214
20	0.10647	0.00328	+0.00028 -0.00173	0.00238	+0.00000 -0.00114
21	0.09966	0.00268	+0.00003 -0.00047	0.00200	+0.00000 -0.00077
22	0.09719	0.00275	+0.00000 -0.00134	0.00200	+0.00000 -0.00052
23	0.10353	0.00267	+0.00020 -0.00175	0.00193	+0.00000 -0.00020
24	0.11515	0.00328	+0.00005 -0.00182	0.00211	+0.00023 -0.00000
25	0.12054	0.00451	+0.00116 -0.00175	0.00231	+0.00061 -0.00005
26	0.12501	0.01044	+0.00162 -0.00258	0.00359	+0.00097 -0.00009
27	0.21014	0.02556	+0.00235 -0.00000	0.00684	+0.00211 -0.00014
28	0.06309	0.00440	+0.00807 -0.01638	0.00284	+0.00000 -0.00208
29	0.06531	0.00277	+0.00050 -0.00450	0.00196	+0.00000 -0.00156
30	0.04861	0.00215	+0.00053 -0.00249	0.00150	+0.00000 -0.00093
31	0.05192	0.00221	+0.00000 -0.00189	0.00158	+0.00000 -0.00080
32	0.04638	0.00218	+0.00000 -0.00165	0.00146	+0.00000 -0.00030
33	0.05614	0.00269	+0.00000 -0.00106	0.00151	+0.00017 -0.00000
34	0.06095	0.00379	+0.00000 -0.00151	0.00162	+0.00064 -0.00002
35	0.06722	0.00929	+0.00075 -0.00248	0.00257	+0.00110 -0.00004
36	0.03543	0.01829	+0.00022 -0.00099	0.00392	+0.00075 -0.00002



$K^+$ Target: Deuterium  
(*excl. VM included*) $Q^2 = 2.5 \text{ GeV}^2$ 

Table B.15

Bin	mult	$\sigma_{\text{stat}}$	$\sigma_{\text{RICH}}$	$\sigma_{\text{MC}}$	$\sigma_{\text{evol}}$	Bin	mult	$\sigma_{\text{stat}}$	$\sigma_{\text{RICH}}$	$\sigma_{\text{MC}}$	$\sigma_{\text{evol}}$
1	0.24722	0.00626	+0.00597 -0.00792	0.00450	+0.00770 -0.00030	19	0.13506	0.00435	+0.00000 -0.00572	0.00345	+0.00000 -0.00184
2	0.25394	0.00598	+0.00568 -0.01420	0.00427	+0.00561 -0.00019	20	0.10198	0.00283	+0.00074 -0.00127	0.00220	+0.00000 -0.00098
3	0.28343	0.00611	+0.00429 -0.01754	0.00438	+0.00440 -0.00013	21	0.09630	0.00244	+0.00000 -0.00066	0.00190	+0.00000 -0.00068
4	0.25083	0.00617	+0.00256 -0.01921	0.00418	+0.00236 -0.00005	22	0.10724	0.00264	+0.00000 -0.00101	0.00210	+0.00000 -0.00052
5	0.24562	0.00626	+0.00344 -0.01892	0.00404	+0.00018 -0.00000	23	0.09902	0.00246	+0.00006 -0.00185	0.00187	+0.00000 -0.00017
6	0.26557	0.00768	+0.00333 -0.02137	0.00436	+0.00000 -0.00240	24	0.10301	0.00296	+0.00030 -0.00191	0.00192	+0.00020 -0.00001
7	0.28311	0.01136	+0.00454 -0.02650	0.00518	+0.00000 -0.00490	25	0.11070	0.00422	+0.00086 -0.00130	0.00219	+0.00054 -0.00006
8	0.33623	0.02874	+0.00758 -0.03314	0.00910	+0.00000 -0.00772	26	0.11876	0.01019	+0.00187 -0.00156	0.00339	+0.00089 -0.00008
9	0.30798	0.06682	+0.02230 -0.02963	0.01312	+0.00000 -0.00822	27	0.11252	0.02164	+0.00181 -0.00217	0.00473	+0.00108 -0.00005
10	0.17064	0.00537	+0.00274 -0.00000	0.00414	+0.00143 -0.00031	28	0.05217	0.00334	+0.00719 -0.01411	0.00215	+0.00000 -0.00166
11	0.16375	0.00439	+0.00345 -0.00213	0.00343	+0.00100 -0.00018	29	0.05029	0.00232	+0.00100 -0.00489	0.00159	+0.00000 -0.00114
12	0.14928	0.00394	+0.00304 -0.00438	0.00302	+0.00069 -0.00010	30	0.04740	0.00186	+0.00000 -0.00207	0.00135	+0.00000 -0.00086
13	0.15425	0.00414	+0.00248 -0.00602	0.00320	+0.00048 -0.00005	31	0.04517	0.00195	+0.00000 -0.00206	0.00144	+0.00000 -0.00064
14	0.17016	0.00425	+0.00236 -0.00784	0.00327	+0.00011 -0.00000	32	0.04868	0.00198	+0.00000 -0.00142	0.00137	+0.00000 -0.00029
15	0.16802	0.00504	+0.00239 -0.00805	0.00331	+0.00000 -0.00036	33	0.04529	0.00233	+0.00000 -0.00122	0.00128	+0.00015 -0.00000
16	0.20985	0.00761	+0.00218 -0.01025	0.00426	+0.00000 -0.00090	34	0.06067	0.00355	+0.00000 -0.00107	0.00154	+0.00064 -0.00002
17	0.19783	0.01702	+0.00277 -0.00862	0.00624	+0.00000 -0.00114	35	0.07026	0.00857	+0.00053 -0.00161	0.00246	+0.00116 -0.00003
18	0.23283	0.03957	+0.00395 -0.00900	0.00990	+0.00000 -0.00145	36	0.04864	0.01696	+0.00107 -0.00202	0.00315	+0.00102 -0.00000

$K^-$ Target: Proton  
(*excl. VM included*) $Q^2 = 2.5 \text{ GeV}^2$ 

Table B.16

Bin	mult	$\sigma_{\text{stat}}$	$\sigma_{\text{RICH}}$	$\sigma_{\text{MC}}$	$\sigma_{\text{evol}}$
1	0.14947	0.00511	+0.00489 -0.00543	0.00319	+0.00470 -0.00016
2	0.14156	0.00488	+0.00476 -0.01223	0.00286	+0.00337 -0.00000
3	0.14695	0.00474	+0.00200 -0.01585	0.00275	+0.00256 -0.00000
4	0.10871	0.00436	+0.00161 -0.01567	0.00223	+0.00110 -0.00000
5	0.10874	0.00444	+0.00130 -0.01590	0.00224	+0.00005 -0.00000
6	0.11369	0.00541	+0.00104 -0.01850	0.00241	+0.00004 -0.00125
7	0.12837	0.00749	+0.00123 -0.02186	0.00302	+0.00014 -0.00261
8	0.11474	0.01795	+0.00084 -0.03194	0.00486	+0.00015 -0.00313
9	0.20216	0.04408	+0.00006 -0.03426	0.01128	+0.00026 -0.00653
10	0.09442	0.00412	+0.00232 -0.00000	0.00276	+0.00076 -0.00016
11	0.07541	0.00331	+0.00125 -0.00014	0.00204	+0.00055 -0.00000
12	0.06987	0.00290	+0.00135 -0.00272	0.00180	+0.00044 -0.00000
13	0.05915	0.00269	+0.00084 -0.00423	0.00159	+0.00025 -0.00000
14	0.06629	0.00273	+0.00087 -0.00598	0.00167	+0.00004 -0.00000
15	0.05188	0.00302	+0.00081 -0.00643	0.00147	+0.00002 -0.00018
16	0.05883	0.00412	+0.00066 -0.00691	0.00176	+0.00010 -0.00038
17	0.05956	0.00964	+0.00098 -0.00706	0.00302	+0.00012 -0.00051
18	0.10220	0.02613	+0.00235 -0.00820	0.00716	+0.00021 -0.00101

Bin	mult	$\sigma_{\text{stat}}$	$\sigma_{\text{RICH}}$	$\sigma_{\text{MC}}$	$\sigma_{\text{evol}}$
19	0.05930	0.00312	+0.00000 -0.00188	0.00200	+0.00000 -0.00086
20	0.04011	0.00199	+0.00037 -0.00067	0.00122	+0.00004 -0.00034
21	0.03809	0.00158	+0.00000 -0.00035	0.00102	+0.00006 -0.00023
22	0.03341	0.00152	+0.00000 -0.00085	0.00094	+0.00004 -0.00012
23	0.02543	0.00129	+0.00000 -0.00135	0.00076	+0.00000 -0.00003
24	0.02881	0.00159	+0.00008 -0.00148	0.00083	+0.00007 -0.00000
25	0.02522	0.00206	+0.00016 -0.00094	0.00085	+0.00017 -0.00000
26	0.03508	0.00524	+0.00000 -0.00092	0.00220	+0.00033 -0.00000
27	0.06501	0.01208	+0.00116 -0.00082	0.00590	+0.00071 -0.00000
28	0.00462	0.00268	+0.01202 -0.01801	0.00071	+0.00000 -0.00016
29	0.01259	0.00153	+0.00243 -0.00418	0.00073	+0.00002 -0.00026
30	0.00555	0.00101	+0.00177 -0.00300	0.00061	+0.00002 -0.00009
31	0.00472	0.00101	+0.00105 -0.00200	0.00069	+0.00001 -0.00007
32	0.00422	0.00097	+0.00078 -0.00186	0.00061	+0.00000 -0.00002
33	0.00389	0.00113	+0.00075 -0.00175	0.00062	+0.00001 -0.00000
34	0.00493	0.00144	+0.00035 -0.00059	0.00058	+0.00007 -0.00000
35	0.00410	0.00244	+0.00040 -0.00107	0.00208	+0.00009 -0.00000
36	-0.14006	0.00653	+0.00039 -0.00007	0.02041	+0.00364 -0.00000

$K^-$ Target: Deuterium  
(*excl. VM included*) $Q^2 = 2.5 \text{ GeV}^2$ 

Table B.17

Bin	mult	$\sigma_{\text{stat}}$	$\sigma_{\text{RICH}}$	$\sigma_{\text{MC}}$	$\sigma_{\text{evol}}$
1	0.16521	0.00485	+0.00539 -0.00573	0.00335	+0.00518 -0.00013
2	0.14486	0.00460	+0.00479 -0.01374	0.00286	+0.00342 -0.00000
3	0.14872	0.00446	+0.00244 -0.01706	0.00271	+0.00253 -0.00000
4	0.12361	0.00444	+0.00176 -0.01676	0.00255	+0.00125 -0.00000
5	0.12094	0.00427	+0.00116 -0.01757	0.00239	+0.00000 -0.00002
6	0.12304	0.00537	+0.00128 -0.02040	0.00260	+0.00003 -0.00131
7	0.13770	0.00774	+0.00094 -0.02438	0.00325	+0.00015 -0.00277
8	0.17703	0.02102	+0.00098 -0.03578	0.00669	+0.00035 -0.00483
9	0.23750	0.04893	+0.00000 -0.04426	0.01382	+0.00048 -0.00763
10	0.10116	0.00397	+0.00289 -0.00007	0.00288	+0.00080 -0.00013
11	0.07883	0.00314	+0.00154 -0.00048	0.00214	+0.00056 -0.00000
12	0.07346	0.00273	+0.00155 -0.00271	0.00186	+0.00044 -0.00000
13	0.06947	0.00282	+0.00108 -0.00502	0.00186	+0.00026 -0.00000
14	0.07005	0.00273	+0.00102 -0.00695	0.00176	+0.00003 -0.00000
15	0.06019	0.00302	+0.00080 -0.00729	0.00166	+0.00002 -0.00020
16	0.07306	0.00431	+0.00084 -0.00785	0.00210	+0.00012 -0.00047
17	0.06045	0.00971	+0.00132 -0.00784	0.00315	+0.00018 -0.00051
18	0.09353	0.02782	+0.00332 -0.00618	0.00703	+0.00030 -0.00091

Bin	mult	$\sigma_{\text{stat}}$	$\sigma_{\text{RICH}}$	$\sigma_{\text{MC}}$	$\sigma_{\text{evol}}$
19	0.06395	0.00296	+0.00000 -0.00249	0.00204	+0.00000 -0.00089
20	0.05139	0.00203	+0.00071 -0.00113	0.00141	+0.00005 -0.00043
21	0.03787	0.00146	+0.00000 -0.00013	0.00098	+0.00005 -0.00022
22	0.03596	0.00148	+0.00000 -0.00088	0.00101	+0.00003 -0.00013
23	0.03144	0.00134	+0.00000 -0.00155	0.00085	+0.00000 -0.00003
24	0.02787	0.00158	+0.00012 -0.00143	0.00084	+0.00007 -0.00000
25	0.02666	0.00204	+0.00018 -0.00155	0.00087	+0.00018 -0.00000
26	0.02544	0.00462	+0.00016 -0.00105	0.00181	+0.00028 -0.00000
27	0.06751	0.01336	+0.00046 -0.00054	0.00617	+0.00088 -0.00000
28	0.00921	0.00244	+0.01149 -0.01828	0.00072	+0.00000 -0.00030
29	0.01243	0.00140	+0.00318 -0.00540	0.00069	+0.00001 -0.00026
30	0.00772	0.00103	+0.00166 -0.00306	0.00063	+0.00002 -0.00013
31	0.00633	0.00100	+0.00122 -0.00256	0.00070	+0.00001 -0.00009
32	0.00331	0.00089	+0.00131 -0.00256	0.00060	+0.00000 -0.00002
33	0.00621	0.00106	+0.00059 -0.00158	0.00055	+0.00002 -0.00000
34	0.00375	0.00140	+0.00051 -0.00124	0.00059	+0.00005 -0.00000
35	0.01918	0.00368	+0.00003 -0.00005	0.00221	+0.00048 -0.00000
36	-0.14206	0.00799	+0.00002 -0.00036	0.02268	+0.00434 -0.00000



# Appendix C

## Tables: Multiplicities vs. $Q^2$

In this section, the final multiplicities as a function of  $Q^2$  in four  $z$  bins are tabulated. Table C.1 defines the bin numbers used in Tables C.2 to C.9. The results for the proton and the deuterium target are shown on one page for each hadron. The results corrected for the contribution of exclusive vector mesons are shown first, followed by the results including this contribution.

Bin	$z$		$Q^2$		Bin	$z$		$Q^2$	
	min	max	min	max		min	max	min	max
1	0.250	0.350	1.000	1.500	11	0.450	0.600	1.000	1.500
2	0.250	0.350	1.500	2.000	12	0.450	0.600	1.500	2.000
3	0.250	0.350	2.000	3.000	13	0.450	0.600	2.000	3.000
4	0.250	0.350	3.000	5.000	14	0.450	0.600	3.000	5.000
5	0.250	0.350	5.000	15.000	15	0.450	0.600	5.000	15.000
6	0.350	0.450	1.000	1.500	16	0.600	0.750	1.000	1.500
7	0.350	0.450	1.500	2.000	17	0.600	0.750	1.500	2.000
8	0.350	0.450	2.000	3.000	18	0.600	0.750	2.000	3.000
9	0.350	0.450	3.000	5.000	19	0.600	0.750	3.000	5.000
10	0.350	0.450	5.000	15.000	20	0.600	0.750	5.000	15.000

**Table C.1**  
Binning versus  $Q^2$  in 4  $z$  bins

$\pi^+$ **Target: Proton****Target: Deuterium***(excl. VM subtracted)*

Bin	mult	$\sigma_{\text{stat}}$	$\sigma_{\text{RICH}}$	$\sigma_{\text{MC}}$	mult	$\sigma_{\text{stat}}$	$\sigma_{\text{RICH}}$	$\sigma_{\text{MC}}$
1	1.36009	0.00788	+0.01647 -0.00462	0.00908	1.32178	0.00715	+0.01596 -0.00448	0.00878
2	1.32396	0.01013	+0.01689 -0.00403	0.00938	1.25003	0.00902	+0.01554 -0.00411	0.00877
3	1.36133	0.00904	+0.01642 -0.00455	0.00752	1.32091	0.00830	+0.01575 -0.00428	0.00727
4	1.39614	0.00991	+0.01523 -0.00480	0.00667	1.35321	0.00921	+0.01454 -0.00515	0.00647
5	1.50030	0.01495	+0.01180 -0.00650	0.00694	1.40945	0.01425	+0.01123 -0.00631	0.00669
6	0.76989	0.00605	+0.00375 -0.00261	0.00708	0.75208	0.00548	+0.00367 -0.00257	0.00684
7	0.77209	0.00767	+0.00354 -0.00254	0.00734	0.71212	0.00675	+0.00322 -0.00248	0.00673
8	0.76706	0.00668	+0.00249 -0.00287	0.00560	0.73928	0.00615	+0.00245 -0.00282	0.00539
9	0.76658	0.00719	+0.00134 -0.00311	0.00477	0.72785	0.00666	+0.00097 -0.00313	0.00457
10	0.76181	0.01022	+0.00172 -0.00295	0.00450	0.72438	0.00969	+0.00151 -0.00309	0.00436
11	0.42671	0.00373	+0.00000 -0.00115	0.00432	0.41536	0.00341	+0.00000 -0.00121	0.00417
12	0.39578	0.00435	+0.00000 -0.00123	0.00403	0.39005	0.00398	+0.00000 -0.00117	0.00390
13	0.40006	0.00384	+0.00000 -0.00116	0.00315	0.37225	0.00347	+0.00000 -0.00112	0.00293
14	0.40183	0.00408	+0.00008 -0.00114	0.00266	0.37086	0.00375	+0.00000 -0.00105	0.00249
15	0.36651	0.00541	+0.00003 -0.00108	0.00225	0.35411	0.00519	+0.00000 -0.00094	0.00221
16	0.19969	0.00306	+0.00328 -0.00240	0.00307	0.19005	0.00275	+0.00322 -0.00244	0.00288
17	0.18454	0.00347	+0.00299 -0.00212	0.00291	0.18072	0.00312	+0.00291 -0.00204	0.00274
18	0.19225	0.00304	+0.00325 -0.00250	0.00226	0.17131	0.00269	+0.00254 -0.00197	0.00204
19	0.19089	0.00319	+0.00252 -0.00208	0.00187	0.18181	0.00294	+0.00300 -0.00208	0.00177
20	0.17346	0.00406	+0.00164 -0.00155	0.00155	0.16133	0.00381	+0.00126 -0.00178	0.00145

**Table C.2**

$\pi^-$                       **Target: Proton**                      **Target: Deuterium**  
*(excl. VM subtracted)*

Bin	mult	$\sigma_{\text{stat}}$	$\sigma_{\text{RICH}}$	$\sigma_{\text{MC}}$	mult	$\sigma_{\text{stat}}$	$\sigma_{\text{RICH}}$	$\sigma_{\text{MC}}$
1	1.03556	0.00678	+0.01321 -0.00391	0.00759	1.13288	0.00652	+0.01410 -0.00429	0.00803
2	1.00189	0.00874	+0.01308 -0.00374	0.00782	1.07838	0.00832	+0.01417 -0.00388	0.00809
3	0.99716	0.00767	+0.01266 -0.00381	0.00619	1.09964	0.00752	+0.01391 -0.00422	0.00659
4	0.98411	0.00830	+0.01138 -0.00410	0.00537	1.08554	0.00819	+0.01216 -0.00456	0.00572
5	0.98685	0.01222	+0.00844 -0.00484	0.00541	1.06087	0.01222	+0.00917 -0.00517	0.00565
6	0.55720	0.00511	+0.00307 -0.00180	0.00581	0.61882	0.00494	+0.00324 -0.00200	0.00617
7	0.53098	0.00624	+0.00285 -0.00176	0.00565	0.56011	0.00589	+0.00299 -0.00176	0.00577
8	0.51576	0.00548	+0.00195 -0.00180	0.00441	0.58463	0.00542	+0.00235 -0.00199	0.00476
9	0.48942	0.00576	+0.00135 -0.00176	0.00363	0.54998	0.00572	+0.00134 -0.00196	0.00390
10	0.46518	0.00807	+0.00150 -0.00163	0.00339	0.51303	0.00816	+0.00148 -0.00173	0.00359
11	0.30138	0.00313	+0.00044 -0.00085	0.00351	0.32343	0.00295	+0.00039 -0.00085	0.00363
12	0.26907	0.00359	+0.00011 -0.00077	0.00325	0.29937	0.00346	+0.00017 -0.00085	0.00343
13	0.25227	0.00306	+0.00027 -0.00065	0.00244	0.29161	0.00305	+0.00018 -0.00080	0.00267
14	0.23580	0.00314	+0.00035 -0.00050	0.00195	0.26212	0.00310	+0.00026 -0.00050	0.00206
15	0.19422	0.00401	+0.00016 -0.00032	0.00157	0.22838	0.00419	+0.00019 -0.00030	0.00175
16	0.13122	0.00249	+0.00297 -0.00216	0.00242	0.15156	0.00241	+0.00334 -0.00232	0.00263
17	0.11512	0.00272	+0.00250 -0.00171	0.00222	0.13143	0.00264	+0.00283 -0.00206	0.00234
18	0.10729	0.00219	+0.00268 -0.00193	0.00161	0.13000	0.00231	+0.00328 -0.00225	0.00184
19	0.09452	0.00217	+0.00242 -0.00177	0.00123	0.11850	0.00231	+0.00328 -0.00227	0.00142
20	0.07704	0.00261	+0.00181 -0.00132	0.00097	0.09614	0.00286	+0.00254 -0.00181	0.00112

Table C.3

$K^+$ 

Target: Proton

Target: Deuterium

*(excl. VM subtracted)*

Bin	mult	$\sigma_{\text{stat}}$	$\sigma_{\text{RICH}}$	$\sigma_{\text{MC}}$	mult	$\sigma_{\text{stat}}$	$\sigma_{\text{RICH}}$	$\sigma_{\text{MC}}$
1	0.24324	0.00427	+0.00348 -0.01773	0.00374	0.23007	0.00383	+0.00339 -0.01669	0.00350
2	0.25105	0.00565	+0.00390 -0.01820	0.00401	0.25390	0.00517	+0.00341 -0.01740	0.00395
3	0.25791	0.00502	+0.00384 -0.01777	0.00325	0.25062	0.00477	+0.00431 -0.01717	0.00319
4	0.27513	0.00576	+0.00491 -0.01874	0.00301	0.26601	0.00524	+0.00447 -0.01741	0.00290
5	0.31796	0.00909	+0.00722 -0.01934	0.00350	0.28920	0.00853	+0.00688 -0.01772	0.00324
6	0.15779	0.00322	+0.00233 -0.00598	0.00309	0.15045	0.00294	+0.00254 -0.00596	0.00293
7	0.15451	0.00400	+0.00231 -0.00620	0.00309	0.14897	0.00373	+0.00252 -0.00606	0.00301
8	0.17044	0.00368	+0.00223 -0.00577	0.00263	0.16592	0.00344	+0.00261 -0.00530	0.00254
9	0.18232	0.00409	+0.00285 -0.00428	0.00238	0.16965	0.00376	+0.00303 -0.00404	0.00223
10	0.19565	0.00602	+0.00337 -0.00333	0.00247	0.18076	0.00569	+0.00298 -0.00264	0.00233
11	0.10160	0.00212	+0.00000 -0.00130	0.00196	0.10202	0.00193	+0.00000 -0.00125	0.00192
12	0.10159	0.00268	+0.00000 -0.00109	0.00202	0.10037	0.00238	+0.00000 -0.00097	0.00192
13	0.10967	0.00240	+0.00000 -0.00097	0.00164	0.10026	0.00218	+0.00000 -0.00096	0.00152
14	0.11280	0.00261	+0.00007 -0.00090	0.00141	0.10867	0.00246	+0.00000 -0.00138	0.00136
15	0.11594	0.00367	+0.00074 -0.00045	0.00135	0.10692	0.00351	+0.00116 -0.00045	0.00128
16	0.05532	0.00176	+0.00116 -0.00405	0.00155	0.04653	0.00149	+0.00144 -0.00411	0.00133
17	0.04953	0.00215	+0.00078 -0.00332	0.00153	0.04624	0.00190	+0.00063 -0.00343	0.00136
18	0.05742	0.00200	+0.00034 -0.00327	0.00121	0.05396	0.00173	+0.00000 -0.00237	0.00109
19	0.06233	0.00225	+0.00000 -0.00239	0.00105	0.05343	0.00197	+0.00000 -0.00313	0.00092
20	0.06029	0.00308	+0.00000 -0.00169	0.00091	0.05856	0.00286	+0.00000 -0.00130	0.00088

Table C.4



**K<sup>-</sup>**                      **Target: Proton**                      **Target: Deuterium**  
*(excl. VM subtracted)*

Bin	mult	$\sigma_{\text{stat}}$	$\sigma_{\text{RICH}}$	$\sigma_{\text{MC}}$	mult	$\sigma_{\text{stat}}$	$\sigma_{\text{RICH}}$	$\sigma_{\text{MC}}$
1	0.11359	0.00284	+0.00187 -0.01371	0.00207	0.12440	0.00275	+0.00220 -0.01496	0.00220
2	0.12122	0.00390	+0.00224 -0.01427	0.00235	0.12619	0.00368	+0.00221 -0.01535	0.00237
3	0.11484	0.00337	+0.00211 -0.01441	0.00180	0.12635	0.00336	+0.00223 -0.01598	0.00195
4	0.12151	0.00380	+0.00235 -0.01442	0.00170	0.13323	0.00373	+0.00257 -0.01532	0.00183
5	0.12683	0.00571	+0.00324 -0.01521	0.00189	0.13522	0.00577	+0.00338 -0.01610	0.00201
6	0.06197	0.00201	+0.00081 -0.00414	0.00153	0.06877	0.00193	+0.00099 -0.00423	0.00165
7	0.06822	0.00253	+0.00064 -0.00390	0.00166	0.06781	0.00244	+0.00081 -0.00428	0.00170
8	0.05910	0.00214	+0.00082 -0.00329	0.00122	0.06808	0.00219	+0.00097 -0.00381	0.00137
9	0.06035	0.00225	+0.00091 -0.00227	0.00108	0.06237	0.00227	+0.00113 -0.00276	0.00112
10	0.05259	0.00318	+0.00111 -0.00199	0.00103	0.07255	0.00358	+0.00123 -0.00204	0.00135
11	0.03748	0.00122	+0.00000 -0.00086	0.00095	0.03939	0.00114	+0.00000 -0.00094	0.00095
12	0.03157	0.00139	+0.00000 -0.00057	0.00086	0.03904	0.00148	+0.00000 -0.00084	0.00100
13	0.03219	0.00124	+0.00000 -0.00053	0.00069	0.03325	0.00121	+0.00000 -0.00046	0.00070
14	0.02579	0.00126	+0.00000 -0.00045	0.00052	0.03228	0.00129	+0.00000 -0.00059	0.00060
15	0.02971	0.00165	+0.00048 -0.00032	0.00068	0.02646	0.00160	+0.00042 -0.00040	0.00064
16	0.00442	0.00087	+0.00253 -0.00430	0.00061	0.00721	0.00085	+0.00268 -0.00473	0.00061
17	0.00525	0.00100	+0.00171 -0.00301	0.00058	0.00697	0.00095	+0.00191 -0.00345	0.00054
18	0.00618	0.00091	+0.00194 -0.00329	0.00041	0.00573	0.00083	+0.00193 -0.00352	0.00039
19	0.00698	0.00096	+0.00156 -0.00279	0.00033	0.00642	0.00088	+0.00190 -0.00344	0.00030
20	-0.02004	0.00102	+0.00112 -0.00200	0.00151	-0.01684	0.00117	+0.00141 -0.00266	0.00154

Table C.5

$\pi^+$ **Target: Proton****Target: Deuterium***(excl. VM included)*

Bin	mult	$\sigma_{\text{stat}}$	$\sigma_{\text{RICH}}$	$\sigma_{\text{MC}}$	mult	$\sigma_{\text{stat}}$	$\sigma_{\text{RICH}}$	$\sigma_{\text{MC}}$
1	1.45115	0.00777	+0.01750 -0.00491	0.00967	1.41671	0.00709	+0.01704 -0.00478	0.00938
2	1.38316	0.01003	+0.01760 -0.00419	0.00980	1.31061	0.00897	+0.01625 -0.00428	0.00919
3	1.40312	0.00898	+0.01690 -0.00467	0.00774	1.36503	0.00827	+0.01625 -0.00440	0.00751
4	1.42599	0.00986	+0.01554 -0.00489	0.00681	1.38472	0.00918	+0.01486 -0.00525	0.00661
5	1.52178	0.01491	+0.01195 -0.00659	0.00704	1.43512	0.01421	+0.01142 -0.00641	0.00680
6	0.82939	0.00595	+0.00406 -0.00281	0.00764	0.81389	0.00541	+0.00400 -0.00278	0.00743
7	0.80885	0.00759	+0.00371 -0.00265	0.00771	0.75049	0.00670	+0.00340 -0.00260	0.00711
8	0.79439	0.00663	+0.00258 -0.00297	0.00580	0.76803	0.00612	+0.00255 -0.00292	0.00560
9	0.78292	0.00716	+0.00136 -0.00317	0.00487	0.74630	0.00664	+0.00100 -0.00321	0.00468
10	0.77189	0.01020	+0.00174 -0.00299	0.00456	0.73729	0.00967	+0.00153 -0.00314	0.00443
11	0.47011	0.00363	+0.00000 -0.00117	0.00487	0.46211	0.00333	+0.00000 -0.00124	0.00475
12	0.42083	0.00427	+0.00000 -0.00125	0.00434	0.41811	0.00393	+0.00000 -0.00119	0.00425
13	0.41893	0.00379	+0.00000 -0.00118	0.00331	0.39173	0.00344	+0.00000 -0.00114	0.00310
14	0.41380	0.00406	+0.00006 -0.00116	0.00275	0.38355	0.00373	+0.00000 -0.00106	0.00258
15	0.37239	0.00539	+0.00002 -0.00109	0.00229	0.36229	0.00517	+0.00000 -0.00095	0.00226
16	0.28852	0.00286	+0.00433 -0.00318	0.00401	0.28174	0.00261	+0.00433 -0.00329	0.00384
17	0.24032	0.00332	+0.00362 -0.00258	0.00348	0.23897	0.00302	+0.00358 -0.00252	0.00334
18	0.22799	0.00297	+0.00369 -0.00284	0.00256	0.20892	0.00264	+0.00293 -0.00228	0.00234
19	0.21169	0.00315	+0.00272 -0.00225	0.00201	0.20526	0.00291	+0.00329 -0.00228	0.00194
20	0.18424	0.00403	+0.00171 -0.00162	0.00161	0.17425	0.00379	+0.00133 -0.00189	0.00154

**Table C.6**

$\pi^-$                       **Target: Proton**                      **Target: Deuterium**  
*(excl. VM included)*

Bin	mult	$\sigma_{\text{stat}}$	$\sigma_{\text{RICH}}$	$\sigma_{\text{MC}}$	mult	$\sigma_{\text{stat}}$	$\sigma_{\text{RICH}}$	$\sigma_{\text{MC}}$
1	1.11677	0.00668	+0.01419 -0.00419	0.00816	1.22209	0.00646	+0.01514 -0.00459	0.00864
2	1.05407	0.00865	+0.01372 -0.00391	0.00823	1.13597	0.00826	+0.01489 -0.00406	0.00852
3	1.03477	0.00761	+0.01311 -0.00393	0.00642	1.14223	0.00748	+0.01441 -0.00436	0.00685
4	1.01000	0.00826	+0.01165 -0.00419	0.00550	1.11457	0.00817	+0.01246 -0.00467	0.00587
5	1.00332	0.01218	+0.00856 -0.00491	0.00550	1.08234	0.01219	+0.00933 -0.00526	0.00575
6	0.60954	0.00501	+0.00337 -0.00196	0.00638	0.67685	0.00487	+0.00357 -0.00219	0.00678
7	0.56283	0.00616	+0.00302 -0.00185	0.00601	0.59506	0.00584	+0.00318 -0.00185	0.00616
8	0.53850	0.00543	+0.00203 -0.00187	0.00461	0.61116	0.00538	+0.00246 -0.00208	0.00499
9	0.50433	0.00573	+0.00139 -0.00181	0.00374	0.56695	0.00570	+0.00138 -0.00201	0.00402
10	0.47420	0.00805	+0.00153 -0.00166	0.00345	0.52396	0.00814	+0.00151 -0.00176	0.00366
11	0.34132	0.00303	+0.00030 -0.00084	0.00410	0.36523	0.00288	+0.00022 -0.00083	0.00425
12	0.29238	0.00352	+0.00000 -0.00077	0.00360	0.32503	0.00341	+0.00004 -0.00083	0.00382
13	0.26839	0.00301	+0.00019 -0.00063	0.00262	0.31035	0.00302	+0.00009 -0.00078	0.00288
14	0.24510	0.00312	+0.00031 -0.00048	0.00204	0.27299	0.00308	+0.00021 -0.00048	0.00217
15	0.19915	0.00399	+0.00015 -0.00032	0.00161	0.23478	0.00418	+0.00016 -0.00028	0.00180
16	0.20375	0.00231	+0.00422 -0.00307	0.00344	0.23406	0.00227	+0.00472 -0.00329	0.00374
17	0.15904	0.00258	+0.00321 -0.00220	0.00284	0.18233	0.00253	+0.00365 -0.00267	0.00303
18	0.13583	0.00212	+0.00323 -0.00233	0.00193	0.16506	0.00225	+0.00395 -0.00271	0.00223
19	0.11064	0.00213	+0.00273 -0.00200	0.00139	0.13894	0.00227	+0.00372 -0.00257	0.00162
20	0.08413	0.00259	+0.00193 -0.00141	0.00104	0.10609	0.00284	+0.00275 -0.00195	0.00121

Table C.7

$K^+$ 

Target: Proton

Target: Deuterium

*(excl. VM included)*

Bin	mult	$\sigma_{\text{stat}}$	$\sigma_{\text{RICH}}$	$\sigma_{\text{MC}}$	mult	$\sigma_{\text{stat}}$	$\sigma_{\text{RICH}}$	$\sigma_{\text{MC}}$
1	0.24869	0.00424	+0.00356 -0.01815	0.00384	0.23586	0.00381	+0.00347 -0.01713	0.00360
2	0.25497	0.00563	+0.00396 -0.01851	0.00408	0.25873	0.00516	+0.00347 -0.01775	0.00403
3	0.26189	0.00500	+0.00390 -0.01806	0.00330	0.25463	0.00476	+0.00438 -0.01746	0.00324
4	0.27776	0.00575	+0.00496 -0.01893	0.00304	0.26884	0.00523	+0.00452 -0.01761	0.00294
5	0.31974	0.00907	+0.00726 -0.01947	0.00352	0.29183	0.00852	+0.00695 -0.01789	0.00327
6	0.16621	0.00317	+0.00247 -0.00631	0.00326	0.15997	0.00291	+0.00271 -0.00635	0.00312
7	0.16212	0.00395	+0.00242 -0.00651	0.00324	0.15668	0.00370	+0.00265 -0.00637	0.00316
8	0.17534	0.00365	+0.00230 -0.00595	0.00271	0.17169	0.00342	+0.00271 -0.00549	0.00263
9	0.18599	0.00407	+0.00291 -0.00437	0.00243	0.17380	0.00375	+0.00311 -0.00414	0.00228
10	0.19955	0.00599	+0.00343 -0.00340	0.00252	0.18530	0.00567	+0.00305 -0.00271	0.00238
11	0.11075	0.00208	+0.00000 -0.00144	0.00211	0.11200	0.00190	+0.00000 -0.00141	0.00208
12	0.10910	0.00264	+0.00000 -0.00120	0.00215	0.10773	0.00235	+0.00000 -0.00106	0.00204
13	0.11475	0.00238	+0.00000 -0.00102	0.00171	0.10574	0.00216	+0.00000 -0.00101	0.00159
14	0.11623	0.00259	+0.00007 -0.00093	0.00145	0.11271	0.00245	+0.00000 -0.00143	0.00140
15	0.11797	0.00366	+0.00075 -0.00046	0.00137	0.10930	0.00350	+0.00119 -0.00046	0.00131
16	0.05870	0.00174	+0.00121 -0.00423	0.00162	0.04963	0.00147	+0.00151 -0.00432	0.00139
17	0.05181	0.00213	+0.00081 -0.00343	0.00157	0.04861	0.00188	+0.00065 -0.00356	0.00141
18	0.05960	0.00199	+0.00035 -0.00336	0.00124	0.05604	0.00172	+0.00000 -0.00244	0.00112
19	0.06409	0.00224	+0.00000 -0.00245	0.00107	0.05514	0.00197	+0.00000 -0.00321	0.00094
20	0.06112	0.00308	+0.00000 -0.00170	0.00092	0.06010	0.00285	+0.00000 -0.00133	0.00090

Table C.8

**K<sup>-</sup>**                      **Target: Proton**                      **Target: Deuterium**  
*(excl. VM included)*

Bin	mult	$\sigma_{\text{stat}}$	$\sigma_{\text{RICH}}$	$\sigma_{\text{MC}}$	mult	$\sigma_{\text{stat}}$	$\sigma_{\text{RICH}}$	$\sigma_{\text{MC}}$
1	0.11731	0.00282	+0.00194 -0.01417	0.00215	0.12868	0.00274	+0.00227 -0.01550	0.00229
2	0.12437	0.00388	+0.00230 -0.01465	0.00242	0.12942	0.00366	+0.00226 -0.01576	0.00244
3	0.11667	0.00336	+0.00214 -0.01466	0.00184	0.12866	0.00335	+0.00227 -0.01629	0.00199
4	0.12312	0.00379	+0.00238 -0.01463	0.00172	0.13501	0.00373	+0.00260 -0.01553	0.00185
5	0.12808	0.00570	+0.00328 -0.01536	0.00191	0.13706	0.00576	+0.00342 -0.01633	0.00203
6	0.06712	0.00199	+0.00088 -0.00449	0.00166	0.07517	0.00191	+0.00108 -0.00462	0.00179
7	0.07247	0.00250	+0.00068 -0.00414	0.00176	0.07227	0.00242	+0.00087 -0.00456	0.00181
8	0.06194	0.00213	+0.00086 -0.00345	0.00128	0.07155	0.00218	+0.00103 -0.00401	0.00144
9	0.06251	0.00224	+0.00094 -0.00236	0.00112	0.06498	0.00226	+0.00117 -0.00288	0.00117
10	0.05377	0.00317	+0.00113 -0.00204	0.00105	0.07467	0.00357	+0.00127 -0.00210	0.00139
11	0.04215	0.00120	+0.00000 -0.00100	0.00105	0.04423	0.00112	+0.00000 -0.00109	0.00106
12	0.03462	0.00137	+0.00000 -0.00065	0.00093	0.04285	0.00147	+0.00000 -0.00095	0.00109
13	0.03441	0.00123	+0.00000 -0.00058	0.00073	0.03574	0.00120	+0.00000 -0.00051	0.00074
14	0.02723	0.00125	+0.00000 -0.00048	0.00055	0.03410	0.00128	+0.00000 -0.00062	0.00063
15	0.03061	0.00164	+0.00049 -0.00033	0.00070	0.02740	0.00159	+0.00043 -0.00041	0.00065
16	0.00520	0.00087	+0.00272 -0.00461	0.00062	0.00826	0.00085	+0.00288 -0.00509	0.00063
17	0.00591	0.00099	+0.00181 -0.00319	0.00059	0.00770	0.00095	+0.00203 -0.00366	0.00056
18	0.00674	0.00090	+0.00204 -0.00346	0.00042	0.00632	0.00082	+0.00203 -0.00371	0.00040
19	0.00736	0.00096	+0.00162 -0.00289	0.00034	0.00684	0.00088	+0.00199 -0.00359	0.00031
20	-0.01988	0.00102	+0.00115 -0.00205	0.00151	-0.01656	0.00116	+0.00146 -0.00275	0.00154

Table C.9



# List of Figures

2.1	Diagram of the DIS process . . . . .	6
2.2	Proton structure function $F_2^p$ versus $Q^2$ . . . . .	12
2.3	Splitting functions $P_{ab}$ . . . . .	13
2.4	Fragmentation functions from $e^+e^-$ annihilation . . . . .	17
3.1	Schematic view of the HERA accelerator . . . . .	20
3.2	Schematic view of the target area . . . . .	21
3.3	Schematic view of the HERMES spectrometer . . . . .	22
3.4	Response spectra of the PID detectors . . . . .	24
3.5	Momentum dependence of the Čerenkov angle for different hadrons and radiators. . . . .	25
3.6	Example for a HERA fill. . . . .	26
3.7	TRD response for leptons before and after calibration . . . . .	28
4.1	Overview of the HERMES Monte Carlo chain . . . . .	32
4.2	Momentum smearing . . . . .	35
4.3	HERMES detector resolution . . . . .	36
4.4	Loss functions . . . . .	37
4.5	HSG vs. HMC/HRC: Semi-incl. DIS positron distribution vs. $Q^2$ and $W^2$ . . . . .	38
4.6	HSG vs. HMC/HRC: Hadron multiplicities . . . . .	39
4.7	The massless relativistic string in the Lund model. . . . .	40
4.8	Popcorn baryon production . . . . .	42
4.9	Lund symmetric fragmentation function . . . . .	43
4.10	Independent fragmentation model . . . . .	44
4.11	Cluster fragmentation model . . . . .	45
4.12	Lund parameter influence on hadron multiplicities . . . . .	46
4.13	Lund tuning overview . . . . .	50
4.14	Data-MC agreement vs. $z$ . . . . .	52
4.15	Data-MC agreement vs. $p_t$ . . . . .	53
4.16	Data-MC agreement vs. rapidity . . . . .	54
5.1	Schematic analysis overview . . . . .	58
5.2	The RICH $\mathcal{P}$ -matrices for 1 track/detector half . . . . .	64

5.3	Comparison of $\pi^+$ (left) and $K^+$ (right) multiplicities versus $z$ , with and without unfolding. . . . .	66
5.4	Relative hadron fluxes vs. $z$ . . . . .	66
5.5	Impact of the charge symmetric background correction vs. $z$ . . . . .	69
5.6	Impact of the charge symmetric background correction vs. $zx$ . . . . .	70
5.7	Exclusive vector meson fractions vs. $z$ . . . . .	71
5.8	Exclusive vector meson fractions vs. $x_B$ in two $z$ bins. . . . .	72
5.9	DIS process in first order QED (Born level). The scattering kinematics are well defined by the properties of the incoming and outgoing electron. . . . .	74
5.10	Schematic view of the influence of initial and final state radiation on the Born kinematics. The energy transfer $\nu$ is always increased by the energy of the Bremsstrahlungphoton. This gives rise to the asymmetric shape of the smearing matrices (Fig. 5.13 and 5.14) . . . . .	75
5.11	Higher order QED contributions to the DIS process. . . . .	76
5.12	Bin renumbering scheme for the 2-dimensional binning versus $z$ and $x_B$ . . . . .	78
5.13	The smearing matrix $n(i, j)$ for $\pi^+$ vs $z$ . . . . .	79
5.14	The smearing matrix $n(i, j)$ for $\pi^+$ in the 2D $zx$ binning . . . . .	80
5.15	The matrix $n_{DIS}$ in the 2D $zx$ binning . . . . .	81
5.16	Average $Q^2$ of the multiplicities for several hadron types versus $z$ . . . . .	83
5.17	Average $Q^2$ for $\pi^+$ and $K^-$ . . . . .	84
5.18	Comparison of $F_2^P$ from ALLM97 and CTEQ6M . . . . .	85
5.19	$Q^2$ evolution factors vs. $z$ . . . . .	88
5.20	Overview over the different error contributions . . . . .	89
6.1	Comparison of the updated analysis (this work) with the release from June 2004 . . . . .	91
6.2	Pion multiplicities vs. $z$ from P and D target . . . . .	93
6.3	Target and charge ratios of pion multiplicities vs. $z$ . . . . .	94
6.4	Pion multiplicities vs. $z$ evolved to $Q^2 = 2.5 \text{ GeV}^2$ . . . . .	95
6.5	Pion multiplicities vs. $z$ evolved to $Q^2 = 25 \text{ GeV}^2$ in comparison with EMC . . . . .	96
6.6	Pion multiplicities vs. $x_B$ from P and D target . . . . .	97
6.7	Enhancement and suppression of favoured fragmentation for $\pi^+$ and $\pi^-$ vs. $x_B$ . . . . .	98
6.8	Purities for $\pi^\pm$ and $K^\pm$ . . . . .	99
6.9	Comparison of charged pion results vs. $x_B$ from the old and current analysis . . . . .	100
6.10	Independence of the acceptance correction method from the Monte Carlo tune . . . . .	101
6.11	$Q^2$ evolution: Influence of different FF parametrisations and different evolution formula . . . . .	102
6.12	Acceptance correction factors with and without accounting for lepton acceptance. . . . .	103
6.13	Pion multiplicities vs. $Q^2$ from P and D target . . . . .	103
6.14	Comparison of $(\pi^+ + \pi^-)$ multiplicities vs. $Q^2$ with a parametrisation by S. Kretzer . . . . .	104



---

6.15	Kaon multiplicities vs. $z$ from P and D target . . . . .	106
6.16	Target and charge ratios of kaons multiplicities vs. $z$ . . . . .	107
6.17	Kaon multiplicities vs. $z$ evolved to $Q^2 = 25 \text{ GeV}^2$ in comparison with EMC . . . . .	108
6.18	Kaon multiplicities vs. $x_B$ from P and D target . . . . .	109
6.19	Enhancement and suppression of favoured fragmentation for $K^+$ and $K^-$ vs. $x_B$ . . . . .	110
6.20	Kaon multiplicities vs. $Q^2$ from P and D target . . . . .	110



# List of Tables

2.1	Definition of kinematic variables . . . . .	7
4.1	Comparison of different Lund tunes . . . . .	55
5.1	Statistics obtained from the deuteron and proton data sets. The hadron numbers refer to the 'raw' data, meaning that they do not account for RICH misidentifications. . . . .	57
5.2	Burst level selection cuts . . . . .	60
5.3	Kinematic cuts on event kinematics and single track properties . . . . .	61
A.1	Binning versus $z$ . . . . .	113
A.2	Born multiplicities vs. $z$ : $\pi^+$ with excl. vector mesons subtracted ( $Q^2 = 2.5 \text{ GeV}^2$ ) . . . . .	114
A.3	Born multiplicities vs. $z$ : $\pi^-$ with excl. vector mesons subtracted ( $Q^2 = 2.5 \text{ GeV}^2$ ) . . . . .	115
A.4	Born multiplicities vs. $z$ : $K^+$ with excl. vector mesons subtracted ( $Q^2 = 2.5 \text{ GeV}^2$ ) . . . . .	116
A.5	Born multiplicities vs. $z$ : $K^-$ with excl. vector mesons subtracted ( $Q^2 = 2.5 \text{ GeV}^2$ ) . . . . .	117
A.6	Born multiplicities vs. $z$ : $\pi^+$ with excl. vector mesons included ( $Q^2 = 2.5 \text{ GeV}^2$ ) . . . . .	118
A.7	Born multiplicities vs. $z$ : $\pi^-$ with excl. vector mesons included ( $Q^2 = 2.5 \text{ GeV}^2$ ) . . . . .	119
A.8	Born multiplicities vs. $z$ : $K^+$ with excl. vector mesons included ( $Q^2 = 2.5 \text{ GeV}^2$ ) . . . . .	120
A.9	Born multiplicities vs. $z$ : $K^-$ with excl. vector mesons included ( $Q^2 = 2.5 \text{ GeV}^2$ ) . . . . .	121
A.10	Born multiplicities vs. $z$ : $\pi^+$ from a proton target ( $Q^2 = 25 \text{ GeV}^2$ ) . . . . .	122
A.11	Born multiplicities vs. $z$ : $\pi^-$ from a proton target ( $Q^2 = 25 \text{ GeV}^2$ ) . . . . .	123
A.12	Born multiplicities vs. $z$ : $K^+$ from a proton target ( $Q^2 = 25 \text{ GeV}^2$ ) . . . . .	124
A.13	Born multiplicities vs. $z$ : $K^-$ from a proton target ( $Q^2 = 25 \text{ GeV}^2$ ) . . . . .	125
B.1	Binning versus $x_B$ in 4 $z$ bins . . . . .	127
B.2	Born multiplicities vs. $x_B$ : $\pi^+$ with excl. vector mesons subtracted ( $Q^2 = 2.5 \text{ GeV}^2$ ) . . . . .	128

B.3	Born multiplicities vs. $x_B: \pi^+$ with excl. vector mesons subtracted ( $Q^2 = 2.5 \text{ GeV}^2$ ) . . . . .	129
B.4	Born multiplicities vs. $x_B: \pi^-$ with excl. vector mesons subtracted ( $Q^2 = 2.5 \text{ GeV}^2$ ) . . . . .	130
B.5	Born multiplicities vs. $x_B: \pi^-$ with excl. vector mesons subtracted ( $Q^2 = 2.5 \text{ GeV}^2$ ) . . . . .	131
B.6	Born multiplicities vs. $x_B: K^+$ with excl. vector mesons subtracted ( $Q^2 = 2.5 \text{ GeV}^2$ ) . . . . .	132
B.7	Born multiplicities vs. $x_B: K^+$ with excl. vector mesons subtracted ( $Q^2 = 2.5 \text{ GeV}^2$ ) . . . . .	133
B.8	Born multiplicities vs. $x_B: K^-$ with excl. vector mesons subtracted ( $Q^2 = 2.5 \text{ GeV}^2$ ) . . . . .	134
B.9	Born multiplicities vs. $x_B: K^-$ with excl. vector mesons subtracted ( $Q^2 = 2.5 \text{ GeV}^2$ ) . . . . .	135
B.10	Born multiplicities vs. $x_B: \pi^+$ with excl. vector mesons included ( $Q^2 = 2.5 \text{ GeV}^2$ ) . . . . .	136
B.11	Born multiplicities vs. $x_B: \pi^+$ with excl. vector mesons included ( $Q^2 = 2.5 \text{ GeV}^2$ ) . . . . .	137
B.12	Born multiplicities vs. $x_B: \pi^-$ with excl. vector mesons included ( $Q^2 = 2.5 \text{ GeV}^2$ ) . . . . .	138
B.13	Born multiplicities vs. $x_B: \pi^-$ with excl. vector mesons included ( $Q^2 = 2.5 \text{ GeV}^2$ ) . . . . .	139
B.14	Born multiplicities vs. $x_B: K^+$ with excl. vector mesons included ( $Q^2 = 2.5 \text{ GeV}^2$ ) . . . . .	140
B.15	Born multiplicities vs. $x_B: K^+$ with excl. vector mesons included ( $Q^2 = 2.5 \text{ GeV}^2$ ) . . . . .	141
B.16	Born multiplicities vs. $x_B: K^-$ with excl. vector mesons included ( $Q^2 = 2.5 \text{ GeV}^2$ ) . . . . .	142
B.17	Born multiplicities vs. $x_B: K^-$ with excl. vector mesons included ( $Q^2 = 2.5 \text{ GeV}^2$ ) . . . . .	143
C.1	Binning versus $Q^2$ in 4 $z$ bins . . . . .	145
C.2	Born multiplicities vs. $Q^2: \pi^+$ with excl. vector mesons subtracted . . .	146
C.3	Born multiplicities vs. $Q^2: \pi^-$ with excl. vector mesons subtracted . . .	147
C.4	Born multiplicities vs. $Q^2: K^+$ with excl. vector mesons subtracted . . .	148
C.5	Born multiplicities vs. $Q^2: K^-$ with excl. vector mesons subtracted . . .	149
C.6	Born multiplicities vs. $Q^2: \pi^+$ with excl. vector mesons included . . . .	150
C.7	Born multiplicities vs. $Q^2: \pi^-$ with excl. vector mesons included . . . .	151
C.8	Born multiplicities vs. $Q^2: K^+$ with excl. vector mesons included . . . .	152
C.9	Born multiplicities vs. $Q^2: K^-$ with excl. vector mesons included . . . .	153

# Bibliography

- [Abb00] G. Abbiendi et al. (OPAL Collaboration), *Leading particle production in light flavour jets*, Eur. Phys. J. **C16**, 407–421 (2000).
- [Abe97] K. Abe et al. (SLD Collaboration), *Measurement of leading particle effects in decays of  $Z^0$  bosons into light flavors*, Phys. Rev. Lett. **78**, 3442–3446 (1997).
- [Abe99] K. Abe et al. (SLD Collaboration), *Production of  $\pi^+$ ,  $K^+$ ,  $K^0$ ,  $K^{*0}$ ,  $\phi$ ,  $p$  and  $\Lambda^0$  in hadronic  $Z^0$  decays*, Phys. Rev. **D59**, 052001(pp. 1–33) (1999).
- [Abr96] P. Abreu et al. (DELPHI Collaboration), *Performance of the DELPHI detector*, Nucl. Instrum. Meth. **A378**, 57–100 (1996), [Erratum-ibid. A **396** 281(1997)].
- [Abr97a] H. Abramowicz and A. Levy, *The ALLM parameterization of  $\sigma_{\text{tot}}(\gamma^* p)$ : An update*, (1997), hep-ph/9712415, DESY 97-251.
- [Abr97b] P. Abreu et al. (DELPHI Collaboration), *A measurement of  $\alpha_s$  from the scaling violation in  $e^+e^-$  annihilation*, Phys. Lett. **B398**, 194–206 (1997).
- [Abr98] P. Abreu et al. (DELPHI Collaboration),  *$\pi^\pm$ ,  $K^\pm$ ,  $p$  and  $\bar{p}$  production in  $Z^0 \rightarrow q\bar{q}$ ,  $Z^0 \rightarrow b\bar{b}$ ,  $Z^0 \rightarrow u\bar{u}$ ,  $d\bar{d}$ ,  $s\bar{s}$* , Eur. Phys. J. **C5**, 585–620 (1998).
- [Ack98] K. Ackerstaff et al. (HERMES Collaboration), *HERMES spectrometer*, Nucl. Instrum. Meth. **A417**, 230–265 (1998).
- [Ada97] M. R. Adams et al. (E665 Collaboration), *Inclusive single-particle distributions and transverse momenta of forward produced charged hadrons in  $\mu p$  scattering at 470 GeV*, Z. Phys. **C76**, 441–463 (1997).
- [Adl97] C. Adloff et al. (H1 Collaboration), *Measurement of event shape variables in deep inelastic  $ep$  scattering*, Phys. Lett. **B406**, 256–270 (1997).
- [Aih88] H. Aihara et al. (TPC/Two Gamma Collaboration), *Charged Hadron Inclusive Cross-Sections and Fractions in  $e^+e^-$  Annihilation at  $\sqrt{s} = 29$  GeV*, Phys. Rev. Lett. **61**, 1263–1266 (1988).

- [Air01] A. Airapetian et al. (HERMES Collaboration), *Multiplicity of charged and neutral pions in deep-inelastic scattering of 27.5 GeV positrons on hydrogen*, Eur. Phys. J. **C21**, 599–606 (2001).
- [Air05] A. Airapetian et al. (HERMES Collaboration), *Quark helicity distributions in the nucleon for up, down, and strange quarks from semi-inclusive deep-inelastic scattering*, Phys. Rev. **D71**, 012003 (2005).
- [Ako02] N. Akopov et al., *The HERMES dual-radiator ring imaging Cerenkov detector*, Nucl. Instrum. Meth. **A479**, 511–530 (2002).
- [Aku97] I. Akushevich, A. Ilichev, N. Shumeiko, A. Soroko and A. Tolkachev, *POLRAD 2.0: FORTRAN code for the radiative corrections calculation to deep inelastic scattering of polarized particles*, Comput. Phys. Commun. **104**, 201–244 (1997).
- [Aku98] I. Akushevich, H. Böttcher and D. Ryckbosch, *RADGEN 1.0: Monte Carlo generator for radiative events in DIS on polarized and unpolarized targets*, 1998, hep-ph/9906408.
- [Alb05] S. Albino, B. A. Kniehl and G. Kramer, *Fragmentation functions for light charged hadrons with complete quark flavour separation*, (2005), hep-ph/0502188.
- [Ali80] A. Ali, J. G. Körner, G. Kramer and J. Willrodt, *Heavy quarks in  $e^+e^-$  annihilation*, Nucl. Phys. **B168**, 409 (1980).
- [Alt77] G. Altarelli and G. Parisi, *Asymptotic freedom in parton language*, Nucl. Phys. **B126**, 298–318 (1977).
- [And83a] B. Andersson, G. Gustafson, G. Ingelman and T. Sjöstrand, *Parton Fragmentation and String Dynamics*, Phys. Rept. **97**, 31–145 (1983).
- [And83b] B. Andersson, G. Gustafson and B. Söderberg, *A General Model for Jet Fragmentation*, Z. Phys. **C20**, 317 (1983).
- [And85] B. Andersson, G. Gustafson and T. Sjöstrand, *Baryon Production in Jet Fragmentation and  $\Upsilon$  Decay*, Phys. Scripta **32**, 574–580 (1985).
- [And97] B. Andersson, *The Lund model*, Camb. Monogr. Part. Phys. Nucl. Phys. Cosmol. **7**, 471pp. (1997).
- [Arn89] M. Arneodo et al. (European Muon Collaboration), *Measurements of the  $u$  valence quark distribution function in the proton and  $u$  quark fragmentation functions*, Nucl. Phys. **B321**, 541–560 (1989).
- [Ash88] J. Ashman et al. (European Muon Collaboration), *A measurement of the spin asymmetry and determination of the structure function  $g_1$  in deep inelastic muon proton scattering*, Phys. Lett. **B206**, 364–370 (1988).

- [Ash91] J. Ashman et al. (European Muon Collaboration), *Forward produced hadrons in  $\mu p$  and  $\mu d$  scattering and investigation of the charge structure of the nucleon*, *Z. Phys.* **C52**, 361–388 (1991).
- [Aub85] J. J. Aubert et al. (European Muon Collaboration), *A Determination of Fragmentation Functions of  $u$  Quarks into Charged Pions*, *Phys. Lett.* **B160**, 417–420 (1985).
- [Ava98] H. Avakian et al., *Performance of the electromagnetic calorimeter of the HERMES experiment*, *Nucl. Instrum. Meth.* **A417**, 69–78 (1998).
- [Bau03] C. Baumgarten et al., *The storage cell of the polarized H/D internal gas target of the HERMES experiment at HERA*, *Nucl. Instrum. Meth.* **A496**, 277–285 (2003).
- [Ber02] C. Berger, *Elementarteilchenphysik (in German)*, Springer, 1st edition, 2002.
- [Bia99] N. Bianchi and P. Di Nezza, *Pion electroproduction in Deep Inelastic Scattering*, November 1999, HERMES release report.
- [Bin95] J. Binnewies, B. A. Kniehl and G. Kramer, *Next-to-leading order fragmentation functions for pions and kaons*, *Z. Phys.* **C65**, 471–480 (1995).
- [BjØ69] J. D. BjØrken and E. A. Paschos, *Inelastic Electron-Proton and  $\gamma$ -Proton Scattering and the Structure of the Nucleon*, *Phys. Rev.* **185**, 1975–1982 (1969).
- [Blo69] E. D. Bloom et al., *High-Energy Inelastic  $e-p$  Scattering at  $6^\circ$  and  $10^\circ$* , *Phys. Rev. Lett.* **23**, 930–934 (1969).
- [Blo70] E. D. Bloom et al., *Recent Results in Inelastic Electron Scattering*, (1970), Presented at the XV International Conference on High Energy Physics, Kiev, USSR, Aug 26-Sep4, 1970.
- [Bra82] R. Brandelik et al. (TASSO Collaboration), *Scale Breaking in Inclusive Charged Particle Production by  $e^+e^-$  annihilation*, *Phys. Lett.* **B114**, 65 (1982).
- [Bre99] J. Breitweg et al. (ZEUS Collaboration), *Measurement of multiplicity and momentum spectra in the current and target regions of the Breit frame in deep inelastic scattering at HERA*, *Eur. Phys. J.* **C11**, 251–270 (1999).
- [Bro94] R. Brock et al. (CTEQ Collaboration), *Handbook of perturbative QCD; Version 1.1: September 1994*, (1994), FERMILAB-PUB-94-316.
- [Bru78] R. Brun, R. Hagelberg, M. Hansroul and J. C. Lassalle, *GEANT: Simulation Program for Particle Physics Experiments. User Guide and Reference Manual*, (1978), CERN-DD-78-2-REV.

- [Bus93] D. Buskulic et al. (ALEPH Collaboration), *A Precise Measurement of  $\Gamma_{Z \rightarrow b\bar{b}}/\Gamma_{Z \rightarrow \text{hadrons}}$* , Phys. Lett. **B313**, 535–548 (1993).
- [Bus95] D. Buskulic et al. (ALEPH Collaboration), *Measurement of  $\alpha_s$  from scaling violations in fragmentation functions in  $e^+e^-$  annihilation*, Phys. Lett. **B357**, 487–499 (1995), [Erratum-ibid. B **364** (1995) 247].
- [Cah78] R. N. Cahn, *Azimuthal dependence in lepton production: A simple parton model calculation*, Phys. Lett. **B78**, 269–273 (1978).
- [Cah89] R. N. Cahn, *Critique of parton model calculations of azimuthal dependence in lepton production*, Phys. Rev. **D40**, 3107–3110 (1989).
- [Cal69] J. Callan, C. G. and D. J. Gross, *High-energy electroproduction and the constitution of the electric current*, Phys. Rev. Lett. **22**, 156–159 (1969).
- [Col97] J. C. Collins, *Light-cone variables, rapidity and all that*, (1997), hep-ph/9705393.
- [Cor01] G. Corcella et al., *HERWIG 6: An event generator for hadron emission reactions with interfering gluons (including supersymmetric processes)*, JHEP **01**, 010:1–96 (2001).
- [Die03] M. Diefenthaler, *HSG-Short Tracks*, 2003.
- [Die05] M. Diehl, W. Kugler, A. Schäfer and C. Weiss, *Exclusive channels in semi-inclusive production of pions and kaons*, (2005), 33pp., hep-ph/0506171.
- [Dok77] Y. L. Dokshitzer, *Calculation of the structure functions for deep inelastic scattering and  $e^+e^-$  annihilation by perturbation theory in quantum chromodynamics. (in russian)*, Sov. Phys. JETP **46**, 641–653 (1977).
- [Dür95] M. Düren, *The HERMES experiment: From the design to the first results*, Habilitation thesis, Friedrich-Alexander-Universität Erlangen-Nürnberg, 1995, Hamburg DESY - Int.Rep.HERMES-95-02 (95/07,rec.Aug.) 234 pp.
- [Edé97] P. Edén and G. Gustafson, *Baryon production in the string fragmentation picture*, Z. Phys. **C75**, 41–49 (1997).
- [Eid04] S. Eidelman et al. (Particle Data Group Collaboration), *Review of particle physics*, Phys. Lett. **B592**, 1 (2004).
- [Ell03] F. Ellinghaus, *Beam-Charge and Beam-Spin Azimuthal Asymmetries in Deeply-Virtual Compton Scattering*, PhD thesis, Humboldt-Universität Berlin, 2003, DESY-THESIS-2004-005.
- [Fey69] R. P. Feynman, *Very high-energy collisions of hadrons*, Phys. Rev. Lett. **23**, 1415–1417 (1969).



- [Fie78] R. D. Field and R. P. Feynman, *A parametrization of the properties of quark jets*, Nucl. Phys. **B136**, 1–76 (1978).
- [Gei98] P. Geiger, *Measurement of fragmentation functions at HERMES*, PhD thesis, Ruprecht-Karls-Universität Heidelberg, 1998, DESY-HERMES-98-05.
- [Glü82] M. Glück, E. Hoffmann and E. Reya, *Scaling Violations and the Gluon Distribution of the Nucleon*, Zeit. Phys. **C13**, 119–130 (1982).
- [Glü98] M. Glück, E. Reya and A. Vogt, *Dynamical parton distributions revisited*, Eur. Phys. J. **C5**, 461–470 (1998).
- [GM64] M. Gell-Mann, *A Schematic model of baryons and mesons*, Phys. Lett. **8**, 214–215 (1964).
- [Gol89] D. E. Goldberg, *Genetic Algorithms in Search, Optimization and Machine Learning*, Addison-Wesley Longman Publishing Co., Inc., Boston, MA, USA, 1989.
- [Got87] T. D. Gottschalk and D. A. Morris, *A new model for hadronization and  $e^+e^-$  annihilation*, Nucl. Phys. **B288**, 729–781 (1987).
- [Gri72] V. N. Gribov and L. N. Lipatov, *Deep inelastic ep scattering in perturbation theory*, Sov. J. Nucl. Phys. **15**, 438–450 (1972).
- [Gul04] H. Guler, *HSG for photons, studies and implementation*, Dec 2004, Talk on the HERMES collaboration meeting.
- [Hal84] F. Halzen and A. D. Martin, *Quarks & Leptons: An Introductory Course in Modern Particle Physics*, John Wiley & Sons, Inc., 1984.
- [Hil04a] A. Hillenbrand, B. Maiheu and E.-C. Aschenauer, *Extraction of Pion and Kaon multiplicities from Hermes 2000 data*, March 2004, HERMES Release Report.
- [Hil04b] A. Hillenbrand, B. Maiheu and E.-C. Aschenauer, *Extraction of Pion and Kaon multiplicities from Hermes 2000 data — Additional studies and cross checks*, June 2004, HERMES Release Report.
- [Hil05] A. Hillenbrand, B. Maiheu and E.-C. Aschenauer, *Monte Carlo study of the influence of possible  $\langle \cos \phi \rangle_{UU}$  moments on the HERMES acceptance function for hadrons.*, 2005, HERMES Internal Note 05-004, 37pp.
- [Hom02] B. Hommeiz, H. Jackson, R. Kaiser and Y. Miyachi, *Using the RICH detector for Physics Analysis (Version 1.4)*, 2002, Internal HERMES Note.
- [Hoy79] P. Hoyer, P. Osland, H. G. Sander, T. F. Walsh and P. M. Zerwas, *Quantum chromodynamics and jets in  $e^+e^-$* , Nucl. Phys. **B161**, 349–372 (1979).

- [Ing97a] G. Ingelman, A. Edin and J. Rathsman, *LEPTO 6.5 - A Monte Carlo Generator for Deep Inelastic Lepton-Nucleon Scattering*, Comput. Phys. Commun. **101**, 108–134 (1997).
- [Ing97b] G. Ingelman, J. Rathsman and G. A. Schuler, *AROMA 2.2 - A Monte Carlo Generator for Heavy Flavour Events in  $ep$  Collisions*, Comput. Phys. Commun. **101**, 135–142 (1997).
- [Jam75] F. James and M. Roos, '*MINUIT*' A System for Function Minimization and Analysis of the Parameter Errors and Correlations, Comput. Phys. Commun. **10**, 343–367 (1975), CERN Program Library Long Writeup D506.
- [Kni00] B. A. Kniehl, G. Kramer and B. Pötter, *Fragmentation functions for pions, kaons, and protons at next-to-leading order*, Nucl. Phys. **B582**, 514–536 (2000).
- [Kni01] B. A. Kniehl, G. Kramer and B. Pötter, *Testing the universality of fragmentation functions*, Nucl. Phys. **B597**, 337–369 (2001).
- [Kra05a] B. Krauß, *Deeply virtual Compton scattering and the HERMES recoil-detector*, PhD thesis, Friedrich-Alexander-Universität Erlangen-Nürnberg, 2005, DESY-THESIS-2005-008.
- [Kra05b] P. Kravchenko, *Tuning JETSET parameters for hyperon production*, Apr 2005, Talk on the HERMES collaboration meeting.
- [Kre00] S. Kretzer, *Fragmentation functions from flavour-inclusive and flavour-tagged  $e^+e^-$  annihilations*, Phys. Rev. **D62**, 054001 (2000).
- [Kre01] S. Kretzer, E. Leader and E. Christova, *Fragmentation functions from semi-inclusive DIS pion production and implications for the polarized parton densities*, Eur. Phys. J. **C22**, 269–276 (2001).
- [Kre05] S. Kretzer, 2005, Private communication.
- [Lie03] P. Liebing, *Contribution of diffractive events to the semi-inclusive data*, 2003, DESY-HERMES-03-20.
- [Lie04] P. Liebing, *Can the Gluon Polarization in the Nucleon be Extracted from HERMES Data on Single High- $p_T$  Hadrons?*, PhD thesis, Universität Hamburg, July 2004, DESY-THESIS-2004-036.
- [Lip75] L. N. Lipatov, *The parton model and perturbation theory*, Sov. J. Nucl. Phys. **20**, 94–102 (1975).
- [Man92] L. Mankiewicz, A. Schäfer and M. Veltri, *PEPSI: A Monte Carlo generator for polarized leptonproduction*, Comput. Phys. Commun. **71**, 305–318 (1992).

- [Mar84] G. Marchesini and B. R. Webber, *Simulation of QCD jets including soft gluon interference*, Nucl. Phys. **B238**, 1–29 (1984).
- [Mar00] A. D. Martin, R. G. Roberts, W. J. Stirling and R. S. Thorne, *Parton distributions and the LHC: W and Z production*, Eur. Phys. J. **C14**, 133–145 (2000).
- [Men01] F. M. Menden, *Determination of the gluon polarization in the nucleon*, PhD thesis, Albert-Ludwigs-Universität Freiburg, November 2001, DESY-THESIS-2001-060.
- [Mil02] A. Miller, *Applying Radiative Corrections to Ratios of Cross Sections for Deeply Inelastic Scattering*, 2002, unpublished.
- [Miy04] Y. Miyachi, *RICH Systematic Study: Past, Present and Future*, Sep 2004, Talk at the Sep. 2004 Collaboration Meeting.
- [Miy05] Y. Miyachi, 2005, Private communication.
- [Nas03] A. Nass et al., *The HERMES polarized atomic beam source*, Nucl. Instrum. Meth. **A505**, 633–644 (2003).
- [Nel65] J. Nelde and R. Mead, *A Simplex Method for Function Minimization*, Comput. J. **7**, 308–313 (1965).
- [Pov04] B. Povh, K. Rith, C. Scholz and F. Zetsche, *Teilchen und Kerne (in German)*, Springer, 6th edition, 2004.
- [Pre92] W. H. Press, S. A. Teukolsky, W. T. Vetterling and B. P. Flannery, *Numerical Recipes in C: The Art of Scientific Computing*, Cambridge University Press, 1992.
- [Pum02] J. Pumplin et al., *New generation of parton distributions with uncertainties from global QCD analysis*, JHEP **07**, 012, 1–47 (2002).
- [Rit02] K. Rith, *Spin asymmetries in deep-inelastic electron nucleon scattering: Selected HERMES results*, Prog. Part. Nucl. Phys. **49**, 245–324 (2002).
- [Rut11] E. Rutherford, *The Scattering of the  $\alpha$  and  $\beta$  Rays and the Structure of the Atom*, Proc. of the Manch. Lit. and Phil. Soc., IV **55**, 18–20 (1911).
- [Sjö84a] T. Sjöstrand, *Jet fragmentation of multiparton configurations in a string framework*, Nucl. Phys. **B248**, 469–502 (1984).
- [Sjö84b] T. Sjöstrand, *The merging of jets*, Phys. Lett. **B142**, 420–424 (1984).
- [Sjö88] T. Sjöstrand, *Status of fragmentation models*, Int. J. Mod. Phys. **A3**, 751–823 (1988).

- [Sjö01] T. Sjöstrand et al., *High-energy-physics event generation with PYTHIA 6.1*, Comput. Phys. Commun. **135**, 238–259 (2001).
- [Sjö03] T. Sjöstrand, L. Lönnblad, S. Mrenna and P. Skands, *PYTHIA 6.3: Physics and manual*, 2003, hep-ph/0308153.
- [Sok64] A. A. Sokolov and I. M. Ternov, *On Polarization and spin effects in the theory of synchrotron radiation*, Phys. Dokl. **8**, 1203–1205 (1964).
- [Tal98] H. A. M. Tallini, *A measurement of the quark spin distributions of the nucleon at HERMES*, PhD thesis, University of Liverpool, 1998, DESY-HERMES-98-24.
- [Tyt01] M. Tytgat, *Diffraction production of  $\rho^0$  and  $\omega$  vector mesons at HERMES*, PhD thesis, University of Gent, 2001, DESY-THESIS-2001-018.
- [Wan96] W. Wander, *Reconstruction of high energy scattering events in the HERMES experiment*, PhD thesis, Friedrich-Alexander-Universität Erlangen-Nürnberg, 1996, DESY-HERMES-97-31.
- [Web84] B. R. Webber, *A QCD model for jet fragmentation including soft gluon interference*, Nucl. Phys. **B238**, 492–528 (1984).
- [Wei02] C. Weiskopf, *Measurement of the spin-dependent structure function  $g_1(d)$  of the deuteron at HERMES. (In German)*, PhD thesis, Friedrich-Alexander-Universität Erlangen-Nürnberg, 2002, DESY-THESIS-2002-039.
- [Wen99] J. Wendland, *Improved particle identification at HERMES and polarised valence quark distributions in the proton*, 1999, DESY-HERMES-99-16.
- [Wen03] J. Wendland, *Polarized Parton Distributions Measured at the Hermes Experiment*, PhD thesis, Simon Fraser University, September 2003, DESY-THESIS-2003-032.

# Acknowledgment

First of all I would like to thank my supervisor Prof. Dr. Klaus Rith for his support and for providing me the possibility to work on such an interesting subject in an exciting international community. I am also indebted to him for allowing me to be based the whole time in the great city of Hamburg and giving me the possibility to attend conferences and summer schools, which were not only interesting themselves but also often at interesting places.

In Hamburg, I have to foremost thank Elke-Caroline Aschenauer. Without her guidance and support, this thesis would maybe never have been finished. Our small multiplicity group was completed by Bino Maiheu, with whom I spend considerable time chasing down these last hadrons which mysteriously showed up in the result of one of us, but not in the other. I enjoyed it a lot to work in our small analysis group. I also would like to thank Marc Beckmann, who not only guided me on my first analysis steps, but whose HASY code provided the foundation for my own analysis code. Discussions with and comments from various people contributed a lot to the work presented here. For this I am deeply grateful.

During these years, I had the pleasure to share my office with Mark Henoeh, Phil Tait and Markus Diefenthaler. Together we enjoyed the beautiful view on the back side of building 55. They also helped me to take care of the office plants inherited from Ines, and I'm happy to announce a survival rate of 75% for the last 4 years.

Life outside the office was made enjoyable by a lot of offsite activities, including, of course, the mother of all such events, the offsite meeting itself. For this and all the other activities, a hearty thank you to Andreas, Beni, Bino, Caro, Charlotte, Dominik, Frank, Hayg, Larry, Marc, Ralf, Markus (2x), Phil, Sebastian, Soerne, Uli, Yves . . . and all whom I forgot (sorry!).

Being in Hamburg most of the time naturally limited somewhat the contact with my Erlangen-based colleagues. Nevertheless, I enjoyed our meetings and activities in Erlangen and Hamburg. So thanks to Martin Raithel, Didi Zeiler, Nils Pickert, Bernhard Krauss, Friedrich Stinzing, Tom Michler . . . and especially Christian Vogel, who has always a cryptic solution for an obscure computing problem.

I would like to thank the staff in Hamburg and Erlangen, Sabine Krohn, Soerne Moeller and Eleonore Hassler, the latter in particular for patiently reminding me of those forms I should have filled out last week at the latest.

Last but not least, of course, I want to thank my parents for their huge support in all those years.



# Zusammenfassung

Diese Arbeit beschäftigt sich mit dem Fragmentationsprozess bei HERMES. Sie kann in zwei wesentliche Unterthemen gegliedert werden: die Simulation der Hadronisierung mit Hilfe eines Monte Carlo Modells sowie die Extraktion von ladungs- und hadrontyp-separierten Born-Multiplizitäten.

Im Monte Carlo-Teil wurde das Lund-Modell an experimentelle Hadronspektren angepasst, die aus den HERMES-Daten gewonnen wurden. Im Gegensatz zu früheren Modellanpassungen konnte in dieser Arbeit ein Datensatz verwendet werden, der Informationen des 1998 installierten RICH-Detektors enthielt, welche eine präzise Einteilung der Hadronen in Pionen, Kaonen und Protonen ermöglichten. Diese zusätzlichen Informationen gestatteten ein detaillierteres Anpassen der Modellparameter, welche teilweise erst durch die verbesserten Daten zugänglich wurden. Desweiteren wurde ein neuer iterativer Tuning-Algorithmus implementiert, der aufgrund seiner Parallelisierbarkeit die verfügbare Rechenleistung auf der HERMES-PC-Farm wesentlich besser ausnutzen konnte. Im Rahmen des Monte Carlo-Tunings wurde auch der HERMES *smearing generator* (HSG) implementiert. Dieses Programm simuliert die kinematischen Verschmierungen und die Ineffizienzen des HERMES-Detektors auf statistischer Basis. Dadurch ermöglicht dieses Programm die Berücksichtigung dieser Effekte ohne zeitaufwändige Detektorsimulation, was den Zeitbedarf zur Erzeugung einer gegebenen Statistik um den Faktor 100 reduziert. Der HSG ist damit unverzichtbar für das iterative Fitten des Lund-Modells, das Programm findet aber auch Anwendung bei Monte Carlo-Studien anderer Analysegruppen in der HERMES-Kollaboration.

Die Arbeit am Lund-Modell führte zu einem deutlich verbesserten Parametersatz, wobei besonders starke Verbesserungen bei den (Anti-)Protonenmultiplizitäten erzielt wurden. Die gleichermassen zufriedenstellende Beschreibung von positiven und negativen Kaonen ist ein noch zu lösendes Problem.

Der zweite Teil der Arbeit beschäftigt sich mit der Gewinnung von Born-Multiplizitäten für Pionen und Kaonen. Pionmultiplizitäten aus  $e^+p$ -Streuung wurden bereits früher von der HERMES-Kollaboration veröffentlicht [Air01]. In dieser Arbeit wurde der Datensatz aus dem Jahr 2000 verwendet. Dieser besitzt eine höhere Statistik und ermöglicht eine verbesserte Teilchenidentifikation aufgrund des RICH-Detektors. Die neue Analyse umfasst zusätzlich zu den Protonendaten Ergebnisse, die an einem Deuteriumtarget gewonnen wurden. Desweiteren wurde die Analyse in einigen Punkten erweitert. So wurde mit Hilfe eines Monte Carlo-Modells der Anteil der Hadronen bestimmt, die nicht aus einem tiefinelastischen Streuprozess stammen sondern ihren Ursprung im Zerfall von

bei elastischer Streuung entstandenen Vektormesonen haben. Ausserdem wurde im Vergleich zur alten Analyse eine neue Methode zur Korrektur von radiativen Verschmierungen und Akzeptanzeffekten verwendet.

Die erzielten Multiplizitäten stellen einen Datensatz mit hoher Statistik für die Verteilung von  $\pi^+$ ,  $\pi^-$ ,  $K^+$  und  $K^-$  als Funktion von  $z$ ,  $x_B$  und  $Q^2$  zur Verfügung, sowohl für Streueignisse an einem Proton- wie an einem Deuteriumtarget. Basierend auf diesen Ergebnissen werden demnächst Fragmentationsfunktionen extrahiert, welche es erlauben werden, die Universalität des Fragmentationsprozesses zu testen. Die Multiplizitäten als Funktion von  $z$  zeigen eine zufriedenstellende Übereinstimmung mit Fragmentationsfunktionen des EMC-Experiments, welche bei einer zehnfach höheren Strahlenergie gewonnen wurden. Die  $Q^2$ -Abhängigkeit der Pionendaten ist im Einklang mit theoretischen Vorhersagen. Zusammen mit der schwachen  $x_B$  Abhängigkeit zeigen die Ergebnisse, daß der Faktorisierungsansatz, welcher für die Bestimmung der Quarkhelizitäten [Air05] von fundamentaler Bedeutung ist, bei HERMES gerechtfertigt ist.



# Lebenslauf

**Name:** Achim Hillenbrand  
**Geburtstag:** 10. April 1974  
**Geburtsort:** Erlangen  
**Nationalität:** Deutsch

## Ausbildung:

---

<b>1980-1984</b>	Grundschule Uttenreuth
<b>1984-1993</b>	Emil-von-Behring Gymnasium Spardorf
<b>1993</b>	Abitur
<b>1993-1995</b>	Ausbildung zum Industriekaufmann bei der Siemens AG ( <i>Stammhauslehre</i> )
<b>1995-2000</b>	Studium an der Friedrich-Alexander Universität Erlangen-Nürnberg Fach: Physik Diplom
<b>1997</b>	Vordiplom
<b>1997-1998</b>	Auslandssemester in St. Andrews, Schottland, UK
<b>1999-2000</b>	Diplomarbeit am Lehrstuhl für Theoretische Physik III ( <i>Strahlungseinfangreaktionen im <math>{}^7\text{Li}</math>-System</i> )
<b>Nov. 2000</b>	Diplom-Hauptprüfung
<b>seit Feb. 2001</b>	Wissenschaftlicher Mitarbeiter am Physikalischen Institut der Universität Erlangen-Nürnberg